University of Strathclyde
Department of Physics

Comprehensive Characterisation of Laser Plasma Wakefield Accelerated Electrons

Richard P. Shanks

A thesis presented in fulfilment of the requirements for the degree of Doctor of Philosophy

2012

Abstract

This thesis describes the first experimental diagnosis of all of the key parameters of mono-energetic, laser wakefield accelerated electrons from a single driving laser, such as charge, transverse emittance, energy spread and bunch length. All of the experiments utilise the 35 fs, 45 TW, TOPS laser on the ALPHA-X beam line. Electron beam energy spectra have been measured using a high resolution magnetic spectrometer. These electrons have an average peak energy of 83 $\pm$ 1.3 MeV. The narrowest measured energy spread is $\sigma_\gamma/\gamma = 0.8$ % which is deconvoluted to 0.5 %. This deconvoluted energy spread sets an upper limit to the bunch length of 0.3 μm due to the curve of the electrostatic potential in the accelerating bubble. This short bunch length is confirmed with the use of coherent transition radiation, used to measured a bunch length of 1.6 ± 0.8 fs after 1 m of propagation which is shown to be < 0.3 μm at the source. In addition, a sub-structure of two separate bunches was observed in both the energy and longitudinal distributions. These two measurements of sub-structure are consistent with each other. The energy separation of the two peaks provides a spatial separation due to the curve of the electrostatic potential which, when allowed to propagate 1 m from the source, agrees well with the measure longitudinal bunch structure. This demonstrates that multiple electron bunches can occur within one bubble, resulting from either a complex injection process or interactions within the bubble. The thesis also presents the first single shot transverse emittance measurement of mono-energetic LWFA electrons. The emittance was measured as low as $\varepsilon_{n,x} = 1.1$ π mm mrad with an average value of $\varepsilon_{n,x} = 2.2 \pm 0.7$ π mm mrad, normalised to 125 MeV. This is an upper limit to the emittance and gives a bunch radius at the source of 3 μm. To produce an electron beam with an emittance of 2.2 π mm mrad, the electrons were injected within a radius of $3.4 \pm 0.4 \mu$m at the rear of the accelerator. The energy spread and beam divergence were both found to increase with increasing charge, Q. The increase in the divergence is proportional to $Q^{\frac{1}{2}}$ (although $Q^{\frac{1}{3}}$ is within errors) caused by an increase in the transverse forces per unit length i.e. an increase in peak current. The increase in energy spread is therefore due to an increase in beam loading caused by the increase in peak current and not due to an increase in bunch length.

Acknowledgements

It would have been impossible to complete this thesis without the help of several people. None more so than my supervisor, Prof. Dino Jaroszynski, whose vision and ambition pushed me to get the best out of myself and my work. Thanks to Riju, first for all his time at the start of my PhD teaching me how to operate and maintain the complex laser system and secondly for his attitude of "keep gathering data until something fails" which saw us working until the early hours of the morning on many occasions. I would like to take the opportunity to thank Mark for al his help, specifically for his work in the analysis of the energy spectra and for developing the laser machining techniques and the machining of the emittance masks. I would like to show my appreciation to my office mate, Enrico, for being my sounding board for all my thoughts and ideas throughout my PhD. Thanks to Gregor for all his time working on the laser and keeping it up to the standards required for LWFA, possibly the only person in the world to have remotely fixed an advanced laser system from a tractor. Thanks also to Greogory for his time working on the design of optical systems. I owe a big thank you to all of the group's experimentalists in general, whose continual contributions in and out of the lab are too numerous to mention. I would also like to thank the groups theoreticians, Bernhard, Rana and Gurav for all their time helping me to develop theories and run simulations. Thanks also to my fellow PhD students, Maria-Pia, Silvia, John, Grace, Constantin, Xue and Sijia for sharing in the highs and lows of experimental physics. Special thanks to the technicians, Tom and David, for their ability to take one of my ideas and turn it into a design and then into an actual device.

I would also like to thank my parents whose support and guidance throughout my whole life, not just my PhD, have got me where I am today. Finally, Franzi, your patience during my long working hours and your support, encouragement and motivation throughout the PhD kept me going.

The Role of the Author

The three key experimental results in this thesis are the energy spread, emittance and bunch length measurements. In the energy spread measurement the author was respon-

sible for running the experiment, collecting the data and performing the preliminary analysis of the data. Mark Wiggins carried out the detailed analysis of the data. The author was responsible, for the design, set-up, data collection, analysis methods and preliminary analysis of the data in the transverse emittance measurements. The analysis methods were then implemented in software capable of batch processing by Enrico Brunetti and the processing of the data and associated statistic analysed by Enrico and Grace Manahan. The emittance masks were laser micro-machined by Mark Wiggins. During the bunch length measurements the author was responsible for the design, setting-up, data collection and analysis of the results.

List of Publications

The following key publications resulted from the work in this thesis:

1. Shanks, R. P., Anania, M. P., Brunetti, E., Cipiccia, S., Ersfeld, B., Gallacher, J. G., et al. "Pepper-pot emittance measurement of laser-plasma wakefield accelerated electrons. *Spie-Int Soc Optical Engineering.* Vol. 7359 (2009).

2. Brunetti, E., Shanks, R. P., Manahan, G. G., Islam, M. R., Ersfeld, B., Anania, M. P., et al. "Low emittance, high brilliance relativistic electron beams from a laser-plasma accelerator. *Physical Review Letters*, 105(21), 4 (2010).

3. Wiggins, S. M., Issac, R. C., Welsh, G. H., Brunetti, E., Shanks, R. P., Anania, M. P., et al. "High quality electron beams from a laser wakefield accelerator. *Plasma Physics and Controlled Fusion*, 52(12), 8, (2010).

4. Wiggins, S. M., Shanks, R. P., Issac, R. C., Welsh, G. H., Anania, M. P., Brunetti, E., et al. "High quality electron beams from a laser wakefield accelerator. *2010 Conference on Lasers and Electro-Optics (Cleo) and Quantum Electronics and Laser Science Conference (Qels)*, 2, (2010).

5. Manahan, G. G., Brunetti, E., Shanks, R. P., Islam, M. R., Ersfeld, B., Anania, M. P., et al. "High resolution, single shot emittance measurement of relativistic electrons from laser-driven accelerator. *Spie-Int Soc Optical Engineering.* Vol. 8079, (2011).

Contents

Abstract **II**

Acknowledgements **III**

List of Figures IX

List of Tables XV

1 Introduction **1**

2 The Laser-Plasma Particle Accelerator **6**

2.1 Ponderomotive Force 6

2.2 Laser Wakefield Acceleration 8

2.2.1 Plasma Waves 8

2.2.2 Wavebreaking 12

2.2.3 Injection 13

2.2.4 Transverse Emittance 14

2.2.5 Acceleration length 15

2.2.6 Phase-Space Evolution 17

2.2.7 Beam Loading 18

2.3 Plasma Optics 25

2.3.1 Self - Focusing and Guiding 25

2.4 OSIRIS Simulations 26

3 Experimental Methods **29**

3.1 The TOPS Laser System 29

3.1.1 The Oscillator 29

3.1.2 The Pulse Stretcher 30

3.1.3 Laser amplifiers 33

3.1.4 Compressor 34

3.1.5 Laser Delivery 35

3.2 Gas Jet 37

3.3 Beam Profile Monitors . . . 37
3.4 Charge Calibration . . . 39
3.4.1 Image Plate . . . 39
3.4.2 Set-up . . . 40
3.4.3 Result . . . 40
3.4.4 Cross calibration of LANEX 1 and LANEX 1.5 . . . 41
3.5 Quadrupoles . . . 43
3.6 Electron Spectrometer . . . 45

4 Emittance **47**
4.1 Introduction . . . 47
4.2 Theory of Emittance . . . 47
4.2.1 Transverse Phase Space . . . 47
4.2.2 Emittance . . . 50
4.2.3 Pepper-Pot Measurement Technique . . . 52
4.3 Experimental Set-up of the Emittance Measurement . . . 54
4.3.1 Pepper-pot Design Considerations . . . 54
4.3.2 The Pepper-pot Set-up . . . 55
4.3.3 Determining the Pepper-pot Mask Thickness . . . 60
4.3.4 Effects of the Laser Beam Block . . . 63
4.4 Experimental Results . . . 65
4.4.1 Low Resolution Measurement . . . 65
4.4.2 Emittance Measurement Re-design . . . 68
4.4.3 High Resolution Measurement . . . 73
4.5 Conclusions and Future Work . . . 77

5 Energy Spread Measurements **79**
5.1 Introduction . . . 79
5.2 Resolution Simulation . . . 79
5.2.1 Effects of Emittance for a Fixed Source Size . . . 80
5.2.2 Effects of Emittance from an Effective Source Size . . . 82
5.2.3 Without the use of Quadrupole Beam Transport . . . 83
5.2.4 With the use of the Quadrupole Lenses in Beam Transport . . . 86
5.3 Measured Energy Spectra . . . 86
5.3.1 Without Quadrupoles . . . 87
5.3.2 With Quadrupoles . . . 89
5.3.3 Energy Spread Scaling with Charge . . . 92
5.3.4 Multiple Energy Peaks . . . 94

5.4 Conclusions and Future Work 94

6 Transition Radiation **95**
6.1 Introduction 95
6.2 Theory of Transition Radiation 95
6.2.1 The Ginzburg-Frank Formula 95
6.2.2 Foil Size Effects 97
6.2.3 Radiated Energy 98
6.2.4 Coherent Transition Radiation 98
6.2.5 Radiation Scaling with Charge 102
6.2.6 Effects of Transverse Bunch Distribution 104
6.2.7 Two Foil Transition Radiation System 108
6.2.8 Electron Bunch Evolution 111
6.3 Experimental Set-up of Transition Radiation Measurement 116
6.3.1 Two Foil Set-up 116
6.3.2 TR Detection 117
6.3.3 TR Calibration 124
6.4 Experimental Results 127
6.4.1 Analysis Techniques 127
6.4.2 Transition Radiation Spectra 132
6.4.3 Charge within the Electron Bunch 153
6.5 Conclusion and Future Work 156

7 Discussion **158**
7.1 Narrow Energy Spread 158
7.2 Transverse Emittance 158
7.3 Charge Dependence 159
7.4 Multiple Electron Bunches 160

8 Conclusion **166**
8.1 Future Work 168

References **170**

List of Figures

2.1 Density wave perturbations in the (a) linear and (b) nonlinear regime. 10
2.2 Diagram of the accelerating wakefield bubble of radius, R 11
2.3 Simplified model of a linear electric field, E, and corresponding electrostatic potential, ϕ 12
2.4 Background injection where background electrons at the bubble radius, R, whereas electrons within the bubble radius, $\rho < R$, are not injected. 14
2.5 Phase-space evolution 18
2.6 Relative energy spread as a function of bunch length inside the accelerator 19
2.7 OSIRIS simulation of a loaded accelerating potential. 20
2.8 When the unloaded wakefield (black line) is optimally loaded (dotted line) by an electron bunch at ξ_s the wake is flattened at an electric field, E_s. The underloaded field (red) and the overload field (green) have a field gradient across the electron bunch of $\pm\delta$E leading to an energy chirp. 21
2.9 Reduced model showing beam loading effects on energy spread . . . 23
2.10 Phase-space diagram of beam loading for a chirped bunch injection . . 24
2.11 OSIRIS simulation of emittance development through the accelerator. 28

3.1 Schematic of the Oscillator 30
3.2 Schematic of the chirped pulse amplification 31
3.3 Layout of a parallel grating compressor 32
3.4 Layout of a anti-parallel grating stretcher 32
3.5 Layout of a multipass amplifier 33
3.6 The TOPS parallel grating compressor. 35
3.7 The TOPS accelerator chamber. 36
3.8 Layout of the profile monitors on the electron beam line. 38
3.9 (a) Image Plate image and (b) LANEX screen image of the electron beam profile. The red circles indicate the background area. 41

3.10 Calibration curve of the charge within the electron bunch as a function of the LANEX counts 42
3.11 Demonstration of the force acting on an electron beam in a steering magnet. 43
3.12 Schematic of the magnetic quadrupole. 44
3.13 Horizontal focusing of electron spectrometer. 45
3.14 Vertical focusing from the fringe field of the electron spectrometer. . . 46

4.1 Trajectory and phase-space of a laminar beam 48
4.2 Trajectory and phase-space of a real beam 49
4.3 Demonstration of emittance as an area in phase-space. 50
4.4 Diagram of the pepper-pot measurement 53
4.5 Experimental set-up of the emittance measurement beam line 56
4.6 GPT simulations of electron beam trajectories for the low resolution measurement. 57
4.7 GPT simulated images of the of the low resolution emittance measurement. 58
4.8 Transverse profile of low resolution GPT simulations. 59
4.9 GEANT 4 simulations of the effectiveness of emittance mask thickness (part a). 61
4.10 GEANT 4 simulations of the effectiveness of emittance mask thickness (part b). 62
4.11 GEANT 4 simulations of scattering angle of aluminium foil laser beam block. 64
4.12 Phase-space growth due to the beam interaction with a foil. 65
4.13 GEANT 4 simulations of scattering angle of tungsten foil. 66
4.14 (a) Image from a pepper-pot emittance measurement for a 2 mrad divergence beam. The normalised r.m.s. emittance (corrected for hole size and for 82 MeV electrons) is 8.7 π mm mrad. (b) shows the phase-space diagram and (c) charge distribution across the electron bunch. . 67
4.15 (a) Image from a pepper-pot emittance measurement for a 2.5 mrad divergence beam. The normalised r.m.s. emittance (corrected for hole size and for 82 MeV electrons) is 9.8 $\pm$ 1 π mm mrad. (b) shows the phase-space diagram and (c) charge distribution across the electron bunch. 68
4.16 GPT simulations of electron beam trajectories for the high resolution measurement. 70

4.17 GPT simulated images of the of the high resolution emittance measurement. 71
4.18 Transverse profile of high resolution GPT simulations. 72
4.19 (top) Image from a pepper-pot emittance measurement for a 1.3 mrad divergence beam. The normalised r.m.s. emittance (corrected for hole size and for 125 MeV electrons) is $2.2 \pm 0.6\ \pi$ mm mrad. (left) shows the phase-space diagram and (right) charge distribution across the electron bunch. 74
4.20 Histogram of recorder emittance along the (a) x-axis and (b) y-axis. . 75
4.21 Source size as a function of emittance. 75
4.22 Emittance evolution for an electron beam drifting from a source. . . . 76
4.23 Dependance of angle on charge for the both the horizontal (green) and vertical (blue) with the $Q^{1/2}$ and $Q^{1/3}$ dependance shown. 76

5.1 Simulation of electron spectrometer trajectory 80
5.2 Simulated spectrometer screen from a fixed source without quadrupoles 81
5.3 Simulated spectrometer screen from a fixed source with quadrupoles . 82
5.4 Measured energy spread growth with emittance/divergence 83
5.5 Simulated spectrometer screen from a fixed divergence beam without quadrupole transport 84
5.6 The effects of emittance on spectrometer resolution without quadrupole beam transport 85
5.7 Simulated spectrometer screen from a fixed divergence beam with quadrupole transport 87
5.8 Effects of emittance on spectrometer resolution without quadrupole beam transport 88
5.9 Low energy spread electron spectrum without quadrupoles 89
5.10 Low energy spread electron spectrum with quadrupoles (0.8 %) 90
5.11 Low energy spread electron spectrum with quadrupoles (0.8 %) 90
5.12 Low energy spread electron spectrum with quadrupoles (1.4 %) 91
5.13 Multiple electron spectrometer images 92
5.14 Energy spread charge scaling 93

6.1 Angular distribution of TR 96
6.2 The effect of electron bunch angular spread on TR distribution 98
6.3 Gaussian electron bunches and their TR spectrum 100
6.4 Extreme electron bunches and their TR spectrum 101
6.5 TR signal scaling with charge 103

6.6 Effect of bunch width on TR 104
6.7 The effect of bunch width on the angular distribution 106
6.8 TR spectrum from a single foil 107
6.9 Angular interference of the two foil system 109
6.10 The effect of angular spread in the electron bunch on the two-foil far field TR distribution. 110
6.11 Far field TR distribution including angular spread and bunch width. . 111
6.12 On axis interference between the two foils as a function of wavelength 112
6.13 TR spectrum for several bunch shapes (Figure 6.8) from a two foil system (including angular spread and bunch width). 113
6.14 r.m.s. bunch length after 1 m for a 90 MeV electron beam as a function of beam divergence. 114
6.15 Effects of energy difference, ΔE, on bunch separation 115
6.16 Effects of energy spread, σ_γ/γ, on r.m.s. bunch length. 115
6.17 ALPHA-X experimental set-up: a high powered laser is focused onto a gas jet to produce mono-energetic electrons. The electrons are imaged on three LANEX targets and focused into an electron spectrometer by a quadrupole triplet magnetic lens. 116
6.18 The two foil set-up of the transition radiation experiment. TR foil 1 and laser block is mounted in a gate valve so that it can be removed. Pellicle TR foil 2 mounted in front of a LANEX screen and removed out of the page in this figure. TR sent out of the vacuum through a zinc selenide window (ZnSe). LANEX screen imaged with a Flea CCD through a window. 117
6.19 ZnSe Transmission curve. 118
6.20 Lens set-up used to gather the TR into the spectrometer. 119
6.21 TR beam width at the detector from the two foils 120
6.22 Fraction of TR beam measured by the detector 121
6.23 TR spectrum for several bunch shapes (figure 6.8) from a two foil system including fraction of beam measured. 122
6.24 Transmission spectra of the filters used in the TR set-up, measured with an FTIR. 123
6.25 Diode calibration curve. 125
6.26 MCT calibration curve. 125
6.27 Black body calibration curve of the spectrometer for both the short and long wavelength gratings. 126

6.28 Two false colour images of the electron beam transverse profile with the identification of the distribution centre and r.m.s. spread for (a) no FFT filtering and (b) with FFT filtering. A linear colour scaling has been used. 128
6.29 Transition Radiation signal as a function of transverse electron bunch parameter (a) distribution centre on X-axis (b) distribution centre on Y-axis (c) r.m.s. spread on X-axis. Demonstrates that there is a correlation with the beam's transverse parameter and TR signal and is the same for each wavelength. Combines with Figures 6.30 and 6.31. . . 129
6.30 Transition Radiation signal as a function of transverse electron bunch parameter (d) r.m.s. spread on Y-axis (e) ratio of two r.m.s. spreads (f) area of beam. Demonstrates that there is a correlation with the beam's transverse parameter and TR signal and is the same for each wavelength. Combines with Figures 6.29 and 6.31. 130
6.31 Transition Radiation signal as a function of transverse electron bunch parameter (g) charge inside the r.m.s. area (h) key. Demonstrates that there is a correlation with the beam's transverse parameter and TR signal and is the same for each wavelength. Combines with Figures 6.29 and 6.30. 131
6.32 Transverse bunch properties of (a) x position, (b) y-position, (c) r.m.s. spread in x, (d) r.m.s. spread in y, (e) r.m.s. ratio, (f) area and (g) charge. 133
6.33 TR spectrum using (a) sort 1A and (b) sort 1B. 136
6.34 Distribution of charge across the spectrum for sort parameter 1B (black) and 1C (red). The average charge across the spectrum is shown by the solid line, with $\pm$ one standard deviation shown by the dashed line. Sort 1C has much lower scatter in the charge than 1B. 137
6.35 Spectrum from sort 1C, showing the smoothest spectrum due to the narrow range of electron charge. 138
6.36 Electron bunch shape (a) and TR spectrum (b) for a short bunch (green) a long bunch (red) and the combined long bunch with a short structure (black). 139
6.37 Varrious bunch shapes (a) and their TR spectrum (b). 141
6.38 Effects of varying the bunch length on the TR spectrum. 142
6.39 Effects of varying the electron beam energy on the TR spectrum. . . . 144
6.40 Effects of varying the electron beam width on the TR spectrum. . . . 145
6.41 Effects of varying the electron beam angular spread on the TR spectrum. 146

6.42 (a) Electron bunch shape (green) which consists of a substructure of two bunches (red and blue) and (b) TR spectrum. 148
6.43 Effects of varying the bunch length on the TR spectrum. 150
6.44 Various electron bunch shapes (a) and their TR spectrum(b). 152
6.45 Effects of varying electron bunch energy on sectrum 2. 153
6.46 Electron propagation to the TR screen of a mono-energetic peak with a long tail at the screen position, measured for large diameter aperture (> 5 cm) (black), measure in an aperture the same size as the TR screen (2 cm diameter) without the quadrupoles (red) and with the quadrupoles (green). 154
6.47 Example mono-energetic electron peak with low energy tail with the raw data (black), smoothed data (red) with a double Gaussian fit (green) used to obtain the fraction of the charge in the peak. 155

7.1 Phase-space plot with two electron bunches of the same energy. The first has passed de-phasing and has an up chirp whereas the second before de-phasing has a down chirp. 162
7.2 Phase-space of two bunches, one bunch at de-phasing with a minimum energy spread and the second bunch (a) before de-phasing and (b) after de-phasing. 162
7.3 TR measured electron distribution (red) and a GPT calculated distribution from the high resolution measured energy spectrum with a 0.15 μm (black) and 0.3 μm (green) mono-energetic source bunch length. . 164

List of Tables

6.1 Sort 1A: removed all shots which do not produce TR at 8.2μm and then was applied across the entire spectrum. 134
6.2 Sort 1B: sort parameters set by the standard deviation in each of the electron's transverse properties. 135
6.3 Sort 1C: focuses on creating a narrow selection region for the charge. 135
6.4 Bunch shapes used in Figure 6.37, the two bunches are seperated by 10 fs. 140
6.5 Sort 2: focuses on creating a narrow selection region for the charge. . 147

Chapter 1

Introduction

Particle accelerators are at the forefront of scientific research and technology. One application of accelerators is as a source of tuneable radiation with wavelengths varying from the infrared to X-ray regions of the electromagnetic spectra. Synchrotron light sources, which are based on accelerator technology, are used as diagnostic tools in many different areas of science and industry, for example: physics, biology, chemistry, pharmaceuticals, materials science, engineering, oil and gas. However, conventional radiation sources, such as Diamond in the UK, are large scale facilities. Diamond is the largest scientific facility to be built in the UK in over 40 years. Current synchrotron light sources are around the size of five football fields and are extremely expensive. To be used more widely as a research tool they must become much smaller and cheaper. A laser-plasma wakefield accelerator (Tajima & Dawson, 1979) combined with a magnetic undulator, can provide a source of synchrotron radiation from a device that is hundreds of times smaller and cheaper than conventional sources, and potentially with the capability of producing femtosecond duration pulses, as has been demonstrated by (Schlenvoigt et al., 2008; Fuchs et al., 2009), but currently at a low repetition rate, limited by current laser technology. Ultrashort duration light pulses are powerful tools for time-resolved studies of molecular and atomic dynamics.

Conventional accelerators use radio frequency (RF) resonant cavities as accelerating structures. These are limited to $\sim$100 MV/m by ionisation of the walls of the cavity and electron multipactor effect in the presence of the high electric fields, but are typically restricted to around 20 MV/m. The bunch duration of the electrons in most of these accelerators is relatively long, $>$1 ps, limiting their application in ultrafast physics. However, this can be overcome using magnetic compressors or electron bunch slicing techniques (Khan, Holldack, Kachel, Mitzner, & Quast, 2006) and the bunch duration reduced to $<$100 fs.

Plasma, on the other hand, is already completely ionised and therefore can with-

stand much higher electric fields, in excess of $\sim$100 GV/m, which is three orders of magnitude larger than in conventional RF accelerators (Esarey, Sprangle, Krall, & Ting, 1996). Plasma as a medium for acceleration was first proposed by Tajima and Dawson (1979). They proposed using plasma density waves that are driven by the ponderomotive force of a high intensity, ultra-short laser pulse to accelerate charged particles. As a high intensity femtosecond laser pulse propagates through an under-dense plasma it expels electrons in its vicinity due to its ponderomotive force. These expelled electrons set up a plasma density wave in the wake of the laser pulse. The density structure has dimensions of the order of the relativistic plasma wavelength, $\lambda_p = 2\pi c/\omega_p$. The wake travels at approximately the group velocity of the laser pulse, $v_g \simeq c(1-n_e/n_c)^{1/2}$, where $\omega_p = (e^2 n_e/\gamma m_0 \varepsilon_0)^{1/2}$ is the relativistic plasma frequency, n_e is the plasma density, $n_c = m\varepsilon_0\omega_0^2/e^2$ is the critical density, ω_0 is the laser frequency, and c is the speed of light in vacuum.When the plasma wave becomes relativistic, $\gamma > 1$, plasma electrons are self injected into the rear of the accelerating structure and are accelerated to relativistic energies (Katsouleas, 2004), until they pass the midpoint. At the midpoint, the electrons start to be decelerated by the electric field of the front of the accelerating structure, this is known as de-phasing and limits the acceleration. Decreasing the plasma density, which in turn increases the plasma wavelength, can increase the de-phasing length. As the electrons are accelerated by the potential, they acquire energy from the wave and thus damp the amplitude of the wake (Reitsma, Cairns, Bingham, & Jaroszynski, 2005).

The high accelerating field reduces the distance required to reach high energies. For example, it would take several meters to obtain 50 MeV electrons in a conventional accelerator, whereas it was first shown by Mangles et al. (2004); Geddes et al. (2004); Faure et al. (2004) that a plasma accelerator can achieved this in just 1 mm. To reach high energies in plasma accelerators it is essential to guide the laser pulse in plasma to increase the interaction length. This has been successfully achieved in a discharge plasma capillary waveguide (used to guide the laser pulse over a much greater distance than it's Rayleigh length) where 1 GeV electrons have been produced over a distance of 3 cm (Leemans et al., 2006). However, RF accelerator technology has reached a high level of maturity with proven success and therefore plasma accelerators require significant development to be competitive.

The laser wakefield accelerator (LWFA) has a significant advantage over conventional accelerators due to some of their inherent properties. One such property is the electron bunch duration, predicted to be of the order of 10 fs (Pukhov & Vehn, 2002), given by the short scale length of the accelerator structure for typical densities of $n_p \approx 10^{18} - 10^{19}$ cm^{-3}. The short bunch duration and high charge (>10 pC)

(Mangles et al., 2004; Geddes et al., 2004; Faure et al., 2004) should allow peak currents $\geq$1 kA to be produced. A low emittance is also expected because of the very small transverse dimensions of the electron bunches.

These properties make the LWFA electron beams an attractive driver of undulator radiation. The undulator radiation is given by:

$$\lambda = \frac{\lambda_u}{2h\gamma^2}\left(1+\frac{K^2}{2}+\gamma^2\vartheta^2\right), \tag{1.1}$$

where λ_u is the undulator period, h is the harmonic number, γ is the Lorentz factor, K is the undulator parameter and ϑ is the angle of radiation relative to the electron axis. The wavelength of the emitted radiation is dominated by the $\lambda_u/2h\gamma^2$ term, which is simply a double Doppler contraction of the undulator period. The radiation wavelength is increased by the $(1+K^2/2)$ term due the periodic deviation of the electrons as a result of the periodic magnetic field of the undulator (Luchini & Motz, 1990). The wavelength emitted also increases with angle as described by $\gamma^2\vartheta^2$ term (Luchini & Motz, 1990).

The linewidth of the radiation, $\delta\lambda$, is given by (Gallacher et al., 2009),

$$\left(\frac{\delta\lambda}{\lambda}\right)^2 = \left(\frac{2\sigma_\gamma}{\gamma}\right)^2 + \left(\theta^2\gamma^2\right)^2 + \frac{1}{N_u^2}. \tag{1.2}$$

To produce narrow bandwidth undulator radiation, it is essential to minimise the parameters on the right-hand-side of equation, 1.2. First the energy spread, σ_γ, must be minimised by creating highly mono-energetic electron bunches. To minimise the second term a low divergence or a highly collimated electron beam should be used. The natural bandwidth of the undulator is given by the third term where N_u is the number of undulator periods.

Therefore to create monochromatic undulator radiation, it is essential to use monoenergetic electron bunches. In addition, it is also essential to minimise the angular spread of the electron bunch, which requires a low emittance, ε. Emittance is a measure of the beam quality and is a measure of the transverse momentum spread. The emittance is the area of an ellipse encompassing the beam in transverse phase-space and is given by $\varepsilon = x_0\, x_0'$ at the focus, where x_0 is the width of the beam and x_0' is the divergence from the focus.

The emittance is defined as,

$$\varepsilon = \gamma_0 x^2 + 2\alpha x x' + \beta_0 x'^2, \tag{1.3}$$

where α, β_0 and γ_0 are ellipse parameters such that $\gamma_0\beta_0 - \alpha^2 = 1$. At the focus,

$z_0 = 0$, α = 0 so that $\gamma_0\beta_0 = 1$. At this position the beam width and divergence are given by,

$$x_0 = \sqrt{\varepsilon\beta_0}, \tag{1.4}$$

$$x_0' = \sqrt{\varepsilon\gamma_0}. \tag{1.5}$$

As the beam propagates, γ_0 remains constant, $\gamma(z) = \gamma_0$ but β_0 evolves as, $\beta(z) = \beta_0 + z^2/\beta_0$ as defined in Wiedemann (2007).

The beam divergence remains constant but the width changes as $x(z) = \sqrt{\varepsilon\beta(z)}$. To keep the beam width variation minimal over the undulator length, L_u, the β parameter is set so that x only increases to $\sqrt{2}x_0$ at the entrance and exit of the undulator with the focus in the centre, $x(L_u/2) = \sqrt{2}x_0 = \sqrt{2\varepsilon\beta_0} = \sqrt{\varepsilon\beta(L_u/2)}$. Therefore, $\beta(L_u/2) = 2\beta_0 = \beta_0 + (L_u/2)^2/\beta_0$, thus $\beta_0 = L_u/2$ and the corresponding angle is given by $\theta_{min} = \sqrt{2\varepsilon/L_u}$. To minimise the angle, to create monochromatic undulator radiation, it is essential to keep the emittance to a minimum.

The LWFA has the potential to provide a convenient and compact driver of a free - electron laser (FEL) (Jaroszynski et al., 2006; Gruner et al., 2007). The high peak current and low emittance of the electron beams will maximise the FEL gain parameter, ρ, and thus minimise the gain length, L_{gain}, required for a self amplified spontaneous emission (SASE) FEL (Bonifacio, Pellegrini, & Narducci, 1984). The gain length is given by

$$L_{gain} = \frac{\lambda_u}{4\pi\sqrt{3}\rho}. \tag{1.6}$$

The gain parameter is given by,

$$\rho = \frac{1}{2\gamma}\left(\frac{I}{I_A}\left(\frac{\lambda_u A_u}{2\pi\sigma_x}\right)^2\right)^{\frac{1}{3}}, \tag{1.7}$$

where I is the beam current, I_A = 17 kA is the Alfven current, σ_x is the beam radius, $A_u = a_u(J_0(\xi) - J_1(\xi))$, $a_u^2 = K^2/2$, $\xi = a_u^2/(2(1+a_u^2))$ and J is a Bessel function (McNeil & Thompson, 2010).

The gain parameter must be maximised so that the gain length can be minimised, allowing the FEL size become feasible. The LWFA can achieve this by utilising the short electron bunch length and low emittance, which will in turn maximise the beam current and allow the beam to be focused to a small radius.

To use a LWFA as a source for either an FEL or a synchrotron source it is essen-

tial that the beam's key parameters are understood and optimised. In this thesis, new tools are developed to diagnose all the key parameters which have resulted in the lowest measured energy spread, the first single shot emittance measurement and the first bunch length measurement from a single laser driven wakefield accelerator.

Chapter 2

The Laser-Plasma Particle Accelerator

2.1 Ponderomotive Force

All charged particles in an electromagnetic field feel the force of both magnetic and electric fields, given by the Lorentz force,

$$\mathbf{F}_L = m\frac{d\mathbf{v}}{dt} = -e\left(\mathbf{E}\left(\mathbf{r}\right) \; + \; \mathbf{v}\times\mathbf{B}\left(\mathbf{r}\right)\right), \tag{2.1}$$

where e is the charge, m is the particle mass, $\mathbf{E}$ is the electric field, $\mathbf{v}$ is the electron velocity and $\mathbf{B}$ is the magnetic field. An electron will feel a continuously oscillating force in a continuously oscillating electromagnetic wave, such as

$$\mathbf{E}(\mathbf{r}) = \mathbf{E}_0(\mathbf{r}) \; \cos \; \omega t, \tag{2.2}$$

where ω is the angular frequency of the light and t is time. The force acting on the electron with an initial position, $\mathbf{r}_0$, is given by the first order of Equation 2.1, when $\mathbf{v}$ is small $\mathbf{v}\times\mathbf{B}$ can be neglected and the force is simply given by,

$$\mathbf{F}_1 = m\,\frac{d\mathbf{v}_1}{dt} = -e\mathbf{E}(\mathbf{r}_0), \tag{2.3}$$

$$\mathbf{v}_1 = -(e/m\omega)\,\mathbf{E}_0(\mathbf{r}_0) \; \sin \; \omega t, \tag{2.4}$$

$$\mathbf{r}_1 = (e/m\omega^2)\,\mathbf{E}_0(\mathbf{r}_0) \; \cos \; \omega t. \tag{2.5}$$

The maximum electron velocity, known as the quiver velocity, $\mathbf{v}_{osc}$, is found when $\mathbf{v}_{osc} = -e\mathbf{E}_0(\mathbf{r}_0)/(m\omega)$. For a continuous wave, the time averaged force is zero and the electron returns periodically to its initial position. However, if the electromagnetic wave is not continuous, as is the case for a focused, pulsed laser, then each oscillation

of the wave varies and an additional force, averaged over the fast oscillations is felt. This second order effect in the electromagnetic field must also be calculated. From the Taylor expansion around $\mathbf{r}_0$ of Equation 2.2,

$$\mathbf{E}(\mathbf{r}) = \mathbf{E}(\mathbf{r}_0) + \mathbf{r}_1 \cdot \nabla \mathbf{E}(\mathbf{r}_0). \tag{2.6}$$

The velocity of the electron, $\mathbf{v}_1$, at $\mathbf{r}_1$ must also be taken into consideration, such that the second order Lorentz force then takes the form,

$$m\frac{d\mathbf{v}_2}{dt} = -e\left(\mathbf{r}_1 \cdot \nabla \mathbf{E}(\mathbf{r}_0) \; + \; \mathbf{v}_1 \times \mathbf{B}_1\left(\mathbf{r}_0\right)\right). \tag{2.7}$$

Using Maxwells equation $\nabla \times \mathbf{E} = -\partial \mathbf{B}/\partial t$, $\mathbf{B}_1$ becomes $-(1/\omega)\nabla \times \mathbf{E}_0 \sin \omega t$. Substituting Equation 2.4 and 2.5 into 2.7 and averaging over time gives,

$$m\left\langle \frac{d\mathbf{v}_2}{dt} \right\rangle = -\frac{e^2}{m\omega^2}\frac{1}{2}\left(\left(\mathbf{E}_0 \cdot \nabla\right)\mathbf{E}_0 \; + \; \mathbf{E}_0 \times \left(\nabla \times \mathbf{E}_0\right)\right). \tag{2.8}$$

Using the vector identity $\mathbf{A} \times \mathbf{B} \times \mathbf{C} = (\mathbf{A} \cdot \mathbf{C})\mathbf{B} - (\mathbf{A} \cdot \mathbf{B})\mathbf{C})$ Equation 2.8 provides the force, $\mathbf{F}_p$,

$$\mathbf{F}_p = -\frac{e^2}{4m\omega^2}\nabla \mathbf{E}_0^2. \tag{2.9}$$

This time averaged force is known as the ponderomotive force and can be understood as the force arising from the gradient of the time averaged oscillating potential. The ponderomotive force derivation can be found in Chen (2006); Kruer (2003).

It is useful at this point to define the vector potential, $\mathbf{A}$, such that, $\mathbf{E} = -\frac{\partial \mathbf{A}}{\partial t}$ and $\mathbf{B} = \nabla \times \mathbf{A}$. This can be normalised as $\mathbf{a}_0 = e\mathbf{A}_0/m_e c = e\mathbf{E}_0/\omega m_e c$. The peak amplitude of the vector potential and the normalised vector potential are given by $A_0 = |\mathbf{A}_0|$ and $a_0 = |\mathbf{a}_0|$. a_0 is a useful quantity since the motion of the electrons are relativistic for $a_0 > 1$. Relativistic effects can usually be neglected for $a_0 < 1$. a_0 is related to the intensity of the laser, I_0, by,

$$a_0 = \frac{e}{m_e c\omega}\sqrt{\frac{2I_0}{\varepsilon_0 c}}, \tag{2.10}$$

where m_e is the electron mass, c is the speed of light, ε_0 is the permittivity of free space, and e is the electron charge. $a_0 > 1$ for a laser intensity $> 10^{18}$ Wcm^{-2} for 1 μm radiation. Equation 2.9 then takes the form,

$$\mathbf{F}_p = -\frac{e^2}{4m\omega^2}\nabla \mathbf{E}_0^2 = -\frac{mc^2}{4}\nabla \mathbf{a}_0^2. \tag{2.11}$$

It can be seen from Equation 2.11 that the acceleration is inversely proportional to

the square the mass and of the frequency. Acceleration of the ions is therefore much smaller than for the electrons and the ions can usually be considered too heavy to be affected by the ponderomotive force. The ponderomotive force is highest where the gradient in the laser intensity is steepest. For a Gaussian laser pulse the negative gradient of the front edge creates a positive ponderomotive force accelerating the electron forward. The positive gradient at the rear of the laser pulse creates a decelerating force as the pulse passes the electron. The electron is then left with a positive displacement from its initial position.

2.2 Laser Wakefield Acceleration

As a high power laser pulse passes through plasma, the ponderomotive force drives the electrons. This creates charge separation between the displaced electrons and immobile ions in the plasma. The electrons are then pulled back towards the ions, consequently over-shoot and carry on oscillating to create a plasma density wave in the wake of the laser pulse. As is discussed by Tajima and Dawson (1979), this plasma wave can create a strong electric field that can accelerate injected electrons to high momenta in short distances. A perturbed plasma oscillates at the characteristic plasma frequency.

The plasma wavelength, $\lambda_p = 2\pi c/\omega_p$, is 10.6 μm for a typical plasma density of $n_e = 10^{19}$ cm^{-3}. The plasma wavenumber is given by $k_p = \omega_p/c$. The plasma wave propagates with the laser pulse and the phase velocity of the plasma wave, v_ϕ is approximately equal to the group velocity of the laser pulse in the plasma. The group velocity of the laser pulse is found by differentiating the dispersion relation for an electromagnetic wave in a cold plasma,

$$\omega^2 = c^2k^2 + \omega_p^2, \tag{2.12}$$

where ω is the frequency of the laser in the plasma, k is the laser wavenumber. The group velocity is therefore,

$$v_\phi \approx v_g = \frac{d\omega}{dk} = \frac{c^2k}{\omega} = c\sqrt{1 - \frac{\omega_p^2}{\omega^2}}. \tag{2.13}$$

The group velocity is 0.997c for the typical plasma density used above.

2.2.1 Plasma Waves

The linear plasma wave generated in the wake of the laser field have been described by Dawson (1959); Sprangle, Esarey, Ting, and Joyce (1988); Esarey et al. (1996); Esarey,

Schroeder, and Leemans (2009). The equation for a harmonic oscillator is first used to describe the plasma wave $\partial^2 \delta n/\partial t^2 + \omega_p^2 \delta n = 0$ where the resonant frequency is equal to the plasma frequency. $\delta n = n - n_0$ is the perturbation in the electron density. The plasma wave will be driven by the laser pulse and can be described by the harmonic oscillator equation (Mori, 1997),

$$\left(\frac{\partial^2}{\partial t^2} + \omega_p^2\right) \delta n = n_e c^2 \nabla^2 \mathbf{a}^2/2. \tag{2.14}$$

Here, the driving force is the ponderomotive force ($\propto \nabla a^2$) defined in Equation 2.11. Equation 2.14 can be solved to find the evolution of the density perturbation,

$$\frac{\delta n}{n_e} = \left(\frac{c^2}{\omega_p}\right) \int_0^t dt' \ \sin[\omega_p (t - t')] \ \nabla^2 \mathbf{a}^2/2. \tag{2.15}$$

For low amplitude density perturbations ($\delta n/n_e \ll 1$) the plasma wave remains sinusoidal. The electric field is found using Gauss's law, $\nabla \cdot \delta E = -e\delta n/\varepsilon_0$, which results in a sinusoidal oscillation for the electric field. Figure 2.1 (a) shows an example of electron perturbation (solid line) with the corresponding electric field (dotted line). It is useful at this point to define a frame of reference co-moving with the laser pulse, $\zeta = z - v_g t$.

As the laser intensity increases and a_0 becomes larger than one, the plasma perturbation, ($\delta n/n_e \to 1$). For these large amplitude oscillations the variation in velocity and position is such that one part of the wave catches up with other parts resulting in a steepening of the wave. A detailed description of the nonlinear plasma wave can be found in Kruer (2003). However, a simpler form of the plasma oscillation is provided by E. A. Jackson (1960) which results in,

$$\frac{\delta n(z)}{n_e} = \sum_{n=0}^{\infty} \frac{(-1)^n}{n!} \ \frac{\partial^n}{\partial z^n} [D(z)]^n, \tag{2.16}$$

where D(z) = $\delta n(z_0)/n_e \ \sin(k_p z)$.

Figure 2.1 (a) shows the normalised electron density perturbation in the linear regime, when $\delta n(x_0)/n_e = 0.01$ ($a_0 \ll 1$). The electron density is shown by the solid line as a sinusoidal oscillation, with the corresponding electric field (integrated electron density)) represented by the dashed line and also having a simple sinusoidal oscillation. However, when the initial perturbation is increased towards one the plasma wave takes on a non-sinusoidal shape as shown in Figure 2.1 (b) where $\delta n(x_0)/n_e = 0.6$. The corresponding electric field is modified from the sinusoidal oscillation to a saw tooth structure.

Optimum wakefield excitation occurs when the ponderomotive force of the laser

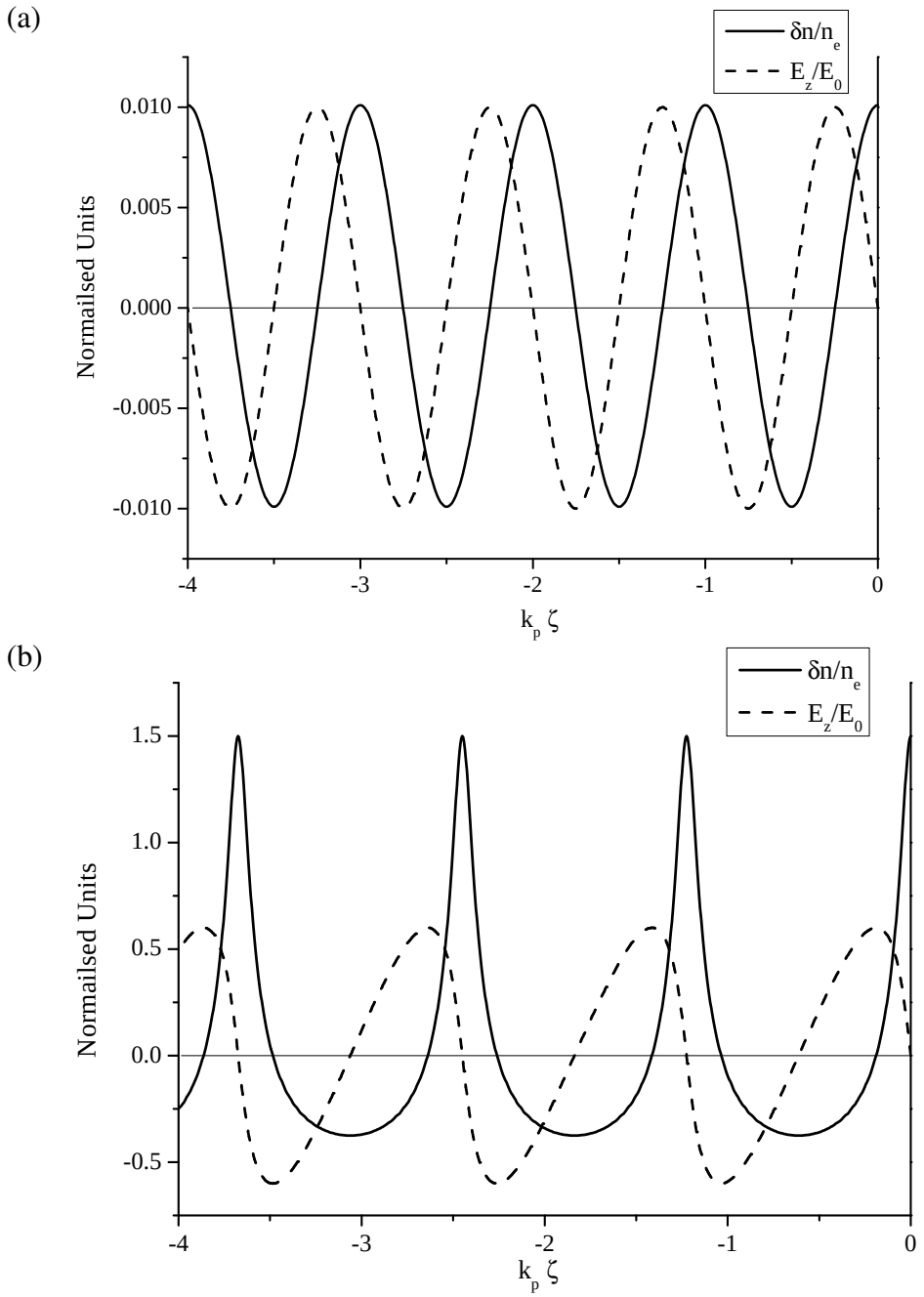

Figure 2.1: Density wave perturbations in the (a) linear and (b) nonlinear regime. The electron density perturbation is represented by the solids line with the corresponding electric field by the dotted line. The linear regime (a) is for an initial perturbation of $\delta n(x_0)/n_e = 0.01$ while the for nonlinear regime (b) $\delta n(x_0)/n_e = 0.6$.

pulse acts in resonance with the plasma oscillation. In this condition the forward driving force at the leading edge of the laser pulse changes to drive the electrons back at the time when the plasma wave pulls the electrons back, so that the two work together. This condition is reached when the pulse length is equal to half the plasma wavelength

($c\tau = \lambda_p/2$), when τ is the laser pulse length.

In addition to the longitudinal ponderomotive force used to create the 1-D wake, the ponderomotive force of the laser acts transversely. This force causes a radial expulsion of the electrons. After the laser has passed the electrons feel the restoring Coulomb force of the positive ions and are pulled back on axis. This sets up a radial plasma wave, as shown in Figure 2.2. The electrons that are expelled transversely create a sheath of electrons, denoted by the dotted line in Figure 2.2, which forms a bubble (Pukhov & Vehn, 2002), of positively charges ions. This sheath of electrons crosses at the rear of the bubble creating a strong electric field (Kostyukov, Nerush, Pukhov, & Seredov, 2009). For high a_0, (> 1 (Lu et al., 2007)), the bubble takes on a spherical structure with radius $R = \sqrt{a_0}\,\lambda_p/\pi$.

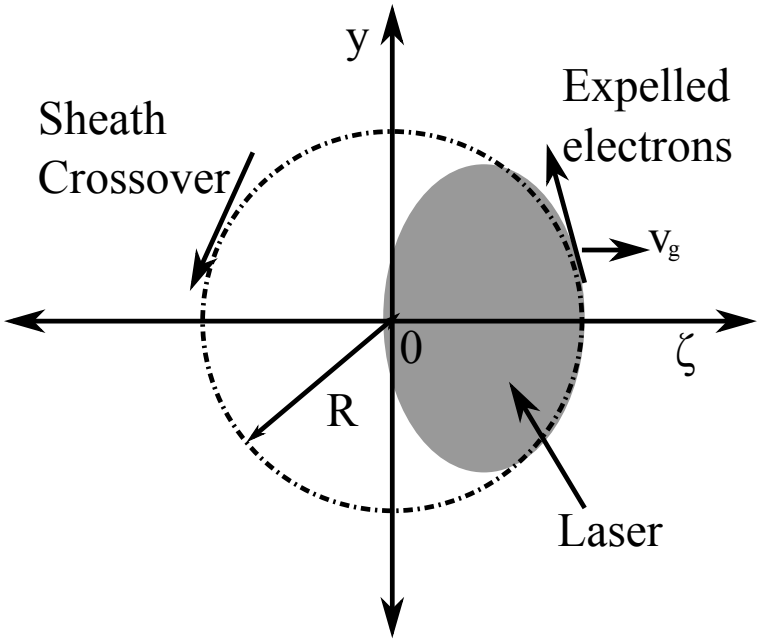

Figure 2.2: Diagram of the accelerating wakefield bubble of radius, R

The saw-tooth electric field is approximately linear across the bubble for a highly nonlinear wake. Therefore, a linear function can be used to create a simplified model of the electric field such that $E(\zeta) = E_N\,\zeta/R$. The centre of the bubble is at $\zeta = 0$, where $E(0) = 0$. The electric field has a maximum at the rear of the bubble, $E(R) = E_N$, where (Lu et al., 2007)

$$E_N = \frac{\sqrt{a_0} m_e c \omega_p}{e}. \tag{2.17}$$

The electrostatic potential, ϕ, is found by integrating over the electric field, $\phi(\zeta) = -\int E(\zeta) d\zeta$. The maximum energy, ϕ_{max}, of an electron placed at the rear of the

bubble occurs when the electron is accelerated to the centre, $\zeta = 0$, and is found by integrating over the electric field from $-R$ to 0 where $\phi_{max} = E_N R/2$ (in the bubble's frame of reference). The electrostatic potential across the plasma wave is given by

$$\phi(\zeta) = -\frac{E_N \zeta^2}{2R} + \frac{E_N R}{2}. \tag{2.18}$$

For $n_e = 10^{19}$ cm^{-3} and $a_0 = 2$, $E_N = 430$ GeV/m and a $R = 4.8$ μm.

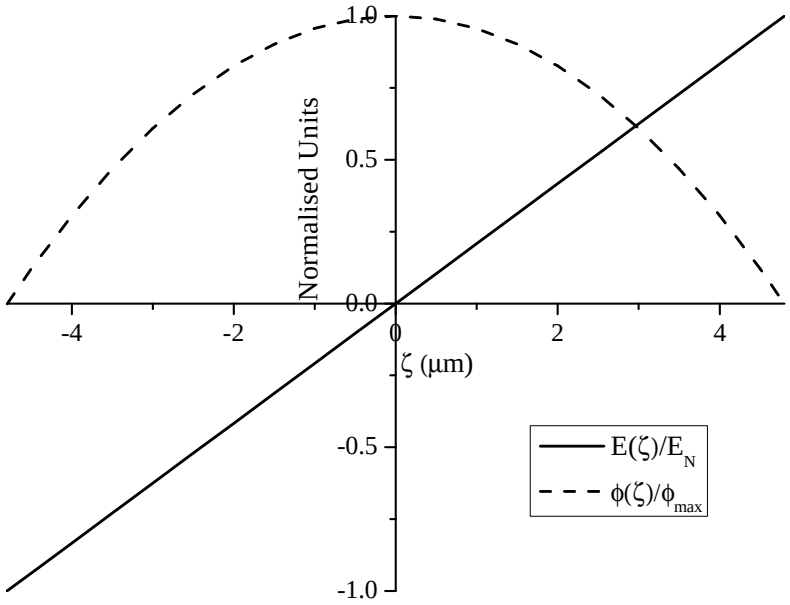

Figure 2.3: Simplified model of a linear electric field, E, and corresponding electrostatic potential, ϕ

2.2.2 Wavebreaking

Wavebreaking of a plasma wave occurs when the velocity of the electrons exceed the phase velocity of the plasma wave. This concept is important as it gives the limit of the electric field obtainable in the plasma wave and, furthermore, because electrons which exceed the phase velocity of the plasma wave can be trapped and accelerated. The velocity of an electron in a cold linear wave is given by $(e/m_e\omega_p)E_0$. The maximum electron velocity is equal to the phase velocity of the plasma wave which is equal to the group velocity of the laser pulse, v_g. The maximum electric field occurs when the electron velocity reaches v_g and the maximum electric field is given by Dawson (1959),

$$E_{max} = \frac{m_e \omega_p v_g}{e}. \tag{2.19}$$

A typical plasma density of $n_e = 10^{19}\text{cm}^{-3}$ leads to a maximum field of ≈ 300 GV/m. However, this electric field is only valid for the linear, non-relativistic plasma waves, as the electrons are travelling with the group velocity of the laser pulse, the relativistic properties of the electrons in the plasma wave act to increase the maximum electric field. This was done by Akhiezer and Polovin (1956) where the maximum electric field is now given by:

$$E'_{max} = E_{max}\sqrt{2\left(\gamma_p - 1\right)}, \tag{2.20}$$

where $\gamma_p = \left(1 - v_p^2/c^2\right)^{-\frac{1}{2}} = \omega_0/\omega_p$. For the same plasma density discussed above ($n_e = 10^{19}\text{cm}^{-3}$) the maximum electric field becomes around five times greater, E_{max} = 1500 GV/m.

2.2.3 Injection

Electrons are injected into the wake when their velocity is greater than the phase velocity of the accelerating bubble. At wavebreaking electrons at the rear of the bubble reach this criteria and are trapped and accelerated. Thermal induced wavebreaking occurs near wavebreaking when thermal excitation give the electrons the extra velocity required to get above the phase velocity of the plasma wave and become trapped in the wake. However, this mechanism relies on the intensity of the laser being high enough to drive the wake to the point of wavebreaking, which becomes increasingly difficult at higher plasma densities, as these plasmas can withstand a higher maximum electric field, as given in Equation 2.20.

Alternative models are discussed by Kostyukov et al. (2009) and Kalmykov, Yi, Khudik, and Shvets (2009) where the electrons are injected from the background plasma outside the bubble or by the expansion of the bubble radius as the bubble is formed.

The injection method discussed by Kostyukov et al. (2009) is for the electrons to be injected into the bubble from the background plasma. Here a spherical bubble is assumed with radius R as shown in Figure 2.4 propagating in the $\xi = z - v_g t$ frame with $\xi = 0$ at the centre of the bubble. In this frame, background electrons travel in a negative direction. ρ is the distance of the electrons from on axis. If a background electron has a $\rho < R$, as shown by the dotted line in Figure 2.4, then it enters the bubble at some positive value of ξ. The electron is then accelerated negatively before it passes $\xi = 0$ and feels the positive force. The extra energy the electron gains in the negative acceleration means that the positive acceleration is not sufficient to stop the electron so that it can be injected and the electron over shoots the bubble. However, if $\rho = R$, then

it only feels positive acceleration as it enters the bubble at $\xi = 0$. This electron can therefore be stopped and injected into the bubble, as shown by the solid line in Figure 2.4.

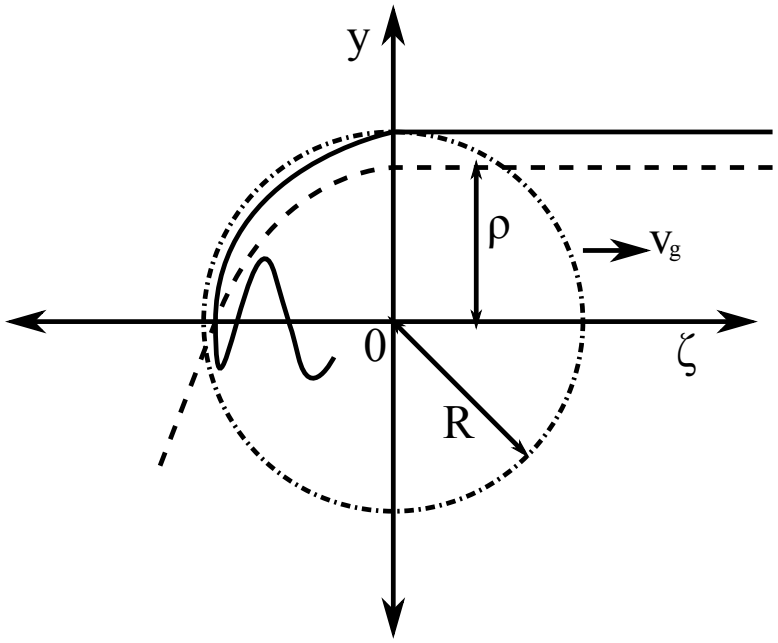

Figure 2.4: Background injection where background electrons at the bubble radius, R, whereas electrons within the bubble radius, $\rho < R$, are not injected (Kostyukov et al., 2009).

Similarly to Kostyukov et al. (2009), the model by Kalmykov et al. (2009) injects electrons from the background, however this model assumes that the bubble is expanding as it propagates. As the bubble expands background electrons in the expanding region are injected into the bubble, trapped and accelerated. As the bubble reaches a steady state (for example when self-focusing has reached a balance) injection stops and a mono-energetic bunch of electrons is produced.

2.2.4 Transverse Emittance

Looking in the frame of reference travelling with the laser, such that the background electrons and ions travel backwards (i.e. $v_z = -v_g \approx -c$) the transverse force, F_x, acting on the electrons is given by Pukhov, Gordienko, Kiselev, and Kostyukov (2004); Brunetti et al. (2010),

$$F_x = -m_0 \omega_p^2 \left(1 + v_z v_g / c^2\right) x/2, \tag{2.21}$$

where x is the particle's position. Prior to injection the electrons move with a veloc-

ity, $v_z \approx -c$, which results in minimal transverse forces as electric and magnetic fields cancel and, therefore, the electrons keep their initial position and a low transverse emittance. During injection the longitudinal velocity of the electrons is reversed and the transverse force rapidly increases the transverse emittance. The transverse momentum is created in the electron beam during injection and is dependent on the electron's transverse displacement as that time, x_0. After injection $v_z \approx c$ and the transverse forces saturate along with the emittance given by (Brunetti et al., 2010)

$$\varepsilon_{n,x} = x_0^2 \, k_p \, \gamma_g^{\frac{1}{2}} \, 8^{-\frac{1}{2}}. \tag{2.22}$$

Therefore, to obtain a low emittance electron beam the capture cross sectional area at the rear of the bubble must be small.

2.2.5 Acceleration length

Pump Depletion

As the laser pulse propagates through the underdense plasma it gives energy to the excited wake. As the laser drives the electrons in the plasma a 'snow ploughing' effect creates a higher density in the front of the laser pulse, whereas the bubble structure creates a void of electrons in the rear. The laser loses its energy at the front, which causes it to etch backwards. This loss of energy at the front is known as pump depletion. The rate of etching (or etching velocity), v_{etch}, is given by Decker, Mori, Tzeng, and Katsouleas (1996),

$$v_{etch} = c\frac{\omega_p^2}{\omega_0^2}. \tag{2.23}$$

The length over which the laser deposits its energy is the pump depletion length, L_{pd}, is given by Lu et al. (2007) for a Gaussian beam for an $a_0 > 0$,

$$L_{pd} = \frac{\lambda_p^3}{\lambda_0^2} a_0 \frac{\sqrt{2}}{\pi}. \tag{2.24}$$

After this acceleration length the laser will not have sufficient energy to drive a wakefield accelerator.

Dephasing Length

The electrons are injected when they have a velocity greater than the group velocity of the laser pulse, $v_g \simeq c(1 - \omega_p^2/2\omega_0^2)$. The electrons will then be accelerated so that they travel faster than v_g and therefore the bubble velocity. This causes the trapped

electrons to drift from the rear of the accelerating bubble to the front. As they pass the mid-point of the bubble they feel a decelerating force from the front of the bubble. The time for the electrons to reach this point is the dephasing time, $t_d = L_d/c$, when L_d is the dephasing length. The slippage is the difference between the distances travelled the electron bunch and the accelerator. The phase velocity of the accelerator, v_ϕ, is given by the group velocity of the laser, v_g, minus the etching velocity, v_{etch},

$$\begin{aligned} v_\phi &= v_g - v_{etch} \\ &= c\left(\left(1 - \frac{\omega_p^2}{2\omega_0^2}\right) - \frac{\omega_p^2}{\omega_0^2}\right) \\ &= c\left(1 - \frac{3\omega_p^2}{2\omega_0^2}\right). \end{aligned} \tag{2.25}$$

The slippage distance is $x = (c - v_\phi)t_d$. At time t_d the slippage is equal to the radius of the bubble, $x = R = \sqrt{a_0}\,\lambda_p/\pi$. The dephasing length is therefore given by,

$$L_d = \frac{2}{3}\frac{\lambda_p^2}{\lambda_0^2}\,R = \frac{2}{3}\frac{\lambda_p^3}{\lambda_0^2}\frac{\sqrt{a_0}}{\pi}. \tag{2.26}$$

The electron beam energy is found by integrating the electric field over the propagation distance. The maximum bunch energy in the bubble's frame of reference is given by $\phi_{max} = E_N R/2$ as shown in Section 2.2.1. The maximum electron energy, $E_{K,max}$, in the laboratory frame is found by integrating the electric field over L_d, such that $E_{K,max} = E_N L_d/2$,

$$E_{K,max} = \frac{2}{3}\frac{\lambda_p^2}{\lambda_0^2}\,\phi_{max} = \frac{2}{3}\frac{\lambda_p^2}{\lambda_0^2}\frac{a_0 m_e c^2}{e}. \tag{2.27}$$

For $n_p = 10^{19}$ cm^{-3}, $\lambda_p = 10.6\,\mu$m, $\lambda_0 =$ 800 nm and $a_0 = 2$ then the dephasing length is approximately 0.56 mm. For the same values the pump depletion length is 1.7 mm. Therefore the electrons will reach dephasing before the laser has been depleted. The maximum energy is 120 MeV. The energy of the electron beam in the laboratory frame as it propagates through the bubble is given by,

$$E_K(\zeta) = \frac{2}{3}\frac{\lambda_p^2}{\lambda_0^2}\,\phi(\zeta). \tag{2.28}$$

2.2.6 Phase-Space Evolution

An alternative way of looking at the dephasing of the electron bunch as it propagates through the accelerator and reaches dephasing is through its longitudinal phase-space evolution. Here, the electron bunch's energy, E_K, is shown as it evolves in the co-propagating frame of reference, ζ, as demonstrated in Figure 2.5. (Typically the electron's momentum is used in phase-space, however, energy is used here for simplicity as the two are scaled by a factor of c.)

Figure 2.5 (a) shows the electron bunch before it reaches dephasing at $\zeta = 0$ with a length $\delta\zeta_1$. At this position the electrons at the front of the electron bunch have accelerated through more of the bubble and therefore have higher energy then the electrons at the rear, causing a down chirp in the energy and giving the electrons an energy spread $\delta \mathrm{E}_1$. It should also be noted that this energy spread would cause the fast leading electrons to drift away from the rear electrons resulting in an increase of the bunch length after propagation.

In Figure 2.5 (b) the electrons have followed the electrostatic potential trajectory (the dotted line) to the point of dephasing at $\zeta = 0$ with maximum energy, $E_{K,max}$. At this point the electrons at the front reach the end of the accelerating potential and actually start to feel the decelerating potential from the front of the bubble. The electrons therefore start to slow and the electrons at the rear of bunch continue to accelerate such that they obtain a similar energy to the front. At this point the electrons have their minimum energy spread and maximum energy.

At the position in Figure 2.5 (c), the electron bunch is past dephasing so that the whole bunch starts to slow. Again the energy chirp increases the energy spread of the bunch, however now the chirp is in the opposite direction. This electron bunch would actually initially compress as it drifts from the accelerator to reach a minimum bunch length at some distance from the accelerator.

The difference in the energy, δE, for two electron separated by $\delta\zeta$ is, $\delta E = E_K(\zeta) + E_K(\zeta + \delta\zeta)$. An electron bunch at dephasing will have an increase in energy spread with increased bunch length as the bunch curves around the electrostatic potential curve, as shown in Figure 2.6. The relative energy spread, $\delta E / E_{K,max}$, is given by

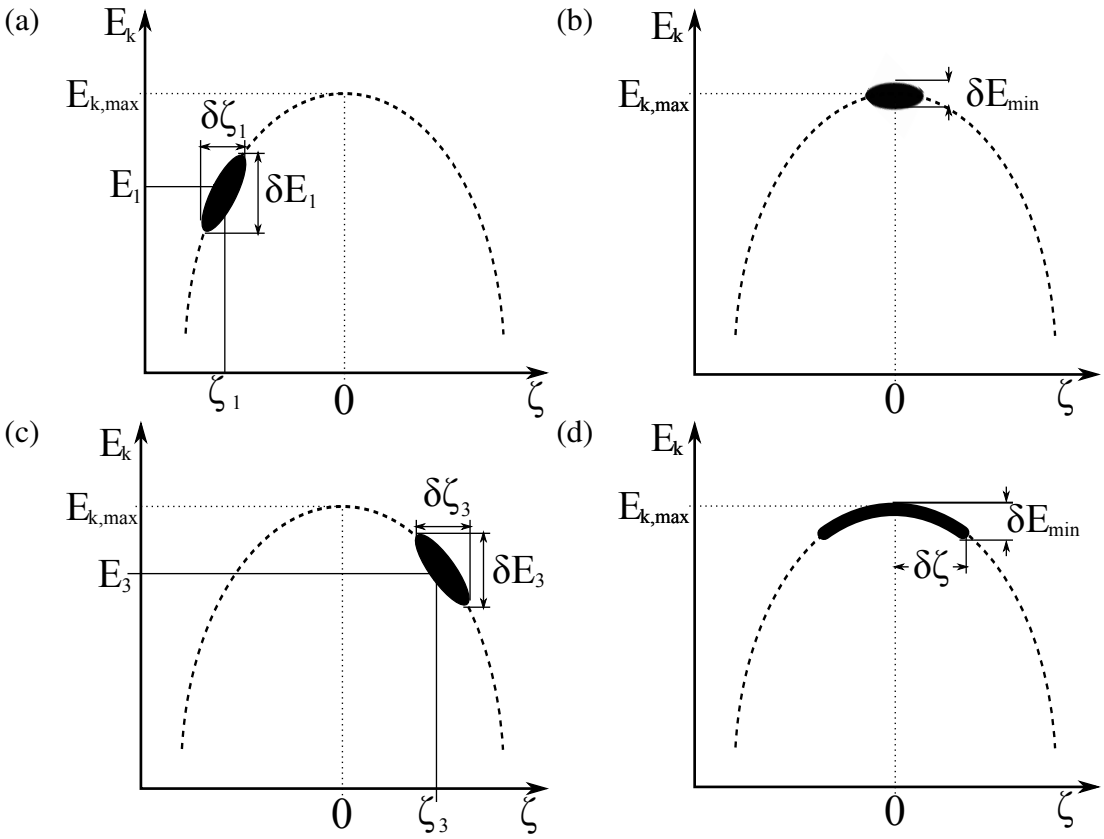

Figure 2.5: Longitudinal phase-space (a) before dephasing (c) during phase-space rotation at the dephasing length and (c) after dephasing and (d) when the bunch is long

$$\begin{aligned}\frac{\delta E}{E_{K,max}} = \frac{\delta\phi}{\phi_{max}} &= (\phi(0)-\phi(\delta\zeta))\frac{2}{E_N R} \\ &= (\frac{E_N R}{2}+\frac{E_N\delta\zeta^2}{2R}-\frac{E_N R}{2})\frac{2}{E_N R} \\ &= \frac{\delta\zeta^2}{R^2}. \end{aligned} \tag{2.29}$$

Equation 2.29 shows that the relative energy spread due to the curve of the electrostatic potential does not depend on the maximum electric field in the bubble but only on the bubble radius and therefore on the plasma density and the laser intensity.

2.2.7 Beam Loading

As the electrons are injected into the wake behind the laser pulse they create their own electric field which will act to combine with and dampen the electric field of the relativistic plasma wave, this is known as beam loading (Katsouleas, Wilks, Chen,

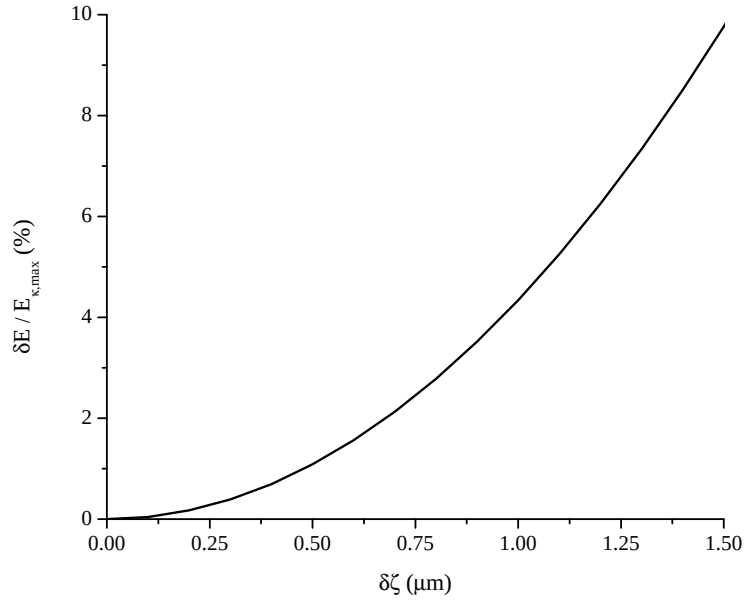

Figure 2.6: Relative energy spread as a function of bunch length inside the accelerator

Dawson, & Su, 1987). This damped electric field will reduce the amplitude of the perturbed electric field which will lead to reduced/no injection in the following waves. Further injected electrons will act to further damp additional plasma waves. In addition to stopping the injection process, the damping of the electric field can also create a modified accelerating potential.

Mono-Energetic Injection

Electrons injected simultaneously along the bunch length will have no energy chirp. Under these circumstances it is important not to introduce an energy spread from a non-linear accelerating field. With the correct electron bunch charge density the accelerating potential can be flattened, providing a uniform acceleration force to all the electrons in the bunch. A 2D snapshot of a 3D wakefield particle-in-cell (pic) simulation is shown in Figure 2.7 (top) and the wakefield, E_z, (bottom) taken from Tzoufras et al. (2008).

Here the wake is shown in the frame of reference co-moving with the laser pulse, $\xi = ct - z$. $\xi = 0$ is defined at the maximum bubble radius, $r_b = R_b$ and the wakefield, $E_z(\xi = 0) \simeq 0$. The unloaded bubble shape (inner most particle trajectory) is shown by the dotted line and the wakefield potential shown by the black line. An electron bunch is placed at ξ_s and the bubble structure is shown to be deflected and extended by the electric field of the electron bunch. The beam loading is shown to damp the wakefield at $-E_s$ and locally flatten the potential.

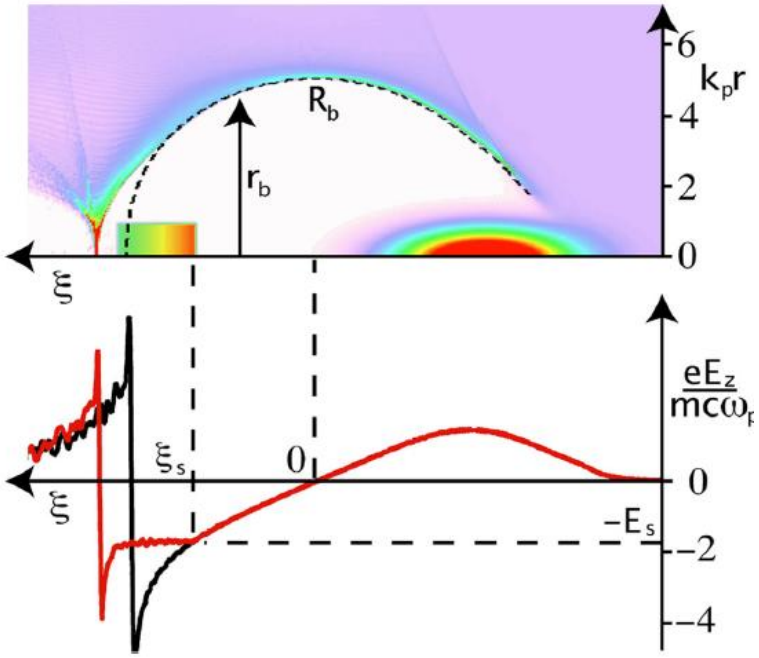

Figure 2.7: OSIRIS simulation of a loaded accelerating potential with the unloaded beam represented by the dotted line. The bottom plot shows the wakefield potential, E_z, of the loaded and unloaded accelerator in red and black respectively (Tzoufras et al., 2008).

In Figure 2.8 the wakefield is optimally loaded creating a uniform accelerating potential and minimal energy spread, denoted by the dotted line. However, for bunches that have more or less charge, the beams would be either over or under loaded respectively. As shown in Figure 2.8 when the wake is under loaded (red) the wakefield potential is not flattened, resulting in a variation in the field of $+\delta$E. Now the electrons at the front of the bunch feel the field, Es, whereas electrons at the rear feel the field, Es + δE. This causes the electrons at the rear to accelerate more than at the front causing a larger spread in the electron bunch's energy. As the electrons at the rear gain more energy, they will catch up with the electrons at the front causing bunch shortening.

Similarly, as the charge within the electron bunch increases beyond the optimal beam loading (green), the wakefield becomes over loaded. Now there is a variation in the field of -δE and the electrons at the rear feel a field E_s - δE, which is less than the front's field, E_s. Electrons at the rear therefore gain less energy than those at the front resulting in a larger energy spread, which will serve to increase the bunch length after propagation.

A reduced model, using the quasi-static approximation (Reitsma et al., 2005), has been used to demonstrate the effects of beam loading and bunch length on the energy

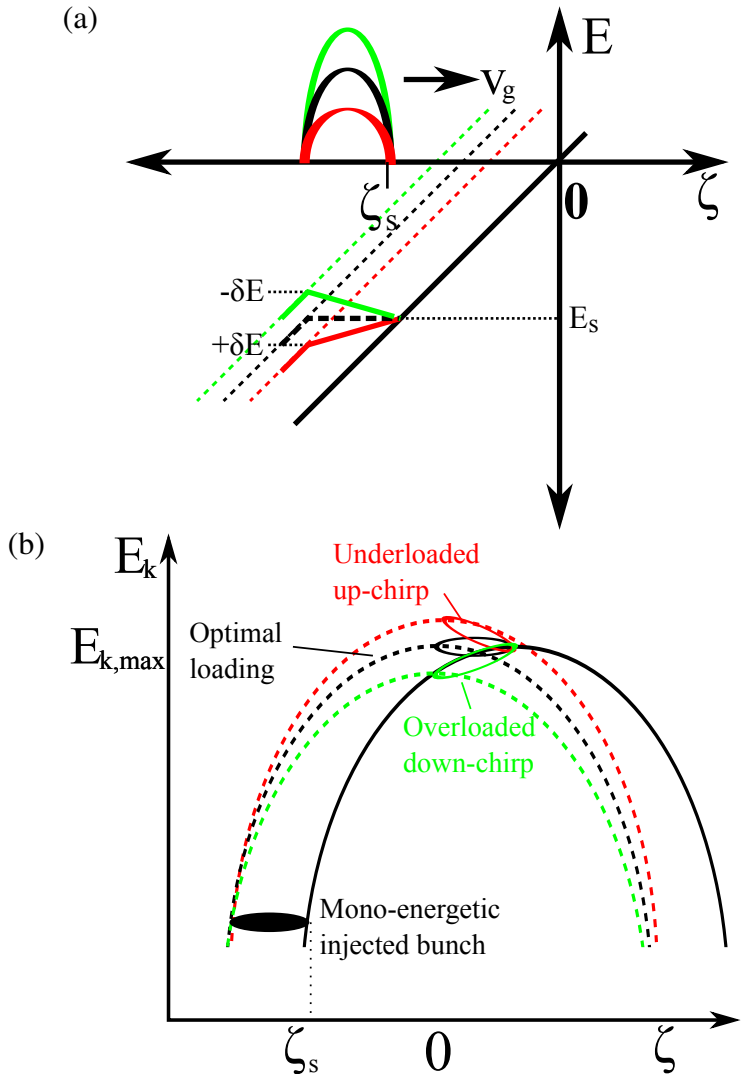

Figure 2.8: When the unloaded wakefield (black line) is optimally loaded (dotted line) by an electron bunch at ξ_s the wake is flattened at an electric field, E_s. The underloaded field (red) and the overload field (green) have a field gradient across the electron bunch of $\pm\delta$E leading to an energy chirp.

spread of LWFA electron bunches. In this simulation the laser beam and electron beam feed back into the system so that the evolution is fully self consistent. The plasma density used in the simulation is 1.2×10^{19} cm^{-3} and the laser had an $a_0 = 2$ and spot size of 10 μm (FWHM). This model does not include self-injection therefore a 6 MeV bunch is placed at the optimum position for acceleration. The initial electron bunch has no energy spread and is assumed to be injected simultaneously with a Gaussian distribution.

Beam loading has been simulated under two injection conditions of constant or varied injection rates. In a varied injection rate, the bunch length is kept constant and the peak current increased with increasing charge, i.e. the number of electrons

injected per unit length varies. For constant injection rate, the current remains the same, however the bunch length increases as more charge is injected.

Figure 2.9 (a) shows the effect of varied injecting rate. The four r.m.s. bunch lengths used in Figure 2.9 (a) are i = 0.1 μm, ii = 0.3 μm, iii = 0.6 μm and iv = 0.7 μm. For each of these plots a minimum energy spread can be seen. This minimum energy spread reached increases with increasing bunch length and also requires an increased charge. This indicates an optimum current for each of the lengths, which are 21 kA, 16 kA and 14 kA for i, ii and iii respectively (the three minima shown in the plot). Before this minimum, there is not sufficient loading to damp the electric field and create uniform accelerating gradient. At the optimum charge the minimum variation in electric field is achieved. After the optimum the field will be over loaded increasing the electric field variation. The second trend to be noted is that the minimum energy spread decreases with decreasing bunch length. This is because the bunch does not linearly flatten the field across its length due to the Gaussian distribution. The non-linearity in the flattened wake is larger for longer bunches. Therefore to obtain a narrow energy spread, the bunch length must be minimised.

The effects of varying bunch length are further investigated in the continuous injection rate model. This is shown in Figure 2.9 (b), here the current is fixed at A = 0.46 kA, B = 1.38 kA, C = 2.29 kA and D = 4.5 kA. The bunch length range started at $\sim$ 0.2 - 0.3 μm (r.m.s.) for all the shots extending to 1.3 μm for A and 2 μm for D (ranging in between). The increase of the initial bunch length results in increased energy spread. There are two mechanisms for a longer bunch length resulting in an increase in energy spread. The first is that if the beam is not optimally loaded then a longer beam will have a higher change in energy. The second is during the phase-space rotation at de-phasing a long bunch will extend over the phase-space rotation curve resulting in a longer bunch length. The increased beam loading effects of the higher current beams results in reduced energy spread for the same bunch length showing for these parameters that the beam is under loaded. It should also be noted that it is not charge alone which determines the beam loading but the charge per unit length or current, $I = Q/T$, where T is the bunch length in time. Therefore a low charge beam can achieve optimal beam loading provided the bunch length is suitably short.

Chirped Energy Injection

The above assumes that electrons are injected with a constant energy. However, if the electrons at the front are injected first they will undergo some acceleration before the electrons at the rear are injected causing an energy chirp during injection. An up chirp is defined here as an in increase in electron energy with time, i.e. the bunch has lower

(a)

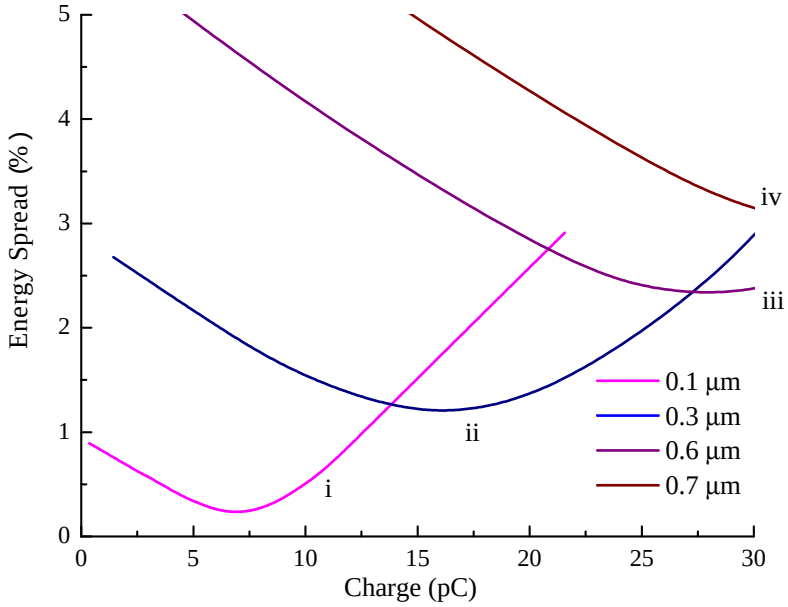

(b)

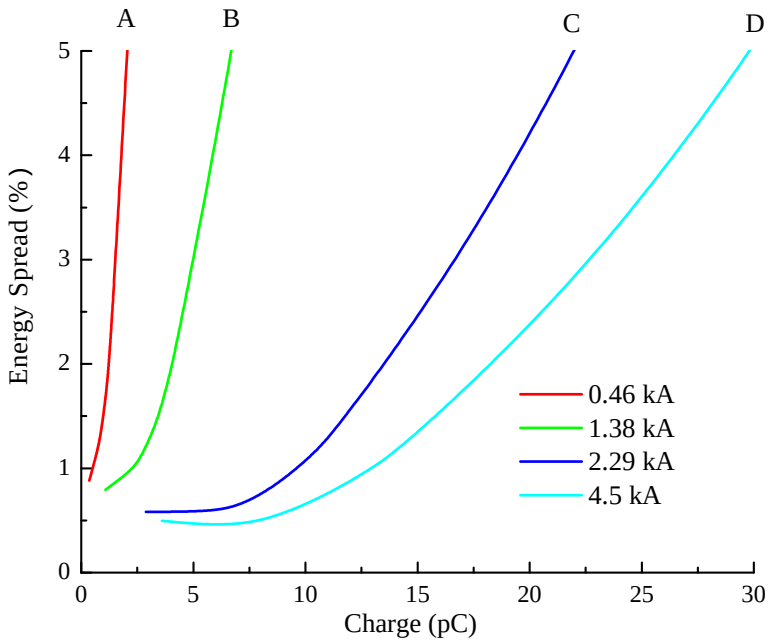

Figure 2.9: Reduced model showing beam loading of electron bunches in various initial conditions. (a) The fixed bunch length and varied injection rate are shown by i = 0.1 μm, ii = 0.3 μm, iii = 0.6 μm and iv = 0.7 μm. (b) Fixed current or continuous injection rates are given by lines A = 0.46 kA, B = 1.38 kA, C = 2.29 kA and D = 4.5 kA.

energy at the front and higher energy at the rear, whereas a down chirp decreases in energy with time, i.e. the bunch has higher energy at the front and lower energy at the rear. These electrons follow the electrostatic potential curve and the chirp is minimised during the phase-space evolution discussed in Section 2.2.6, as represented by the black bunch in Figure 2.10. Beam loading results in the electrons at the rear being accelerated over a reduced electric field. These electrons will follow damped potential curve and do not reach the same maximum energy as the electrons at the front, as shown by the green and red bunches in Figure 2.10. Under these circumstances, any increase in charge will result in over loading the wake and increasing energy spread. It may be possible that the electron bunch reaches a minimum energy spread after dephasing, however this would rely on the loading being matched to the wake structure.

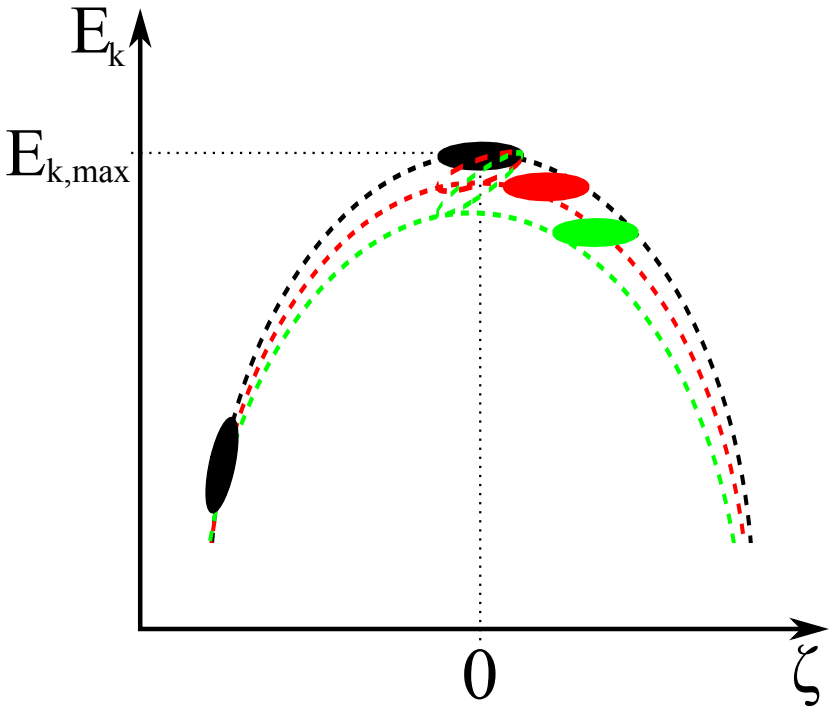

Figure 2.10: Phase-space diagram of beam loading for a chirped bunch injection. The unloaded wake (black) creates the minimum energy spread at dephasing whereas the slightly loaded (red) and very loaded (green) show the damped accelerating field applied to the electrons at the rear of the bunch.

Maximum Energy

As well as beam loading affecting bunch length and energy spread, it also lowers the accelerating potential. The damping of the electric field increases and the average electric field over the bunch decreases as the charge increases. This means that the

lower charge bunches can be accelerated to higher average energy than high charge beams.

2.3 Plasma Optics

2.3.1 Self - Focusing and Guiding

As a laser beam propagates through the plasma any radial refractive index variation will act as a lens. When the refractive index, η, has a maximum on axis, ($\partial\eta/\partial r < 0$), the gradient acts as a focusing lens. The index variation can arise from two sources. The index of refraction for an electromagnetic wave propagating in a plasma is given by, $\eta = (1-\omega_p^2/\omega^2)^{\frac{1}{2}}$. ω_p is the plasma frequency with the initial plasma frequency given by, $\omega_{p0}^2 = n_0\, e^2/(m\, \varepsilon_0)$. The plasma frequency varies with the plasma density such that $\omega_p(r)^2 = \delta n(r)\, n_0\, e^2/[\gamma_\perp(r)\, m\, \varepsilon_0]$. $\delta n(r)$ is the radial variation of the electron density, $\delta n(r) = n(r)/n_0$. As the laser amplitude grows, it can cause a variation in the electron density and mass. The generalised expression for the refractive index under these circumstances becomes (Mori, 1997; Esarey et al., 2009).

$$\eta(r) = 1 - \frac{\omega_{p0}^2}{2\omega^2}\left(\frac{n(r)}{n_0\gamma_\perp(r)}\right). \tag{2.30}$$

Therefore the refractive index will reach a maximum where the electron density reaches a minimum (due to either the expulsion of electrons by the ponderomotive force) and where the electrons are most relativistic (due to interaction with the most intense part of the laser).

Relativistic guiding occurs when the electrons in the plasma, which interact with the laser pulse, acquire relativistic velocities. As the laser passes through the plasma the electric field accelerates the electrons, through the Lorentz force as discussed previously. At high intensities $a_0 > 1$ the electrons will reach relativistic velocities thus causing their mass to increase, creating a corresponding decrease in the refractive index. The quiver motion of the electrons becomes relativistic at elevated laser intensities, and the Lorentz factor starts to increase as $\gamma_\perp^2 = 1 + a^2(r)$. Combining this with Equation 2.30 gives the relativistic refractive index (Mori, 1997),

$$\eta = 1 - \frac{\omega_{p0}^2}{2\omega^2}\left(1 - \frac{a^2}{2}\right). \tag{2.31}$$

Self-focusing occurs when the laser profile has a maximum on axis, $\partial a^2/\partial r < 0$, as is the case for a Gaussian bunch distribution and $\partial\eta/\partial r < 0$. The phase velocity of the laser pulse $v_p = c/\eta$ is at a minimum on axis where the electrons are most relativistic

and the refractive index is at its maximum. The radial variation of the phase velocity causes a curve in the phase front to develop, which focuses the laser.

The 'snow-plough' effect at the front of the laser pulse also acts radially, i.e. electrons are expelled from on axis to create a transverse density channel. This transverse density profile has a minimum density on axis, which also corresponds to the maximum laser intensity. The self-created plasma gradient (and therefore refractive index gradient) acts as a lens propagating with the laser pulse, focusing the beam.

Similarly, a preformed plasma channel can create a density gradient in advance of the laser interacting with the plasma. Here, a plasma density gradient is created to act as a waveguide and allow the laser to be guided over longer distances.

Pulse compression

Similarly to the effects of graded transverse refractive index, a longitudinal refractive index variation also occurs. The group velocity, $v_g = \eta c$, also varies with refractive index, such that a laser beam propagating in a low density, high refractive index plasma will have a greater group velocity than a laser beam propagating in a high density plasma. This process can lead to compression of a laser pulse propagating in a plasma bubble (Mori, 1997). Take, for example, a laser pulse propagating in a plasma bubble, such that the rear of the pulse is in the low-density centre of the bubble and the front of the laser pulse is in a high-density front of the bubble. The high refractive index in the centre of the bubble will cause a greater group velocity than the front of the laser pulse, which will cause the rear to catch the front, thus compressing the laser pulse and increasing the intensity.

2.4 OSIRIS Simulations

OSIRIS (Fonseca et al., 2002) simulation have been carried out by Brunetti et al. (2010) which can be used to demonstrate the wakefield acceleration. OSIRIS is a 1, 2 or 3D, fully relativistic particle-in-cell code for modelling plasma-based accelerators. Here, the 2D-particle-in-cell (PIC) code used parameters similar to those in the experiment. A 30 fs laser pulse with an initial $a_0 = 3$ and waist, $w_0 = 20\ \mu$m that quickly reduced to 10 μm due to self focusing which, in turn, increases the a_0. A plasma density of $n_p = 10^{19}$ cm^{-3} was used.

As the laser propagates through the plasma it expels most of the electrons to create the sheath of the bubble of radius, R. The sheath crosses at the rear of the bubble creating strong electrostatic fields. This field causes electrons to gain a velocity greater than the bubble and become trapped. The electrons that are trapped load the wakefield

and flatten the potential and also deflects further electrons from being injected creating a bunch > 0.4 μm long, as shown in Figure 2.11 (a).

Figure 2.11 (b) shows the transverse phase-space of the simulated electron bunch on the x-axis, where the beam is shown in the focusing cycle of the betatron oscillations. The 3.3 mrad divergence corresponds to the measured spot divergence.

Figures 2.11 (c - f) show the development, along the accelerator in time, of the electron beam's parameters, such as bunch length σ_z, radius σ_r, energy γ, energy spread σ_γ and σ_γ/γ and the normalised emittance $\varepsilon_{n,x}$. A rapid increase in emittance is shown in Figure 2.11 (e) along with the stabilisation of the emittance at $\sim 0.1 - 0.2$ π mm mrad. As the electrons propagate along the accelerator they undergo betatron oscillations shown in Figure 2.11 (c), which acts to rotate the transverse phase-space as the beam focuses and defocuses, however emittance is conserved. The betatron oscillations are seen to damp at a rate proportional to $\gamma^{-1/4}$. Also shown is the bunch length of 0.3 μm. The energy, γ in Figure 2.11 (d), increases rapidly just after injection with reduced acceleration as the beam reaches dephasing where the energy spread is at its minimum. Figure 2.11 (d) shows the relative energy spread, σ_γ/γ, decreasing to $< 0.5\%$.

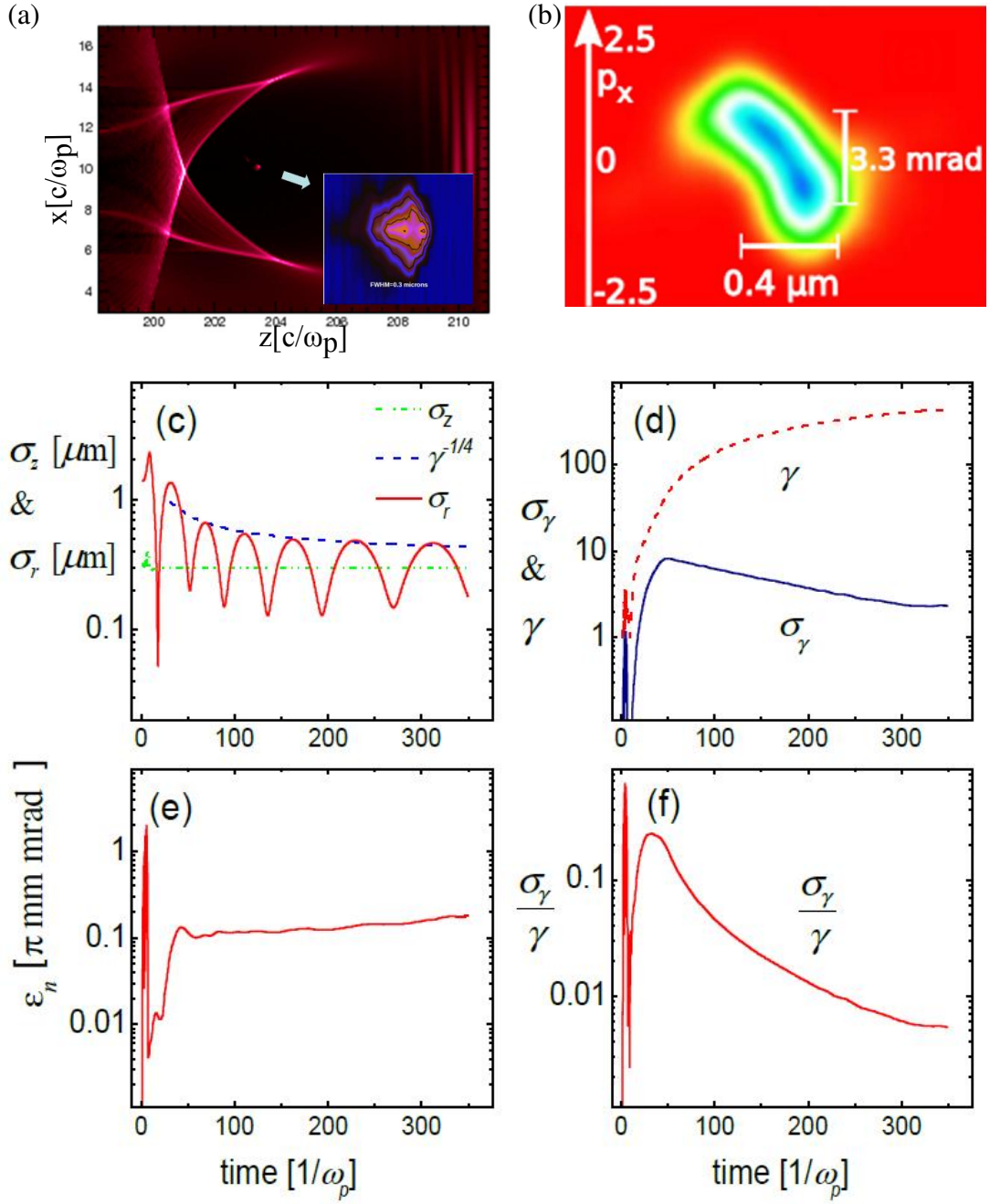

Figure 2.11: OSIRIS simulation of emittance development through the accelerator, (a)snap-shot of the wakefield accelerator (b) phase-space of the beam (c) beam width and length (d) energy and energy spread (e) transverse emittance and (f) energy spread (σ_γ/γ) (Brunetti et al., 2010)

Chapter 3

Experimental Methods

3.1 The TOPS Laser System

All the experiments carried out in this thesis utilise the Terahertz to Optical Pulsed Source (TOPS) laser system (Jaroszynski et al., 2000). The laser amplifies a train of short pulses from an oscillator that is stretched to lower the intensity to below the damage threshold of the optics. These low energy pulses are amplified in several stages before passing through a compressor and being re-compressed to high intensity. This section describes each of these stages in more detail, additional information about high power femtosecond laser systems can be found in Reid and Wynne (2000); Backus, Durfee, Murnane, and Kapteyn (1998); Simon (1989).

3.1.1 The Oscillator

The femtosecond laser pulse train is generated in an oscillator. The TOPS oscillator produces the pulses through self-mode locking, where many longitudinal modes are held in phase by mode locking (Christov, Stoev, Murnane, & Kapteyn, 1996). This gives rise to constructive interference within the cavity. The self-mode locked cavity utilises a titanium doped sapphire (Ti:sapphire) crystal which has a gain bandwidth from 700 to 1100 nm, peaked at 800 nm. Mode locking is achieved by the use of a nonlinear lens formed by the intensity distribution in the crystal. This nonlinear lens arises from the optical Kerr effect which, is due to the non-linear refractive index of materials at high laser intensities. The intensity dependent refractive index, $\eta(\mathrm{I})$ varies as

$$\eta(I) = \eta_0 + \eta_2 I, \tag{3.1}$$

where η_0 is the linear refractive index and η_2 is the nonlinear refractive index. η_2 is

typically very small and is therefore, only important at high intensities. Typically, the transverse profile of a laser has a higher intensity at the centre than the edges, which results in an increase in the refractive index of the material towards the centre. The gradient in the refractive index acts as a lens focusing the beam causing self-focusing. Not only can this occur as whole-beam self focusing but can occur in small intensity perturbations across the laser profile. These small perturbations are magnified in a potential runaway process which could result in the beam splitting into filaments and, ultimately, damage to the optics. However, the controlled Kerr lens in the oscillator couples the spatial and temporal modes and maintains phase locking. The cavity is aligned with the high intensity lens effect taken into consideration, which restricts continuous wave (CW) operation.

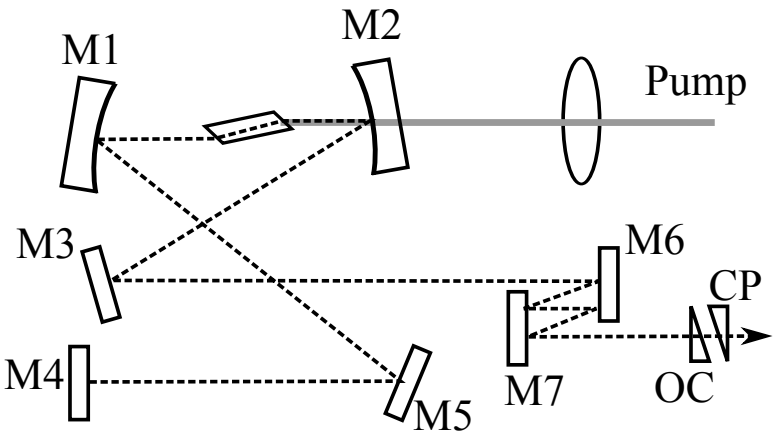

Figure 3.1: Schematic of the Oscillator

The oscillator is as shown in Figure 3.1. The cavity consists of a Brewster angled Ti:sapphire crystal placed between two focusing mirrors M1 and M2, three high reflective mirrors M3, M4 and M5 and an output coupler (OC). Dispersive mirrors, M6 and M7 correct frequency dispersion (or frequency chirp) occurring in the crystal (Stingl, Spielmann, Krausz, & Szipocs, 1994). The OC is wedged to remove unwanted back surface reflections and the spatial chirp removed by the compensation plate (CP). The oscillator outputs $<$20 fs, 9 nJ pulses with a $\sim$ 48 nm bandwidth centred around 800 nm in a 75 MHz pulse train.

3.1.2 The Pulse Stretcher

Chirped Pulse Amplification (CPA)

The output energy produced by the TOPS laser is of the order of 1.6 J delivered in 30 - 40 fs. Such high energy and short pulse duration would result in a laser intensity suf-

ficient to damage most optics (including the amplifiers). The solution is to stretch the laser pulse in time, from $\sim$ 20 fs to $\sim$ 200 ps. This five orders of magnitude stretching reduces the power by the same factor and enables the laser to be safely amplified. The stretcher introduces a deliberate dispersion by delaying the high frequency components relative to the low frequency components, thus producing a chirp. This chirped pulse can then be amplified as indicated in Figure 3.2. After amplification it is re-compressed to produce a high power pulse sufficient to drive a LWFA.

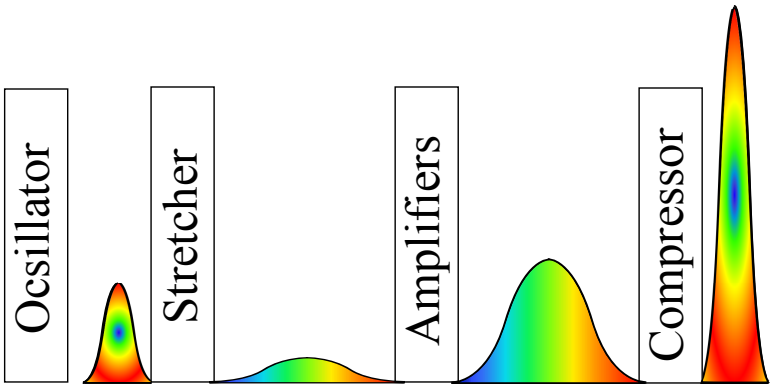

Figure 3.2: A schematic diagram of chirped pulse amplification. The pulse is stretched into a chirped pulse before amplification to avoid damage and other unwanted non-linear effects. After amplification it is compressed to produce the high peak power required.

The Stretcher

The stretcher disperses the laser pulse, stretching it in time. This is achieved using a pair of gratings, as shown in Figure 3.3 (Treacy, 1969). Here, a longer path is created for the red than the blue, which produces a negative dispersion and results in a down chirped pulse. The path length of the light travelling through the parallel grating pair is given by

$$P(\omega) = L\frac{1+\cos\theta(\omega)}{\cos(\gamma-\theta(\omega))}, \tag{3.2}$$

where γ is the angle of incidence and θ is the angle between the incident light hitting the grating and the diffracted light so that

$$\theta(\omega) = \gamma - \arcsin\left(\frac{2\pi c}{\omega d} - \sin\gamma\right). \tag{3.3}$$

L is the separation between the two gratings. The group delay is given by $P(\omega)/c$ and high orders are found from the derivatives of the group delay.

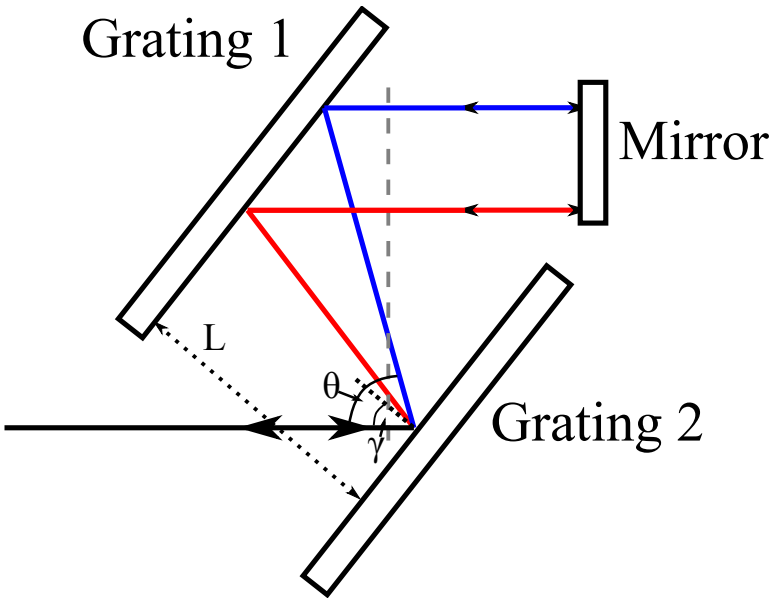

Figure 3.3: Parallel grating pair used to add negative dispersion to a light pulse.

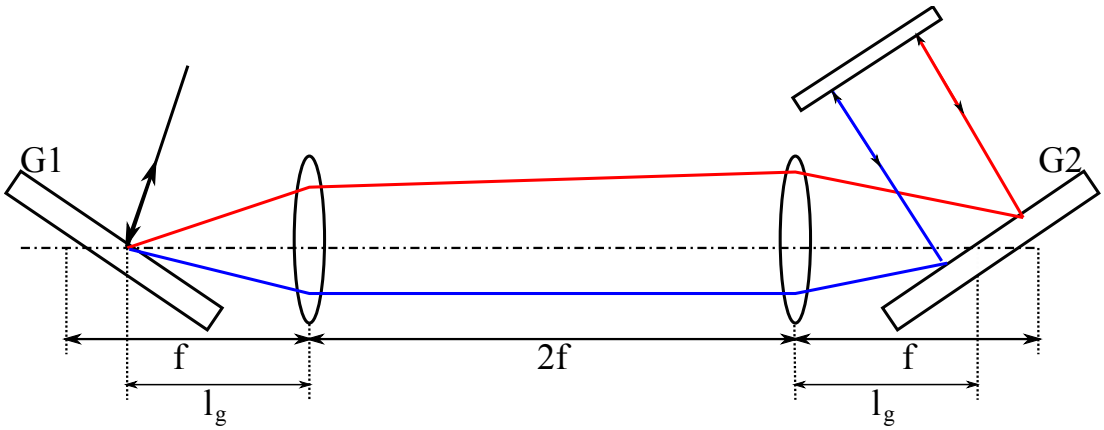

Figure 3.4: Anti-parallel grating pair used to add positive dispersion.

After the amplifiers the pulse must be compressed be creating a positive dispersion in a second device. For this a one-to-one magnification telescope is placed between an anti-parallel pair of gratings as shown in Figure 3.4. This set-up can be used to create an effective grating separation, $L = l_{eff} = 2(l_g - f)$ (Martinez, Gordon, & Fork, 1984; Martinez, 1987). l_g is the distance from the grating to the lens and f is the focal length of the lens. If f is equal to l_g there is no dispersion. When the grating is placed outside the focal length of the lens a negative dispersion is created like the parallel grating discussed above. The grating must be placed inside the focal length of the lens to obtain a change in sign of the dispersion. In this set-up the path length for the red light is shorter than for the blue light creating an up chirped pulse. It is this type of

gratings combined with focusing optics which is used in the TOPS stretcher. However, the TOPS laser replaces the lenses with concave and convex mirrors in an all reflective Offner configuration (Cheriaux et al., 1996). This set-up works the same as with lenses but has the advantage of having no aberrations.

3.1.3 Laser amplifiers

The TOPS laser consist of one regenerative amplifier, and three multipass amplifiers.

Regenerative Amplifier

The regenerative amplifier uses a fast acting Pockels cell which allows the transmission of the laser at a 10 Hz repetition rate. The Pockels cell, acting as a wave plate, rotates the polarisation of the laser allowing the beam to pass through a thin film polariser and then enter the cavity. When the laser pulse has made the required number of trips through the amplifier the Pockels cell once again rotates the polarisation and allows the beam to exit the cavity (Diels & Rudoplh, n.d.). The TOPS regenerative amplifier is used to amplify the laser pulse from <1 mJ after stretching, before passing it to the first multipass amplifier.

Multipass Amplifier

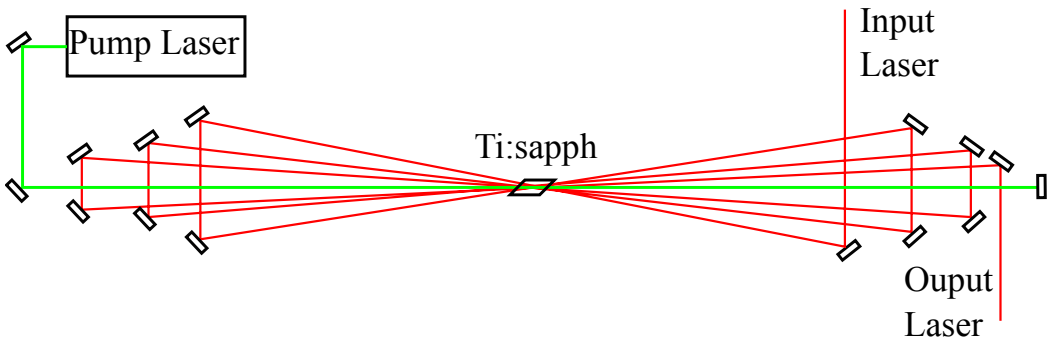

Figure 3.5: Multipass amplifier used in the high amplification stages of the TOPS .

In a multipass amplifier the laser beam has a single long path which passes through the amplifying crystal multiple times, an example of which is shown in Figure 3.5. Here the laser enters the cavity and is passed through the amplifier six times and then leaves without requiring a Pockels cell.

The first multipass amplifier is a six pass amplifier pumped by a 110 mJ Big Sky CFR 200 pump laser (10Hz). This typically produces a 20 - 30 mJ pulse. Before the

laser is allowed to enter the next cavity the laser energy is measured to ensure good alignment and amplification. The pulse is passed to the second multipass amplifier which has a water cooled crystal pumped by 2× Thales SAGA 220 with a combined pump energy of 1.1J. The laser is focused through a spatial filter to remove higher order transverse modes passing into the laser amplifier. During alignment and low power operation, the SAGA pumps are time delayed to remove their pump potential but keep the heating effect they impart to the crystal. It is essential to align the laser while warm to take into account thermal lens effects. Before the laser is allowed to enter the last amplifier the laser energy, bandwidth and profile are all measured to ensure damage will not occur in the final amplifier and that suitable amplification will occur.

The last amplifier is a 22 × 22 × 20 mm, cryogenically cooled Ti:sapphire crystal. Cryogenic cooling prevents thermal lens effects allowing the laser to be aligned without the use of the pump lasers. The crystal is pumped with three YAG lasers (two, 1 W and one, 2W). Producing a final amplified pulse of ∼1.6 J. The laser power is increased slowly during alignment to ensure no damage occurs. Each pump laser is started individually and the laser power recorded at each stage. On exit of the last amplifier, the laser beam is expanded to a 4.4 cm diameter beam and sent to the compressor.

3.1.4 Compressor

The compressor uses the parallel grating design discussed in Section 3.1.2. Ignoring dispersion from the amplifiers, the pulse should be completely recompressed by a compressor with an identical grating to that of the stretcher so that complete compensation of path lengths occurs, as demonstrated by Equation 3.2. However, as additional dispersion is added by the amplifier it is essential to compensate for this. Simply adjusting the grating spacing, l_g will not compensate fully. To compensate higher order dispersion introduced by the amplifier it is possible to use a grating-prism combination. In the TOPS compressor, Figure 3.6, the grating line density is modified so that it is no longer the same as the stretcher. This allows for compression down to 34 fs. The increase in the line density of the gratings has the advantage of increase efficiency $(\sim 70\%)$ and is more compact than the grating prism combination (in addition prisms cannot be used in high power laser systems).

TOPS compressor

The TOPS compressor, Figure 3.6 is contained inside a cylindrical vacuum chamber. The uncompressed beam enters the chamber through a wedged window and enters the

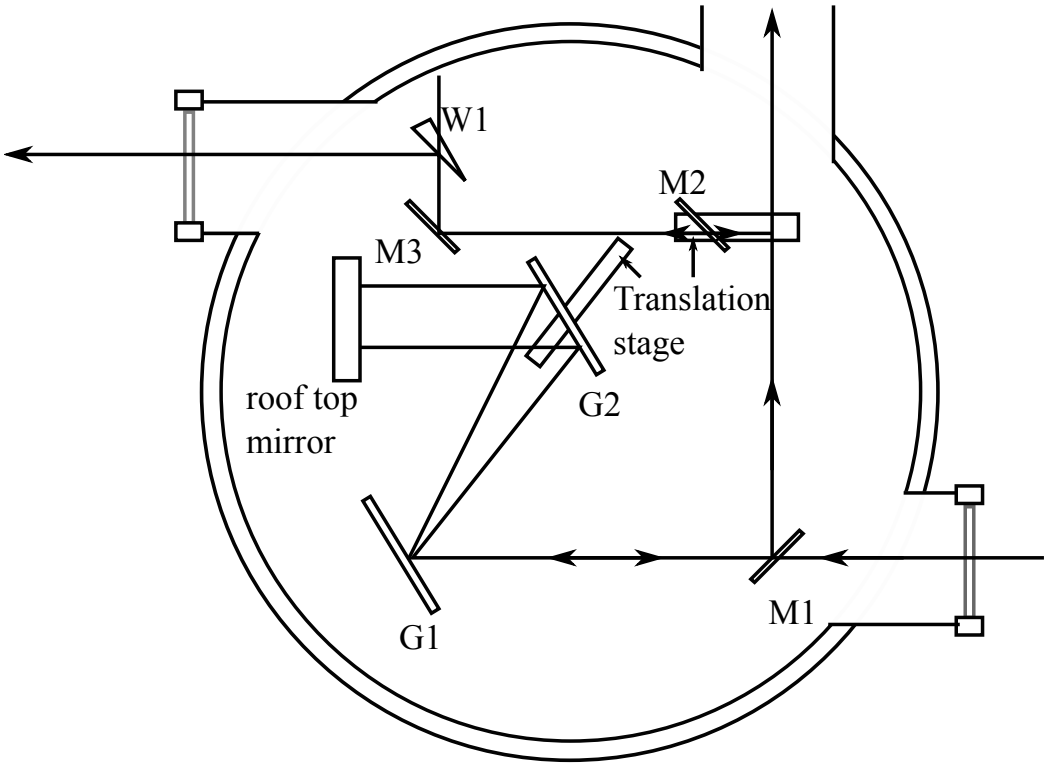

Figure 3.6: The TOPS parallel grating compressor.

parallel grating pair. A roof top mirror is used to transmit the beam back through the gratings at a lower height. The beam reflects off mirror, M1, and is sent to the accelerator chamber. The second grating, G2, is mounted on a motorised translation stage to allow fine adjustment of the pulse duration. Mirror, M2, is also mounted on a translation stage and can be moved into the beam line under vacuum. With M2 in place the beam is reflected out of the compressor to the auto-correlator. A wedge, W1, is used to reduce the intensity of the laser.

3.1.5 Laser Delivery

The 800 nm laser passes from the compressor to the accelerator chamber through a vacuum beam line. The accelerator chamber is located inside a one meter thick, reinforced concrete walled bunker designed to contain any radiation produced in the acceleration process. The accelerator chamber and compressor are separated by an anti-reflection coated pellicle to ensure the compressor remains clean. A gate valve and a bypass valve are used to isolate the two sides of the vacuum. The laser enters the accelerator chamber from the compressor and is directed to the focussing optics by mirror M1, as shown in Figure 3.7.

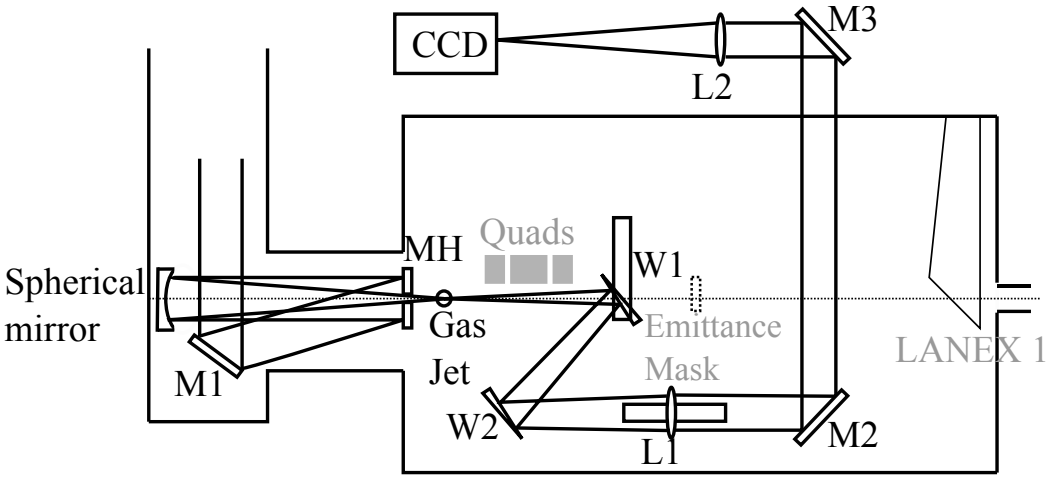

Figure 3.7: The TOPS accelerator chamber.

The focusing optics consists of an on axis spherical mirror focused through the mirror with a hole, MH. The laser is sent to the spherical mirror by MH which then focuses the laser back through MH to the gas jet position. The electron beam axis is defined by an alignment helium neon laser beam, which travels the length of the electron beam and enters through the rear of the spherical mirror, shown by the dotted line in Figure 3.7. The 800 nm laser beam is centred on all mirrors and aligned with the HeNe laser beam on the spherical mirror and the wedge, W1. This ensures the laser is on axis with the beam line. Care must be taken to ensure the laser passes through the centre of the hole in MH as clipping would cause damage.

The spherical mirror has a focal length, f = 75 cm and a beam radius of $W = 22$ mm on the spherical mirror. The focal spot waist was measured as $W_0 = 20$ μm ($1/e^2$ of the intensity). The focal spot is given by the Gaussian propagation formula,

$$W_0 = M^2 \frac{\lambda f}{\pi W}, \tag{3.4}$$

where M^2 estimates the difference between the real and ideal Gaussian beam and $\lambda = 800$nm is the wavelength of the laser. The measured focal spot is greater than that of a perfect beam giving an M^2 value of 2.4 for the high power laser. The distance over which the spot radius remains less than $\sqrt{2}W_0$ is known as the Rayleigh length given by,

$$L_R = \frac{\pi W_0^2}{\lambda}, \tag{3.5}$$

for the parameters measured here, $L_R = 1.5$ mm

A charge coupled device (CCD) is used to image the focal spot of the laser in-

side the chamber but only when the chamber is not in vacuum. The beam is therefore taken out of the chamber and analysed in air. The beam is first attenuated by reflection using two wedges with 4 % reflection on each. The beam is collimated by lens L1 and sent out of the vacuum where it is focused onto a CCD. L1 is mounted on a motorised translation stage to allow accurate collimation of the beam in vacuum (the optimum position of the lens changes between vacuum and air). W1 is also mounted on a translation stage to enable the wedge to be removed from the beam line and allow the electrons accelerated in the gas jet to transmit down the beam line.

The laser undergoes some losses as it transmits from the last amplifier through to the focusing optics and onto the target. 10 % of the laser beam is lost from the last amplifier to the compressor. A further 36 % of the beam is lost in the compressor and another 13 % is lost as it progresses to the spherical mirror. Resulting in only 51 % of the laser from the last amplifier reaching the target. The laser typically has a energy of 1.6 J measured at the last amplifier resulting in 0.82 J on target.

The power provided by a 0.82 J pulse delivered in 35 fs (FWHM). The laser energy, LE, is given by $LE = \int P(t)dt$ where $P(t) = P_0 \exp(-4\ln 2 t^2/\tau^2)$ at time, t, and τ is the pulse duration (FWHM). and the power given by $P_0 = 2\sqrt{\ln 2/\pi}\, LE/\tau$ Similarly the power is given by $P_0 = \int_0^\infty 2\pi r I(r) dr$ where $I(r) = I_0 \exp(-2r^2/\omega^2)$ at radius, r, and ω is the waist at $1/e^2$. The intensity is therefore given by $I_0 = 2P_0/\pi\omega^2$. The laser power is therefore 22 TW and when focused down to 20 μm, the intensity is $3.5 \times 10^{18}\mathrm{Wcm}^{-2}$.

3.2 Gas Jet

The target for the experiment is an underdense plasma created from helium. The gas is injected by a supersonic gas jet pulsed in synchronous with the laser. The gas jet has a throat diameter of 2 mm creating a plume of gas with a density depending on the backing pressure of the gas, the height above the gas jet and the geometry of the nozzle (Semushin & Malka, 2001). The gas jet was characterised using interferometery and a typical set-up of the gas jet (backing pressure of 34 bar and at a distance of 7 mm from the gas jet) results in a plasma density of $10^{19}\mathrm{electrons/cm}^3$.

3.3 Beam Profile Monitors

Scintillation screens are used to monitor the transverse properties of the electron beam at various positions along the beam line as shown in Figure 3.8. Two types of scintil-

lation screen are used (LANEX and YAG:Ce crystal).

The LANEX screen is a scintillation screen that emits in the green. The resolution of the screens have be found for the 'fine' and 'medium' grain screens as 40 μm and 76 μm, respectively (Jing et al., 1993). The increase in resolution between the two screens corresponds to an increase in thickness from 75 μm to 140 μm for the 'fine' and 'medium' screens. The LANEX 'normal' will have resolution between that of the two knowns screens because its thickness is between the two screens. However the resolution of the 'normal' screen is not known and therefore resolution corrections use the resolution of the LANEX 'fine' to ensure it is not over corrected.

The YAG:Ce crystal is a cerium doped yttrium-aluminium-garnet crystal which emits in the green under scintillation (Ludziejewski et al., 1997). The high resolution crystal used in the emittance measurements is a 100 μm thick crystal with a 10 μm resolution limit (Ingleby, 2009).

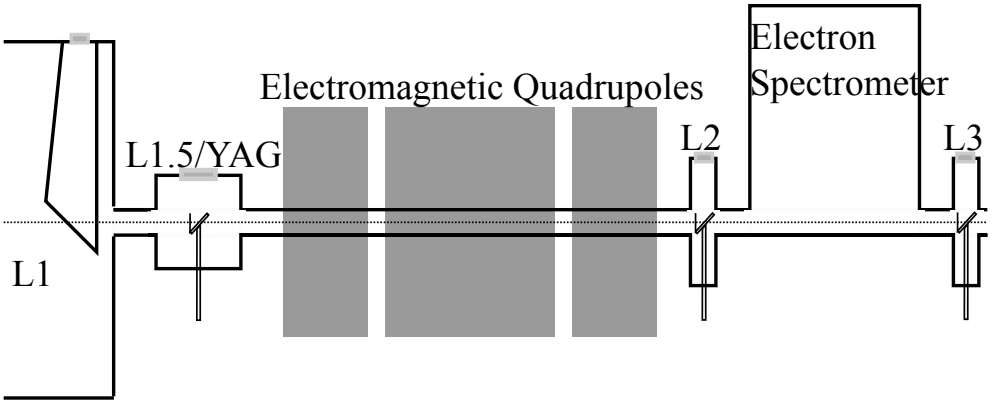

Figure 3.8: Layout of the profile monitors on the electron beam line.

LANEX 1, L1, is placed at the exit of the accelerator chamber and can be seen in both Figure 3.7 and 3.8. L1 is mounted at 45° to the beams line and viewed from behind (an angle of 45° cancels out distortion introduced by the screen's angle). The screen is viewed through a Perspex window with a CCD. L1 is covered with a layer of aluminium foil to protect it from the laser and prevent laser light from saturating the CCD. L1 is mounted in two sliding pipes which extend to the chamber wall to prevent stray laser light saturating the CCD. The two pipes slide past each other so the LANEX screen can be removed from the beam line by a manual 'vacuum feed through'. A small hole in the rear of the pipe allows the counter propagating alignment HeNe to enter and locate the center of the screen. A 1 cm^2 grid is marked on L1 for calibration.

LANEX 2, L2, is mounted on a cross piece after the electromagnetic quadrupoles. L2 is mounted normal to the beam line with a mirror placed behind at 45°. The screen is inserted in and withdrawn from of the beam line by a pneumatic feed through controlled from outside the bunker. The co-propagating HeNe laser beam is used to locate the centre and a cross wire placed for reference. LANEX 3, L3, is similar to L2 except mounted after the electron spectrometer at the entrance to the undulator.

LANEX 1.5, L1.5 and the YAG:Ce crystal, YAG, are mounted in the vacuum cube after the chamber and before the electromagnetic quadrupoles, 1 m from the gas jet. L1.5 is mounted on the rear of the transition radiation screen as discussed in Section 6.3. It is mounted at 45° and viewed from the rear, like L1. The YAG is mounted normal to the beam and viewed by a 45° mirror like L2 and L3. Both screens (only one at a time) are mounted on a pneumatic vacuum feed through that enables the screens to be removed from outside the bunker.

All screens are viewed with a 12 bit Point Grey Research Flea cameras using an Edmund Optics objective unless stated otherwise.

3.4 Charge Calibration

It is essential to be able to estimate the charge for some of the experiments. The most reliable method to obtain a charge measurement is to combine it with the profile monitors already in use, i.e. calibrating the light given off by the LANEX screen to the charge. To do this the LANEX screen is first calibrated by simultaneously measuring the charge for each image produced on the LANEX. The charge was measured using a calibrated Fuji Film image plate (Glinec et al., 2006).

3.4.1 Image Plate

The image plate is a two dimensional detector of ionizing radiation. A Fuji Biological Analysis System (BAS) IPs was used and consists of a photostimulable phosphor layer (barium fluoro-halogenite doped with europium 2+ ions, BaFX:Eu2+) coated on a polyester support layer (Meadowcroft, Bentley, & Stott, 2008). The image plate is coated with a Mylar protective layer on the top surface and a magnetic base layer which is used to mount the sample into the reader. The electrons are excited from the Eu2+ ion by the electrons and trapped in a meta-stable state. The excited state is then secondarily excited by a helium neon laser at 632.8 nm causing the state to emit through photo-stimulated luminescence (PSL) at 400 nm. This blue light is emitted in direct proportion to the stored energy. All information can be erased from the image plate using visible light, ready for re-use.

The Fuji scanner output the data in an image using a logarithmic scale known as the quantum level (QL) which must be converted to the linear PSL scale using (Fuji, 2008):

$$PSL = \left(\frac{R}{100}\right)^2 \times \left(\frac{4000}{S}\right) \times 10^{L\left(\frac{QL}{G}-\frac{1}{2}\right)} \tag{3.6}$$

where R = 25 is the scanning resolution in μm , S = 4000 is the sensitivity, L = 5 is the latitude and G = 65535 is the bit depth of 16 bit.

The absolute calibration of the image plate was carried out by Tanaka et al. (2005) and then extended to higher energies by Nakanii et al. (2007). Here a LINAC accelerator of various energies with known charge was used to calibrate the image plate. Fading of the image plate signal was found to stabilise after 45 minutes, which is when the calibration was performed. The sensitivity of the image plate was found to be stable across small electron beam energies at high energies (> 10MeV) and a calibration value of 0.0064 PSL/electron is given for 100 MeV electrons.

3.4.2 Set-up

The LANEX screens were calibrated using the charge measured using the image plates. The calibration was performed on LANEX 2, which is situated after the electromagnets quads and before the electron spectrometer. A carousel was designed for the calibration which consisted of a large disk with 12 targets. Each of the targets could be rotated into the beam line using a stepper motor attached to the carousel. The carousel was mounted 15 cm behind LANEX 2 and before the electron spectrometer. Circular image plates were wrapped in aluminium foil (~ 15 μm) to ensure protection from the laser light and to ensure that background light could not partially erase the image plate before reading. The carousel was mounted inside a vacuum chamber on the beam line. A window in the vacuum chamber was used to align the targets and to mount and remove the image plates from the target holder.

The LANEX screen was mounted as discussed in Section 3.3. The electrons were generated and optimised onto LANEX 2. The electrons were focused using the electromagnetic quads to create a strong contrast peak and remove low energy electrons through over focusing into a large angled background.

3.4.3 Result

The image plates were processed in the image plate reader and the image, in QL scale, converted to the PSL scale using Equation 3.6. This image was then saved as a 32 bit

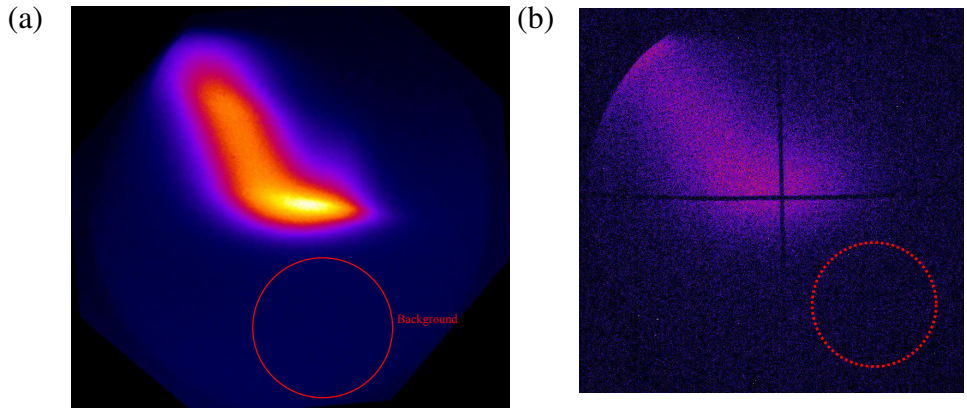

Figure 3.9: (a) Image Plate image and (b) LANEX screen image of the electron beam profile. The red circles indicate the background area.

TIFF image file to ensure accuracy. Figure 3.9 (a) shows an example PLS scale image of one of the electron shots. The background was sampled from an area away from the electron, as denoted by the red dotted circle, and scaled to represent the same area as the full beam. This background was subtracted from the full image. It was important to remove this background as any radiation produced along the beam line during the alignment and electron beam optimisation process would have been gathered and saved in the image plate throughout the experiment.

The LANEX images were processed in a similar manner. An example LANEX image is shown in Figure 3.9 (b) which is the same shot as on the image plate. A background measurement with the laser off, was first subtracted from all the images. A second background was then subtracted similarly to the image plate, by selecting a region away from the electron beam image and scaling it to be the same area as the region of interest. This background corrects for low energy, large angle electrons or for any stray laser light.

In total, 8 shots produced usable images. The charge measured on the image plate has been plotted as a function of the integrated signal, count, measured from the LANEX . The calibration curve this produces is quite linear, as shown in Figure 3.10. The gradient of this line provides the convertion number at 2.92×10^{-20} C/count.

3.4.4 Cross calibration of LANEX 1 and LANEX 1.5

To cross calibrate the charge from LANEX 2 to LANEX 1 and LANEX 1.5 consecutive shots were measured on the screens and the charge measured on one screen was used to calibrate the other.

50 consecutive shots were measured on LANEX 2 and the calibration found in the

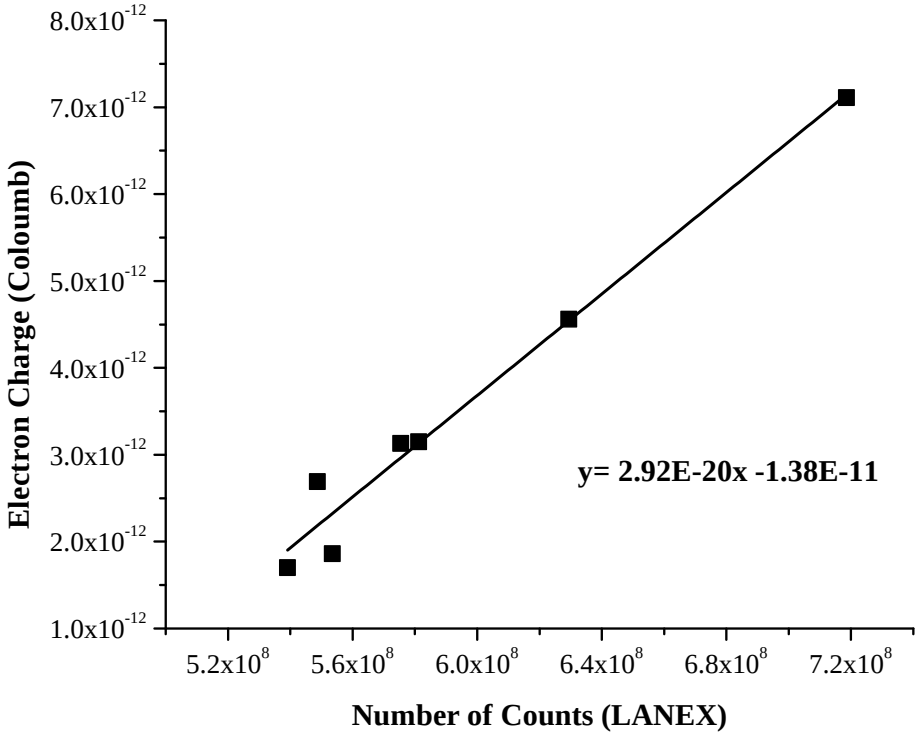

Figure 3.10: Calibration curve of the charge within the electron bunch as a function of the LANEX counts

previous section used to find a charge of 11.4 ± 0.7 pC where the error in the mean over the 50 shots is used and corresponds to 6 %. 100 consecutive shots were measured on LANEX 1 which gave a number of counts of $3.1 \times 10^8 \pm 0.1 \times 10^8$ counts, again using the error in the mean corresponding to 3% which is slightly less than LANEX 2 because it is averaged over more shots. This produced a calibration of 3.7×10^{-20} C/count. When the fast Fourier transform, FFT, is taken of the image (low pass of 1, high pass of 40) the calibration becomes 4.6×10^{-20} C/count due to the removal of noise.

The image on LANEX 1 had a tail coming from the low energy electrons being focussed to the side. This was due to a slight misalignments of the permanent magnetic quadrupoles. This tail was ignored in the calibration, however it could introduce a 10% error of 0.3×10^{-20} C/count if included.

LANEX 1 was used to calibrate LANEX 1.5. A charge 9.8 ± 0.3 pC was measure averaged over 100 consecutive shots. The signal on LANEX 1.5 were 2.9×10^8 $\pm 0.1 \times 10^8$ counts. (Both screens have an error in the mean of $\sim 3\%$.) The calibration was therefore created for LANEX 1.5 at 3.4×10^{-20} C/count for no FFT filtering on

the image and 4.5×10^{-20} C/count with FFT filtering.

3.5 Quadrupoles

To utilise the high quality electron beams produced in laser wakefield accelerators it is necessary to deliver the electrons to their application location using a beam transport system. The beam transport system on the ALPHA-X beam line consists of magnetic quadrupole, focusing lenses and beam steering coils.

The electron beam is manipulated through its interaction with an electromagnetic field and undergoes a force (the Lorentz force) given by Equation 2.1. The beam transport uses magnetic fields to interact with the electrons and therefore only the $\vec{v} \times \vec{B}$ part of Equation 2.1 is important. The force direction is at 90° to velocity and the magnetic fields as it is the cross product of the two. This is most simply demonstrated by the steering magnets, which applies a magnetic field across the beam line. Figure 3.11 shows that for a steering magnet with fields propagating from left to right and the beam moving into the page the electron beam would be directed down. One steering coil is mounted in each of the three electromagnetic quadrupoles in alternating directions. The current can be reversed in each of the coils to allow steering in both the positive and negative direction.

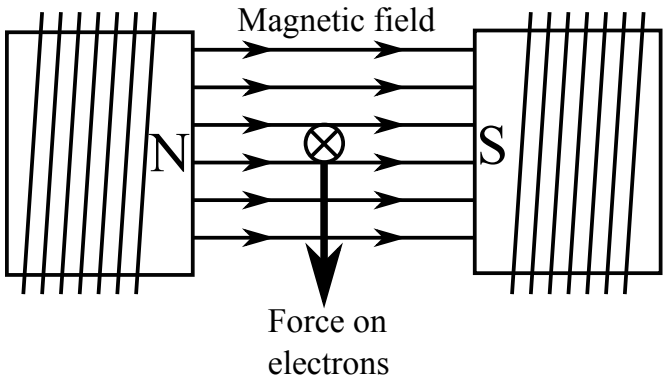

Figure 3.11: Demonstration of the force acting on an electron beam in a steering magnet.

The quadrupoles work in a similar manner as the dipole steering magnet discussed above. However the quadrupole has four poles rather than the two in the dipole steering magnets, as their names would suggest. In the quadrupoles, two north poles and the two south poles are directly opposite each other, as shown in Figure 3.12. Now the magnetic field is bent from the north to the south poles creating a sweeping force on the electrons, which are travelling into the page in Figure 3.12. This force compresses

the beam on one axis and elongates it on the other. The second and third quadrupole then alter the field direction resulting in an overall focusing effect on both axes.

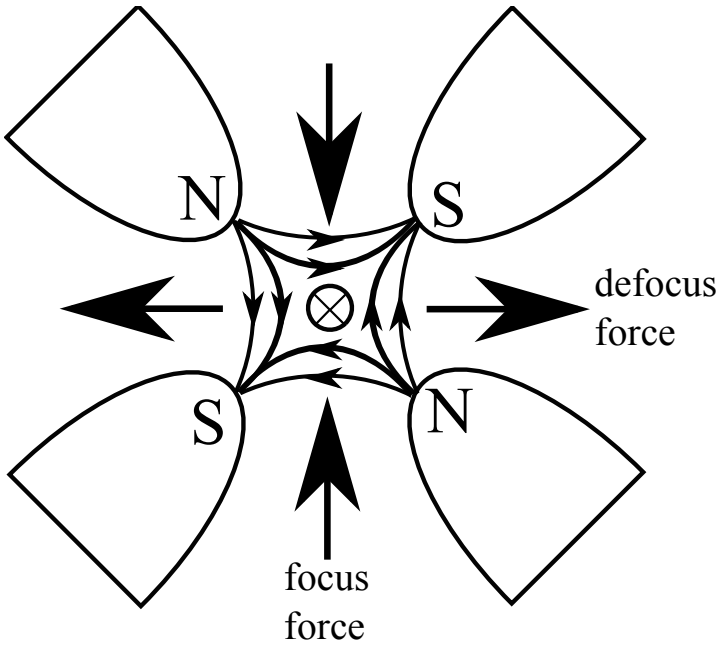

Figure 3.12: Schematic of the magnetic field in a magnetic quadrupole showing the focusing force on one axis and the defocusing force on the other axis.

There are two sets of magnetic quadrupole triplets on the ALPHA-X beam line. The first are permanent magnetic field quadrupoles (permanent quads) which are mounted inside the accelerator chamber and have the advantage of being very compact. Their compactness allows them to be mounted extremely close to the accelerator as shown in Figure 3.7, this will allow the electron beam to be collimated immediately after the accelerator to stop the growth in bunch length due to different path lengths. This is discussed in more detail in Chapter 6. These quads are mounted on a motorised translation stage so that they can be moved in and out of the beam line.

The second set of quadrupoles are electromagnetic quadrupoles (electromagnetic quads) which are mounted after the accelerator chamber and in front of the electron spectrometer, as shown in Figure 3.8. The magnetic fields in these quads are controlled by the current passing through their coils. The quads can be fully adjusted to suit the requirements of the electron beam. As the electron beam velocity varies from day to day, it is important to also be able to vary the magnetic field daily. This will be discussed further in the emittance chapter when the influence of magnetic quadrupoles on the transverse phase space is discussed.

3.6 Electron Spectrometer

The electron energy is measured by an electron spectrometer, which consists of an electromagnet that acts in exactly the same way as the steering magnet discussed above. The electromagnets can be turned on to bend the electrons out of the beam line. The electron deflection depends on its velocity, and therefore by measuring the deflection the electron energy spectrum can be determined. The maximum magnetic field of the spectrometer is 1.7 T. This allows for energy measurements up to 600 MeV for the high energy low resolution screen, with a resolution of 1 - 10%. The low energy high resolution part of the spectrometer bends the electron through a larger angle and thus has a larger dispersion and a higher resolution (0.1%), but is limited to a maximum energy of 100 MeV. The spectrometer utilises the Browne-Buechner design (Browne & Buechner, 1956) to focus the electrons in both the horizontal and vertical planes over a wide energy range. Electrons are detected on a Ce:YAG crystal that is imaged using a 14 bit Grasshoper CCD camera. In addition, the quadrupoles magnets can be used to optimise the system.

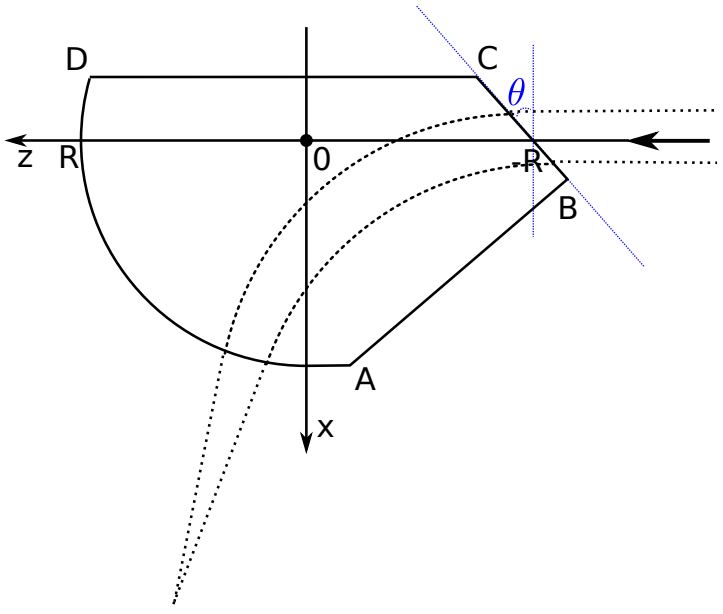

Figure 3.13: Horizontal focusing of electron spectrometer.

As shown in Figure 3.13, the collimated electron beam, represented by the dashed line, enters the spectrometer at R. The different path lengths through the spectrometer cause different trajectories for each side of the beam causing the beam to focus at some distance after the spectrometer. Vertical focusing arises from the electrons passing at an angle, θ, to the fringe fields at the entrance to the spectrometer causing the electrons to pass through a curved magnetic field, as shown in Figure 3.14. These curved magnetic

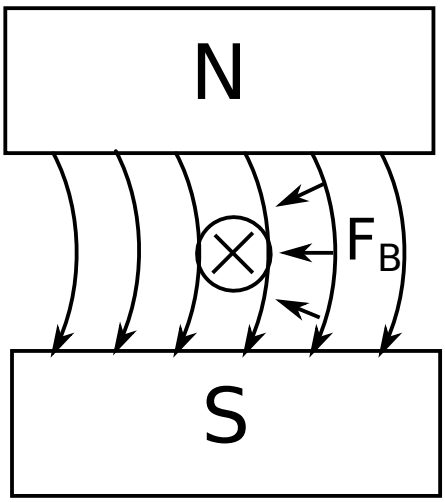

Figure 3.14: Vertical focusing from the fringe field of the electron spectrometer.

fields result in both a horizontal and vertical force to act on the electrons focusing the beam.

Chapter 4

Emittance

4.1 Introduction

Emittance is a measure of the beam quality and determines transverse momentum and position of the beam and thus allows us to compare the quality of beams for application. This chapter will explain what emittance is and the measurement techniques developed to measure it, along with the first, high resolution, single-shot measurements of LWFA electron bunches.

4.2 Theory of Emittance

4.2.1 Transverse Phase Space

The transverse phase-space maps the transverse spread in momentum of the electrons against their position across the beam (Humphries, 1990). Take, for example, a diverging beam emitting from a point source as shown in Figure 4.1 (a). At the point source, (i), the electron beam has zero radius but is diverging in both the positive and negative direction. In the phase-space, Figure 4.1 (b), at position (i), the beam has minimal radius shown on the x-axis but shows transverse momentum on the x'-axis. At (ii) and (iii) the beam is diverging and increasing its radius in the x-axis but the transverse momentum of each of the electrons in the beam remains constant. This appears in phase-space as the line being stretched to positive x for a positive angle and negative x for a negative angle.

A magnetic lens collimates the beam at (iv) such that the beam has a fixed radius and zero divergence. This appears as a rotation of the phase-space from (iii) to (iv), where the electrons have no divergence on the x' axis but keep their radius along x. If a second focusing lens is placed in the beam line, the electrons receive another rotation

in phase-space from (iv) to (v). As the beam focuses the phase-space will rotate back to a focus as at point (i).

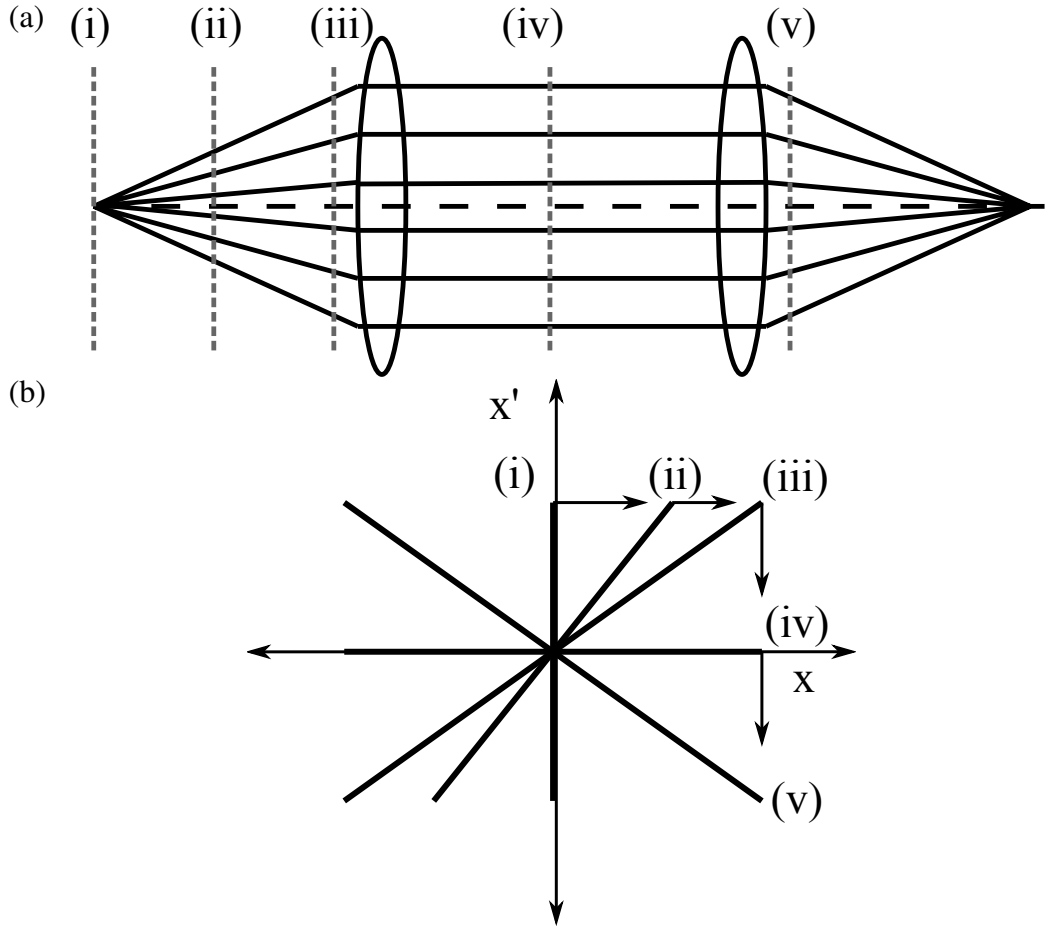

Figure 4.1: (a) A real space trajectory of a laminar electron beam and (b) its phase-space representation. The beam starts at a point source (i) and diverges through (ii) and (iii). The beam is collimated through (iv) and refocused at (v) back down to a point source.

Laminar beams are theoretically perfect beams, whereas actual beams have a range or spread in transverse velocities at any one point and cannot start at and/or be focused back to a point source. This adds a width or thickness to the phase-space 'line', and the beam is now be represented by an ellipse which contains this spread. At the source, (i), in Figure 4.2 (a), a source of radius, σ_x, is used.

In phase-space, Figure 4.2 (b), the focus is represented by the vertical ellipse with a radius of σ_x on the x-axis. This ellipse is stretched horizontally, as before, when the beam diverges. The beam continues to have a spread in transverse velocity but this spread does decrease at any one point on x, as the beam diverges and the phase-space is stretched further through (ii) and (iii). The phase-space is rotated to a beam with a fixed radius, x, and a width corresponding to the spread in transverse momentum or

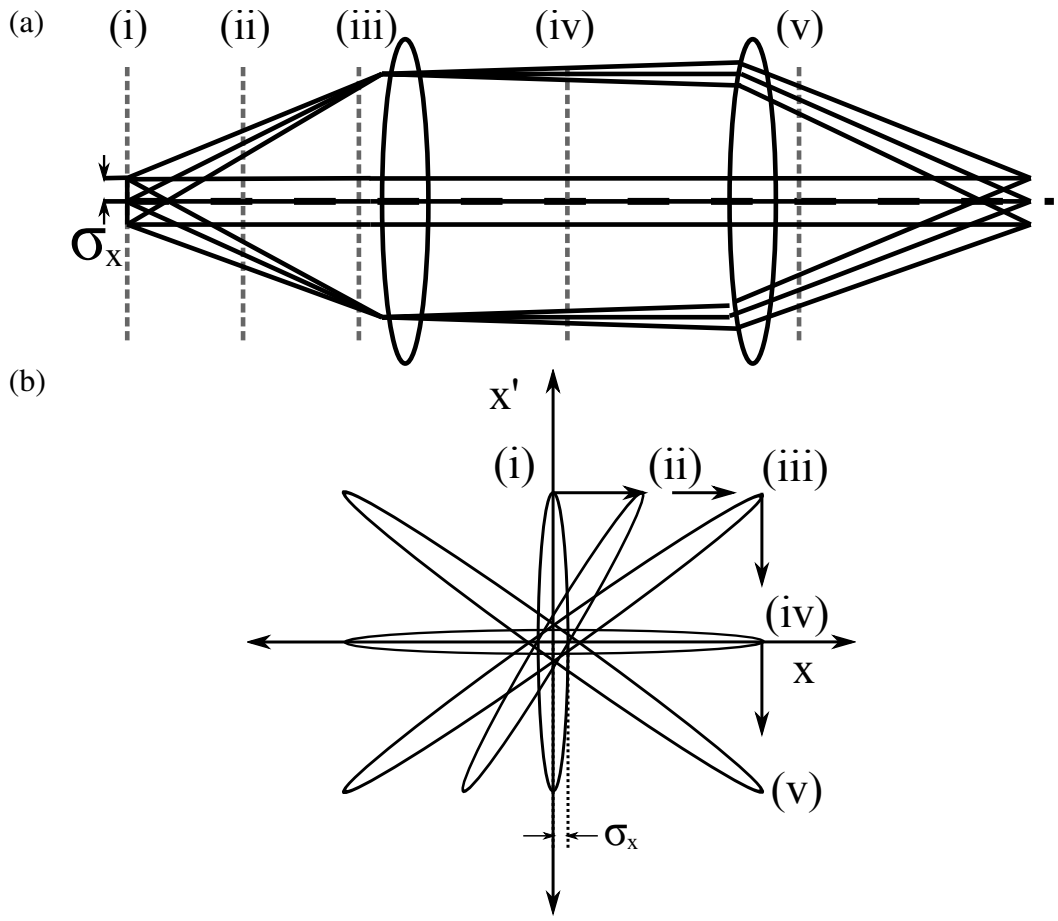

Figure 4.2: (a)a real space trajectory of a real electron beam with transverse momentum spread and (b) its phase-space representation. The beam starts at a source,(i), of width σ_x and diverges through (ii) and (iii). The beam is collimated through (iv) and refocused at (v) back down to the same source size.

angles, σ'_x, as the beam passes through the first lens. This spread in transverse angle is the ratio of the spread in transverse momentum, Δp_x, to the longitudinal momentum, p_z, by

$$\sigma'_x = \frac{\Delta p_x}{p_z}, \tag{4.1}$$

which is position (iv) on Figure 4.2. When the electrons pass through the second lens they are given a transverse velocity and the phase-space is again rotated. This phase-space will again be stretched horizontally until it returns to the area (i), as the electrons drift back to the focus (provided the focal lengths of both lenses are the same). The size of the focal spot depends on the spread in the transverse velocities and is related to the focal length of the lens by

$$\sigma_x = \sigma'_x f, \tag{4.2}$$

therefore, it is possible to create a smaller focal spot by using a shorter focal length lens and focusing the electrons with a steeper angle.

4.2.2 Emittance

When the electron beam is allowed to drift and expand or is passed through focusing lenses, the area of the phase-space is conserved, provided that uniform forces have been applied to the beam. However, if forces are nonlinear, like the fringe fields of a magnet, then the phase-space area can be distorted. Take, for example, a collimated electron beam passing through a nonlinear magnetic lens so that the outer electrons are focused more steeply than the inner electrons. Now the phase-space of a beam focussed by a linear lens, ellipse (v) in Figure 4.2 (b) and the dotted line in Figure 4.3, would take on an S shape curved, shown by the black curve in Figure 4.3.

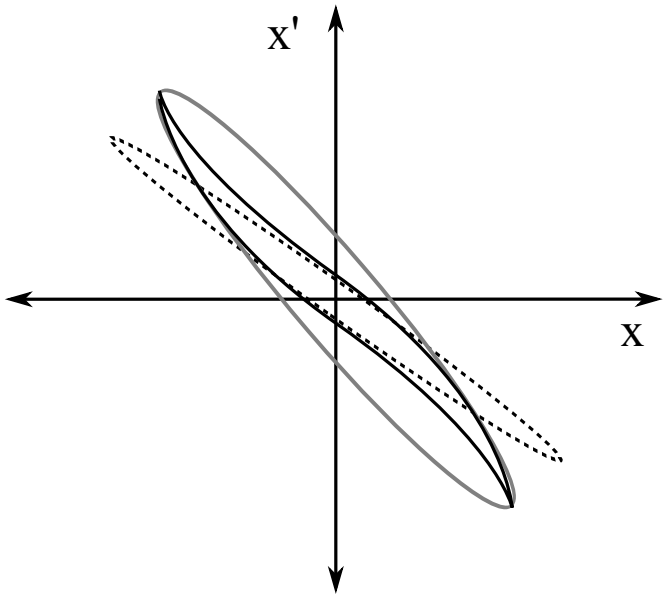

Figure 4.3: Demonstration of emittance as an area in phase-space. The dashed ellipse represents the area of a focused electron beam. The solid S-shaped area is the same focused beam through a non-linear lens which focuses the outer electrons more steeply than the inner. This beam, although having the same area as the first ellipse, cannot be focused to the same spot size. An effective area which encompasses the S-shaped area is instead used, represented by the grey ellipse, and is known as the emittance.

The area of this S would remain the same as the area of the dotted line, however Equation 4.2 would no longer be valid and the beam would not be able to be focused

down to the same spot size. Instead an effective area of the phase-space must be calculated, a single ellipse encompassing the entire beam shown by the grey line in Figure 4.3. This effective area is known as the emittance. The emittance is defined in terms of transverse angle, x' and y', rather than the transverse momentum, p_x and p_y, which are related by,

$$x' = \frac{p_x}{p_z}, \tag{4.3}$$

and

$$y' = \frac{p_y}{p_z}, \tag{4.4}$$

where p_z is the average longitudinal momentum.

Conventionally emittance, ε, is defined as the area of the ellipse given by,

$$\varepsilon_x = \int\int dx dx'. \tag{4.5}$$

The subscript, x, denotes that this is the emittance along the x-axis. When the electron beam is at the focus or is collimated, the phase-space ellipse is aligned with the x' or x axis such that $\sigma_x = x_{max}$ or $\sigma'_x = x'_{max}$ ((i) and (iv) in Figure 4.2). Here, the area of the ellipse is simply given by,

$$\varepsilon_x = \pi x x'. \tag{4.6}$$

The units for the conventional definition of emittance are mm mrad. However, the modern definition of emittance is the area of the ellipse divided by π, such that Equation 4.6 simply becomes,

$$\varepsilon_x = x x'. \tag{4.7}$$

The units become π mm mrad to denote that this convention is being used.

Emittance has now been defined for an ideal beam with sharp boundaries. In experiments, boundaries in distributions are rarely sharp. Therefore, the root-mean-square (r.m.s.) emittance is used. Here, the r.m.s. value is used when measuring the distributions of the particle's position and inclination angle.

Emittance often decreases as electrons are accelerated. Emittance decreases because it is the area in (x,x') phase-space and as p_z increases, x' decreases. Emittance is therefore often normalised by the longitudinal velocity and is referred to as the normalised emittance, ε_n,

$$\varepsilon_{n,x} = \gamma\beta\varepsilon_x. \tag{4.8}$$

Throughout the remainder of this thesis whenever emittance is discussed it will refer to the normalised, r.m.s emittance.

4.2.3 Pepper-Pot Measurement Technique

The particle's displacement in both position and angle must be measured in order to obtain the emittance of an electron beam. Measuring the position of the electrons within an electron beam is relatively simple and can be done using a simple fluorescent screen to obtain a transverse image. A measure of the angle is obtained by converting angular displacement into spatial displacement. To do this a small section of the beam is selected by an aperture or slit and the electrons, which pass through the slit, are allowed to drift to a screen. The average displacement of the spot on the screen, relative to the slit position, gives the angle, x', of the beam and the r.m.s. spread in the spot gives the r.m.s. spread in the angle, σ'_x, of the beam at the aperture position. If the slit is scanned for all points on x then the x' and σ'_x can be found for all x and the (x, x') phase-space can be reconstructed.

A diagnostic system based on single slit measurements requires many shots to enable construction of the electron beam phase-space. The multi-slit measurement works by having multiple slits in an array, thus enabling a single shot measurement for one axis (Zhang, 1998).

The pepper-pot is a generalisation of the multi-slit measurement, as it is the equivalent of performing a multi-slit measurement on both axes simultaneously. The pepper-pot mask is an array of holes where each column of holes acts as a slit on one axis and each row of holes acts as a slit on the other axis. This is the equivalent of a 2D multi-slit measurement (Zhang, 1998).

One axis of the pepper-pot mask is shown in Figure 4.4. The beam, travelling from left to right, hits the mask and is broken up into little beamlets. The position of the hole in the mask selects a position in the beam, x. The position of the beamlet on the screen provides the divergence, x', at x, $x' = (X - x)/L_{drift}$ and the r.m.s. beamlet, σ_x, gives the r.m.s spread in the divergence, $\sigma'_x = \sigma_x/L_{drift}$, where L_{drift} is the drift distance from the mask to the screen.

This is repeated for each position in x and the (x, x') phase-space is reconstructed as shown in Figure 4.4 (b). The emittance can then be calculated using

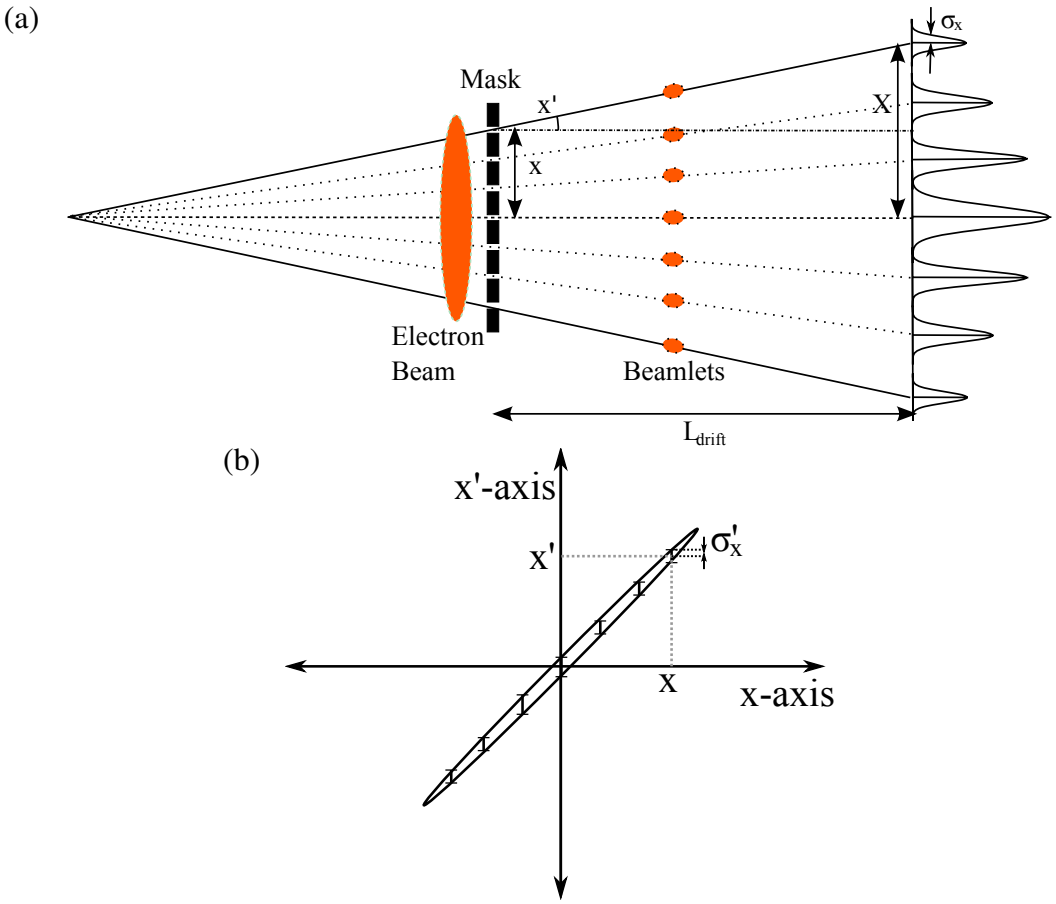

Figure 4.4: (a)Trajectory of a beam passing through a pepper-pot mask. At the mask the beam is split into beamlets which drift to the screen. The hole position selects the position of the beam, x, and the beamlets position on the screen provides the angle, x′, and the angular spread, σ'_x. Each of the holes in the mask measure a position in phase-space, (b), allowing the reconstruction of the emittance ellipse.

$$\varepsilon_{x,rms} = \sqrt{< x^2 >< x'^2 > - < xx' >^2}. \tag{4.9}$$

However, it is possible to measure the emittance directly from the pepper-pot beamlets as shown by Zhang (1998)

$$\varepsilon^2_{x,rms} = \frac{1}{N^2}\left\{\left[\sum_{j=1}^{p} n_j(x_j-\bar{x})^2\right]\left[\sum_{j=1}^{p}\left[n_j\sigma'^2_{x'_j}+n_j(x'_j-\bar{x}')^2\right]\right]-\left[\sum_{j=1}^{p} n_j x_j x'_j - N\bar{x}\bar{x}'\right]\right\}, \tag{4.10}$$

where $N=\sum_{j=1}^{p} n_j$; n_j is the number of electrons passing through the jth hole, x_j is the jth hole position, $\bar{x}=(\sum_{j=1}^{p} n_j x_j/N)$ is the mean hole position, $\sigma'_{x'_j}=\sigma_{x'_j}/L_{drift}$ is the r.m.s. divergence of the jth beamlet, $x'_j=(X_j-x_j)/L_{drift}$ is the divergence of the jth

beamlet, X_j is the peak position of the detected jth beamlet, $\bar{x}'$ is the mean divergence of all the beamlets, L_{md} is the distance from the mask to the detector and p is the total number of beamlets.

4.3 Experimental Set-up of the Emittance Measurement

4.3.1 Pepper-pot Design Considerations

The three parameters that are evaluated in the electron beam emittance measurement are the beam divergence, divergence of the beamlets and the charge within each of the beamlets. This requires the image measured on the screen to have clearly defined peaks which will provide their peak position, r.m.s. spread and charge. However, low emittance beams from a small source will have low divergence beamlets. It is therefore essential to optimise the magnification in the system without sacrificing the contrast of beamlets against the background.

The parameters available to optimise the pepper-pot measurement are the distance from the gas-jet to the mask, L_{gm}, the distance from the mask to the detector (or drift distance), L_{drift}, mask hole size, σ_h, hole separation, d and mask thickness, D. Treating the hole in the mask like a pin hole camera, the magnification in the system is given by, $M = \frac{L_{gm}+L_{drift}}{L_{gm}}$. Therefore, system magnification is maximised by decreasing the distance between the gas-jet and the mask and increasing the drift distance. However, there is a minimum distance that the pepper-pot mask can be placed from the gas-jet due to the damage the laser will cause to the mask. To limit damage, the distance was set to 31 cm, i.e. beyond the quadrupoles and the first wedge.

Mask Design

The primary purpose of the pepper-pot mask is to break the electron beam into small beamlets which can be used to calculate the phase-space distribution of the beam. Space charge effects are minimal, even in the full beam, as the beams typically used in the experiments here are highly relativistic. Therefore any mask hole size will provide beamlets which are free from space charge effects.

Two factors limit the minimum hole size used in the mask. The first is that the acceptance angle of the hole through the mask must be greater than the divergence of the electron beamlet, σ'_x, passing through the hole given by

$$\sigma'_x = \frac{\sigma_x}{L_{gm}}, \tag{4.11}$$

and

$$\sigma_x' < \frac{\sigma_h}{2D}, \tag{4.12}$$

where σ_x is the electron beam source size. If this is not satisfied then the mask will act as a collimator removing the higher divergence electrons and effectively cleaning the emittance and giving a false underestimation.

The second factor limiting the minimum size of the hole is the total charge in a beamlet, Q. The reduction in the charge transmitted through the hole is given by

$$Q = Q_0 \frac{d^2}{\sigma_0^2}, \tag{4.13}$$

where σ_0 is the radius of the beam at the mask, and Q_0 is the total charge in the beam before the mask. As the fraction of the charge in the beam is reduced it will become increasingly difficult to resolve the beamlets on the screen above the background noise.

The upper limit of the hole size is set by being able to clearly resolve the peaks on the screen separately from each other. The spot size on the screen, σ_x, is a combination of the r.m.s hole width, σ_h, the resolution of the screen, σ_{res} and the the divergence of the beam (Equation 4.11) which is given by

$$\sigma_x^2 = \sigma_h^2 M^2 + \sigma_{res}^2 + (\sigma_x' L_{drift})^2. \tag{4.14}$$

The spot separation is on the screen is given by the magnified separation of the holes on the screen, M $\times$ d. The hole separation on the screen is required to be much greater than σ_x to clearly resolve the peaks.

4.3.2 The Pepper-pot Set-up

The emittance set-up is as shown in Figure 4.5. The measurement is destructive and scatters the electrons, therefore the emittance mask is mounted on a rotation stage which enables the mask to be rotated in and out of the beam line. The mask is aligned using a HeNe laser beam which was co-aligned with the electron beam line. The holes of the emittance mask are aligned with the centre of the HeNe beam and the transmitted and back reflected light used to ensure that the mask is placed normal to the beam line. Firstly, the mask is rotated off axis and the electron beam optimised on Lanex 1 (L1). Once an optimised beam is obtained, the mask is rotated on axis.

The mask is placed 31 cm from the gas jet and the transmitted electrons are measured on the LANEX 1 providing a drift distance of 32.5 cm and a magnification of M= 2.05. The mask consisted of an array of 11 $\times$ 11 holes laser micromachined in 250 μm thick tungsten (the mask thickness will be discussed in more detail later). A

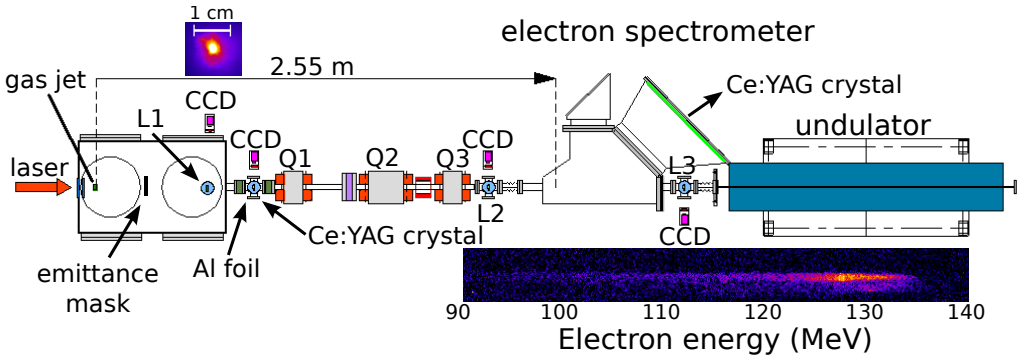

Figure 4.5: Experimental layout of the emittance beam line. The gas-jet is placed in it normal position within the gas-jet chamber. The emittance mask is placed 31 cm after the gas-jet and the transmitted electrons measured on LANES 1, L1, or later on the Ce:YAG crystal placed 30 or 61 cm after the emittance mask. The emittance mask, LANEX 1 and the YAG crystal are removable from the beam line to allow the electrons to be transmitted through to the electron spectrometer to obtain the energy for normalisation.

slight taper of the hole gives an effective hole diameter of 52 ± 7 μm.

A 52 μm diameter hole in 250 μm of tungsten gives an acceptance angle of 50 mrad, as given by Equation 4.12. This acceptance angle is much greater than the divergence of both the electron beam ($\geq$ 1.5mrad) and the created beamlets, therefore, the holes do not act as collimators and affect the measurement.

The primary function of the low resolution emittance measurement was to test the effectiveness of the mask and the experimental set-up. The mask is therefore designed to be able to cope with a large range of emittance and to ensure successful measurement.

The spot separation for a perfect beam is 1mm due to the magnification in the system and the hole separation on the mask. To clearly resolve the r.m.s spread of the spots measured on the screen, given by Equation 4.14, they would need to be much smaller than the magnified hole separation. The maximum spot size clearly resolvable on the screen is ~ 200 μm. This set-up will therefore be able to resolve electron beam with a maximum source size of ~ 190 μm ($= 200$ μm $\times L_{gm}/L_{drift}$). For a divergence of 2 mrad and an energy of 100 MeV this would give a maximum emittance measureable of ~ 75 π mm mrad.

As the holes in the mask act like a pin hole camera, the resolution corrected size of the spot measured on the screen will be the size of the source. Errors in the hole size correction due to the resolution ($\pm$ 30 μm) and error in the hole radius ($\pm$ 7 μm) result in an error in the source size of $\sigma_{x,error} = \pm$ 31 μm. This source size error results in an error in the emittance resolution of ~ 4.2 π mm mrad for a 1 mrad beam at 80

MeV (using equations 4.7 and 4.8). The spot position and divergence is averaged over many pixels and can therefore be found with relatively low error ($\ll 30\ \mu$m) therefore the major error will come from the hole size correction as $\varepsilon_{\text{error}} = \gamma\sigma'_{\text{x}}\sigma_{\text{x,error}}$.

General Particle Tracer Simulations of Set-up

The General Particle Tracer (GPT) code (Van Der Geer & Loos, 2001b, 2001a) was used to check the design of the pepper-pot and ensure that hole spacing and magnification would still allow measurement for a wide range of emittances. GPT is a Runge-Kutta based code developed for the design of accelerators and beam lines allowing full 3D particle tracking techniques for interaction with built-in or external 2D/3D field maps including space charge effects between particles.

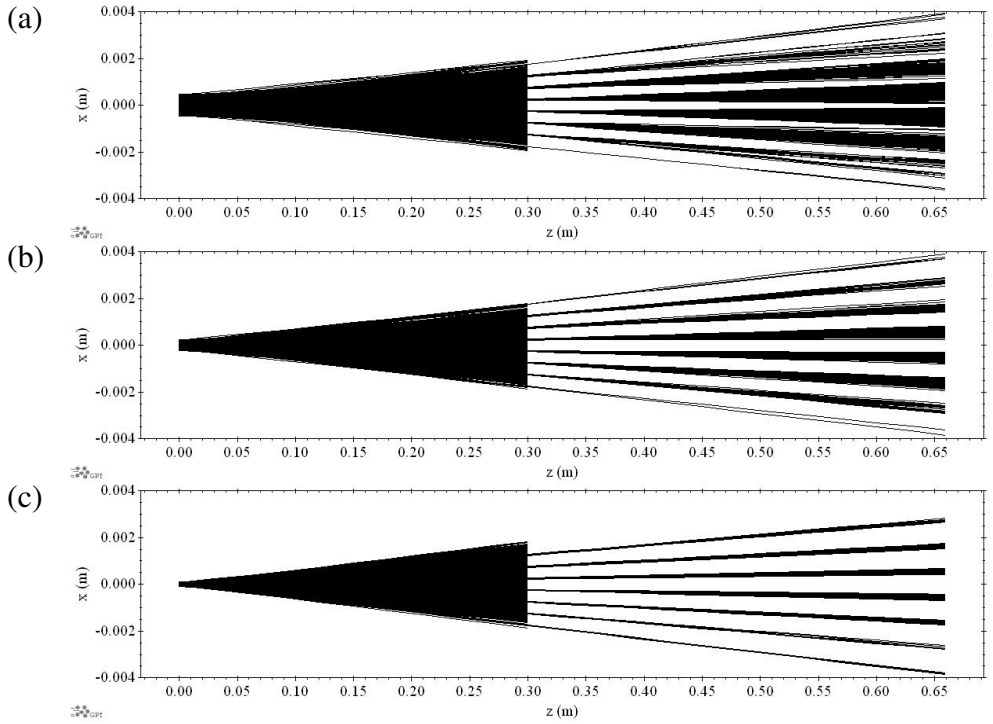

Figure 4.6: GPT simulations of electron beam trajectories for the low resolution measurement. The electron beam was fixed with a divergence of 2 mrad and an energy of 85 MeV. The mask was placed 30 cm after the source where the formation of the beamlets can be seen. The beamlets were recorded at 60 cm where they would hit LANES 1. The images created can be seen in Figure 4.7. The simulation was repeated for measurements with emittance of (a) 50, (b) 25 and (c) 10 π mm mrad.

The actual layout of the experiment was used as the input parameters in the GPT simulation as accurately as possible, however a multi-slit design of the mask was used instead of a pepper-pot design. This is the equivalent of a one dimensional pepper-pot measurement and, as rotational symmetry in the electron beam is assumed, the

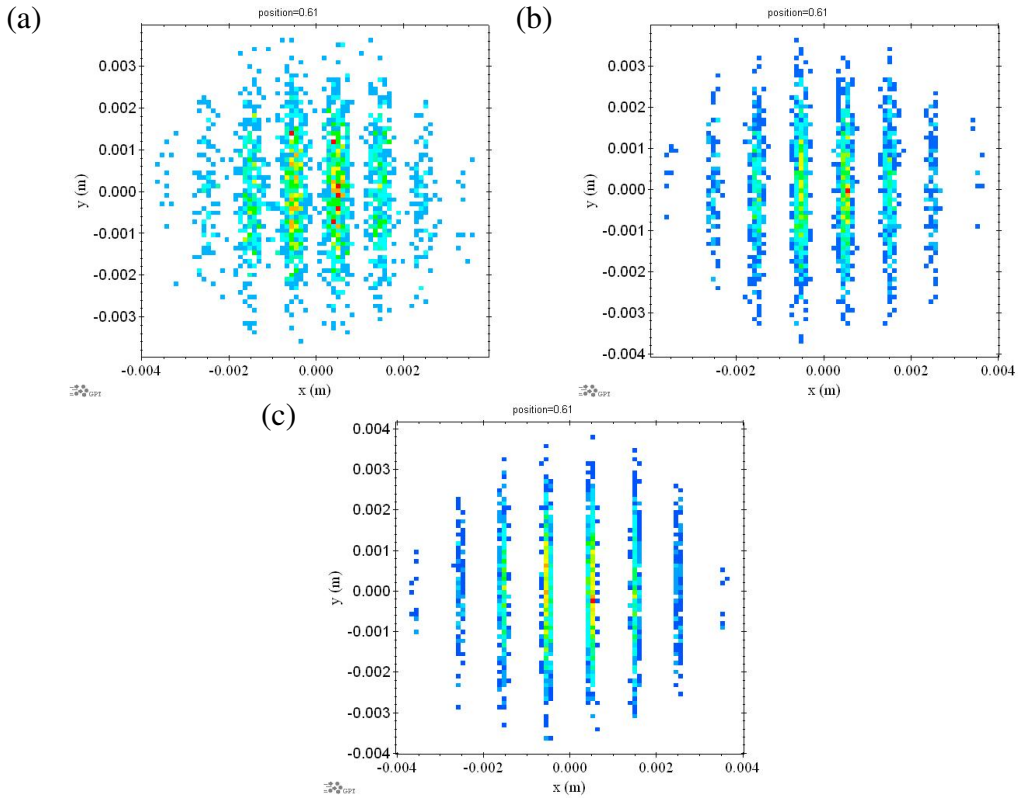

Figure 4.7: GPT simulated images of the of the low resolution emittance measurement for (a) 50, (b) 25 and (c) 10 π mm mrad. The electron beamlets are starting to blur at 50 π mm mrad however are much clearer for the lower emittance beams. A linear colour scaling is used to show electron beam charge density.

simulation provides all the information required.

The mask was placed 30 cm from the gas jet and a screen placed 30 cm after that where the electrons' properties were recorded. The mask stopped and removed any electrons which hit it. Scattering of electrons through the mask could not be calculated in GPT but will be discussed later. Only electrons which passed through the slits were recorded on the screen. The mask was created with 52 μm slits, 500 μm between the centres of each of the slits and a material thickness of 250 μm.

The electron beam's divergence was fixed at 2 mrad (r.m.s.) as this was typical at the time of design, and the emittance therefore altered by modifying the source size. The energy was fixed as at 85 MeV.

Figure 4.6 shows the trajectory for 5 different emittances decreasing from top to bottom of (a) 50, (b) 25 and (c) 10 π mm mrad.

The electrons being stopped at the mask and the electron beams being split into their beamlets can quite clearly be seen. The beam is split into 8 beamlets for a 2 mrad divergence beam. At 50 π mm mrad the beamlet diverges across the drift distance such

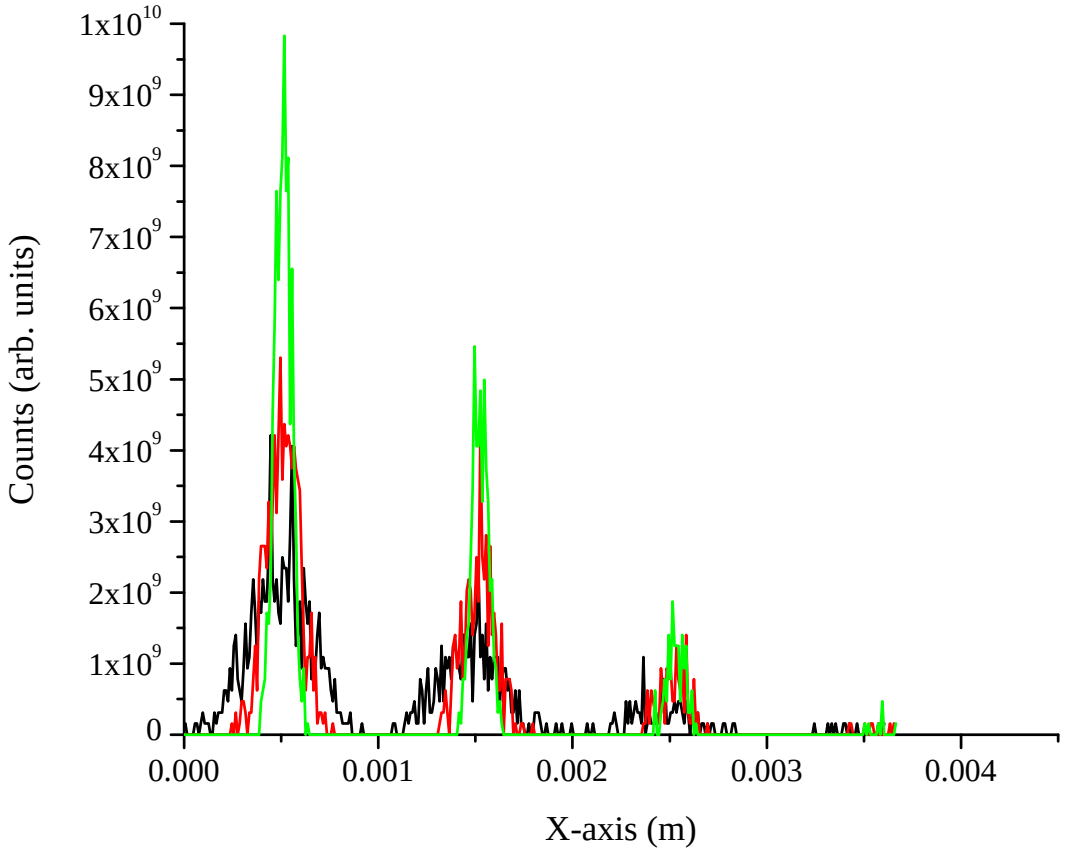

Figure 4.8: Transverse profile of low resolution GPT simulations showing the increase beamlet width for increasing emittances with the 50, 25 and 10 π mm mrad beam represented by the black, red, green, blue and light blue lines respectively. Only peaks with positive x have been included due to symmetry around 0.

that the beamlets become blurred at the screen. The beamlets become more separated with lower emittance and their spot size tends towards the magnification slit width for very low emittance.

Figure 4.7 shows the image that would be seen on the LANEX screen in this measurement. The effect of the emittance on the beamlet divergence is clearly seen. The wide lines of the high emittance beams decrease to low, clear lines for the lower emittance beams.

The intensity profiles of the beamlets are plotted in Figure 4.8 and show the increasing beamlet width for increasing emittance which will lead to resolution issues. The 50, 25 and 10 π mm mrad beams are represented by the black, red and green lines respectively.

4.3.3 Determining the Pepper-pot Mask Thickness

In this experiment the role of the mask is to create easily measurable beamlets from the full beam of electrons. To do this some previous experiments used a thick mask to stop the electrons so that only the beamlets are transmitted to the screen (Bhat et al., 2007; Yan et al., 2008; Delerue, 2011). However, the stopping distance for tungsten with a density, $\rho = 19.25$ g cm^{-3}, would need to be 30 mm for an 85 MeV beam, given by Equation 4.15 (Anderson, Rosenzweig, LeSage, & Crane, 2002; J. B. Rosenzweig & Travish, 1994).

$$L_s = \frac{E(MeV)}{1.5(MeV\ cm^2\ g^{-1})\rho(g\ cm^{-3})}. \tag{4.15}$$

With such a thick mask there is a strong possibility that the conditions given by Equation 4.11 would be violated and the mask would act as a collimator and clean up the beam emittance. A second problem is that machining constant diameter holes in thicker mask material is more difficult. The micro-machining is carried out by focusing a femtosecond laser onto the metal surface and therefore a finite depth of focus makes machining high aspect ratio holes in a thick material extremely difficult.

To eliminate this problem the mask was designed to scatter the electrons to a large angle (Flottmann, 1996), so any electrons that reach the detector screen through the mask would create a uniform background. The beamlet signals will then be clearly discernible on top. This large angled background can then simply be subtracted away (or fitted as a baseline) leaving only the beamlet images.

GEANT 4 Simulations of Mask

The code GEANT 4 (Agostinelli et al., 2003) is used to test the effects of various thickness of tungsten to be used for the mask. GEANT 4 is a toolkit based on the Monte Carlo code method designed to simulate the passage of particles through matter. Secondary electrons and x-rays produced in the mask are ignored as they would not create peaks and would only add to the background.

An electron beam of near perfect emittance (i.e. all electrons were emitted from a point source) and a divergence of 2 mrad was used. Figure 4.9 (a) and (b) show the image the electrons would make on a screen placed 1 m from the source with no mask present. A clear 2-D Gaussian distribution can be seen.

To simulate the effects of the mask a multi-slit mask was used (similar to the set-up of the GPT simulation in Section 4.3.2). The mask consisted of 50 μm slits separated by 500 μm. The mask was placed half way between the electron source and the detector screen. All electrons that pass through the slit and scattered through the mask are

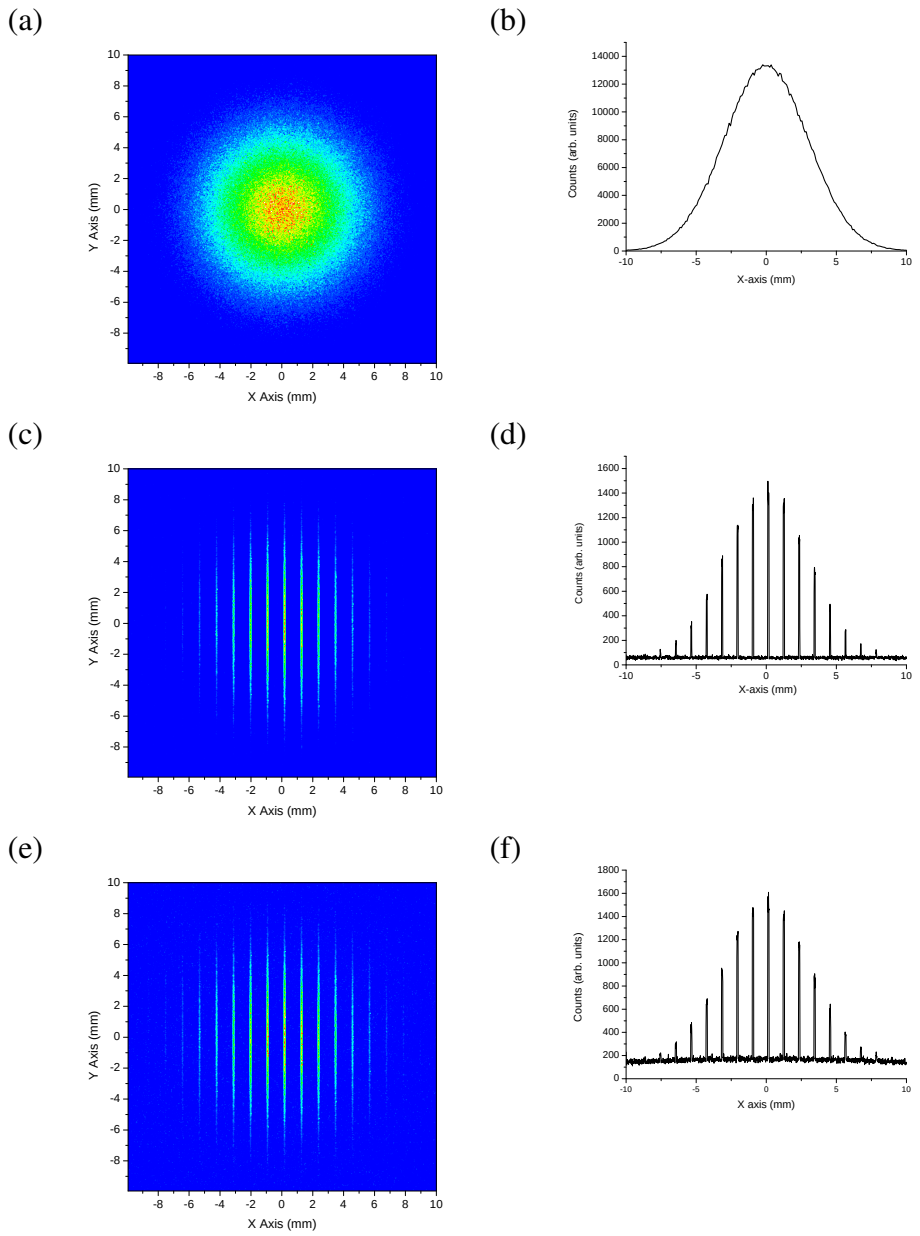

Figure 4.9: GEANT 4 simulations of the effectiveness of emittance mask thickness. Part (a) and (b) show the image and profile after 1 m of theoretical electron beam with zero emittance, 85 MeV and a divergence of 2 mrad. In parts (c) and (d) a 1 mm thick mask is put in placed halfway between the source and the screen position. The electrons are scattered through the mask to a defuse, flat background. Part (e) and (f) use a 0.5 mm mask, the background is still quite diffuse, although a decrease in the scattering angle can be seen.

recorded at the screen position.

Figure 4.9 (c) and (d) shows the effect of using a 1 mm thick tungsten mask. From the image the beamlets are quite clear. The profile shows that the electrons that pass through the mask are scattered into such a large angle that they create a flat baseline of

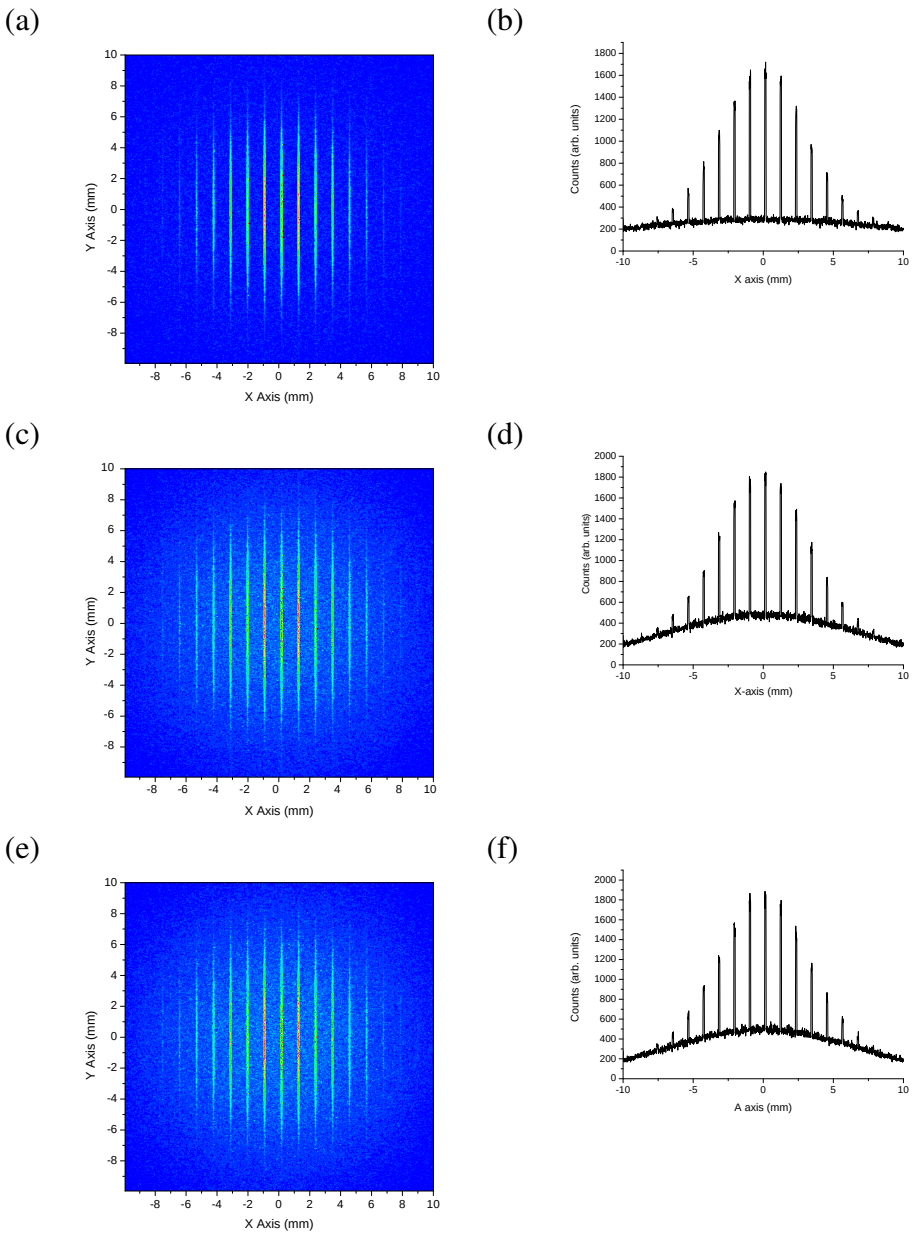

Figure 4.10: Continuation of the GEANT 4 simulations of the effectiveness of emittance mask thickness in Figure 4.9. Part (a) and (b) use a 0.25 mm mask and (c) and (d) use a 0.1 mm thick mask. A further decrease of scattering angle is seen but is still sufficient to clearly resolve the peaks. The simulation was repeated for various energies and part (e) and (f) shows the result of a 150 MeV beam passing through a 0.25 mm thick mask. The mask still sufficiently scatters the electrons which pass through the mask.

background. When the tungsten thickness is reduced to 0.5 mm, as shown in Figure 4.9 (e) and (f), the image is still clear and the scattering angle is a low angle, broad curve that increases the level of the background. Figure 4.10 (a) and (b) shows the effect of a 250 μm thick mask and (c) and (d) shows the result of a 100 μm thick mask. Both

of these thickness show a further decrease in the scattering angle, however, the angle is still sufficient to create a background that can be subtracted. The simulation was repeated for several energies to ensure that the mask would still work. Figure 4.10 (e) and (f) shows the result of 150 MeV electrons acting on a 250 μm thick mask. Compared to 85 MeV, 250 μm mask thickness (Figure 4.10 (a) and (b)), the scattering angle is reduced but is still large.

From these simulations it is clear that a thin mask is as effective as a thick mask and simultaneously resolves the problems of mask manufacture and collimation.

4.3.4 Effects of the Laser Beam Block

Another important design consideration is the method of blocking the high intensity laser from the detector screen without scattering or otherwise affecting the electron bunch. If the laser beam block is positioned incorrectly it increases the emittance significantly, making the measurements impossible. Therefore, for the emittance measurement the laser beam block was place immediately prior to the detector screen preventing any scattered angle from turning into an increase in in beamlet width.

GEANT 4 was again used to determine the scatter due to the aluminium foil as the electron bunch passed through it. To do this, an electron beam is created, emitting from a point source with no divergence (as GEANT 4 does not calculate space charge effects, this type of beam is possible). As before the electrons are recorded at 1 m but with the aluminium foils placed at 0.5 m.

Figure 4.11 (a) shows the x-axis distribution of the electron beam for an aluminium foil with thickness ranging from 1 to 200 μm. The r.m.s. distributions for each of the aluminium foil thicknesses were used to calculate the r.m.s. scattering angle. Figure 4.11 (b) shows the increasing r.m.s scattering angle with increasing aluminium foil thickness. As can be seen, the scattering angle is only a few mrad for 30 μm of aluminium and as the electron bunch already has a divergence of several mrad, the overall divergence of the beam will not be greatly affected. This holds true for the effect on beam divergence but does not for the effect on beam emittance.

If a beam, with divergence of 2 mrad, is investigated after 1 m of propagation then the transverse phase-space would look similar to that shown in Figure 4.12 (a). Here the thickness of the emittance ellipse is set-by the electron bunch source size and for a 5 μm source size would have a 5 μrad thickness. If the aluminium foil was placed at this position (1 m from the gas jet) then the electrons would be scattered at every point across the 2 mm beam. This would result in the 5 μrad thickness of the emittance ellipse being increased to 1 - 1.5 mrad thickness (in the case of a 15 μm foil) as shown in Figure 4.12 (b). This very large increase in the emittance ellipse area

(a)

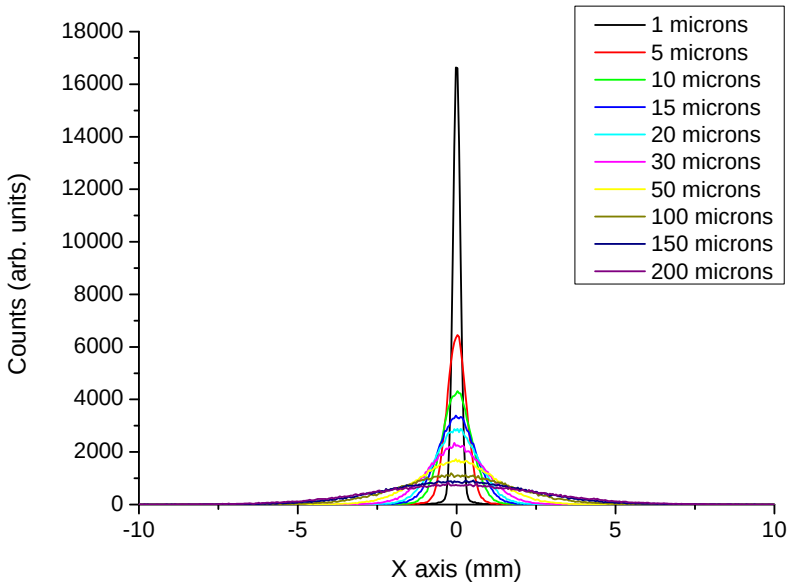

(b)

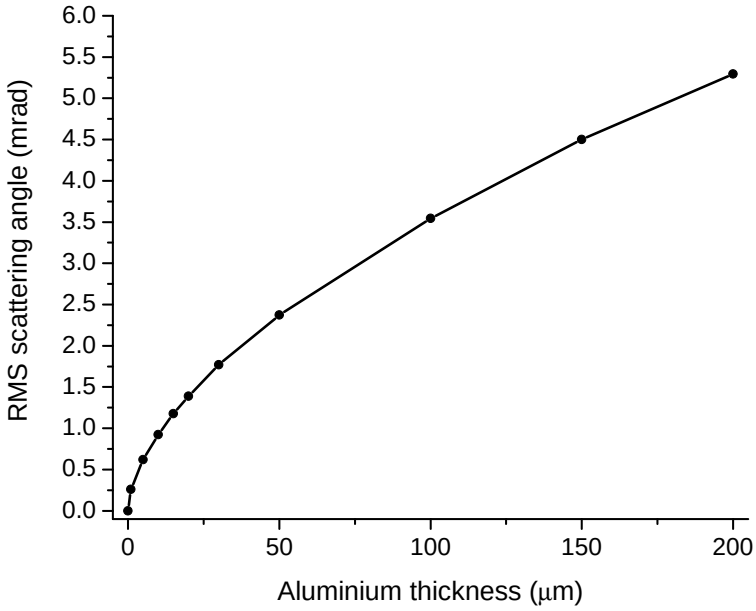

Figure 4.11: GEANT 4 simulations of scattering angle of aluminium foil laser beam block. (a) is the profile of the electron beam as it passed through various thicknesses of aluminium and (b), the scattering angle as a function of aluminium thickness.

would only appear as a 50 % increase in the beam divergence, but would increase the beam emittance by 2 orders of magnitude. An emittance of 100 π mm mrad would be impossible to measure on the set-up used here.

It should also be noted that at the electron beams focus (or source), the transverse

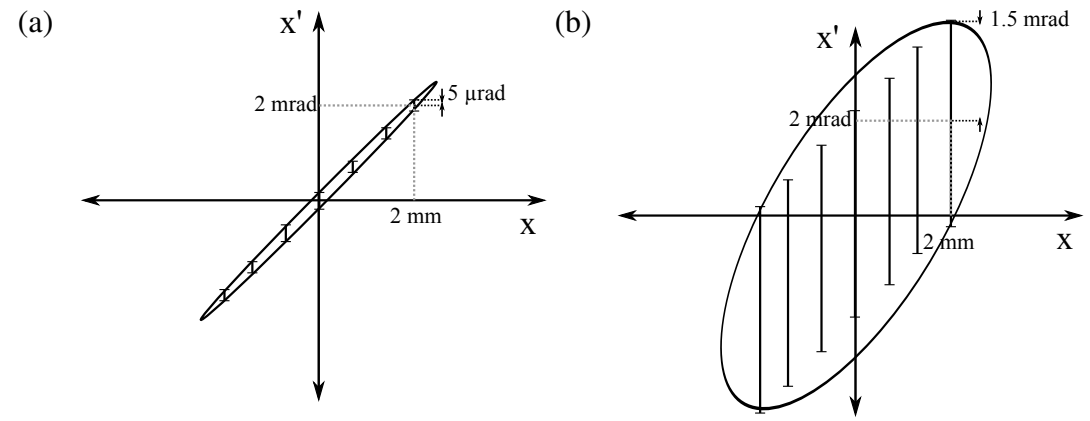

Figure 4.12: Phase-space growth due to the beam interaction with a foil. (a) the phase-space for a beam emitting directly from a small source. (b) the electron beam has interacted with an aluminium foil which has induced a scattering angle across the entire beam, i.e. the emittance width has been stretched vertically, increasing the emittance by up to two orders of magnitude.

phase-space will be as shown in Figure 4.2 (b)(i). In this situation all the scattering would go into the divergence and the effects on the emittance would be minimal. As the foil is moved further away from the source to where the beam is expanding, the effects on the emittance increase.

To resolve this problem the laser beam block is placed immediately in front of the detector screen to ensure that any scattering effects are negligibly small.

The scattering angle was also calculated for tungsten, in the same way as for aluminium. Figure 4.13 (a) shows the distribution for increasing thicknesses of tungsten. Figure 4.13 (b) shows the increasing scattering angle for increasing metal thickness. The large difference in scattering angle between the two metals should be noted and helps to explain why the thin emittance mask works.

4.4 Experimental Results

4.4.1 Low Resolution Measurement

The experiment was carried out as described in Section 4.3.2. The spots on the screen were measured as expected and the emittance calculated from the images.

Two examples are shown in Figure 4.14 and 4.15. Part (a) of both of these figures shows the image of the electron beamlets as measured on the LANEX screen (false colour has been added for clarity). Parts (b) show the transverse phase-space for the two shots. The ellipse represents the emittance area and shows the linearity of the peak position and the narrow width of the beamlets and therefore, the ellipse. The error bars

(a)

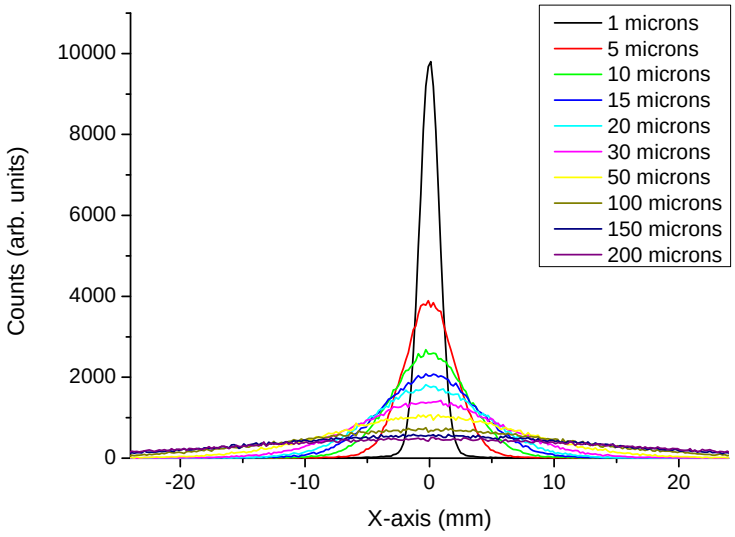

(b)

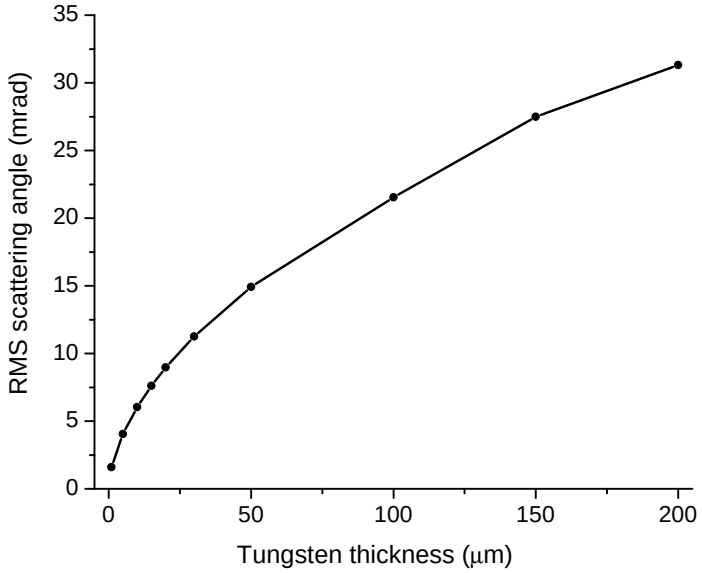

Figure 4.13: GEANT 4 simulations of scattering angle of tungsten foil. (a) is the profile of the electron beam as it passed through various thicknesses of tungsten, note the increase in spread compared to the aluminium and (b), the scattering angle as a function of tungsten thickness, this large angle scattering confirms the effectiveness of tungsten as a suitable material for the mask.

on each of the points are corrected r.m.s beamlet divergence. Parts (c) are the charge distributions across the beamlets, used to weight their importance.

The emittance of Figure 4.14 is 8.7 π mm mrad (normalised to 82 MeV) (Shanks et al., 2009). The emittance in Figure 4.15 is 9.8 π mm mrad (Shanks et al., 2009). The

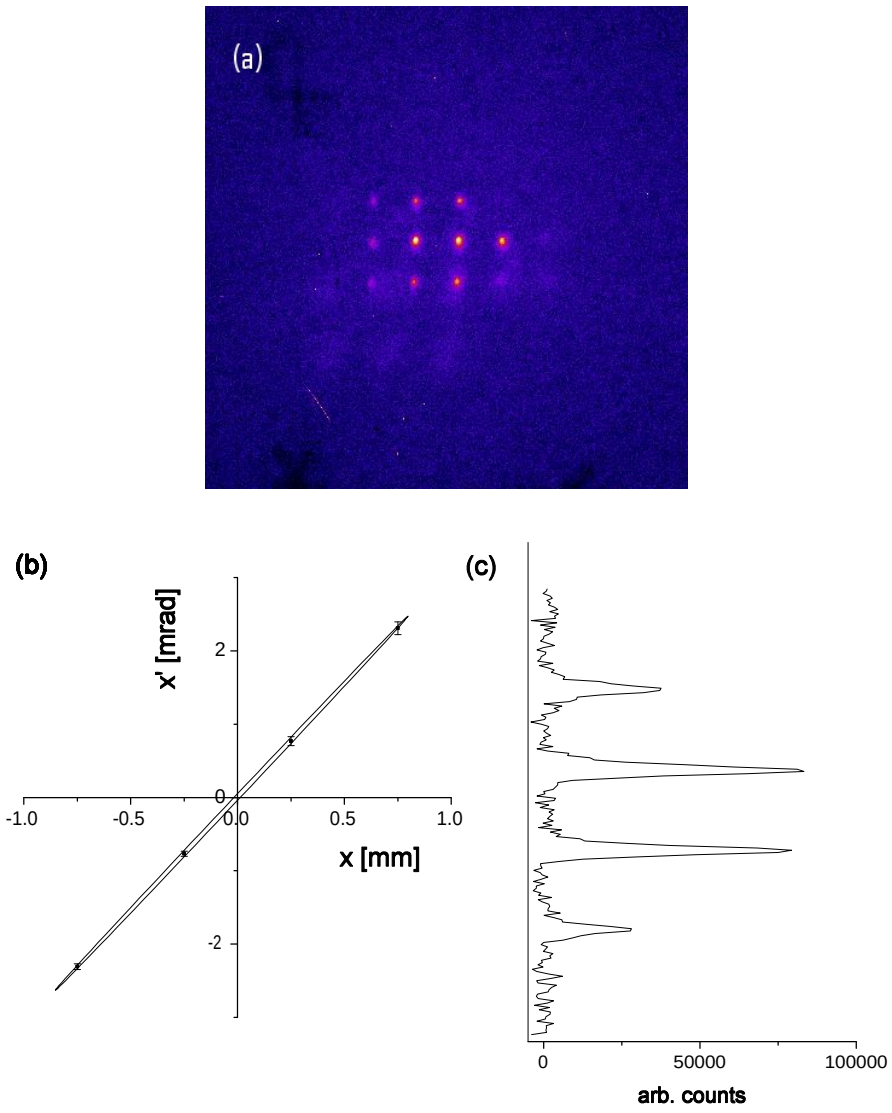

Figure 4.14: (a) Image from a pepper-pot emittance measurement for a 2 mrad divergence beam. The normalised r.m.s. emittance (corrected for hole size and for 82 MeV electrons) is 8.7 π mm mrad. (b) shows the phase-space diagram and (c) charge distribution across the electron bunch.

emittance of these beams at their divergence (of 2 and 2.5 mrad) would correspond to source sizes of 31 μm. The resolution limit due to the uncertainty in the hole size and LANEX resolution for these beams are 8.4 and 10 π mm mrad. Thus, the emittance measured is resolution limited and the value found is an over estimation. A more accurate measurement of the emittance would require a higher resolution experiment with clearer measurement of the beamlets.

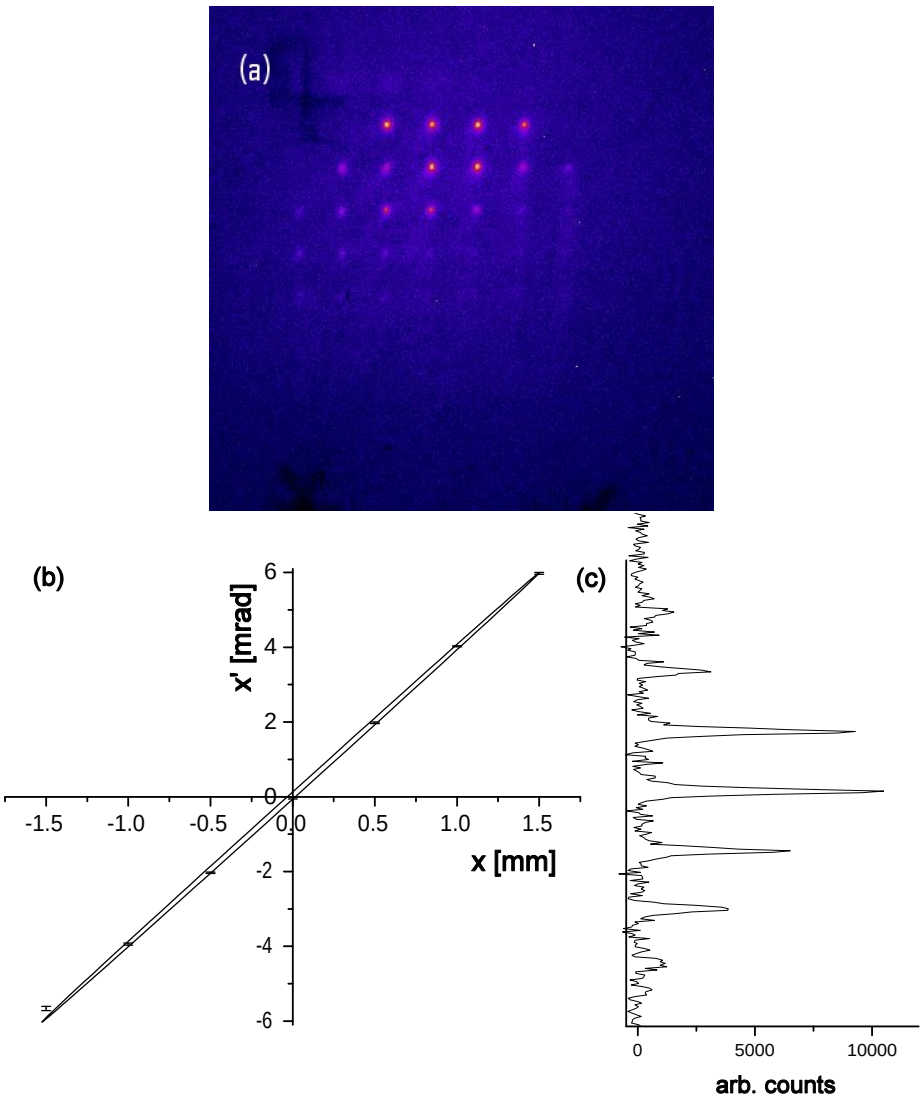

Figure 4.15: (a) Image from a pepper-pot emittance measurement for a 2.5 mrad divergence beam. The normalised r.m.s. emittance (corrected for hole size and for 82 MeV electrons) is 9.8 $\pm$ 1 π mm mrad. (b) shows the phase-space diagram and (c) charge distribution across the electron bunch.

4.4.2 Emittance Measurement Re-design

After the low resolution measurement had been taken it was clear that the emittance was $\ll 10\ \pi$ mm mrad and therefore a much higher resolution system was required.

To achieve this the following points have been considered

1. Increasing the resolution of the detector screen. Previously, the LANEX regular screen had a resolution $> 100\ \mu$m. This was replaced with a 100 μm thick Ce:YAG crystal with a resolution of 10 μm

2. The magnification, M, within the system was increased. The drift distance from the mask to the detector screen was doubled (now 61 cm). This increased M to 3.05 (as discussed in Section 4.3). The increased drift distance between the mask and the detector screen allowed for an increase in σ_x. The increase in M resulted in an increase in hole magnification and therefore an increase in the spot measured on the high resolution YAG:Ce screen, as shown by Equation 4.14.

3. For low divergence electron beams the hole spacing would result in very few holes actually being placed across the beam. This would result in an inaccurate measure of the beam with increased error. The hole spacing was therefore reduced from 500μm to 150μm.

4. The increased magnification, increased drift distance and decreased hole separation resulted in an increased possibility of the holes measured on the detector screen merging together. This problem was reduced by reducing the hole size in the mask. This would have a second advantage of decreasing the hole sizes dominance in Equation 4.14 and therefore reducing the error in the measurement. To facilitate the machining of smaller holes, the machining laser was focussed to a smaller spot size. This also reduced the depth of focus, therefore to create holes with minimal taper, the mask thickness was reduced from 250 μm to 125 μm. This also allowed the acceptance angle of the holes to remain high. This attention in the machining process allowed for holes diameter of 25 $\pm$ 5 μm.

5. The reduced hole diameter and increased magnification resulted in a reduction in the charge density of the beamlets on the YAG screen. To ensure good resolution the camera used to image the detector screen was replaced by a 14-bit Point Grey Research Grasshopper camera. The objective lens was replaced with one which had a larger diameter and zooming ability which ensured greater capture of light and increased resolution.

As before, the holes in the mask act like a pin hole camera looking at the source and the resolution corrected size of the spot measured on the screen will be the size of the source. The spot position and divergence are averaged over many CCD pixels and can therefore be found with relatively low error (< 1 μm). The errors in the spot size are therefore largely due to the error of ± 5 μm in the hole diameter which results in an error in the source size, $\sigma_{x,error} = \pm 2.2$ μm. This source size error results in an error in the emittance resolution of ~ 0.4 π mm mrad for a 1 mrad beam at 100 MeV (using equations 4.7 and 4.8).

GPT Simulations of the Re-designed Set-up

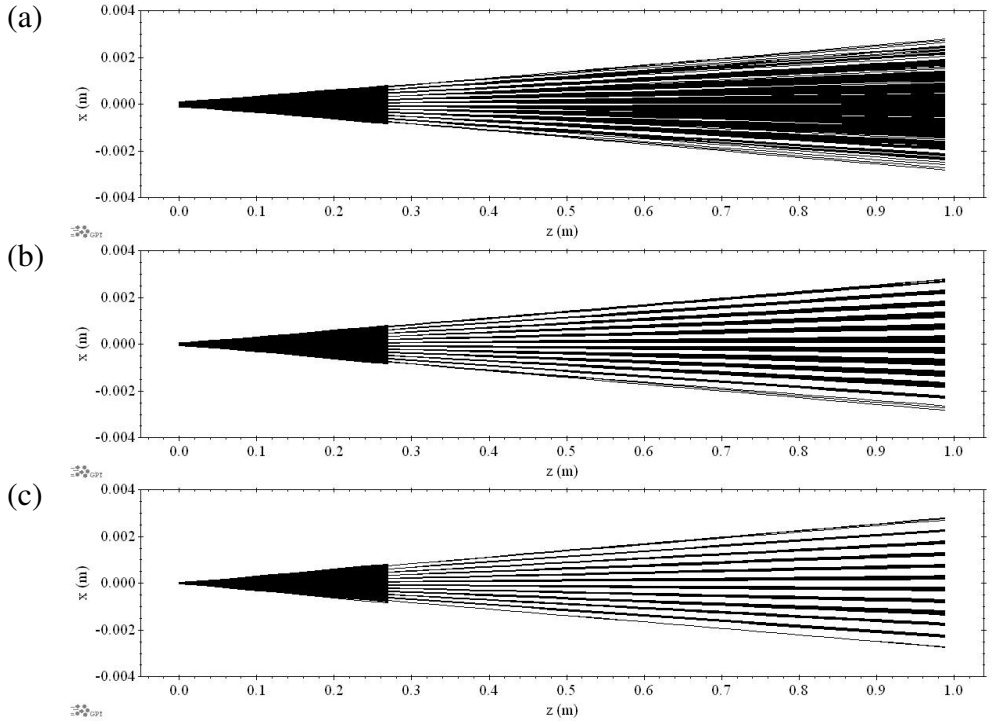

Figure 4.16: GPT simulations of electron beam trajectories for the high resolution measurement. The electron beam was fixed with a divergence of 1.5 mrad and an energy of 115 MeV. The mask was placed 29.5 cm after the source where the formation of the beamlets can be seen. The beamlets were recorded at after a drift distance of 61 cm where they would hit the YAG:Ce crystal. The images created can be seen in Figure 4.17. The simulation was repeated for measurements with emittance of (a) 10, (b) 5 and (c) 2 π mm mrad.

Again, GPT was used to asses the effectiveness of the pepper-pot design. The mask was set with the new design parameters:

- Slit width of 25 μm
- Slit spacing of 150 μm
- Mask thickness of 125 μm
- Drift distance of 61 cm
- Gas jet to mask distance of 29.5 cm

The electron beam parameters were also modified to represent the electrons being produced at the time of the measurement. The electron energy was increased to 115 MeV and the divergence decreased to 1.5 mrad.

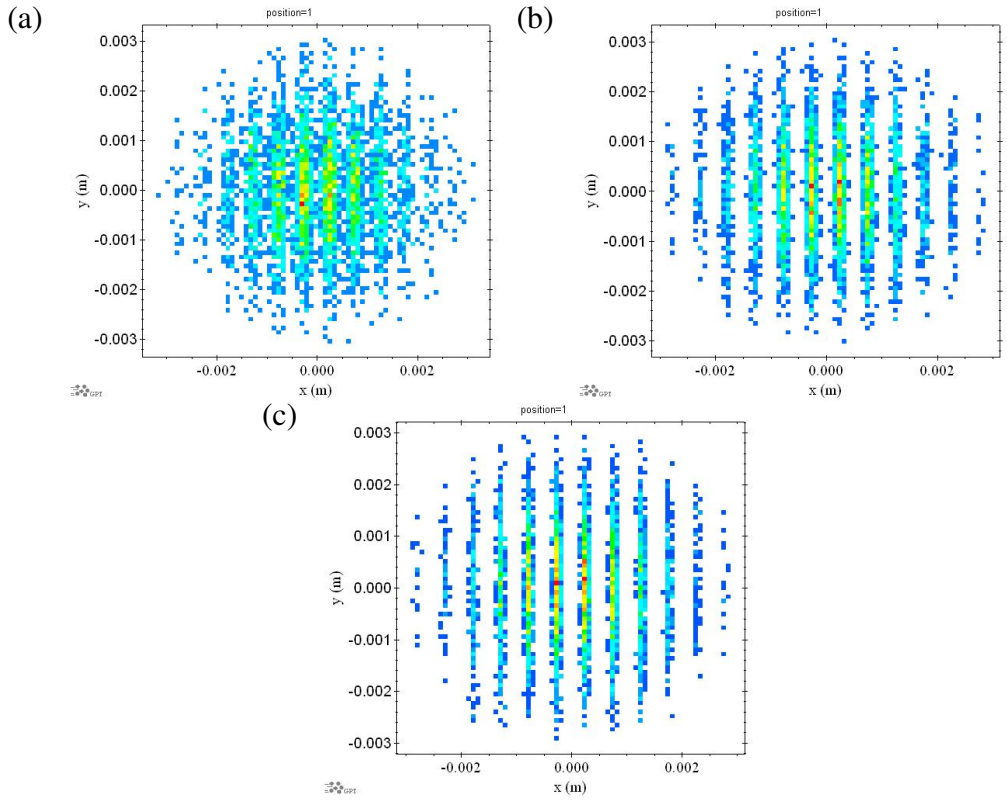

Figure 4.17: GPT simulated images of the of the high resolution emittance measurement for (a) 10, (b) 5 and (c) 2 π mm mrad. The electron beamlets are starting to blur at 10 π mm mrad however are much clearer for the lower emittance beams. A linear colour scaling is used to show electron beam charge density.

The effects of this new set-up can be seen in figures 4.16 and 4.17. In these figures the trajectories and images of (a) 10, (b) 5 and (c) 2 π mm mrad beams are shown. The much larger drift distance and narrower beamlets are clear. Now the blurring of the beamlets occurs at the much lower emittance of 10 π mm mrad. The closer hole separation allows for the formation of more beamlets, even for a lower divergence and lower emittance beam.

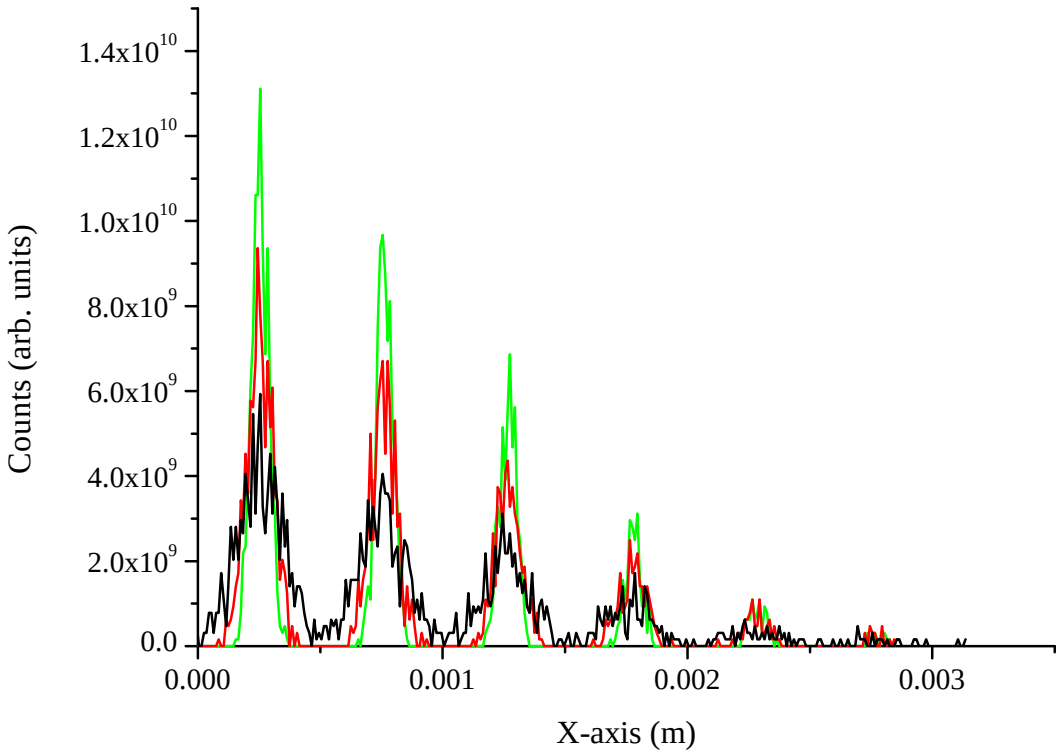

Figure 4.18: Transverse profile of low resolution GPT simulations showing the increase beamlet width for increasing emittances with the 10, 5 and 2 π mm mrad beam represented by the black, red and green lines respectively. Only peaks with positive x have been included due to symmetry around 0.

4.4.3 High Resolution Measurement

An example of the high resolution image is show in Figure 4.19 (a). Here many beamlets can still be seen despite the low 1.3 mrad divergence of the beam. The background scattered electron can also be seen stronger than in the previous measurement but still diffuse enough to see the beamlets on top. Again the transverse phase-space of this shot is shown in part (b). The r.m.s width of each of the beamlets is even narrower than previously seen and the linearity of the peak position demonstrates the beam quality. The r.m.s emittance along the x-axis is 2.2 ± 0.6 π mm mrad.

The electron energy for the experimental run was 125 ± 3MeV averaged over 200 consecutive electron spectra. Normalised emittance values were obtained for 64 of 400 consecutive shots and their x and y axis emittance are presented in Figure 4.20. Shot to shot angular pointing variations of the electrons caused some of the shots to clip the edge of the mask with part of the beam. A clipped beam would reduce the area of the observable phase-space distribution and give an underestimation of the emittance. It is essential to ensure only clear shots are used. The emittance along the horizontal axis, which is laser polarisation axis, is 2.2 ± 0.7 π mm mrad with the best shot of 1.1 π mm mrad which is close to the resolution of the system. The vertical emittance has an average value of 2.3 ± 0.6 π mm mrad with the lowest emittance recorded at 1.2 π mm mrad (Brunetti et al., 2010; Manahan et al., 2011).

Figure 4.21 shows the relationship between the emittance and the source size for an electron beam with a divergence of 1.5 mrad and an energy 125 MeV. Highlighted is the conversion for the value of an emittance 2.2 ± 0.6 π mm mrad, which is a typical value. This emittance occurs for a value corresponding to a source at the accelerator of 6 ± 2 μm. Emittances as low as 1.1 π mm mrad have been obtained, which gives a source radius as low a ~ 2.5 μm.

It is possible that the emittance for LWFA electron beams could be as low as 0.25 π mm mrad, because beams with divergence as low as 0.6 mrad have been observed on our measurements. In Figure 4.22, GPT is used to show that space charge does not destroy the low beam emittance. For emittance > 1.6 π mm mrad, space charge has little effect with an increase of just 6 %. The effect is greater for a beam of 0.1 π mm mrad with an increase of 400 %. However, the emittance only increases to 0.5 π mm mrad in the first meter of propagation.

The overall volume of the electron bunch is given by $\delta V = \sigma_z \sigma_r^2$. Due to the charges role in the cut-off of injection there may be a dependence of bunch length on charge. Should initial bunch radius remain constant with charge, this would result in a linear dependence of bunch length with charge. However, should the bunch length remain constant, then the initial bunch radius would scale with the square root of the

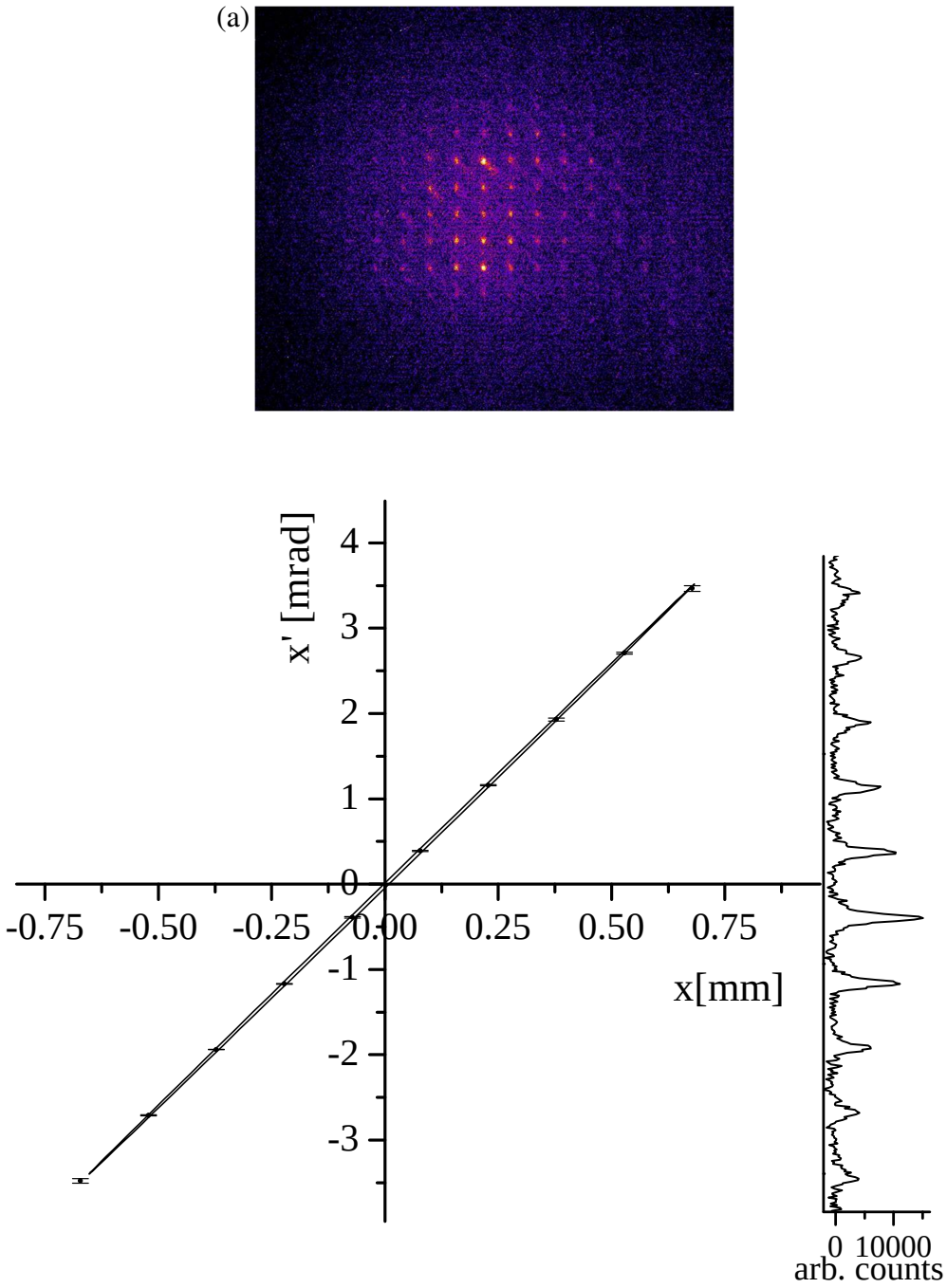

Figure 4.19: (top) Image from a pepper-pot emittance measurement for a 1.3 mrad divergence beam. The normalised r.m.s. emittance (corrected for hole size and for 125 MeV electrons) is 2.2 $\pm$ 0.6 π mm mrad. (left) shows the phase-space diagram and (right) charge distribution across the electron bunch.

charge, $r_0 \propto Q^{1/2}$. As the emittance depends on the initial bunch radius, the emittance scales with charge and through that, the angular divergence of the electron beam would scale with the square root of the charge like the initial bunch width $\theta \propto Q^{1/2}$. Figure

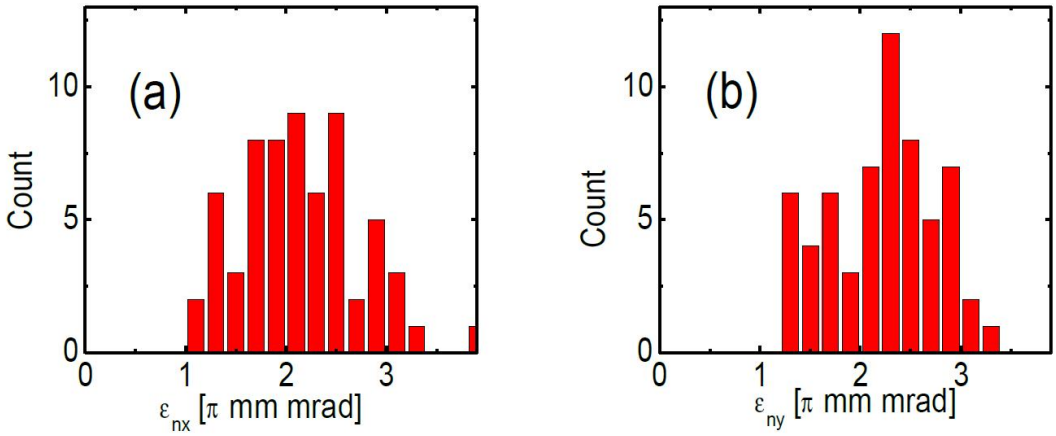

Figure 4.20: Histogram of recorder emittance along the (a) x-axis and (b) y-axis.

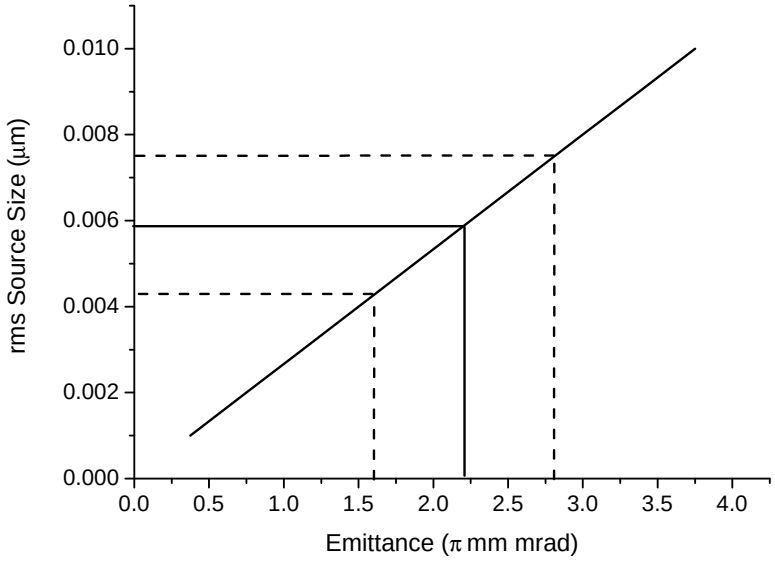

Figure 4.21: Source size as a function of emittance for a 1.5 mrad 125 MeV beam. Shown is a typical value of a $2.2 \pm 0.6\,\pi$ mm mrad coresponding to a source of $6 \pm 2\,\mu$m.

4.23 shows the experimentally obtained dependence of bunch divergence on charge.

A spread in the divergence can be seen for a given charge due to the point in the transverse phase-space rotation in which the electron bunch exits the accelerator, however an overall trend of increased divergence with charge can be seen. Also plotted is the divergences $Q^{1/2}$ and the $Q^{1/3}$ dependence. Due to the spread in divergence the exact dependence on charge is not clear. However, the demonstration of a dependence

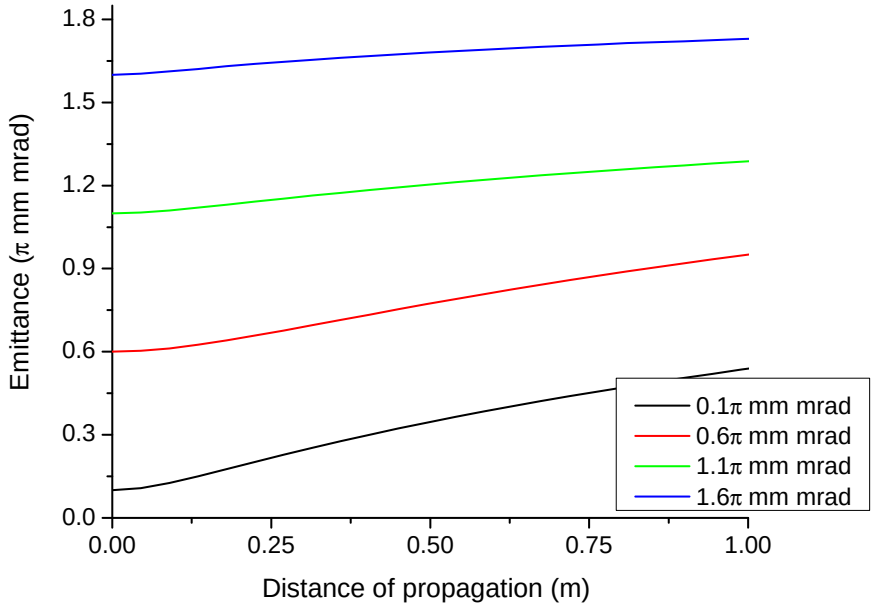

Figure 4.22: Emittance evolution for an electron beam drifting from a source.

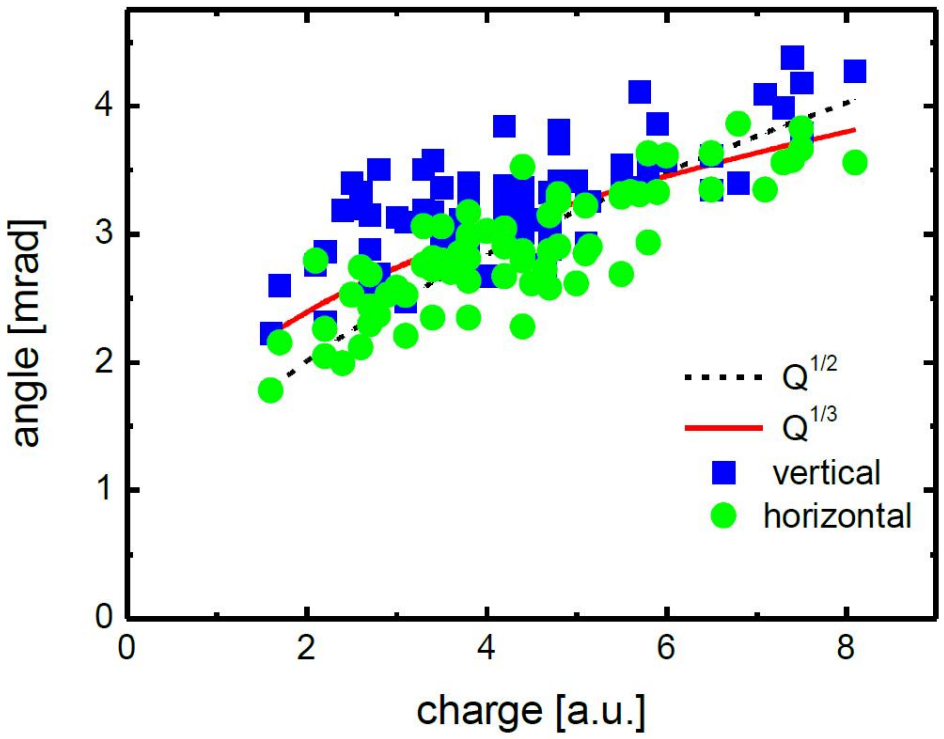

Figure 4.23: Dependance of angle on charge for the both the horizontal (green) and vertical (blue) with the $Q^{1/2}$ and $Q^{1/3}$ dependance shown.

means that the bunch length is either constant with charge or slowly varying, i.e. less than a linear dependence.

4.5 Conclusions and Future Work

In conclusion, this chapter demonstrates the first, high resolution, single shot emittance measurement of a mono-energetic laser-wakefield accelerated electron bunch. An upper limit has been set for the average emittance measured of $\varepsilon_{n,x} = 2.2 \pm 0.7\ \pi$ mm mrad and $\varepsilon_{n,y} = 2.3 \pm 0.6\ \pi$ mm mrad for the horizontal and vertical emittances respectively. The emittance has been normalised to a measured energy of 125 $\pm$ MeV averaged over 200 consecutive shots.

This work agrees with emittance measurements that were carried out on non-monoenergetic electrons produced in laser wakefield accelerated electrons, often seen in the tail of the monoenergetic peak (Fritzler et al., 2004). This measurement selected the 55 MeV part of the beam and measured the average emittance over many shots using a slit scan technique to find a normalised emittance of 2.7 $\pm$ 0.9 π mm mrad. The single shot emittance measurements of the monoenergtic peak made here have been repeated by Sears et al. (2010) to produce a normalised emittance of 2.3 π mm mrad normalised to 20 MeV.

This chapter also discussed the design of a thin emittance mask, designed to scatter electrons over a large angle to produce a background that can be subtracted to determine the beamlets properties. The thin mask consists of of 25 μm holes machined in 125 μm thick tungsten. This enables high resolution emittance measurements.

The measurements are improved by increasing the resolution of the system. This could be carried out by further improving the accuracy in which the spots are detected in the following areas.

1. Improving the accuracy and reducing the diameter of the holes drilled in the tungsten to make the mask. Although the thin mask allowed for holes with relatively small error, refining the machining process could yield further improved masks. Reducing the hole radius will reduce the importance of the hole correction on the measured beamlet radius. However, unless the hole radius is small compared to the electron beam source size then a correction will be necessary. A reduced error in the manufactured holes will allow for more accurate hole correction and reduced uncertainty in the emittance.

2. Increasing the magnification of the beamlets by increasing the drift distance between the mask and the detector screen will increase the resolution of the beam-

lets.

3. Increased magnification and decreased hole radius will result in lower charge density spot and will therefore require a high sensitivity camera, reducing the effects of background noise.

4. A high resolution screen will also reduce the correction and error in spot detection.

Chapter 5

Energy Spread Measurements

5.1 Introduction

In this chapter measurements of the electron beam energy and energy spread are discussed. Calculation of the effects of emittance on electron energy spectrometer resolution (σ_γ/γ) shows that the increase in emittance due to the laser beam block foil does not impair energy spread measurements, and the effects on the resolution limits are found to be minimal. However, the effect of beam divergence is shown to have an important effect on resolution limits. Quadrupole focusing magnets are therefore used to collimate and to reduce the minimum resolution.

5.2 Resolution Simulation

The General Particle Tracer (GPT) code (Van Der Geer & Loos, 2001b, 2001a) has been used to simulate electron transport in the spectrometer. Figure 5.1 shows a sample simulation of the electron beam propagation from a 3 μm source with an emittance of 1 π mm mrad. The beam is monitored at 0.15 fs intervals represented by the dots. The electron spectrometer field entrance is positioned 2.5 m after the gas jet where the magnets bend the electrons to intercept the Ce:YAG scintillation crystal located at the focal plane. In the simulation the spectrometer was set with a magnetic field of 0.59 T which is the same as that used in the energy spread measurements. This field enabled a measurement range of 50 - 100 MeV across the width of the 30 cm Ce:YAG screen. The YAG screen was simulated by recording the electron's position as it crossed the screen, which is represented by the green line in Figure 5.1.

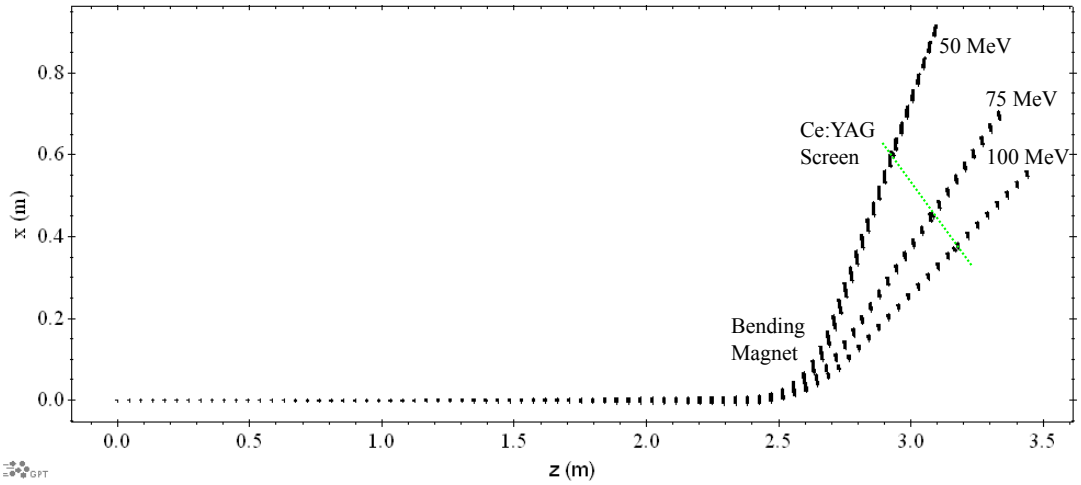

Figure 5.1: Simulation of electron beam, sampled at 0.15 fs intervals, bent by the spectrometer to the CeYAG screen (green). Simulated is the transport of 50, 75 and 100 MeV beam in a 0.59 T magnetic field.

5.2.1 Effects of Emittance for a Fixed Source Size

To test the effect of emittance of the electron beam from the gas jet, a source size of 3 μm was used and the emittance varied by altering the divergence. Sample images of the simulated screen are shown in figures 5.2 and 5.3.

Figure 5.2 shows the energy spectrum image at the YAG screen position for an emittance of (a) 0.1, (b) 1 and (c) 2 π mm mrad, which corresponds to a divergence of 0.2, 2 and 4 mrad respectively. It is shown that the spectrometer focuses the electron beam on the y-axis to a $\sim$ 0.25 mm high spot. For the low divergence beam, (a), the minimum resolvable energy spread decreases. As the divergence increases the energy spread measured also increases. Electrons not sent to the correct energy position when the resolution is low (i.e. sent to lower or higher energy positions than the actual electron energy) are not optimally focussed onto the screen and therefore have a larger spot height. The red line in Figure 5.4 shows the decreasing resolution with increasing emittance/ beam divergence.

Figure 5.3 shows beams with the same emittance values as used in figure 5.2. However, now the quadrupoles are used to transport the electrons to the spectrometer. Only two of the quadrupoles are used in the simulation and the same magnetic field is used in the experiment, Q1 = 3.1 T/m and Q2 = 1.5 T/m. A similar butterfly shape is evident as without the quadrupoles. However, here the spread on the energy axis has been reduced and the height of the beam reduced.

Finally, the effects of the quadrupole beam transport are shown in Figure 5.4. The black line shows the effect of emittance/divergence on the resolution of the spectrome-

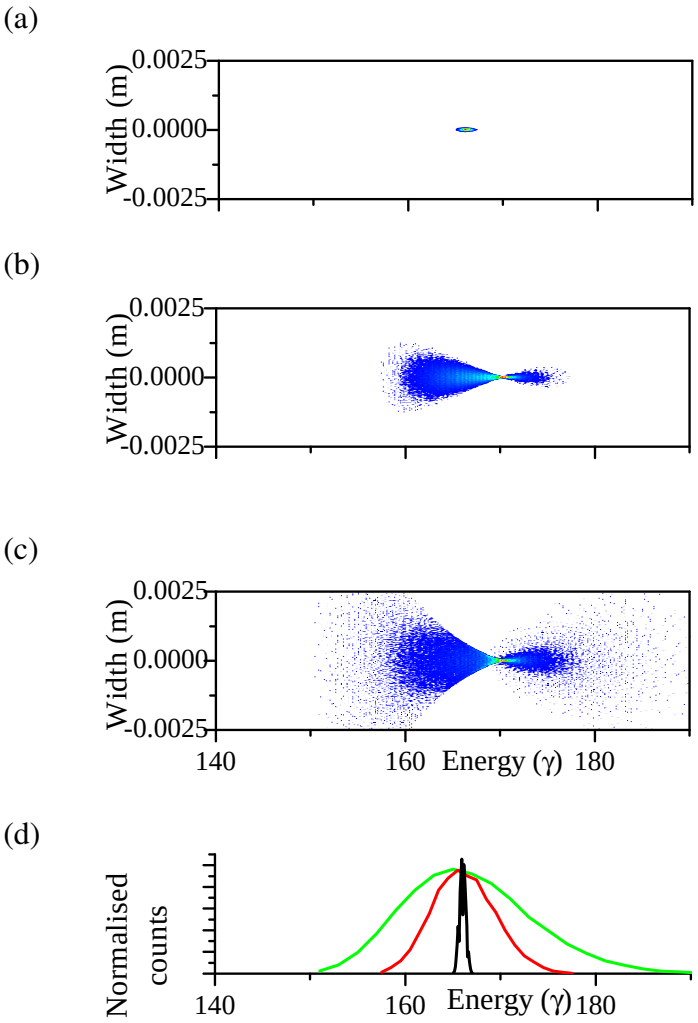

Figure 5.2: Simulated spectrometer screens for electrons from a 3 μm source, emittance of (a) 0.1, (b) 1 and (c) 2 π mm mrad without the use of quadrupole beam transport. A linear colour scale has been used. (d) is the energy profile showing the same peak position but increasing spread for 0.1, 1 and 2 π mm mrad beams represented by the black, red and green curves respectively.

ter and as discussed before it is shown that the resolution limit increases with increasing emittance. The red line shows the same trend for the beam which has passed through the quadrupoles, however the improvement in the resolution limit is clearly seen. A typical beam divergence of around 2 mrad gives a resolution limit of ≈ 1.4 %. Lower beam divergence of 1 mrad, which has been observed during the experiments, will provide a resolution limit for the system < 0.7 %.

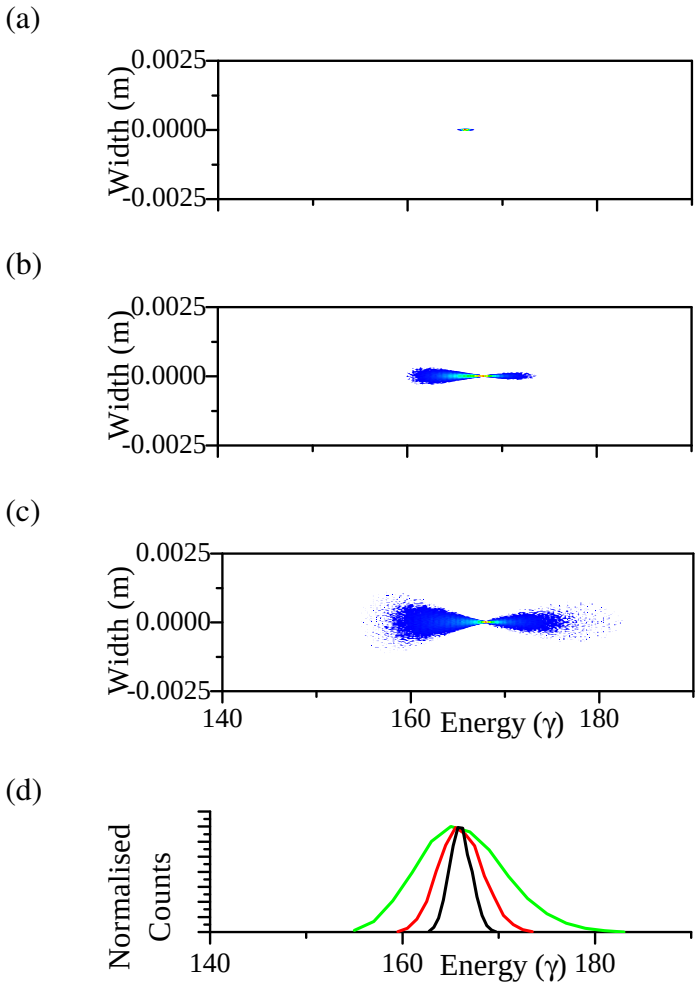

Figure 5.3: Simulated spectrometer screens for electrons from a 3 μm source, with an emittance of (a) 0.1, (b) 1 and (c) 2 π mm mrad using the quadrupole beam transport. A linear colour scale has been used. (d) is the energy profile showing the same peak position but increasing spread for 0.1, 1 and 2 π mm mrad beams represented by the black, red and green curves respectively.

5.2.2 Effects of Emittance from an Effective Source Size

In the experimental set-up used to measure the energy a thin metal foil was used to prevent the high intensity laser beam from propagating down the beam line and saturating or even damaging the detectors. The foil was placed at the exit of the accelerator vacuum chamber at the start of the beam line, 70 cm from the gas jet. The electrons transmit through this foil increasing the beam's emittance by up to two orders of magnitude. This is discussed in more detail in Section 4.3.4, where it is shown that in the above configuration, the emittance is increased but the beam divergence is unchanged. This is the equivalent of a beam emitting from an increased source size, i.e.

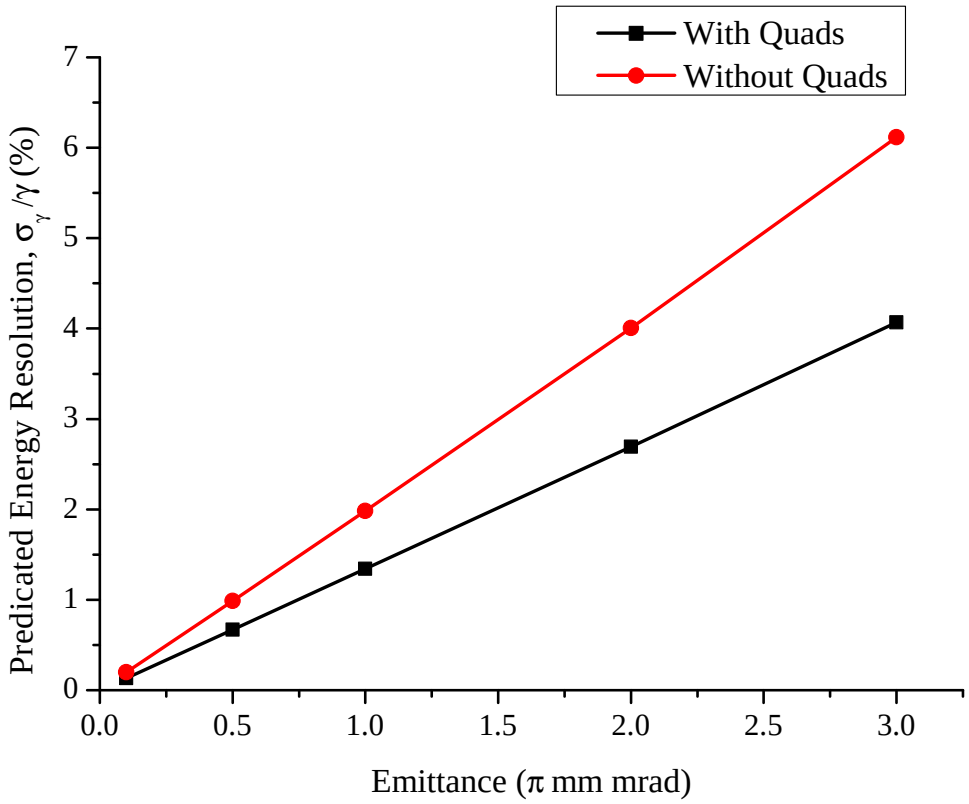

Figure 5.4: Growth of measured energy spread with increasing emittance/divergence without quadrupoles (black) and the reducing in the resolution limit with the use of the quadrupoles (red), for a 88 MeV beam, 3 μm source. Quadruples are set to the experimental values, Q1 = 3.1 T/m and Q2 = 1.5 T/m. r.m.s. spread calculated from GPT simulation.

with constant divergence, an increased emittance requires an increased source radius, which shall be called the effective source size. GPT was used to simulate the effect of the foil by fixing the divergence and varying the source radius to give the appropriate emittance.

5.2.3 Without the use of Quadrupole Beam Transport

Figure 5.5 shows the simulated images on the YAG screen for a 1.5 mrad divergence beam with an emittance of (a) 1, (b) 100 and (c) 200 π mm mrad. It is shown in these images, that the height of the beam increases as the emittance increases. This is to be expected as larger emittance beams cannot be focused down to as small a spot size as those with a low emittance. However, the energy spread is unchanged even over the

very large emittance variation simulated here.

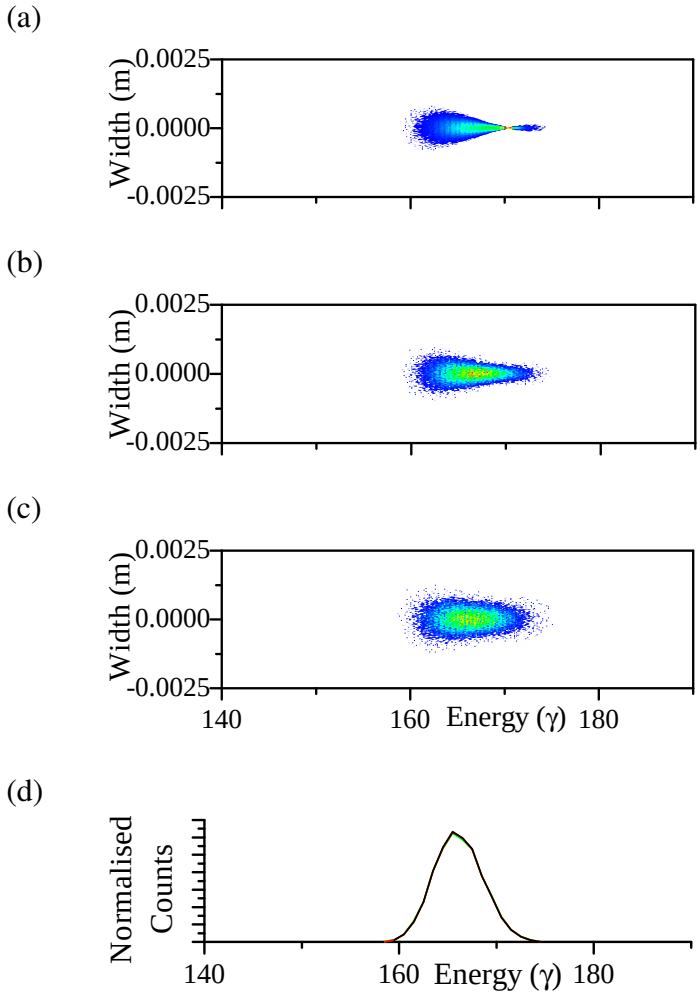

Figure 5.5: Simulated spectrometer screens for electrons with a 1.5 mrad divergence, emittance of (a) 1, (b) 100 and (c) 200 π mm mrad without the use of the quadrupole beam transport. A linear colour scale has been used. (d) is the energy profile showing the same peak position but increasing spread for 1, 100 and 200 π mm mrad beams represented by the black, red and green curves respectively, although due to the similarity in spread the differences in the profile are minimal.

Figure 5.6 (a) shows the dependence of the height of the spot measured on the screen as a function of the emittance. This has been carried for beams with a fixed divergence of 1, 1.5 and 2 mrad shown by the black, red and blue lines respectively. As the emittance increases the effective source size also increases and this results in an increase in the beam focal size. The emittance is a function of the effective source size multiplied by the divergence, therefore, to keep the emittance constant, the effective source size must increase if the divergence is decreased. The increase in width is greater for the lower divergence beams than the higher divergence beams as they

(a)

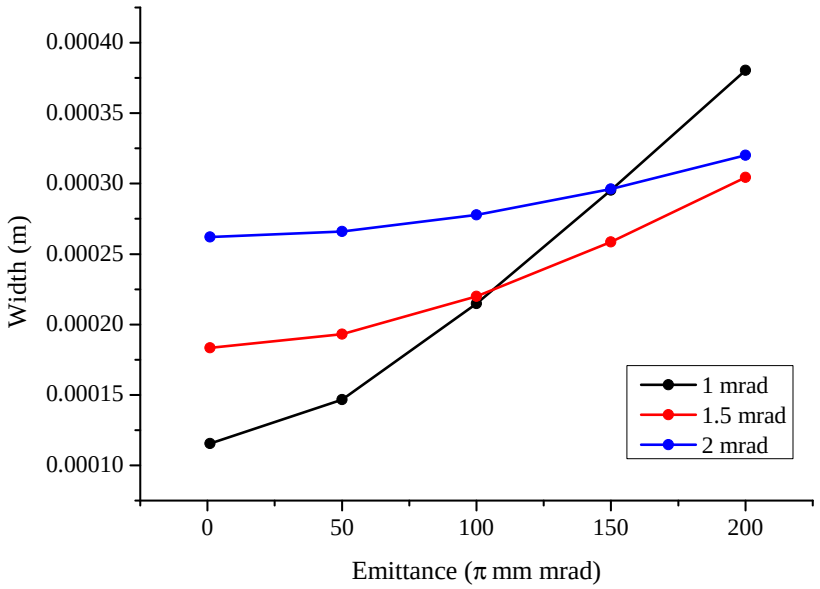

(b)

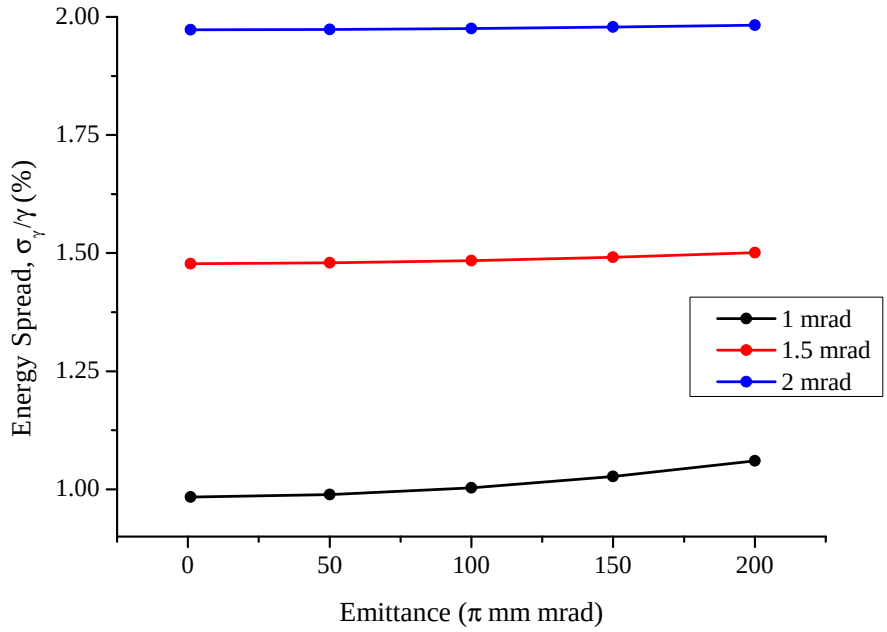

Figure 5.6: The effects of emittance in electron spectrometer, without quadrupole beam transport, on the width (a) and the energy spread (b) for a fixed divergence of 1, 1.5 and 2 mrad beam given by the black, red and blue lines respectively. r.m.s. spread calculated from GPT simulation.

require a larger effective source for a fixed emittance.

The effect of emittance on energy spread resolution is shown in Figure 5.6 (b),

again for a divergence of 1, 1.5 and 2 mrad represented by the black, red and blue lines respectively. Here it is shown that, for a fixed divergence, the emittance does not greatly affect the energy spread resolution. Therefore, the effect of emittance is negligible and only beam divergence is important. This also means that the influence of the laser beam block foil is not important. It is shown that the resolution for the 1, 1.5 and 2 mrad beams is approximately 1, 1.5 and 2 % respectively. This is comparable to the value shown by the red line (no quadrupoles) in Figure 5.4.

5.2.4 With the use of the Quadrupole Lenses in Beam Transport

Figure 5.7 shows the simulated electron spectrometer images for the same beam as shown in Figure 5.5. However the beam is now transmitted through the quadrupole magnetic lenses (as in the experiment set-up in Section 5.3.2, Q1 = 47mT and Q2 = 22 mT). A similar trend is shown as the emittance is increased from 1 (a) to 100 (b) and then to 200 π mm mrad (c) for the 1.5 mrad divergent beam. The quadrupoles increase the height of the spot while decreasing the energy spread resolution.

The influence of the quadrupoles on the energy spread and verticle width are clearly shown in Figure 5.8. In graph (a) it is shown that the width increases for all values of divergence as the emittance increases.

Figure 5.8 (b) shows the energy spread remains constant across the wide range of emittances. However, now the value has decreased for each of the divergences so that the resolution limit becomes approximately 0.7, 1 and 1.35 % for the 1, 1.5 and 2 mrad beams respectively. The beam divergence is typically between 1 and 2 mrad for the wakefield accelerator and we see that the resolution limit is between 0.7 and 1.4 % depending on beam divergence in this range.

5.3 Measured Energy Spectra

The electron spectrometer was set-up with the same magnetic field used in the simulations of 0.59 T. The images were recorded using a 12 bit Point Grey Research Flea camera, then converted to a linear scale and the plotted profile used to measure the r.m.s energy spread by fitting a Gaussian peak.

In this section, examples of low energy spread electron beams will be shown, with and without the use of quadrupole beam transport, to demonstrate the reduction in energy spread measured (Wiggins et al., 2009; Wiggins, Shanks, et al., 2010; Wiggins, Issac, et al., 2010; Wiggins et al., 2011). A relationship between the charge in the electron beam and the energy spread will also be shown.

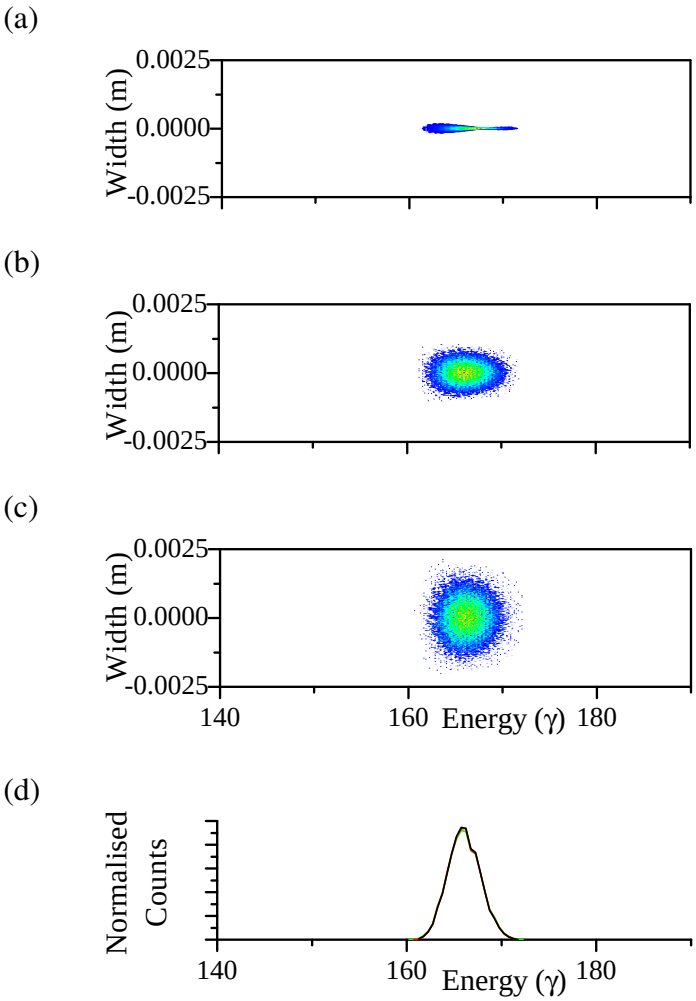

Figure 5.7: Simulated spectrometer screens for electrons with a 1.5 mrad divergence, emittance of (a) 1, (b) 100 and (c) 200 π mm mrad with the use of the quadrupole beam transport. A linear colour scale has been used. (d) is the energy profile showing the same peak position but increasing spread for 1, 100 and 200 π mm mrad beams represented by the black, red and green curves respectively, although due to the similarity in spread the differences in the profile are minimal.

5.3.1 Without Quadrupoles

Figure 5.9 show (a) the profile of charge (corrected for non-linear energy axis) and (b) the image of the lowest energy spread measurement made without the use of quadrupole beam transport. The spectrum represents a peak energy of 89 MeV with an energy spread, $\sigma_\gamma/\gamma = 1.5$ %. The spectrum shows a slight shoulder on the low energy side of the peak. This shoulder is a second peak with 3.4 MeV less energy than the first with 4 % spread. The spectrum has 61 % of the charge in the mono-energetic peak.

(a)

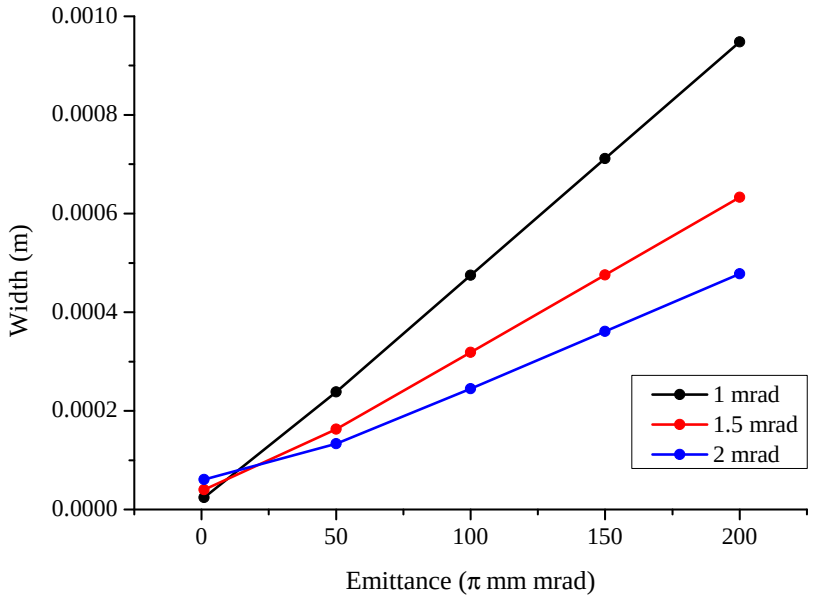

(b)

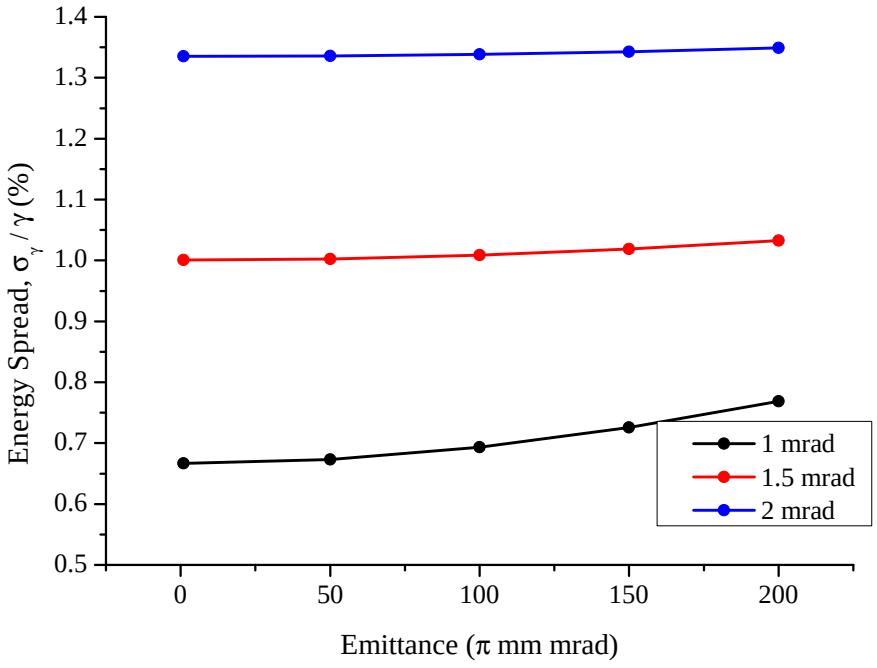

Figure 5.8: Effects of emittance on the width (a) and the energy spread (b) for a fixed divergence of 1, 1.5 and 2 mrad beam given by the black, red and blue lines respectively with the use of quadrupole beam transport. r.m.s. spread calculated from GPT simulation.

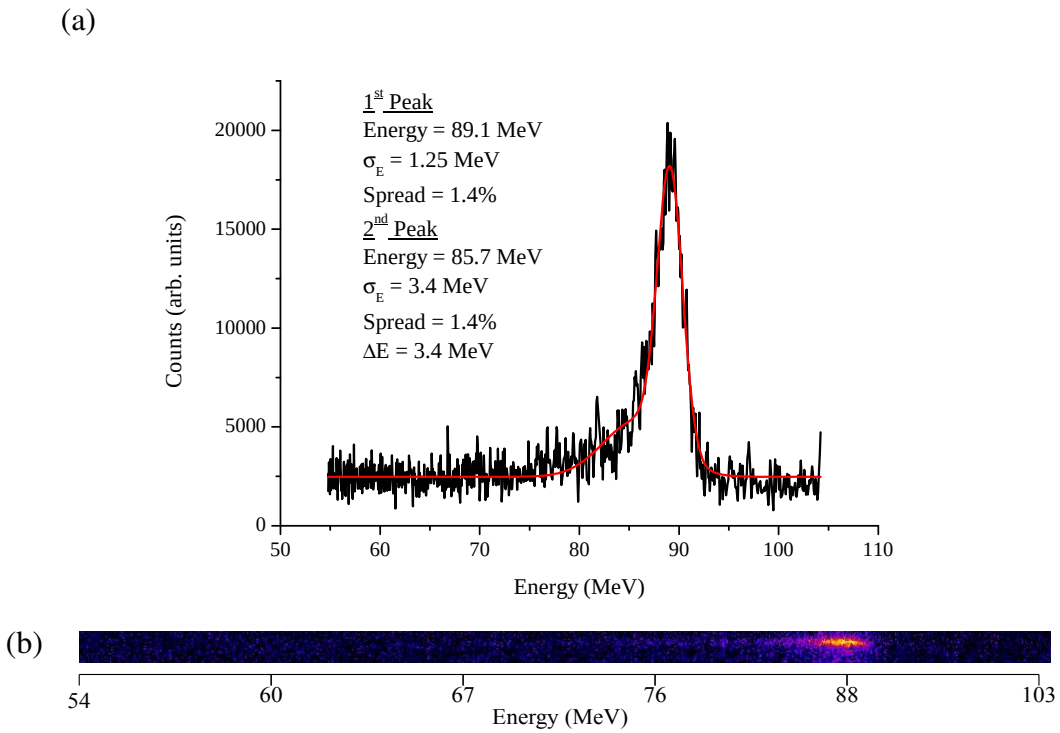

Figure 5.9: The (a) profile and (b) image of a 1.5 % energy spread electron beam with central energy of 89 MeV without the use of quadrupoles. (Shot G7)

5.3.2 With Quadrupoles

Figures 5.10, 5.11 and 5.12 show (a) the profile and (b) the image of the lowest energy spread measurement made with the use of quadrupole beam transport. Figure 5.10 is of a beam with a peak energy of 88.2 MeV and an energy spread $\sigma_\gamma/\gamma = 0.8$ %. Similarly, Figures 5.11 and 5.12 are of beams with peak energy of 79.4 and 85.2 MeV and energy spreads $\sigma_\gamma/\gamma = 0.8$ % and 1.4 % respectively. These measurements represent the lowest measured energy spread of any laser-plasma wakefield accelerated electrons (at the time of writing). All three of these spectra also have a second peak at lower energy. The energy differences from the first peak are 1.7 MeV, 5 MeV and 7.2 MeV and the energy spreads are 3.5 %, 5 % and 3.8 % for Figures 5.10, 5.11 and 5.12 respectively. Figure 5.12 has a third peak at an even lower energy with a greater spread.

(a)

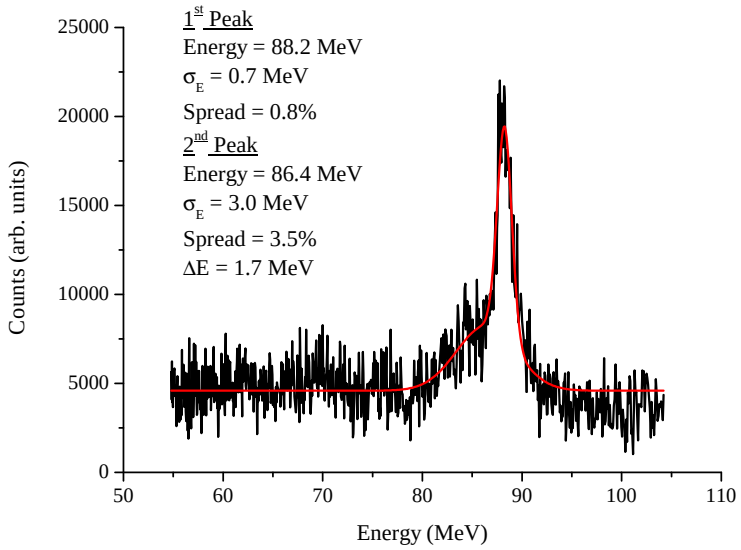

(b)

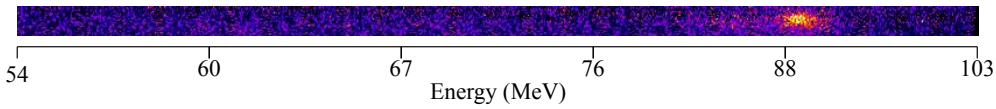

Figure 5.10: The (a) profile and (b) image of a 0.8 % energy spread electron beam with central energy of 88.2 MeV with the use of quadrupoles. (Shot H32)

(a)

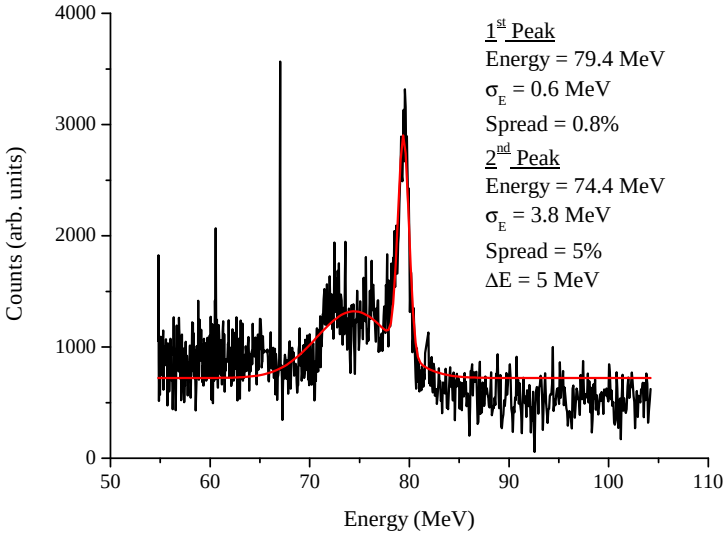

(b)

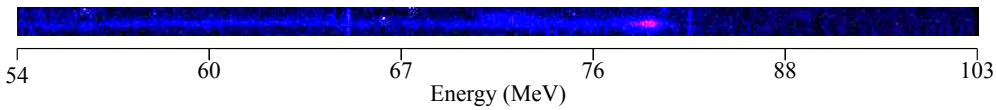

Figure 5.11: The (a) profile and (b) image of a 0.8 % energy spread electron beam with central energy of 79.4 MeV with the use of quadrupoles. (Shot H61)

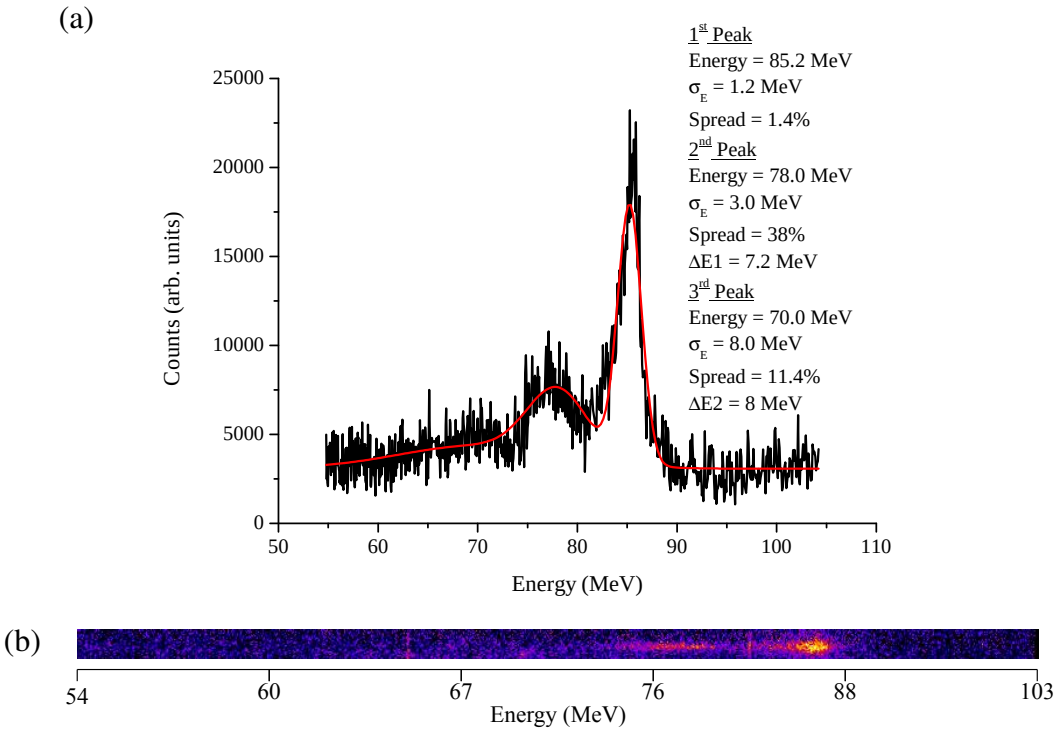

Figure 5.12: The (a) profile and (b) image of a 1.4 % energy spread electron beam with central energy of 85.2 MeV with the use of quadrupoles. (Shot H40)

5.3.3 Energy Spread Scaling with Charge

Figure 5.13 shows ten spectra obtained without the use of focusing quadrupoles (a) and with the use of quadrupoles (b). From fitting the profile of the images in (a) an average energy of 84 $\pm$ 5 MeV and a $\sigma_\gamma/\gamma = 1.8 \pm 0.2$ % is found. The maximum energy and minimum energy spread are 90 MeV and 1.5 % respectively. This energy spread is limited by the resolution of the spectrometer, therefore to minimise resolution problems the quadrupoles were used to better optimise the spectrometer and increase the resolution (as discussed in Section 5.2). Now the high resolution measurements shown in Figure 5.13 (b) give an energy of 82 $\pm$ 4 MeV and a $\sigma_\gamma/\gamma = 1.2 \pm 0.3$ % is found and the lowest energy spread is 0.8 %.

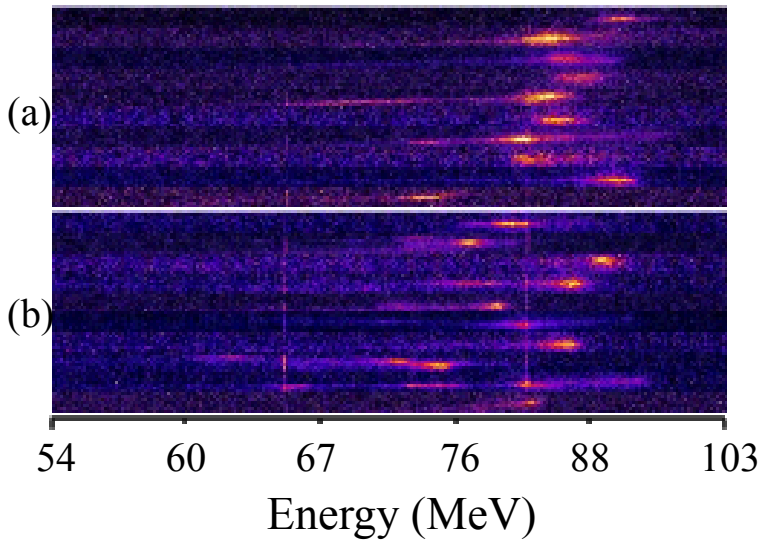

Figure 5.13: 10 electron spectrometer images (a) without quadrupole beam transport and (b) with quadrupoles (Q1 = 3.1 T/m and Q2 = 1.5 T/m).

The energy spread is plotted as a function of the charge in the mono-energetic peak (in arb. units) in Figure 5.14. The spectra obtained without the quadrupoles is denoted by the triangular points and those using the quadrupoles by the circular points. A linear scaling with the charge and energy spread can be seen. In the emittance chapter, however, it is shown that there is a dependence between the beam divergence (and therefore emittance) and the beam charge. The linear scaling in figure 5.14 could just be an increase in resolution with increased charge due to the resolution's dependence on the divergence which, in turn, depends on charge. The divergence depends on the square or cube root of the charge, however, the resolution has a linear scaling with the charge. Also, if the spectrometer was operating at its resolution limit across the range of charges then the energy spread without and with quadrupoles, at a given

(a)

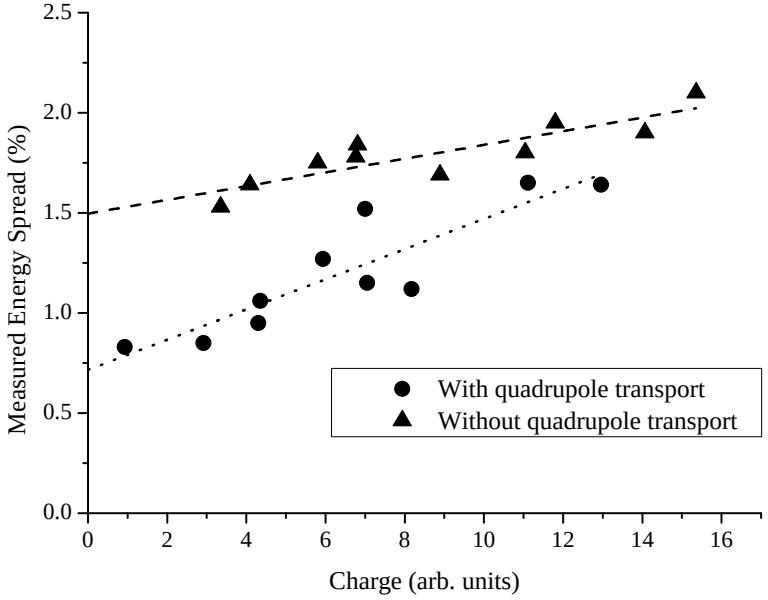

(b)

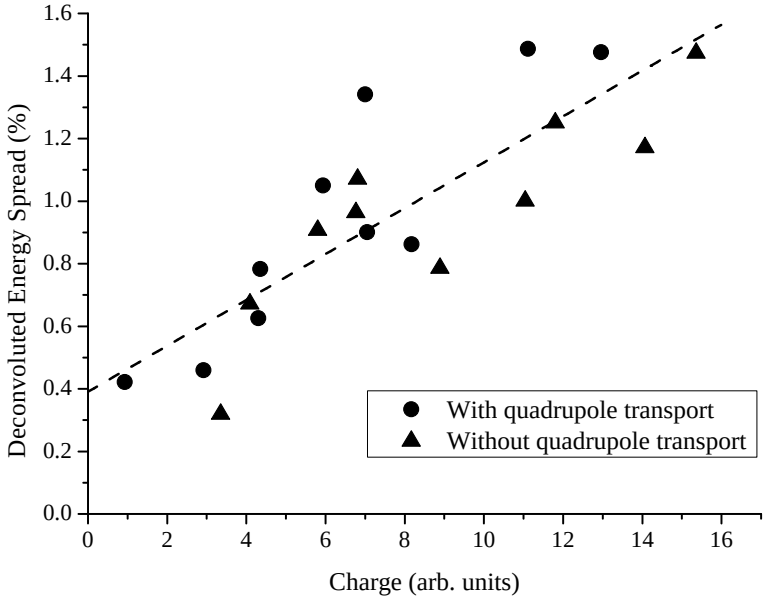

Figure 5.14: the energy spread dependence on charge is shown without the quadrupole beam transport (triangle) and with the quadrupole beam transport (circle).

charge, would correspond to the same divergence, but this is also not the case. For example, a charge of 4 arb. units corresponds to an energy spread of $\sim$ 1 % with the quadrupoles and $\sim$ 1.6 % without quadrupoles. From Figure 5.4, a 1 % energy spread resolution, with quadrupoles, is derived from a 1.5 mrad divergence beam and a 1.6 %

energy spread resolution, without quads, corresponds to a 1.7 mrad divergence beam. Similarly, the corresponding resolution limits divergences at 12 arb. units of charge are 2.4 and 1.8 mrad, again not the same. Therefore, for these two reasons it is the energy spread which is scaling with charge and not the resolution.

As the exact divergence of the electron beam as it enters the spectrometer is not known, the GTP simulations cannot be used to calculate the resolution. However, if it is assumed that there is zero energy spread when there is zero charge, then extending the straight lines fits in Figure 5.14 (a) provides a resolution of 1.5 % and 0.7 % for without and with quadrupoles respectively. The measured values can be de-convolved by subtracting these values in quadrature. Figure 5.14 (b) shows the new de-convoluted values. The de-convoluted values provides a mean energy spread of 1 % both with and without the quadrupole magnets. The lowest energy spread is now 0.4 %.

5.3.4 Multiple Energy Peaks

Of the 20 spectra used in the previous section, 13 had a second higher energy spread peak. The average structure measured consisted of a mono-energetic peak at 83 $\pm$ 1.3 MeV with an energy spread of 1.3 $\pm$ 0.3% (de-convoluted to 0.9 $\pm$ 0.3 %) and a second peak at 79 $\pm$ 1.7 MeV with a larger energy spread of 4.3 $\pm$ 0.9% (de-convoluted to 4.2 $\pm$ 0.9 %). The two peaks are separated by a 4.5 $\pm$ 1.8 % energy difference and 49 $\pm$ 4 % of the charge is in the mono-energetic peak. As the two beams propagate they will drift apart. Depending on their initial relative position and the drift distance, the two beams may or may not contribute together in application, for example, in coherent transition radiation, which is discussed in more detail later.

5.4 Conclusions and Future Work

In conclusion, this chapter represents the lowest energy spread laser-wakefield accelerated electron bunch ever measured. Energy spreads were measured as low as 0.8 % (r.m.s, σ_γ/γ), which is close to the resolution limit of the system. A factor of three increase is shown in the energy spread for a factor of three increase in the charge.

To draw further conclusions about the injection process and the effects of beam load, the charge of the electron bunch would require to be known and this will need to be the focus of future work. However, for typical charge values of a couple of pC and bunch lengths of ~ 0.3 μm results in peak currents in the kA region.

Chapter 6

Transition Radiation

6.1 Introduction

This chapter discusses one of the first measurements of LWFA electrons bunch lengths and the first measurement from a single laser driven accelerator. Coherent transition radiation (CTR), emitted as a relativistic electron bunch travels across a dielectric boundary, has been utilised to measure these short bunch lengths. A two foil system was used to block the driving laser and allow the measurement of femtosecond electron bunches containing picocoulombs of charge.

6.2 Theory of Transition Radiation

6.2.1 The Ginzburg-Frank Formula

As an electron passes across a dielectric boundary, (for example a vacuum to a metal) the electric field of the electron is shielded, creating a discontinuity in the electric field. To balance this discontinuity the electrons in the surface of the boundary travel transversely from the electron as the material accepts the electron. This surface current results in the emission of electromagnetic radiation known as transition radiation as first discussed by (Ginsburg & Frank, 1946). The energy of the radiation emitted is given by the Ginzburg Frank formula (V. Ginzburg & Trytovich, 1990; V. L. Ginzburg, 1982),

$$\frac{d^2U_{GF}}{d\omega d\Omega} = \frac{e^2}{4\pi^3\varepsilon_0 c}\frac{\beta^2\sin^2\vartheta}{\left(1-\beta^2\cos^2\vartheta\right)^2}, \tag{6.1}$$

the energy, U_{GF}, is given per unit angular frequency, ω and per unit solid angle, Ω. The energy is related to the velocity, v, of the electron through the $\beta = v/c$ term. The

energy is converted to energy per unit wavelength through, $\omega = 2\pi c/\lambda$, differentiating to give $d\omega/d\lambda = -2\pi/\lambda^2$ (negative sign lost in equation 6.2 by changing integration limits) to give (Shibata et al., 1994),

$$\frac{d^2U_{GF}}{d\lambda d\Omega} = \frac{e^2}{2\pi^2\varepsilon_0\lambda^2}\frac{\beta^2\sin^2\vartheta}{(1-\beta^2\cos^2\vartheta)^2}. \tag{6.2}$$

It can be seen from Equation 6.2 the energy per unit wavelength depends on $1/\lambda^2$ which results in a decrease in $dU_{GF}/d\lambda$ at longer wavelengths. This is shown in Figures 6.3 and 6.4.

Angular Distribution

The angular distribution is given by the second term in Equation 6.1 and is shown in Figure 6.1 to give the characteristic hollow coned distribution of radiation.

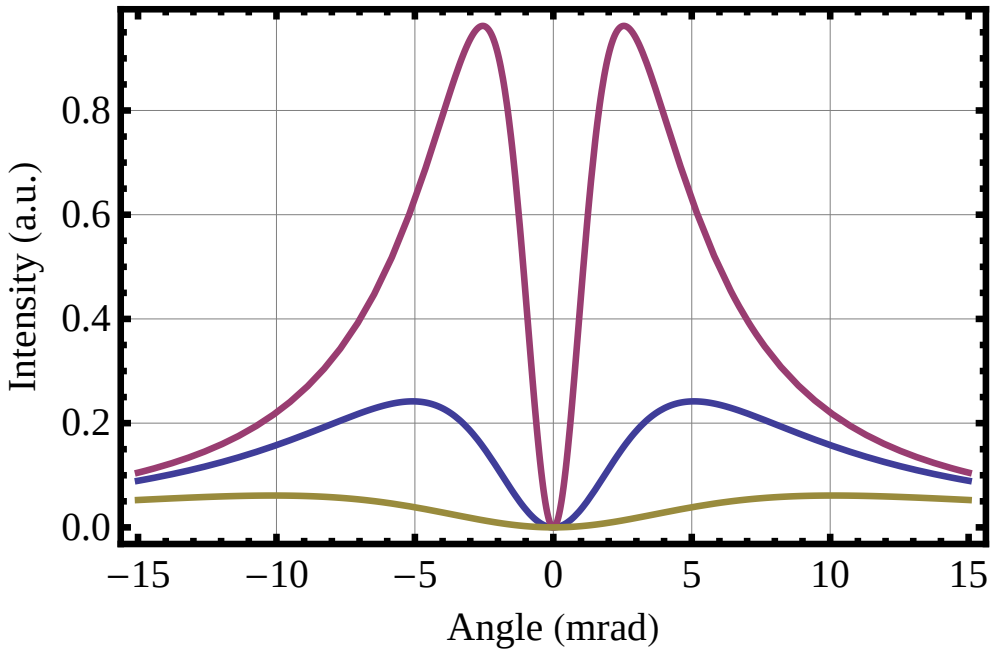

Figure 6.1: Angular distribution of TR for electron energies of 50, 100 and 200 MeV shown by the yellow, blue and red lines respectively.

The angle in which the radiation is emitted is small therefore the approximation $\sin^2\vartheta \approx \vartheta$ and $\cos^2\vartheta \approx (1-\vartheta^2)$ can be made. Under these conditions the second part Equation 6.1 takes the form,

$$\frac{\beta^2\sin^2\vartheta}{(1-\beta^2\cos^2\vartheta)^2} = \frac{\beta^2\vartheta^2}{(1-\beta^2(1-\vartheta^2))^2}. \tag{6.3}$$

For highly relativistic electrons $\beta \to 1$ and $\vartheta_{max} \approx (1-\beta^2) = 1/\gamma$. This is shown by the increased angle of the peak radiation intensity with a decrease in energy in Figure 6.1. A derivation of angular distribution of radiation emitted from an accelerating charge can be found in J. Jackson (1999).

Effects of Angular Spread of Electrons

The above angular distribution is valid for a single electron or for a narrow beam of completely collimated electrons. However, if the electron beam is diverging, as is the case with laser plasma accelerated electrons, each electron emits a cone of radiation along its path and an effective smoothing of the structure occurs, as shown in Figure 6.2. The new structure is a convolution of the electron beams distribution (here a Gaussian distribution is used) and the angular distribution of the TR, given by Equation 6.3, and is shown in Equation 6.4 (Sakamoto et al., 2005),

$$\frac{1}{\sqrt{2\pi}\sigma_x}\int_{-\infty}^{\infty}\frac{\beta^2\left(\vartheta-x\right)^2}{\left(1-\beta^2\left(1-\left(\vartheta-x\right)^2\right)\right)^2}\exp\left(-\frac{x^2}{2\sigma_x^2}\right)dx, \tag{6.4}$$

where x is the electron angle and σx is the r.m.s. angular spread of the electron bunch. Figure 6.2 shows the effect of the increasing electron beam angular spread on the TR angular distribution for an r.m.s. angle, σ_x= 0.1, 0.5, 1, 2, 5 mrad, represented by the dark blue, purple, yellow, green and light blue lines respectively.

6.2.2 Foil Size Effects

The self-field of the electron bunch extends transversely such that the effective source radius of the electron bunch can be defined as (Casalbuoni, Schmidt, & Schmuser, 2005),

$$r_{eff} = \gamma\lambda \tag{6.5}$$

where γ is the Lorentz factor associated with the electrons energy and λ is the wavelength being measured. If the TR foil radius, r_{foil}, is less than the effective source radius then the radiation will be attenuated due to diffraction radiation. The effective source size at $\lambda = 18$ μm (the longest wavelength measured in the following experiments) for 90 MeV beam is, $r_{eff} = 3.2$ mm. The foil has a diameter of 20 mm, r_{foil}= 10mm, and is therefore larger than the effective source size and diffraction radiation effects can be ignored. If the foil size is comparable to the effective source size at a given wavelength, then there will be an attenuation of radiation at that wavelength,

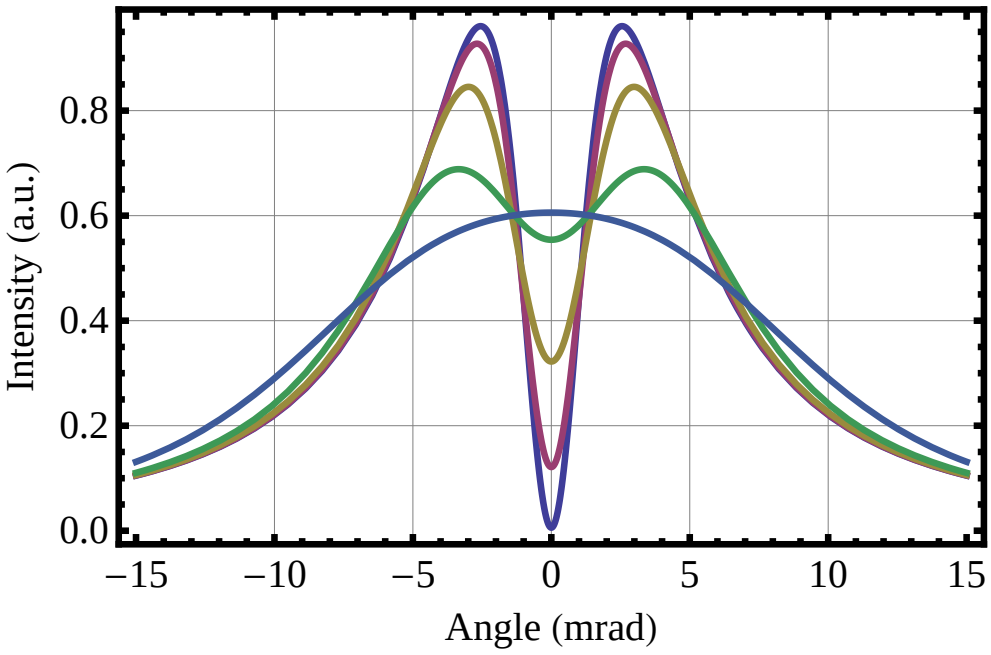

Figure 6.2: The effect of electron bunch angular spread on TR distribution, σ_x= 0.1, 0.5, 1, 2, 5 mrad, represented by the dark blue, purple, yellow, green and light blue lines respectively.

i.e. attenuating the longer wavelengths first, this effect can be calculated from the generalised Ginzburg-Frank formula in Casalbuoni et al. (2005); Schroeder, Esarey, Tilborg, and Leemans (2004).

6.2.3 Radiated Energy

The total radiated spectral energy from an electron crossing a dielectric boundary is found by integrating Equation 6.1 over a hemisphere, i.e. $2\pi\ sin\vartheta\ d\vartheta$,

$$\frac{dU}{d\omega} = 2\pi \int_0^{\pi/2} \frac{e^2}{4\pi^3 \varepsilon_0 c} \frac{\beta^2 \sin^2\vartheta}{\left(1-\beta^2\cos^2\vartheta\right)^2} \sin\vartheta d\vartheta. \tag{6.6}$$

Equation 6.6 produces the energy in J/rad, however integration of Equation 6.2 is equally valid. The lack of a frequency component in the Ginzburg Frank equation shows that the radiated energy is equal at all frequencies (provided the frequencies are well away from the limits of the system).

6.2.4 Coherent Transition Radiation

The previous sections have discussed the emission of transition radiation from a single electron. As a bunch of electrons cross a boundary each electron will emit the

full spectral range of radiation. If the bunch of electrons is long, compared with the wavelength of radiation being produced, then the radiation produced at the front of the bunch will be out of phase with the radiation produced at the rear of the bunch and the radiation will be incoherent. The incoherent intensity of radiation from the bunch, I_{ITR}, will result in a linear scaling of the intensity of radiation from one electron, I_1, with the number of electrons, N, given by $I_{ITR} = N\, I_1$

When the radiation wavelength becomes long compared to the bunch length the electrons emit in phase with each other and the light produced is coherent. Now the radiation scales with the square of the charge, $I_{CTR} = N^2 I_1$.

The electron bunch is characterised by a normalised longitudinal particle distribution, $\rho_{long}(t)$,

$$\int_{-\infty}^{+\infty} \rho_{long}(t)\, dt = 1. \tag{6.7}$$

The particle density is therefore $N\rho_{long}(t)$. The form factor of the electron bunch is given by the Fourier transform of $\rho_{long}(t)$,

$$F_{long}(\omega) = F_{long}\left(\frac{2\pi c}{\lambda}\right) = \int_{-\infty}^{+\infty} \rho_{long}(t) \exp(-i\omega t)\, dt. \tag{6.8}$$

Here, $F_{long}(\omega) \approx 1$, where $\omega \gg 2\pi T$ when T is the electron bunch length and $F_{long}(\omega)$ ≈ 0 when $\omega \ll 2\pi T$.

Therefore using $N^2 |F_{long}(\omega)|^2$ means when $\omega \gg 2\pi T$ the radiation will scale with N^2.

The transition radiation energy density is now given by (Casalbuoni et al., 2005),

$$\frac{d^2 U_{bunch}}{d\omega d\Omega} = \frac{d^2 U_{GF}}{d\omega d\Omega} N^2 |F_{long}(\omega)|^2. \tag{6.9}$$

The wavelength dependent spectral shape is therefore given by the $|F_{long}|^2/\lambda^2$ term. Some example particle distributions are given in figures 6.3 and 6.4.

From Equation 6.10, Figure 6.3 (a) shows Gaussian particle distributions for r.m.s. bunch lengths of $\sigma t = 4$, 6, 8 and 10 fs shown by the blue, purple, yellow and green lines respectively. The spectral distribution of the bunches are shown in Figure 6.3 (b) using the same colour coding.

$$\rho_{gaus}(t) = \frac{1}{\sqrt{2\pi}\sigma t} \exp^{\left(-\frac{t^2}{2\sigma t^2}\right)} \tag{6.10}$$

Figures 6.4 (a) and (b) show a similar particle and spectral distributions for the extreme distribution, given by Equation 6.12.

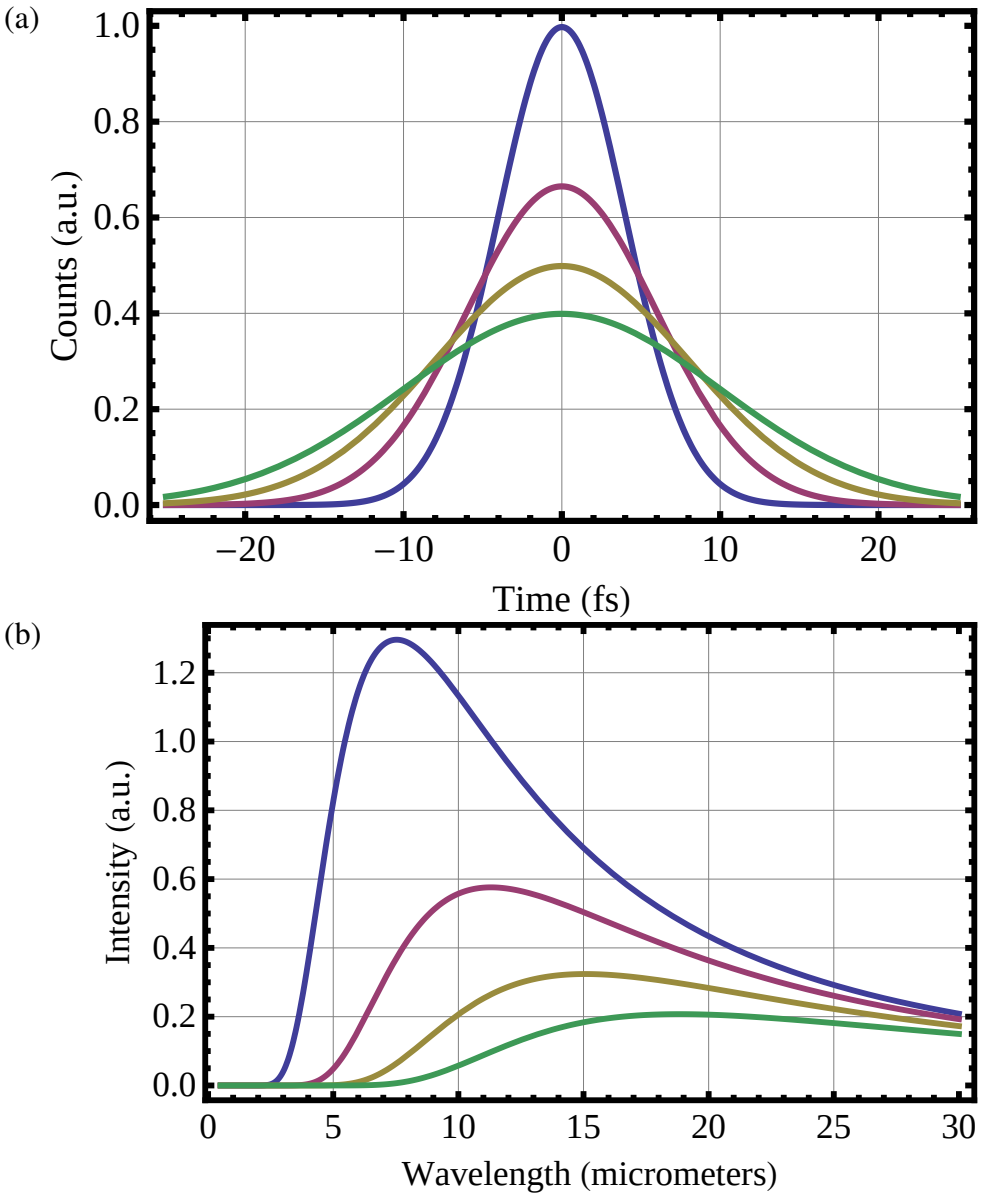

Figure 6.3: (a) Gaussian electron bunches with a distribution with an r.m.s. length of 4 (blue), 6 (purple), 8 (yellow) and 10 (green) fs and (b) their TR spectrum.

$$\beta = \left(\frac{6\,\sigma t^2}{\pi^2}\right)^{\frac{1}{2}} \tag{6.11}$$

$$\rho_{ext}(t) = \frac{1}{\beta}\exp^{(-\exp^{\left(-\frac{t}{\beta}\right)}-\frac{t}{\beta})} \tag{6.12}$$

The extreme function is a sharp rising peak with a slowly decreasing tail, this would accurately represent the profile of a diverging beam or straggling as the beam passes through matter. Similarly the plots are for r.m.s. distributions of $\sigma t = 4$, 6, 8 and 10 fs

shown by the blue, purple, yellow and green coloured lines respectively. The spectral distribution of the bunches are shown in Figure 6.4 (b) with the same colour scale.

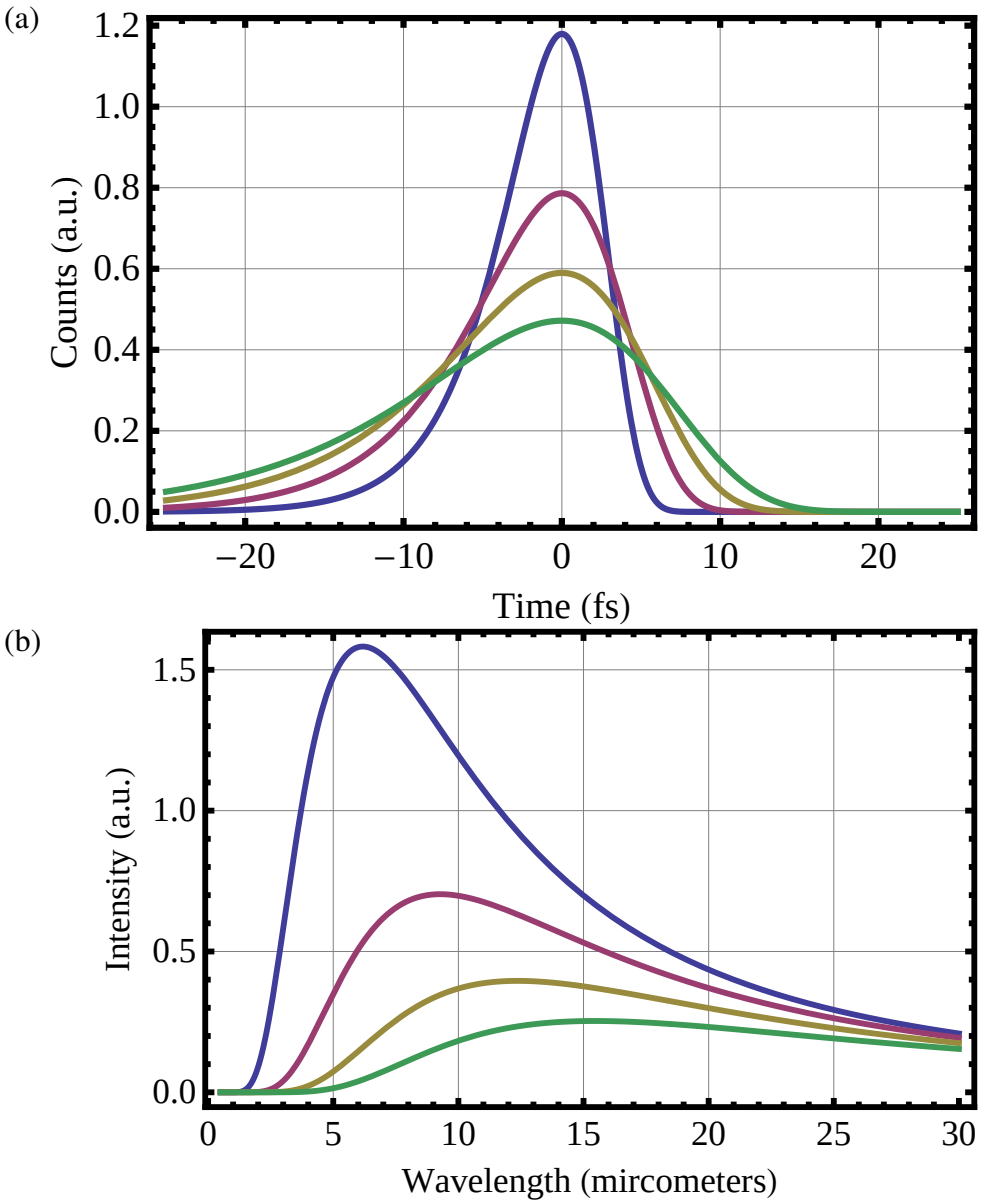

Figure 6.4: (a) Extreme electron bunches with a distribution with an r.m.s. length of 4 (blue), 6 (purple), 8 (yellow) and 10 (green) fs and (b) their TR spectrum.

The spectra for the two distributions have subtle difference in the gradients. The Gaussian distributions produce steeper gradients in its slopes. Taking, for example, the two, 4 fs spectra, here the Gaussian spectrum (Figure 6.3) starts at 3 μm and reaches its maximum at 7.5 μm, whereas the extreme distribution (Figure 6.4) spectrum starts at 2 μm and does not achieve its maximum until 6 μm.

6.2.5 Radiation Scaling with Charge

As was discussed in the previous section, for coherent radiation, the total radiated energy is proportional with the square of the charge. This is true for $\lambda \gg c/T$, as shown in figures 6.3 (b) and 6.4 (b), at 30 μm there is very little change in the signal for different bunch lengths. At this wavelength the radiation depends on charge and not on electron bunch length (provided the bunch length remains $<$ 10fs). However, the maximum measurable wavelength of the experiment in this chapter is less than 30 μm. It can quite clearly be seen in Figure 6.3b that at shorter wavelengths, when $\lambda \gg c/T$ (at 10 μm for example), the radiation intensity is very dependent on bunch length. At this wavelength a charge squared dependence on radiation intensity would still be possible provided the bunch length remains constant.

However, it is not likely that this is the case. We know that with increasing charge there is an increase in the energy spread (Section 5.3.3). An increasing energy spread will increase the bunch length after the bunch has propagated over a distance and it is likely that the initial bunch length will also increase.

Figure 6.5 (b) shows the effect at 13 μm (integrated over a 1 μm bandwidth and a 40 mrad angle) of bunch length increasing with charge on radiated energy at wavelengths comparable to electron bunch length, in this case. The bunch length has been chosen to increase with the square of the charge (proportional to $0.5 \times Q^2$, Q^2, $1.5 \times Q^2$ and $2 \times Q^2$ represented by the blue, red, yellow and green lines respectively) starting with the minimum bunch length of $\approx$ 6 fs. The charge squared dependence represents the non-linear dependence of the energy spread on the charge as shown in Figure 2.9. This will result in a non-linear bunch lengthening as the bunch drifts to the screen. However, a linear scaling of time with charge will result in similar scaling of TR signal with charge, but with altered peak positions and gradients.

Figure 6.5 (b) shows the TR scaling with charge when the bunch length scales with charge shown in Figure 6.5 (a). The squared dependence that the TR has on charge now disappears. Now the radiation reaches a maximum and falls away as the bunch length becomes too long to produce coherent radiation. The rate in which the TR reaches its maximum and then falls away indicates the rate and manner that the bunch length varies with charge. For example, if the TR signal reaches its maximum quickly it would indicate that the bunch length is increasing rapidly (green), whereas if the maximum TR signal is does not arrive until a higher charge then this would suggest a slow build in bunch length with charge (blue).

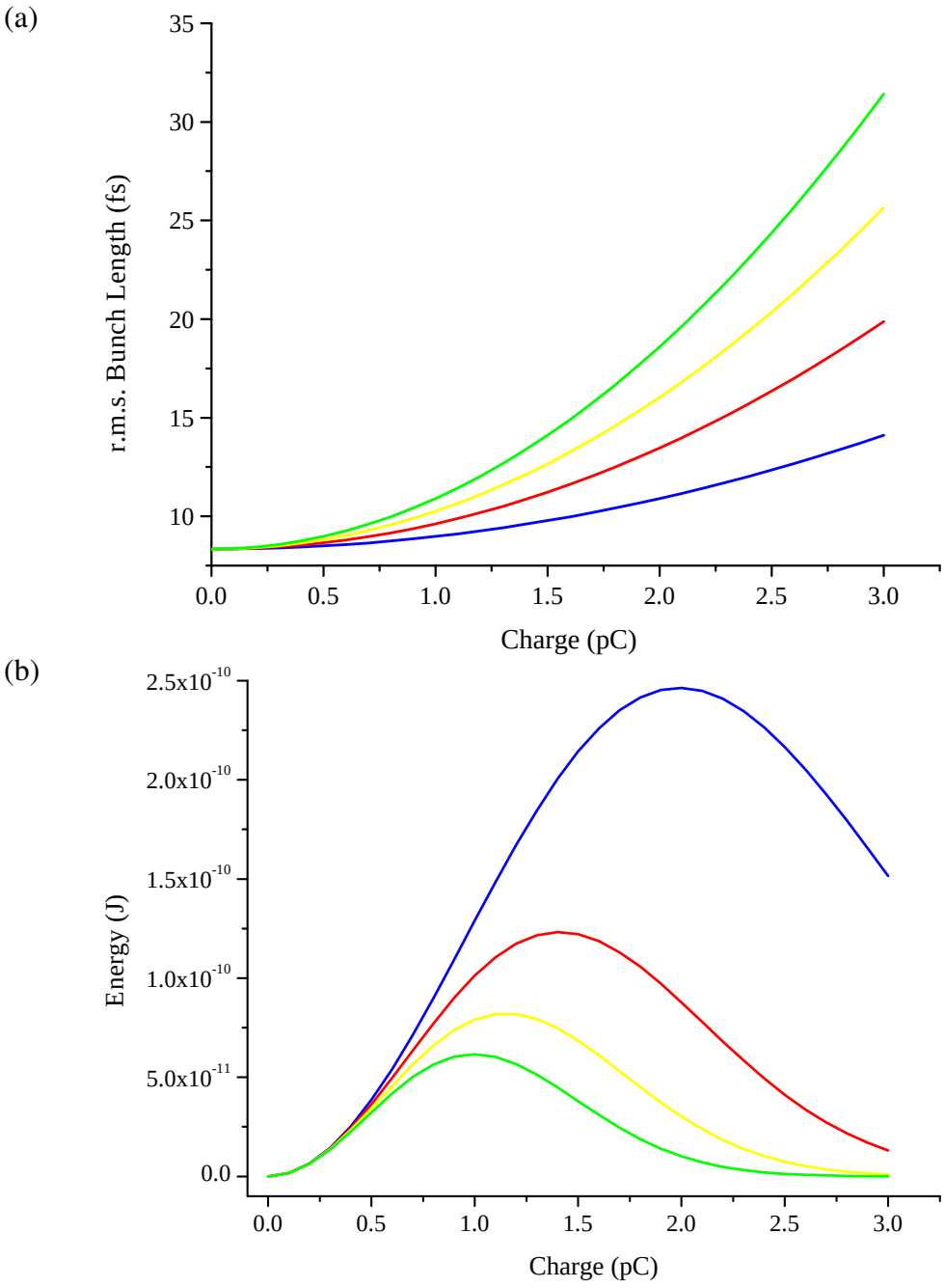

Figure 6.5: The effects of TR signal scaling with charge (b) if the r.m.s. bunch length also varies with charge (a).

6.2.6 Effects of Transverse Bunch Distribution

The Ginzburg Frank formula describes the radiation from a single electron. Section 6.2.4 extends this formula to describe multiple electrons with a longitudinal bunch distribution $\rho_{\text{long}}(\text{t})$ $(= \rho(\text{z/c}))$. This section will discuss the effect of the transverse beam distribution. Take, for example, two electrons at A and B separated by a distance Δx in the transverse direction and separation $\Delta \text{z} = 0$ in the longitudinal direction, as shown in Figure 6.6.

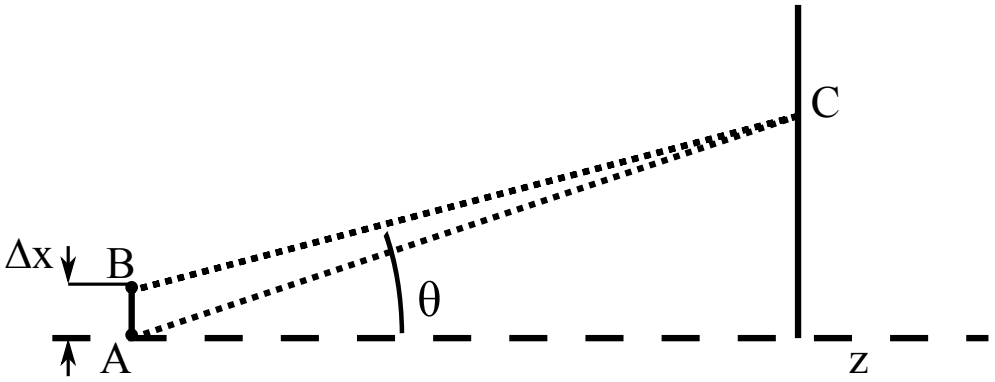

Figure 6.6: Effect of bunch width on TR

When the radiation produced by these two electrons is detected with zero angle to the propagation direction, the radiation will arrive at the detector in phase. However, as the radiation observation position changes to an angle, θ, from the z-axis to point C a path difference is introduced between the two distances AC and BC given by $\Delta r = AC - BC = \Delta x \sin\theta$. The measured bunch length at C will therefore be a combination of both $\Delta x \sin\theta$ and $\Delta z \cos\theta$.

To incorporate the transverse profile distribution, the distribution becomes $\rho(t) = \rho(t_z)\rho(t_\perp)$, where $\rho(t_z)$ is the longitudinal distribution and $\rho(t_\perp)$ is the transverse distribution ($t_z = z/c$ and $t_\perp = r/c$ where r is the radius). The form factor given in Equation 6.8 becomes (Settakorn, 2001),

$$F_{long}(\omega,\theta) = \int_{-\infty}^{+\infty} \rho_{long}(t_\perp)\, exp(-i\omega t_\perp\, sin\theta)\, dt_\perp \int_{-\infty}^{+\infty} \rho_{long}(t_z)\, exp(-i\omega t_z\, cos\theta)\, dt_z. \tag{6.13}$$

For a Gaussian distribution in both the radius, r, and in z direction, the form factor is given by,

$$\mid F_{long}(\omega,\theta) \mid^2 = \exp(-\omega t_\perp \sin\theta)^2 \exp(-\omega t_z \cos\theta)^2 \tag{6.14}$$

If $\sigma r_\perp \, sin\theta \ll \sigma r_z \, cos\theta$, where $\sigma r_\perp$ is the r.m.s. transverse radius and σr_z is the r.m.s. length, then the transverse distribution can be ignored. For example, using σr_z= 3.3 μm (= 10 fs) at $\theta = 1/\gamma = 1/200 = 5$ mrad, $\sigma r_\perp$= 340 μm. Now $\sigma r_\perp \, sin\theta$ = 1.6 μm compared to $\sigma r_z \, cos\theta$ = 3.3 μm. $\sigma r_\perp \, sin\theta$ is less than $\sigma r_z \, cos\theta$, but not much less, as would be required to make the transverse width negligible, and therefore transverse effects must be taken into consideration.

As is shown in Equation 6.13, the further off-axis the radiation is emitted, the greater the effect of transverse electron bunch width. This has the effect of attenuating the off-axis radiation and only leaving the on-axis radiation. The on-axis radiation is minimal due to the $1/\gamma$ cone shaped distribution of radiation, as discussed in Section 6.2.1 which results in very little radiation being produced for large electron bunch widths, as shown in Figure 6.7 (a).

The electron bunch angular spread also increases as the bunch width increases because the electrons investigated here are emitted from a point source. The large angular spread causes the $1/\gamma$ cone to be filled in as shown in Figure 6.2, thus leading to on axis radiation. Now the distribution shown in Figure 6.7 (a) tends to the distribution shown in Figure 6.7 (b), which shows the remaining on-axis radiation.

Integrating over the hemisphere of emitted radiation gives the TR spectrum. Figure 6.8 (b) shows the spectrum for the several bunch shapes shown in Figure 6.8 (a). All of the bunches have a length of 6.5 fs and all of the shapes have a similar trend. The simplest structure is the Gaussian distribution (red) which decreases to a minimum at ~ 6 μm. The flat-top distribution (black) decreases in a similar shape to a minimum at < 7 μm, There is then a rise and fall in the spectrum in typical Sinc^2 oscillations. The triangle distribution (blue) has the same Sinc^2 shape with peaks and dips in a similar place however with a smaller amplitude in the oscillations. The quadratic tail (green) further washes out the Sinc^2 oscillations, however it still has a similar distribution.

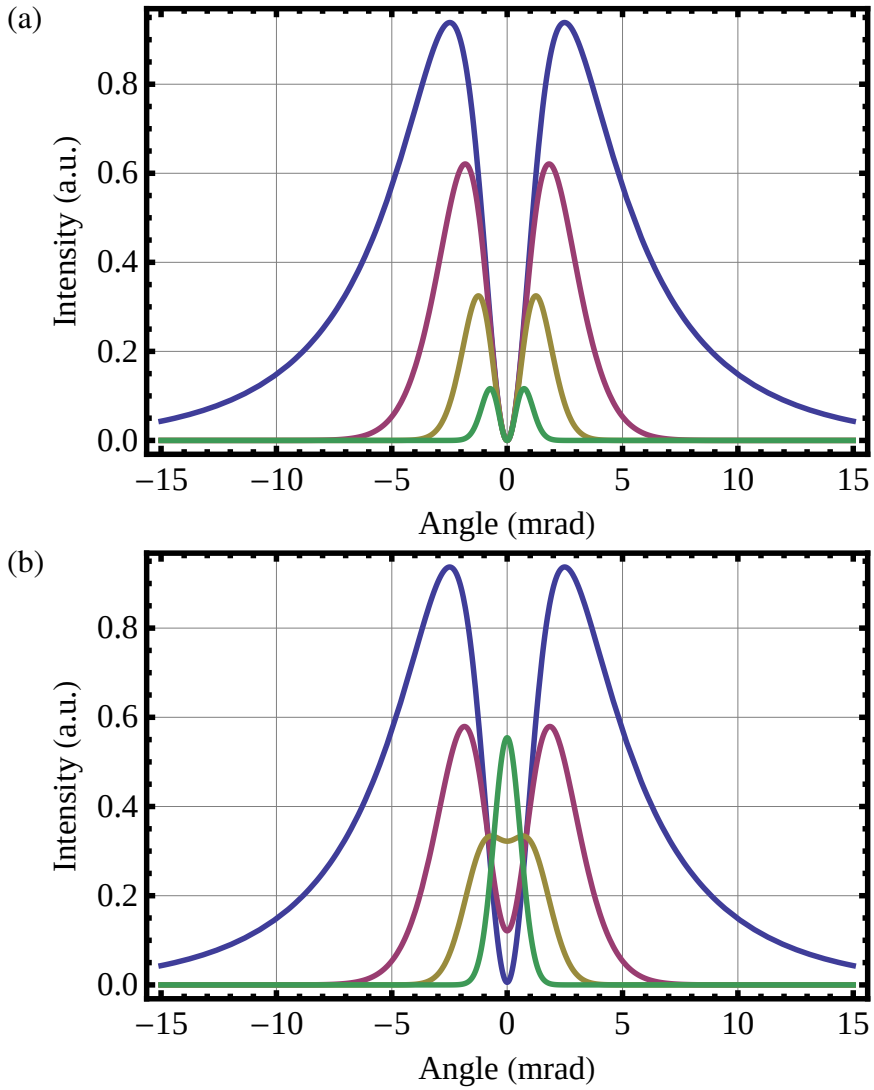

Figure 6.7: The effect of bunch width on the angular distribution of TR for a bunch width of 0.05, 0.25, 0.5 and 1 mm at 5 μm, represented by the blue, red, yellow and green lines respectively. (a) shows the distribution for a collimated electron bunch whereas (b) includes the effects of angular spread for an electron bunch having propagated 1 m from a point source.

(a)

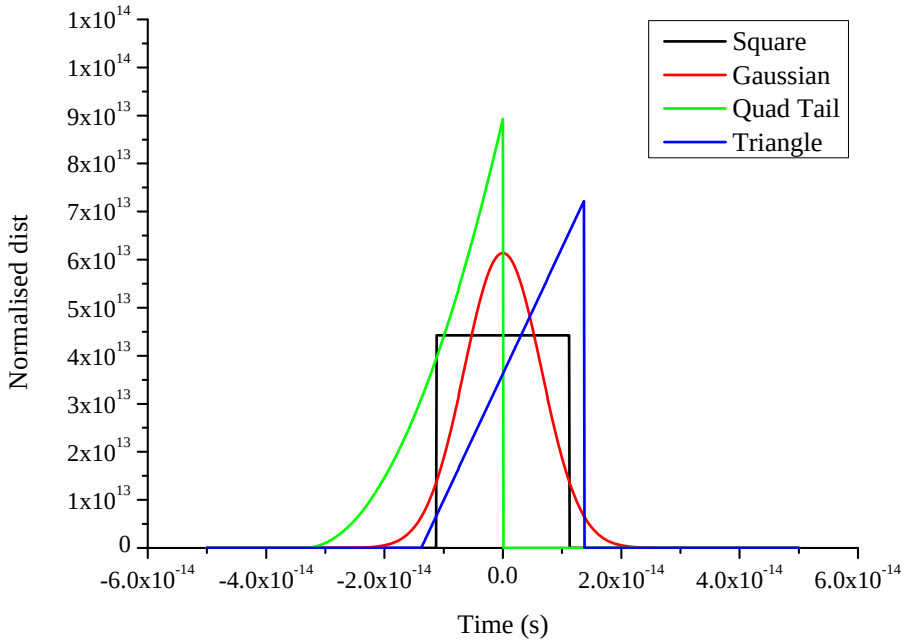

(b)

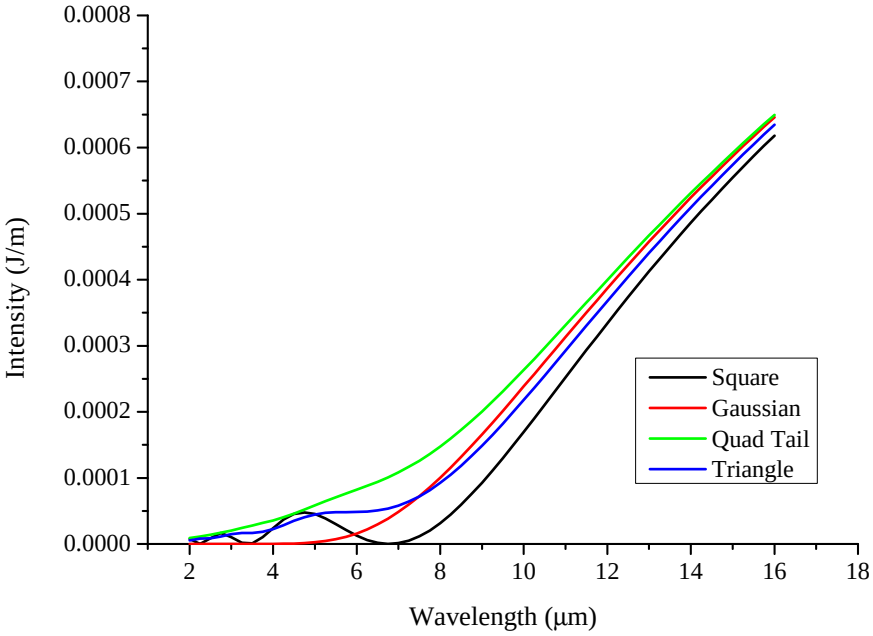

Figure 6.8: (a) Longitudinal electron bunch distribution and (b) their TR spectrum for several bunch shapes for a bunch width of 1.25 mm, a divergence of 3 mrad and an energy 89 MeV

6.2.7 Two Foil Transition Radiation System

In the TR measurements made here two foils were used. The first was to act as a laser beam block and prevent the laser light from propagating to the detector and the second was placed at 45° to take the radiation out of the beam line, to the detector. The foil configuration is discussed in more detail in Section 6.3.1 and the foil configuration is shown in Figure 6.18.

Formation Length

The formation length of forward TR is given by Wartski, Roland, Lasalle, Bolore, and Filippi (1975),

$$Z_f = \frac{\beta\lambda}{\pi(1-\beta\cos\theta)}. \tag{6.15}$$

This is the distance at which the phase difference between the radiation field and the particle field is equal to 1 rad (i.e. $Z_\nu(\omega/\nu(\omega/c)\cos\theta) = 1$). Measurement must be carried out at distances greater than the formation length for the previously discussed equations to hold true or the radiation will be attenuated. In the case of a 90 MeV beam at an angle $\theta = 1/\gamma$ at 18 μm the formation length is found to be 9 cm (less than the 16 cm between the two foils in the experiments here).

Interference

In a two foil system, when the second foil acts as a 45° mirror to the first foil, the TR will be a combination of the forward TR from the first screen and the backward TR from the second screen. If the second screen is placed inside the formation length of the first screen then the TR will be partially suppressed. However, if the separation is greater than Z_ν then the two radiation fields will add in phase as they are both created by the same traversing electron bunch. The phase difference between the two pulses comes from the difference between the particle velocity and the speed of light and is given by $\phi = L/Z_\nu$, when L is the distance between the two foils. From this we see that there is interference between the radiation generated by the two foils and the combined radiation takes the form (Wartski et al., 1975; Shibata et al., 1994),

$$\frac{d^2U_{twofoil}}{d\lambda d\Omega} = \frac{d^2U_{bunch}}{d\lambda d\Omega}\left(1-\cos\left(\frac{L}{Z_f}\right)\right). \tag{6.16}$$

Due to the angular term in Equation 6.15 the TR will move in and out of phase as the angle, θ, between the electron beam and the observation point varies. This effect is displayed in Figure 6.9 where the interference is shown at $\lambda = 2.5,\ 5,\ 10,\ 15\ \mu$m

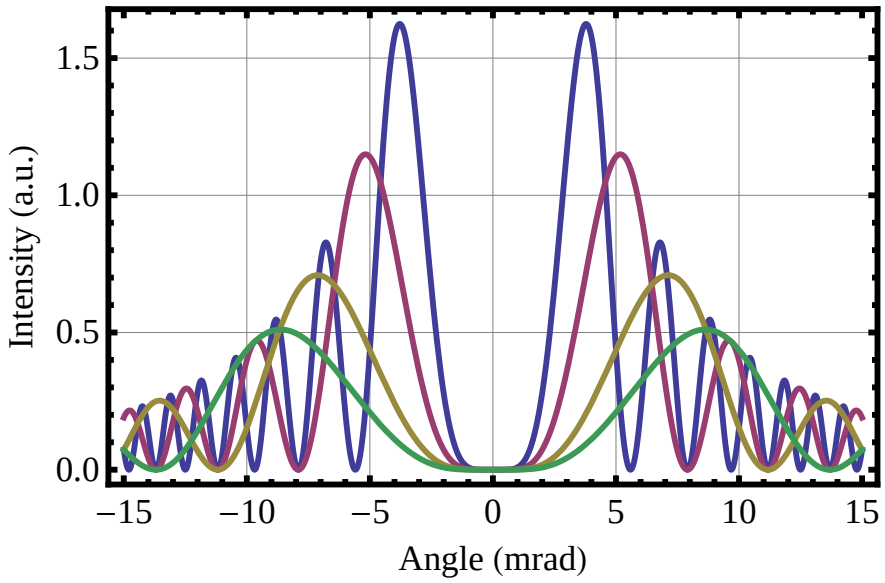

Figure 6.9: Angular interference of the radiation from two foils for $\lambda = 2.5$, 5, 10, 15 μm wavelength radiation represented by the blue, red, yellow and green lines respectively

represented by the blue, red, yellow and green lines respectively, for an electron beam energy of 100 MeV and L = 16 cm.

Effects of Angular Spread of Electrons

Similar to that seen for a single foil, when a beam has some angular properties the angular structure smooths out (Lumpkin, 1997) this is particularly import in the two foil system as the first foil will scatter the electrons increasing the angular spread (Rule, 1987) and the angular part of the equation takes a form similar to Equation 6.17 given by,

$$\frac{1}{\sqrt{2\pi}\sigma_x}\int_{-\infty}^{\infty}\frac{\beta^2(\vartheta-x)^2}{\left(1-\beta^2\left(1-(\vartheta-x)^2\right)\right)^2}\left(1-\cos\left(\frac{L}{Z_f}\right)\right)\exp\left(-\frac{x^2}{2\sigma_x^2}\right)dx, \quad (6.17)$$

where the angles of the electron beam are integrated over to give a structure shown in Figure 6.10 for a beam divergence of x = 0.1, 0.5, 1, 2 mrad represented by the blue, red, yellow and green coloured lines respectively. (Energy = 100 MeV, L = 16 cm and $\lambda = 2.5$ μm).

Figure 6.10 shows that the angular spread also fills in the $1/\gamma$ cone shaped distribution providing on-axis radiation. The angular spread in the electron bunch comes from

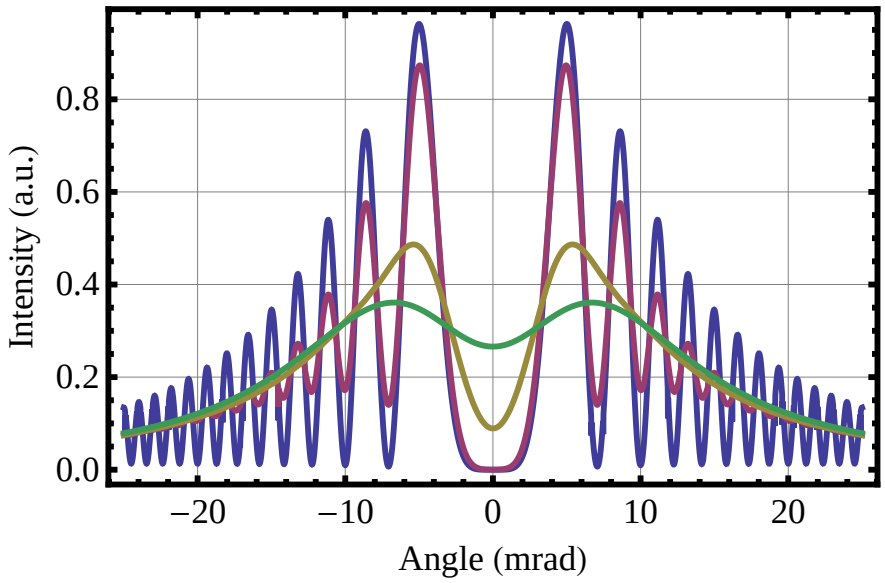

Figure 6.10: The effect of angular spread in the electron bunch of 0.1, 0.5, 1, 2 mrad represented by the blue, red, yellow and green coloured lines respectively on the two-foil far field TR distribution.

two sources. The first source is the natural divergence of the electron beams from the near point source in the wakefield accelerator, resulting in a finite electron beam width at the TR foils. The second source is the electron scattering as it passes through the foil, this has a value of $\sim$ 3 mrad for typical electron bunch parameters as discussed in Section 4.3.4. For a typical beam width of $\sim$ 1 mm, most of the radiation is cone shaped distribution forward as discussed in Section 6.2.6 and shown in Figure 6.11.

Now only on-axis interference needs to be taken into consideration. This interference is given by the interference term in Equation 6.16, where the angle in the formation length, Z_f, is zero. Figure 6.11 shows the effect of both angular spread and width of the electron bunch for 3, 7.5, 12 and 16 μm radiation shown by the blue, red, yellow and green lines respectively. In this plot the electron bunch has an r.m.s. radius of 1 mm and an r.m.s. angular spread of 3 mrad which is typical for this experiment. For the shorter wavelength it is clear that there is more off-axis attenuation, however the peak intensity for the on-axis radiation is seen to decrease with increasing wavelength as the radiation from the two source becomes increasingly out of phase.

Due to the width and angular spread of the electron bunch the radiation is within a small angle from on-axis ($<$ 3 mrad). For small angles the cos θ term in the formation length is $\sim$ 1, therefore the on-axis interference between the two foils must be taken into consideration. The interference term in Equation 6.16 of $(1-cos(L/Z_f))$ for on-axis radiation is shown in Figure 6.12 as a function of wavelength for the measured

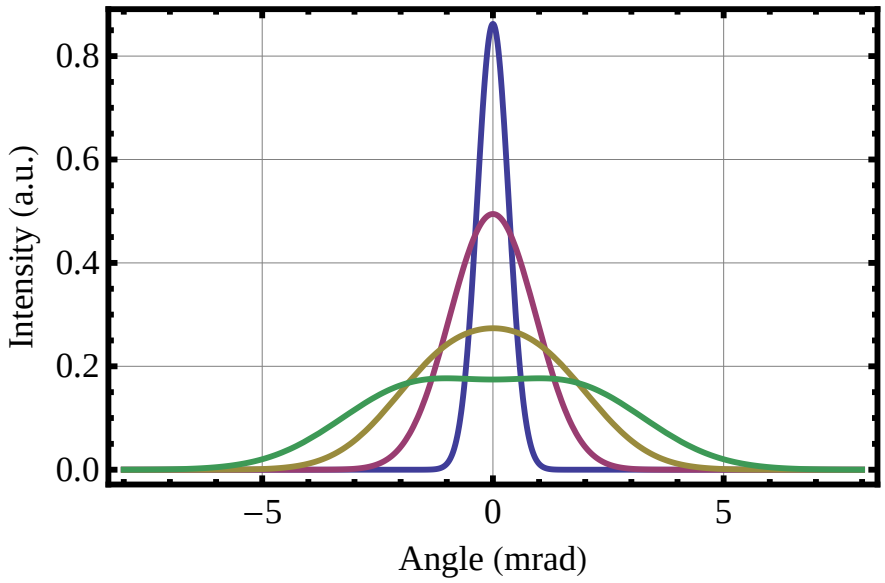

Figure 6.11: Far field TR distribution including angular spread (3 mrad) and bunch width (1 mm) for 3, 7.5, 12 and 16 μm radiation shown by the blue, red, yellow and green lines.

energy of 89 MeV ($\pm$ 1 standard deviation) and the foil separation of 16 cm. Here it is seen that at longer wavelengths the two foils are inside the formation length causing attenuation of the beam signal. Whereas, at ~ 4 μm, the radiation has dephased from the electron bunch causing constructive interference of the two radiation signals.

Including the two foil interference with the single foil spectrum in Figure 6.8 is shown in Figure 6.13. Now the Sinc^2 oscillations are stronger than the attenuated longer wavelengths radiation.

6.2.8 Electron Bunch Evolution

As the electron bunch travels from the gas jet to the TR screen, the beam divergence and energy spread of the electron bunch will cause bunch elongation. In these experiments the energy of the electron bunch is too high and the charge density too low for space charge to be an issue. Charge density is high when the beam is at focus or just leaving the gas jet, however because the beam is diverging the charge density quickly reduces. Therefore, only bunch elongation from energy spread and divergence needs to be considered.

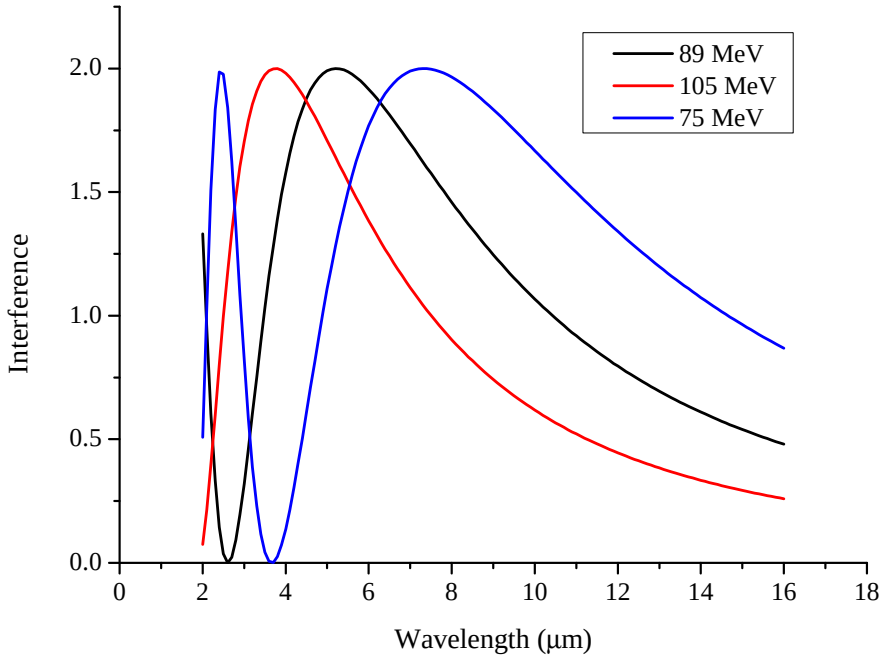

Figure 6.12: On axis interference between the two foils as a function of wavelength for 105, 89 and 75 MeV electrons (red, black and blue curves respectively).

Effects of Beam Divergence

As discussed in Chapter 4, electrons leave the the gas jet with a divergence. The more divergent electrons have a longer path to the TR screen than those that are on-axis. This causes a dispersion between an on-axis electron and diverging electron, $\delta\tau_{div}$, given by Equation 6.18,

$$\Delta\tau_{div}(\theta) = \frac{D}{\beta c}\left(\frac{1}{\cos\theta} - 1\right), \tag{6.18}$$

where D is the distance from the gas jet to the TR screen, θ is the angle of the diverging electron.

The r.m.s. bunch length, $\sigma\tau_{div}$, is given by $\sigma\tau_{div} = \sqrt{\int(\Delta\tau_{div}(\theta) - \mu)^2 p(\theta)\,d\theta}$, where $\mu = \int \Delta\tau_{div}(\theta)p(\theta)\,d\theta$ and $p(\theta)$ is a probability distribution function. Figure 6.14 shows the r.m.s. length of a 90 MeV electron beam after 1m as a function of divergence, for a Gaussian angular distribution $p(\theta) = \frac{1}{\sqrt{2\pi}\sigma\theta}e^{\frac{-\theta^2}{2\sigma\theta^2}}$, where $\sigma\theta$ is the r.m.s. divergence. It should be noted that this does not take into consideration the effects of magnetic quadrupoles.

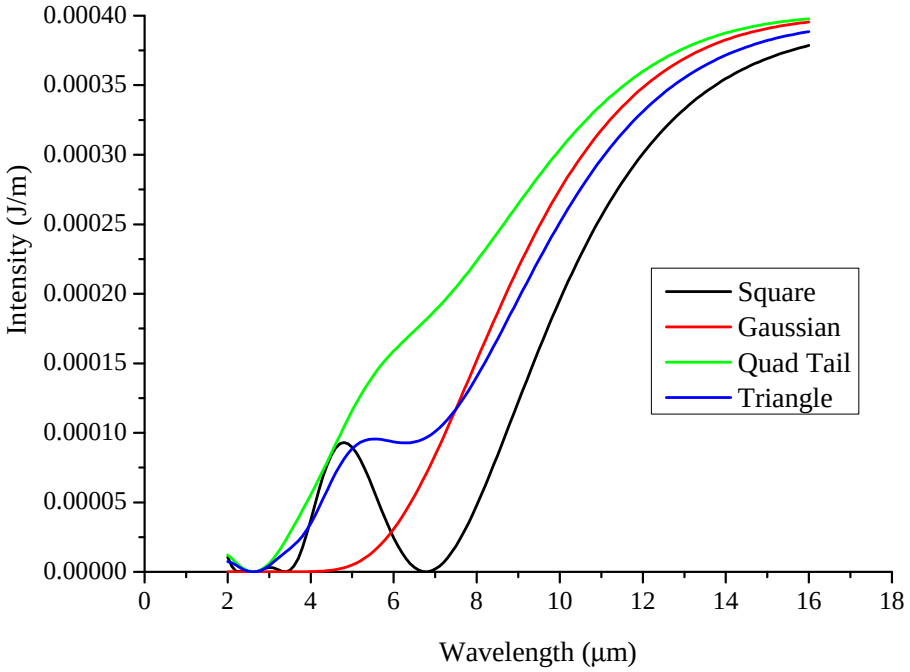

Figure 6.13: TR spectrum for several bunch shapes (Figure 6.8) from a two foil system (including angular spread and bunch width).

Effects of Energy Spread

As the electrons travel from the gas jet to the TR screen, faster or more energetic electrons will reach the screen first and the lower energy electrons will arrive after some delay. The delay between two electrons, $\Delta\tau_{energy}$, travelling with the fractions of the speed of light, $\beta(E)$, is given by Equation 6.19,

$$\Delta\tau_{energy}(E,\ \Delta E) = \frac{D}{c}\left(\frac{1}{\beta(E)} - \frac{1}{\beta(E+\Delta E)}\right). \tag{6.19}$$

where E is the energy of the primary electron and ΔE is the difference in energy to the second electron.

Figure 6.15 shows the delay between a primary electron of E = 90 MeV and a second electron of 90 MeV + ΔE (or delay between two electron bunches with these peak energies). A positive or negative ΔE represents a second bunch that moves faster or slower than the primary bunch respectively. The delay for negative ΔE tends to infinity at -90 MeV as the second bunch is stationary.

The r.m.s. length is given by $\sigma\tau_{energy} = \sqrt{\int(\Delta\tau_{energy}(E,\ \Delta E) - \mu_E)^2 p(\Delta E)\, d\Delta E}$, where $\mu_E = \int \Delta\tau_{energy}(E,\ \Delta E) p(\Delta E)\, d\Delta E$ and $p(\Delta E)$ is a probability distribution func-

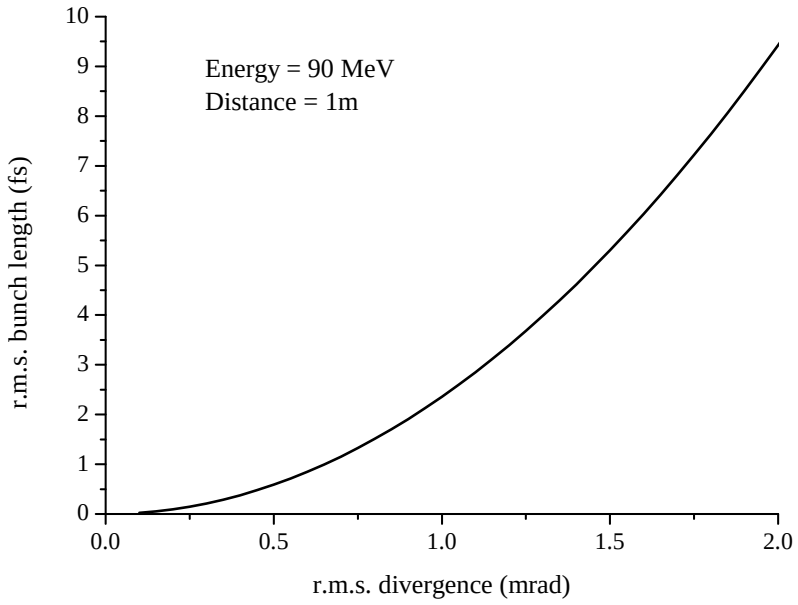

Figure 6.14: r.m.s. bunch length after 1 m for a 90 MeV electron beam as a function of beam divergence.

tion. Figure 6.16 shows the r.m.s. length of a 90 MeV electron beam after 1m as a function of energy spread for a Gaussian angular distribution $p(\Delta E) = \frac{1}{\sqrt{2\pi}\sigma_E} e^{\frac{-\Delta E^2}{2\sigma_E^2}}$, where σ_E is the r.m.s. energy spread.

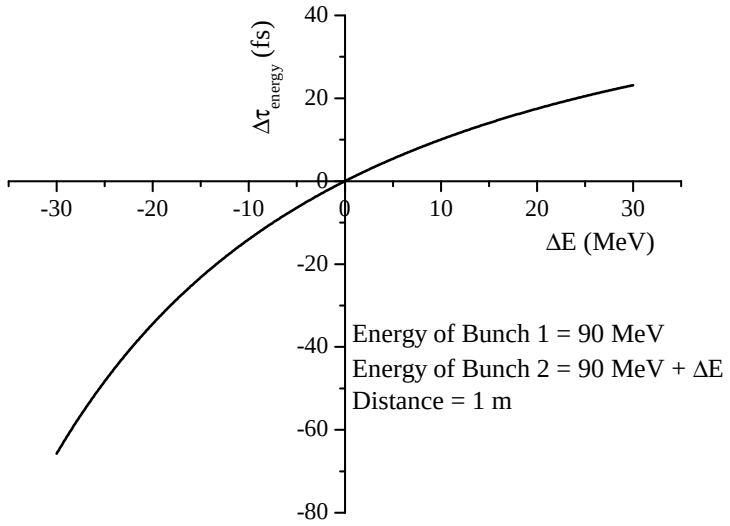

Figure 6.15: Effects of energy difference, ΔE, on bunch separation

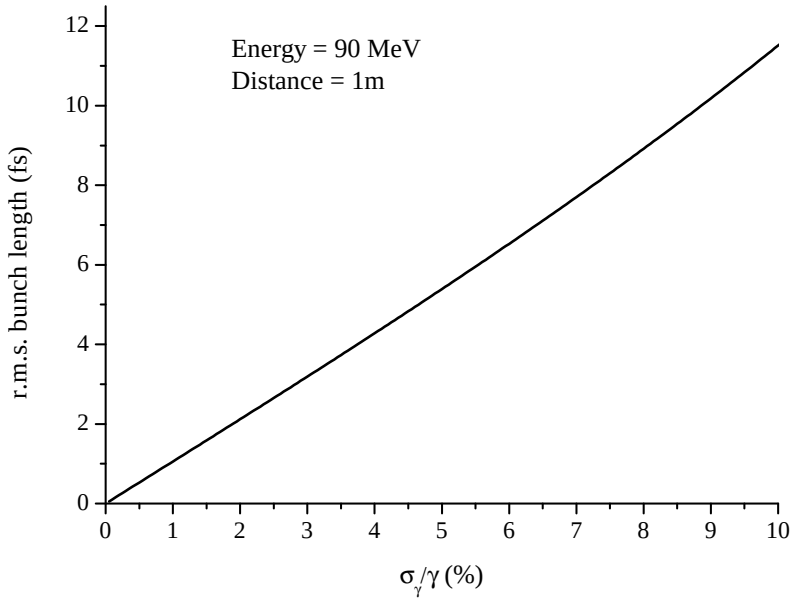

Figure 6.16: Effects of energy spread, σ_γ/γ, on r.m.s. bunch length.

6.3 Experimental Set-up of Transition Radiation Measurement

6.3.1 Two Foil Set-up

The electrons are first created in the gas jet. Permanent magnetic quadrupoles are placed into the beam line and used to transport the electrons down the beam line. As before the electrons are first optimised on LANEX 1, before this screen is removed, and the electrons allowed to travel through to the metal foils. The metal foils are placed at the end of the accelerator chamber before the electromagnetic quadrupoles which are used to transport the electrons down to the electron spectrometer as is shown in Figure 6.17. The TR optics and optical spectrometer are placed on a breadboard on top of the quadrupoles.

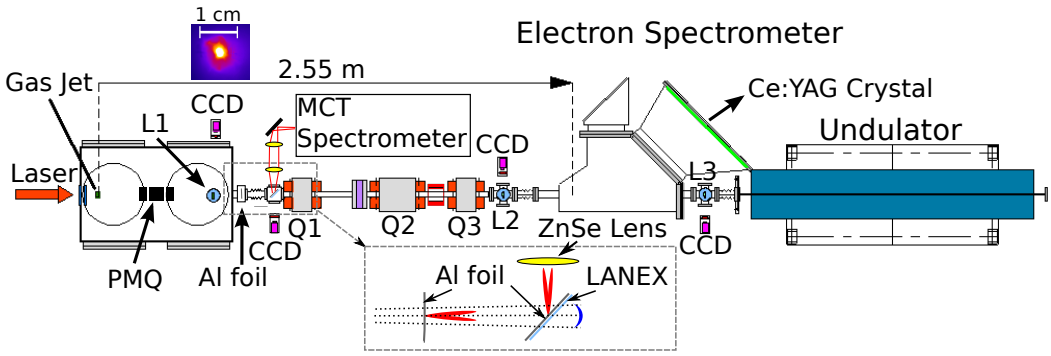

Figure 6.17: ALPHA-X experimental set-up: a high powered laser is focused onto a gas jet to produce mono-energetic electrons. The electrons are imaged on three LANEX targets and focused into an electron spectrometer by a quadrupole triplet magnetic lens.

A two foil system was used as shown in Figure 6.18. The first of the two foils consisted of a 25 μm Mylar pellicle for strength, between three 10 - 15 μm aluminium foils. The first acts as a laser beam block, stopping the high powered laser saturating or destroying any detectors further down the beam line. To do this the foil is mounted in a gate valve to ensure that there is no laser light leakage around the outside of the foil. The gate valve can also be opened to allow the alignment HeNe laser through to the TR optics. The laser block foil also serves as the first source of the TR.

The second foil's primary purpose is as a source of transition radiation. The foil also requires to be of optical quality to enable it to be used as a mirror for the alignment HeNe laser. A mirror was unsuitable as the thickness of the glass base would destroy the electron beam, preventing any useful information from being gathered from the LANEX screen. A 25 μm thick Mylar pellicle was used as a substrate for a 1 μm

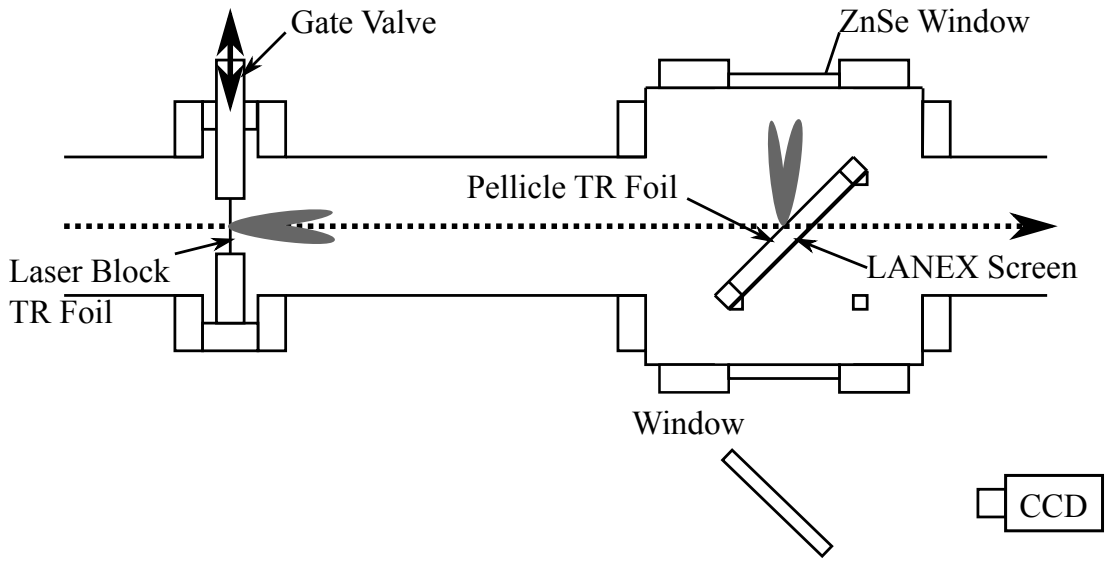

Figure 6.18: The two foil set-up of the transition radiation experiment. TR foil 1 and laser block is mounted in a gate valve so that it can be removed. Pellicle TR foil 2 mounted in front of a LANEX screen and removed out of the page in this figure. TR sent out of the vacuum through a zinc selenide window (ZnSe). LANEX screen imaged with a Flea CCD through a window.

thick deposition of aluminium. This thin mirror requires optical qualities to deliver the HeNe laser for alignment and allow the electrons through to the LANEX for imaging. The separation between the two foils is 16 cm.

The LANEX screen is placed on the reverse side of the pellicle and imaged with a 12 bit Flea camera. This LANEX screen will scatter the electrons, increasing their emittance and prevent them from being delivered to the electron spectrometer. Therefore, both the pellicle and LANEX screen are mounted on a pneumatic, vacuum feed through, pop-in target and this enables them to be completely removed from the beam line. Figure 6.18 provides a more detailed layout of the two foil system.

6.3.2 TR Detection

Lenses

Two ZnSe lenses are used to collect and focus the TR from the two foil system which exits the vacuum through a ZnSe window as shown in Figure 6.19. ZnSe was used du to its uniform transmission over a large bandwidth as shown in Figure 6.20 (Edmund, n.d.). Both lenses have a diameter of 2.5 cm. The first lens has a focal length of 25 cm and the second has a focal length of 20 cm. The two lenses are set-up to image the pellicle foil onto the entrance to the spectrometer and has a demagnification of 0.8.

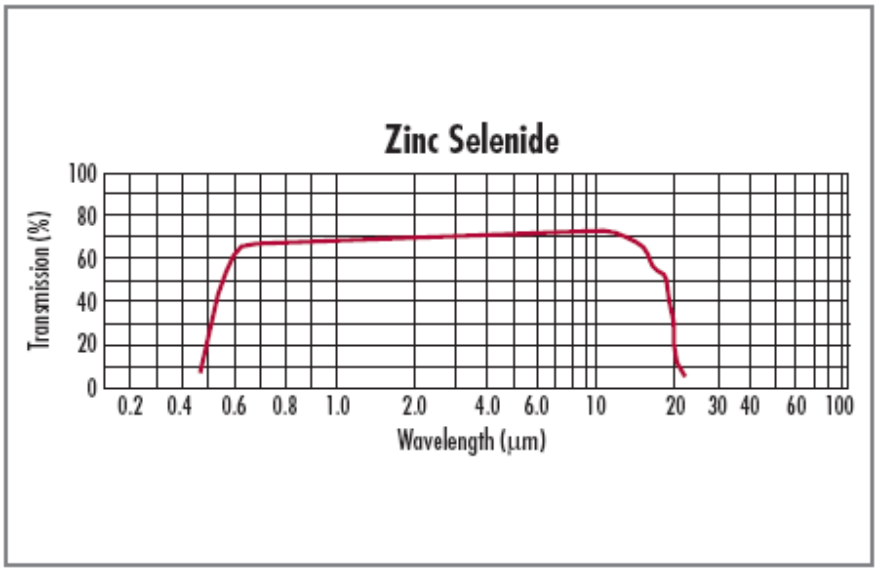

Figure 6.19: ZnSe Transmission curve.

Fraction of Signal Measured by the Detector

The optical beam transport has been calculated for a path through the four focusing optics (two before the spectrometer and two inside the spectrometer). The waist of the electron bunch is used as the source waist, w_0, of the radiation at all wavelengths, thus the shorter wavelengths are less divergent than the longer wavelengths. The beam width, $w(z)$, and radius of curvature, R(z), for the phase front of a Gaussian beam (which can be assumed because of the angular spread of the electrons which causes a Gaussian far field distribution, shown in Figure 6.11) is calculated using (Kraus, 1990),

$$w(z) = w_0 \left(1 + \left(\frac{z}{Z_{RL}}\right)^2\right)^{\frac{1}{2}}, \tag{6.20}$$

$$R(z) = z \left(1 + \left(\frac{Z_{RL}}{z}\right)^2\right), \tag{6.21}$$

$$Z_{RL} = \frac{\pi w_0^2}{\lambda}, \tag{6.22}$$

where z is the propagation direction, Z_{RL} is the Rayleigh length and λ is the wavelength. The angle of the radiation at z is given by $w(z)/R(z)$. As the light interacts with a focusing optic the beams angle becomes, $w(z)/R(z) - w(z)/F(n)$, where $F(n)$ is the focal length of the lens (which is a function of the refractive index of the material, $n(\lambda)$.

After the lens, the distance to the focal point is given by solving Equations 6.20,

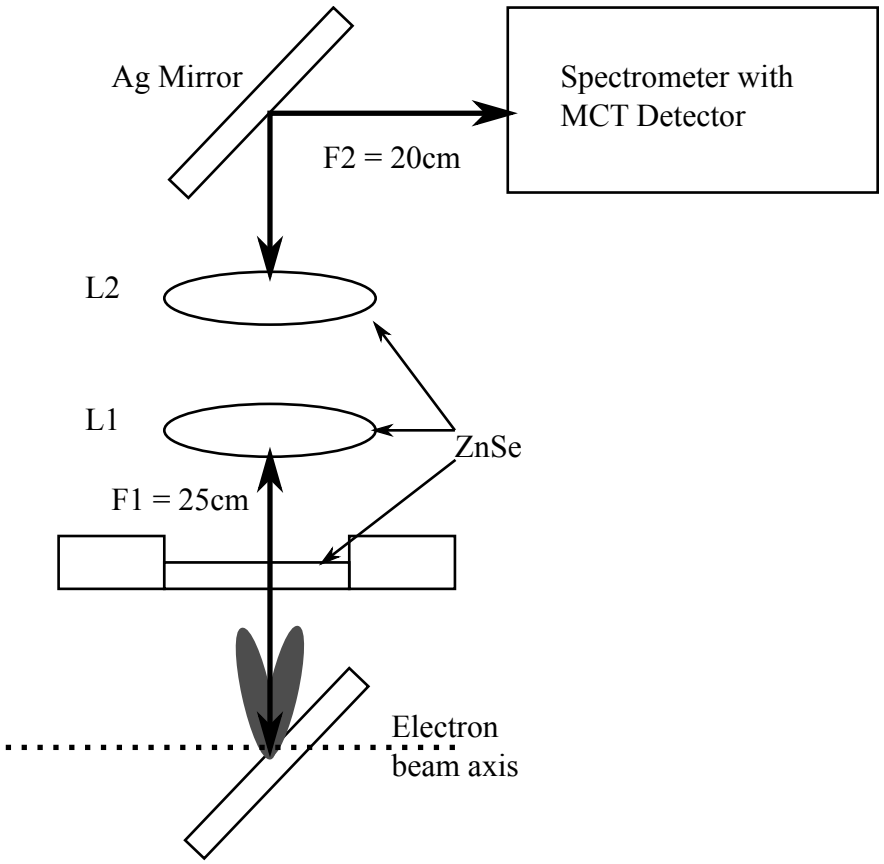

Figure 6.20: Lens set-up used to gather the TR into the spectrometer.

6.21 and 6.22 for z,

$$z = \frac{R}{\left(\frac{R^2\lambda^2}{\pi^2 w^4} + 1\right)}, \tag{6.23}$$

where R and w are the radius of curvature and width of the beam immediately after the lens. The Rayleigh length is found from Equation 6.21,

$$Z_{RL} = z\left(\frac{R}{z} - 1\right)^{\frac{1}{2}} = \frac{zR\lambda}{\pi w^2}. \tag{6.24}$$

These parameters are then used as a new source for the next lens. The distance from the focus point lens 1, z1, to lens 2, z2, is given by z2 = d + z1 where d is the distance between the two lenses. z2 is used as the new source in Equation 6.20 and 6.21 and the process repeated. After the fourth focusing optic, the width of the beam as a function of wavelength at the detector position for various source widths can be calculated. This is shown in Figure 6.21, here the $1/e^2$ width of the intensity (equal to 2σ) is used in the calculation.

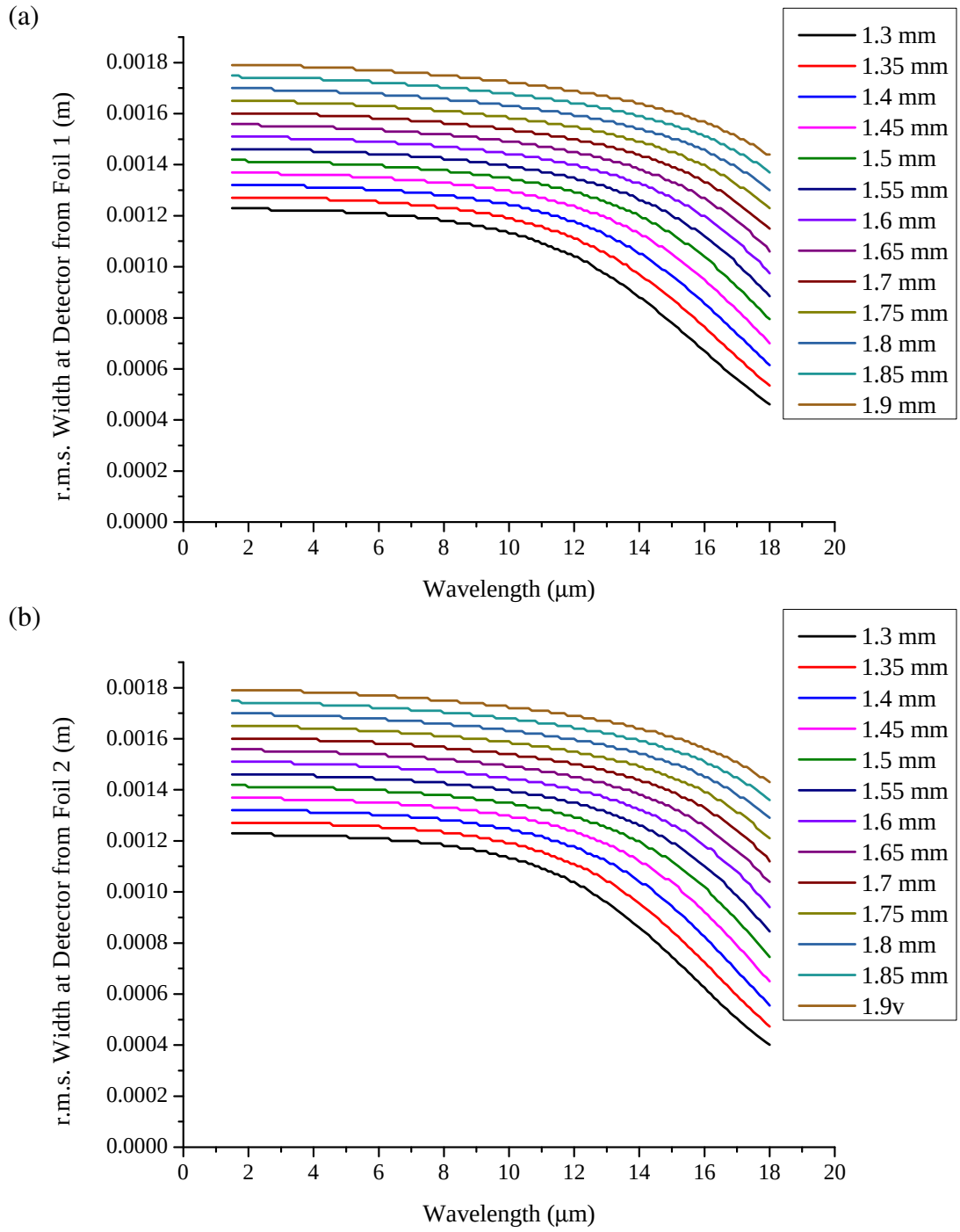

Figure 6.21: TR beam width at the detector from the two foils

Any increase in the width of the beam on the x-axis will result in a loss of signal if it is greater then the detector width. However, a horizontal increase will result in an increase of the system resolution, giving a reduction in the signal at the central wavelength (for a particular spectrometer setting) but an increase in signal which would otherwise have missed the detector, i.e. the overall signal intensity will remain the

same. However it will be averaged over a larger wavelength range. The energy of the signal is therefore given per unit of wavelength measured from the ideal spectrometer resolution, given by,

$$\frac{d\lambda}{dx} = \frac{1}{nFl}, \tag{6.25}$$

where $d\lambda$ is the resolution, dx is the length over which the signal is measured, i.e. the detector width of 1 mm, n is the diffraction order, F is the focal length of the spectrometer and l is the line density of the grating. For the system used in the experiment the ideal resolution is 0.05 μm. The fraction of signal measured, F_{signal}, in the vertical direction is given by using a normalised Gaussian distribution with the width shown in Figure 6.21 and integrating the Gaussian distribution over the width of the detector gives,

$$F_{signal} = Erf\left[\frac{D}{2\sqrt{2}\sigma}\right], \tag{6.26}$$

where Erf is an error function, D is the detector width and sigma is the r.m.s. width of the TR radiation. The fraction of TR measured is shown for various initial beam waists in Figure 6.22.

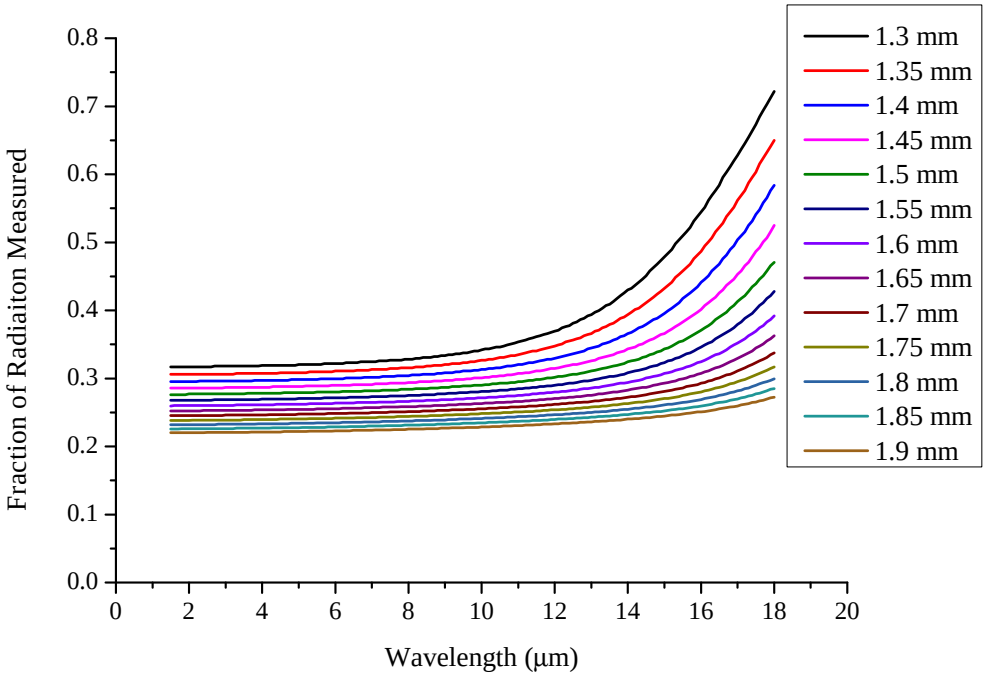

Figure 6.22: Fraction of TR beam measured by the detector

Figure 6.23 includes the effect of losses due to optical mismatching for the TR spectra shown in Figure 6.13. Here the spectra are shown for the four bunch shapes for

the TR emitted from the two foil system, including losses due to light not gathered by the detector. This spectra is calculated for a 1.25 mm bunch width, 3 mrad divergence, 16 cm foil separation and 89 MeV electron bunch.

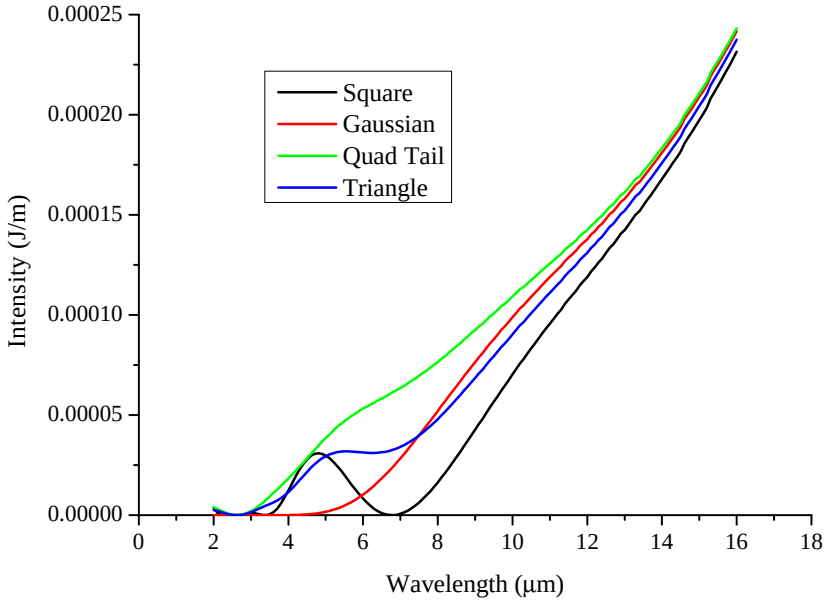

Figure 6.23: TR spectrum for several bunch shapes (figure 6.8) from a two foil system including fraction of beam measured.

Spectrometer

To measure the spectrum of the TR, an Oriel MS127i spectrometer was coupled with a mercury cadmium telluride (MCT) infra-red detector. Two gratings were utilised to cover the full spectrum. The longer wavelength grating has 75 lines/mm and is blazed at 8μm, this grating is suitable from $\sim 5.5\ \mu m - 20\ \mu m$. The shorter wavelength grating has 150 lines/mm, blazed at 5 μm and is suitable from $\sim 2\ \mu$m $- 6.5\ \mu$m. To maximise the gathered light into the spectrometer a large input slit of 5mm was used, sacrificing the resolution. Despite the large input slit the low number of lines/mm of the grating meant that the resolution remains $\pm 0.3\ \mu$m for the 75 lines/mm grating. A range of long pass filters was used to prevent higher orders of the shorter wavelength light being re-measured at longer wavelengths. The transmission of the filters used are shown in Figure 6.24 and these were measured using a Fourier transform infra-red spectrometer (FTIR).

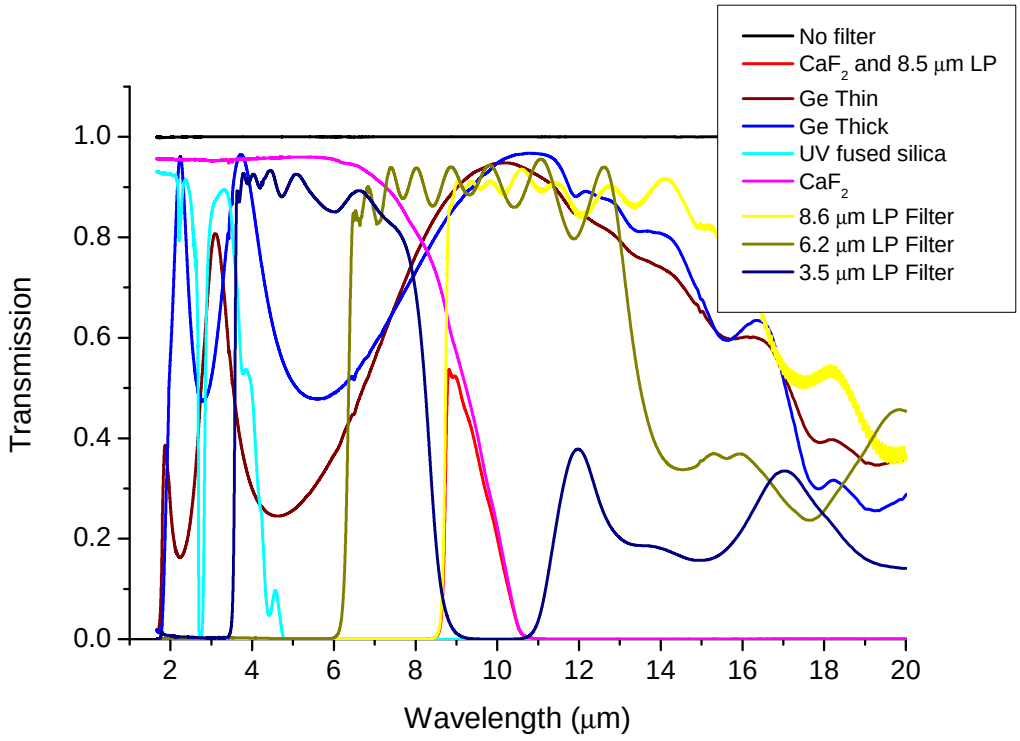

Figure 6.24: Transmission spectra of the filters used in the TR set-up, measured with an FTIR.

An alignment HeNe laser, co-propagating with both the 800 nm laser and the electron beam, is reflected off of the pellicle TR foil and used to align all the optics for the transition radiation, including the spectrometer. The higher orders of the HeNe laser from the grating in the spectrometer are used to calibrate the wavelength of the TR

being measured and ensure accurate alignment onto the MCT.

The spectrometer acts as a monochromator because the MCT is a single element detector. In order to measure the full spectrum each wavelength has to measured separately. 100 shots were typically measured at a wavelength, the spectrometer set to a new wavelength using the HeNe laser, and the process repeated (replacing the long pass filter as necessary).

6.3.3 TR Calibration

Absolute Sensitivity of the MCT

A 1.9 μm pulsed laser was used to calibrate the total energy measured by the MCT. The laser beam was collimated and passed through a beam splitter to send part of the beam onto a reference diode and the rest to the MCT for calibration. A power meter with a sensitivity of 10 μW over $0.3-11$ μm, was placed in front of the MCT and used to calibrate a reference diode. The high sensitivity of the power meter meant that no objects could be placed near it (IR emitted from an object creates a false signal) and for that reason the power meter, without the focusing lens, was used for the calibration. The lens used to focus the light into the MCT was anti-reflection coated for 1.9 μm, therefore keeping losses to a minimum $(< 2\%)$. The diode was calibrated for maximum power range of the laser, the laser's pulse duration was set to give maximum average power at 100 ns (for more accuracy on the power meter). The pulse length was noted for each power of the laser to allow conversion to peak power on the diode. The laser power was tuned by adjusting the pump power. Calibration of the diode is shown in Figure 6.25.

The diode was then used to determine the energy of the laser. The pulse length of the laser was reduced $(\text{to} \sim 50 \text{ ns})$ to minimise the energy and reduce the signal to shorter than that of the MCTs response time. The MCT would be acting as a power meter (i.e. peak power averaged over its 100 ns response time). 7 filters were used, each filter has a transmission of 29% giving an overall transmission of 0.297^2 = 0.000172. Figure 6.26 demonstrates the calibration of the MCT detector providing the voltage output for an input radiation energy. The fit should pass through zero, there is however a 0.39 pJ offset which is low compared to the scale $(\sim 1-2\%)$.

Spectrometer Sensitivity Calibration

Due to the large bandwidth of the spectrum it was essential to calibrate each wavelength for sensitivity. To do this an Oriel Infrared Element black body source was used. The black body source was set to a known temperature by fixing the voltage ap-

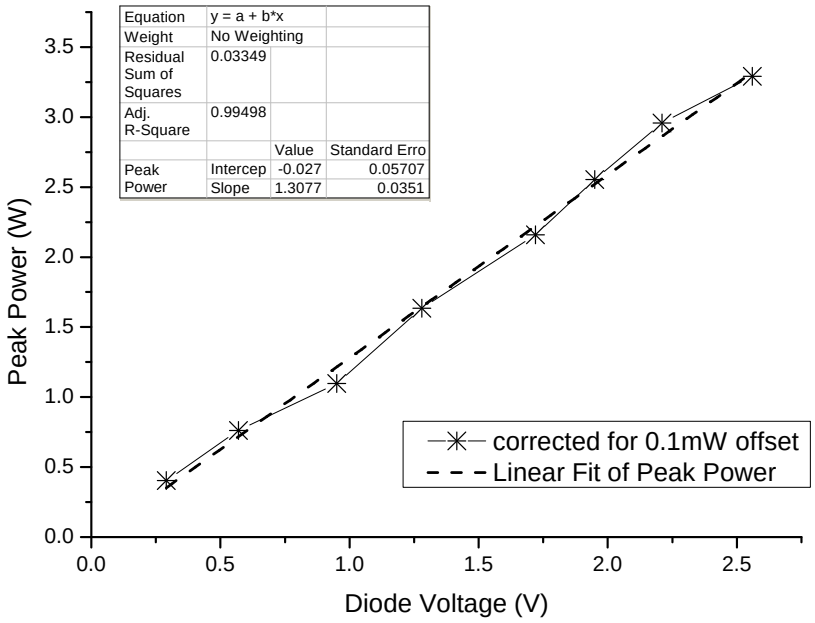

Figure 6.25: Diode calibration curve.

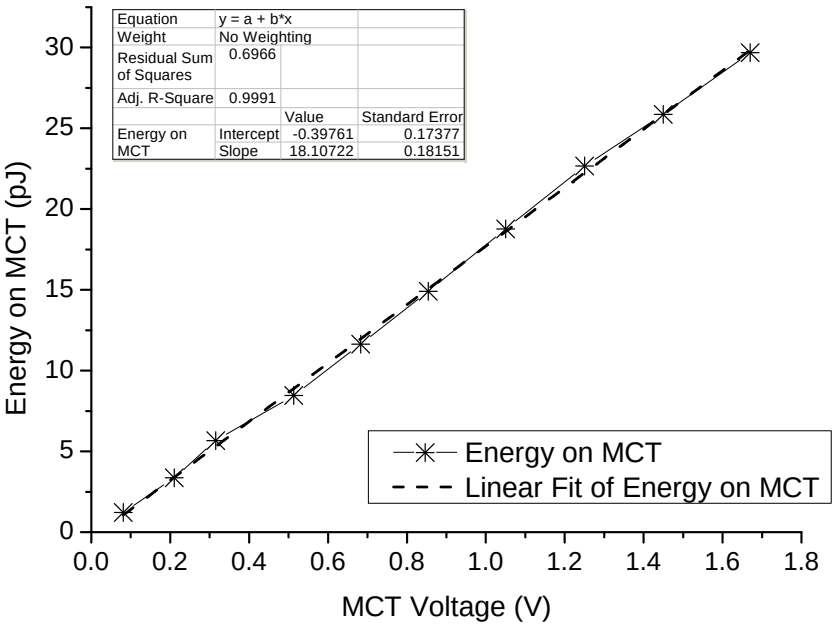

Figure 6.26: MCT calibration curve.

plied to it. The black body was placed next to the spectrometer entrance and the light was passed through a chopper to create a pulsed source. The same order sorting filters were used for the appropriate wavelength as was in the experiment, which consist of a germanium window and a 3.5, 6.2 and 8.6 μm long pass filter as shown in Figure 6.24. The signal was measured through a lock-in amplifier to obtain a clear signal below the noise level. The black body source was too weak to be able to send the light through the three ZnSe optics, however, the transmission through the optics is uniform for the spectra obtained here.

Figure 6.27 shows the calibration curve for the spectrometer normalised to 8.2 μm, the blaze of the 75 lines/mm grating. The curve is as expected from the known properties of the grating and detector. The calibration also takes into account the differences between the two gratings.

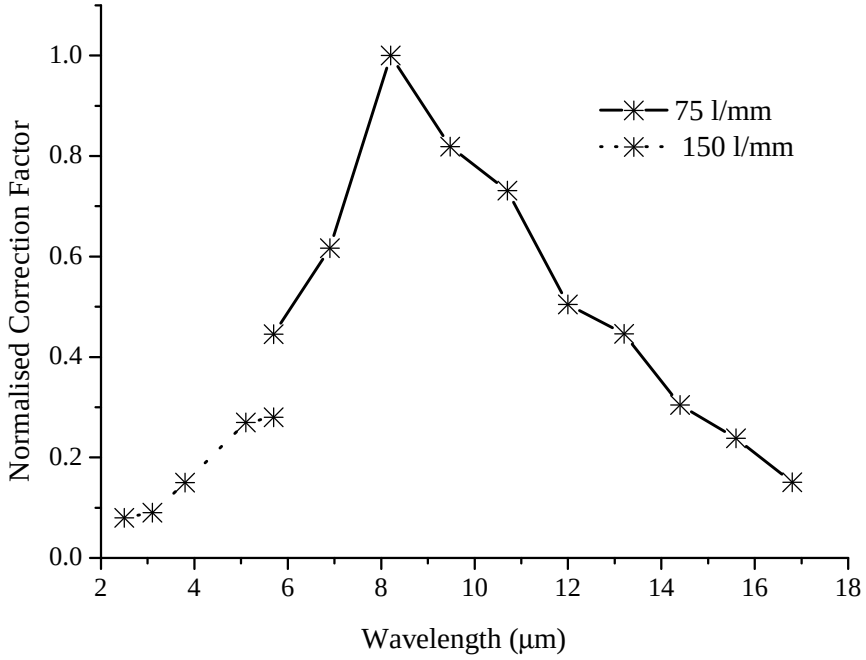

Figure 6.27: Black body calibration curve of the spectrometer for both the short and long wavelength gratings.

6.4 Experimental Results

6.4.1 Analysis Techniques

Electron Beam Profile

As is described in Section 6.18 the electron beam profile is measured on the LANEX screen simultaneously with the TR signal. To minimise the effects of shot to shot variations in the electron bunch, the shots are sorted for similar transverse properties. The images were first smoothed in the transverse distribution with a fast Fourier transform (FFT) which filtered background noise and allows the peak analysis software to operate more effectively. As shown in Figure 6.28, the FFT allows more accurate determination of the peak, however, the largest effect is to reduce the background noise which can otherwise falsely increase the r.m.s. spread of the distribution.

The properties used to sort the electron bunches are as follows:

- Peak position is used to ensure that only electron bunches with similar shot to shot pointing are used. If the electrons are too off-axis then their transition radiation will not make it to the detector.
- The r.m.s. spread on x and y (σ_x and σ_y respectively) is used to ensure the electron beams have a similar transverse emittance.
- The ratio of the r.m.s. spread (σ_x/σ_y) ensures the beam is not oval. (An oval beam consists of several electron beams.)
- Similarly to the individual r.m.s. spreads, the area ($\sigma_x \times \sigma_y$) is used to select like emittances as the source size and divergence are coupled together.
- The coherent transition radiation is proportional to the square of the charge, along with other properties of the electrons due to beam loading, therefore only similar charges within the electron bunch are used.

Electron Beam Selection

The transverse properties of the electrons (such as peak position and divergence) are plotted as a function of the transition radiation they produced, as shown in Figures 6.29, 6.30 and 6.31. This allows for the correlation of the transverse properties with the TR signal.

Figure 6.29 (a) and (b) show the relationship between the centre of the transverse distribution of the electron bunch and its production of measurable transition radiation.

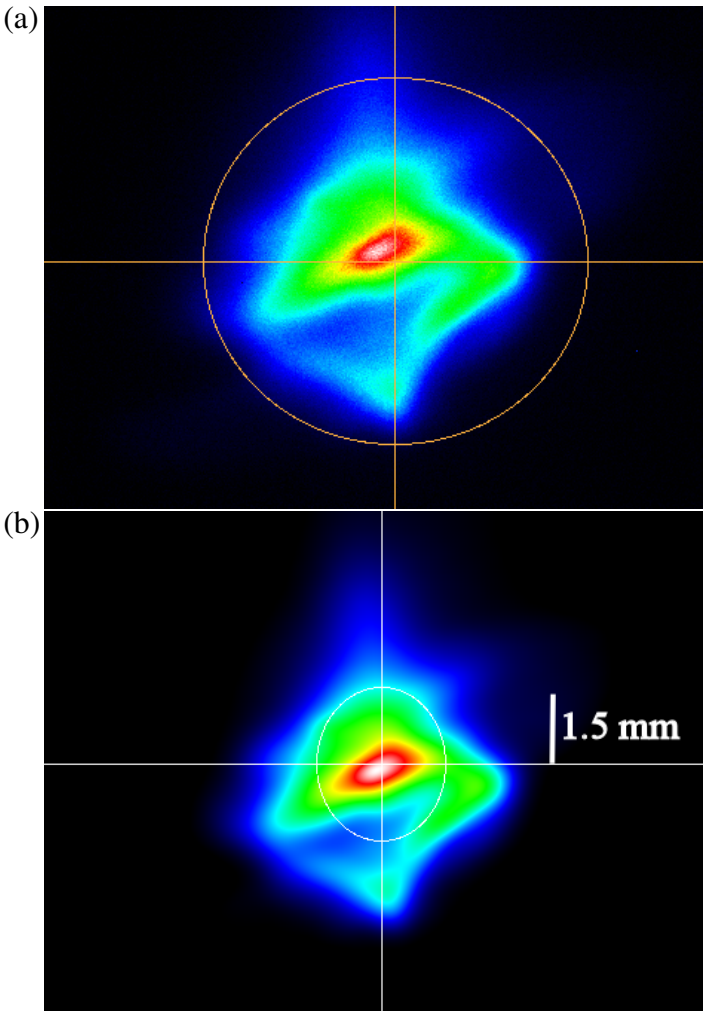

Figure 6.28: Two false colour images of the electron beam transverse profile with the identification of the distribution centre and r.m.s. spread for (a) no FFT filtering and (b) with FFT filtering. A linear colour scaling has been used.

The lenses image the foil onto the detector, therefore the distribution of the electrons is imaged as a distribution of radiation at the detector. If the electrons are too far off-axis then the TR will also be imaged off-axis, i.e. the radiation will miss the detector. The r.m.s. electron distribution on the X and Y axis are 1.5 ± 0.2 mm. This is reasonable considering that the average distribution of the electron bunches is 1.5 ± 0.2 mm also. This shows that there is quite a large distribution for which the detector will still be able to measure a signal.

Figures 6.29 (c) and 6.30 (d) show the relationship between the r.m.s. divergence of the electron bunches and the TR signal they produce. It can be clearly seen that if the electrons are too divergent or too narrow then they do not produce strong, detectable radiation. This may be because large transverse emittance can be produced at the same time as a large longitudinal emittance.

(a)

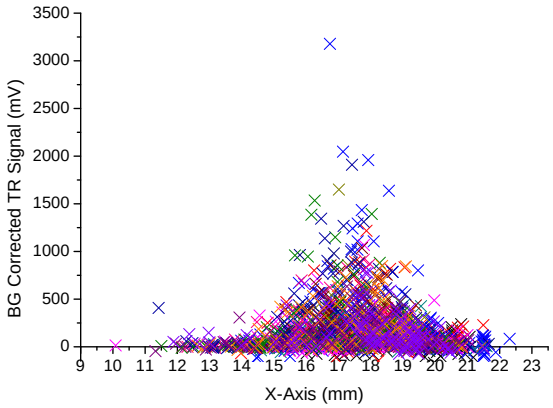

(b)

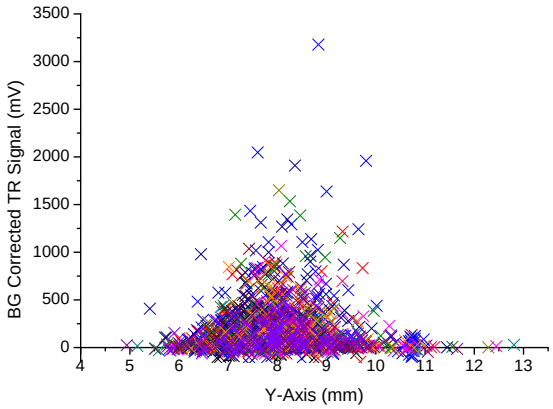

(c)

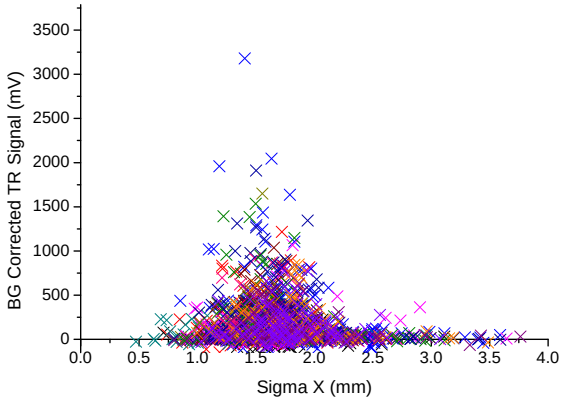

Figure 6.29: Transition Radiation signal as a function of transverse electron bunch parameter (a) distribution centre on X-axis (b) distribution centre on Y-axis (c) r.m.s. spread on X-axis. Demonstrates that there is a correlation with the beam's transverse parameter and TR signal and is the same for each wavelength. Combines with Figures 6.30 and 6.31.

(d)

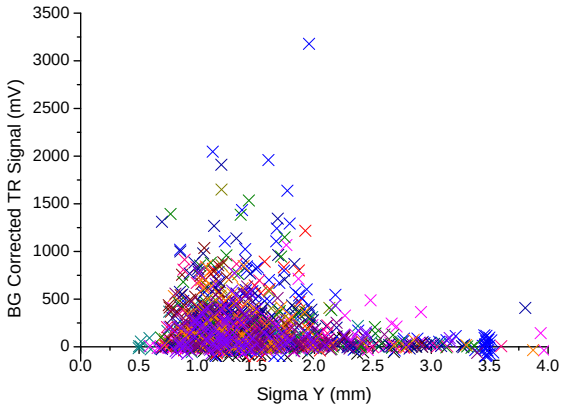

(e)

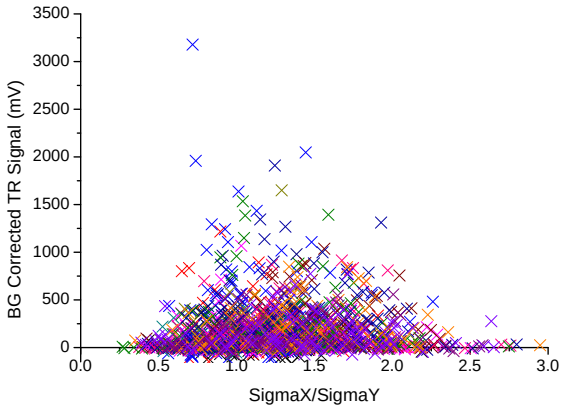

(f)

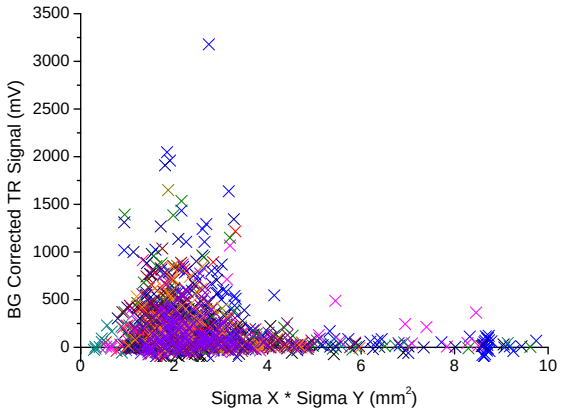

Figure 6.30: Transition Radiation signal as a function of transverse electron bunch parameter (d) r.m.s. spread on Y-axis (e) ratio of two r.m.s. spreads (f) area of beam. Demonstrates that there is a correlation with the beam's transverse parameter and TR signal and is the same for each wavelength. Combines with Figures 6.29 and 6.31.

(g)

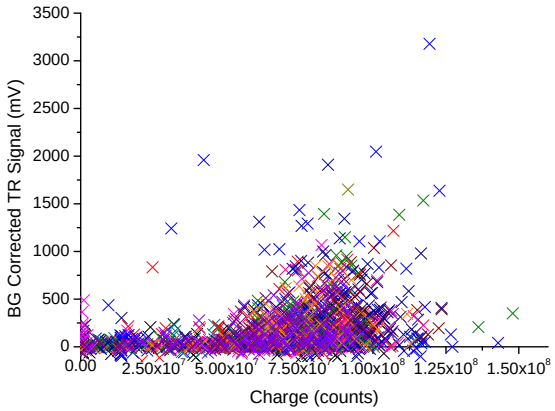

(h)

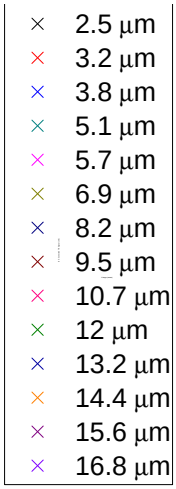

Figure 6.31: Transition Radiation signal as a function of transverse electron bunch parameter (g) charge inside the r.m.s. area (h) key. Demonstrates that there is a correlation with the beam's transverse parameter and TR signal and is the same for each wavelength. Combines with Figures 6.29 and 6.30.

Similarly, the r.m.s. spread ratios and r.m.s. area of the beam were used to select beams with similar transverse emittance, as shown in Figures 6.30 (e) and (f). Keeping the transverse properties as similar as possible should also keep the longitudinal properties as similar as possible.

Due to the strong dependency of the radiation on the charge within the electron bunch, it is important to use only electrons with a similar charge. Figure 6.31 (g) shows the increasing TR signal with increasing charge and demonstrates that if charge was not kept reasonably constant across the spectrum then it could produce false structures.

Once the range for a parameter had been selected, the same range was applied to all wavelengths. For example, on the X-axis any shot with a central distribution out side the range of 16.5 mm to 18.5 mm would be excluded. This range would then, in turn, be applied to all wavelengths. To ensure that this process was carried out without

any bias across all the wavelengths a plot of the mean and r.m.s. spread of each of the parameter was calculated across the spectrum, as shown in Figure 6.32.

The plots shown in Figure 6.32 are for the sort 1C shown in Table 6.3. These plots were made for each set of sort parameters, however only the plots for sort 1C are shown here.

It can be seen in Figure 6.32 that the mean and r.m.s. spread of each parameter is reasonably constant but with some random variations, which is to be expected. There is no periodic structure in any of the plots which could create a structure in the final spectrum. This shows that there is no biasing in the selection process, for example there is not a systematic or step increase in charge towards longer wavelengths which could give a false indication of the onset of coherent transition radiation.

It can also be seen that the electron parameter data for the radiation at 13.2μm does not always fit with the data for the other wavelengths. This is because the sorting process has reduced the number of shots to just 2. The average number of shots at each wavelength is typically 7 and 14 shots per data point (105 and 154 shots per spectrum) for the first and second spectrum respectively. It can be seen in the plot of the TR spectrum for this sort, that this wavelength does not fit with the rest of the data points and has a large error on the mean due to the few shots used to create this data point.

6.4.2 Transition Radiation Spectra

This section discusses two spectra (spectrum1 and spectrum 2) obtained during two separate experimental runs. Both of the spectra where measured with the small permanent magnetic quadrupoles in place. Spectrum 1 has the shortest wavelength transition radiation measured and therefore the shortest bunch length structure.

Spectrum 1

Spectrum 1 measures the shortest wavelength transition radiation. This section will show three different methods (sorts 1A, 1B and 1C) for sorting the data and that these spectra have the same general trend, although one sort method provides a smoother curve.

There are two main reasons for performing this data sorting. The first is to find the beam criteria which produces reliable TR, i.e. selecting beams which are on-axis and reject off-axis radiation. The second is to select similar profile electron beams, thus minimising shot-to-shot variations and producing a reliable average spectrum.

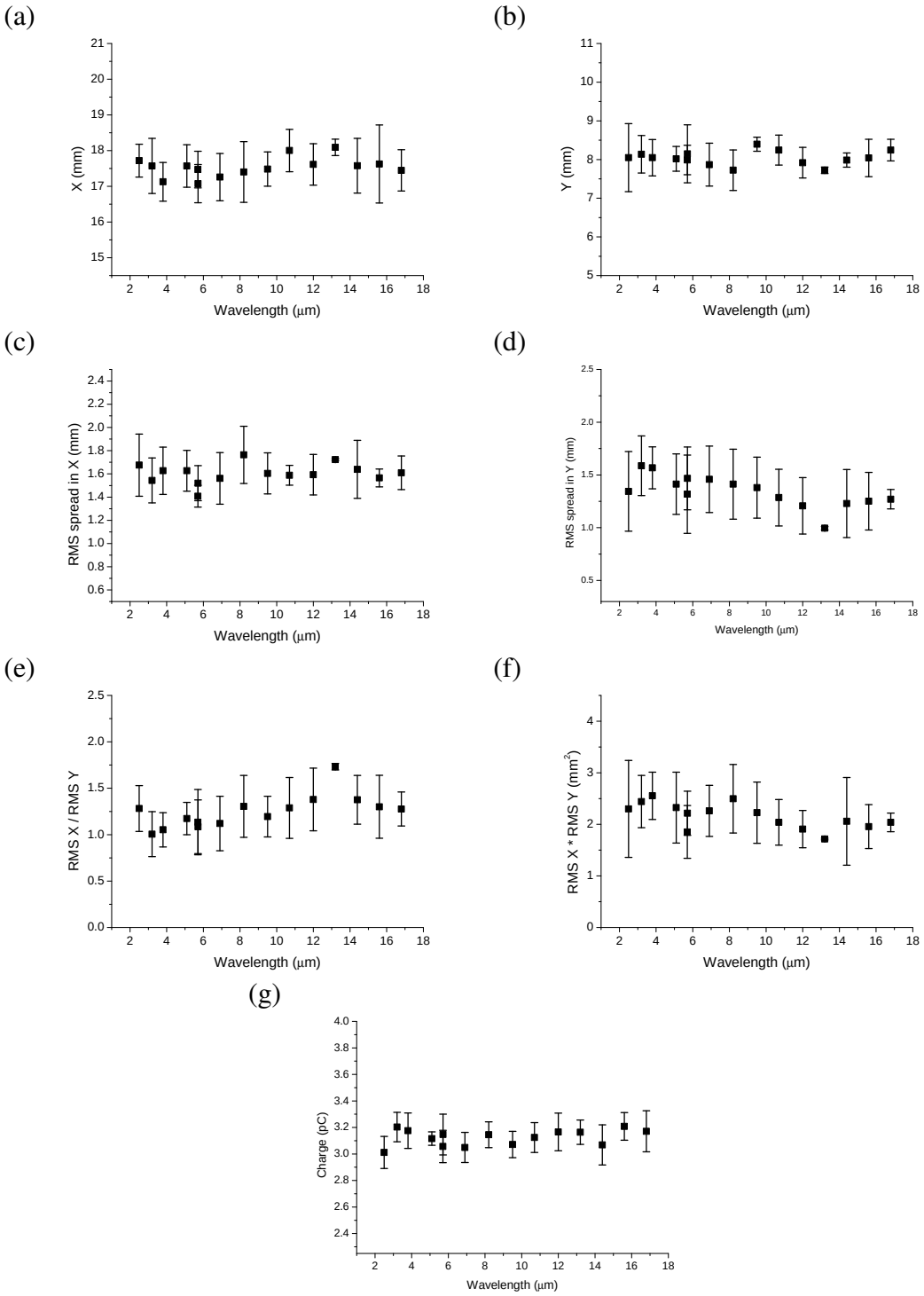

Figure 6.32: Transverse bunch properties of (a) x position, (b) y-position, (c) r.m.s. spread in x, (d) r.m.s. spread in y, (e) r.m.s. ratio, (f) area and (g) charge.

Sort 1A

This sort was achieved by initially focussing on one wavelength, specifically 8.2 μm, which is the blaze of the grating and therefore gave the strongest signal to noise ratio.

The sort parameters described in Table 6.1 filter the data at 8.2 μm so that it removed all noise shots and minimises the spread in TR signal. This sort parameter is then applied across all wavelengths.

As can be seen in Figure 6.33(a), this gave low scatter at 8.2 μm with a small error in the mean. There was still a reasonable variation in the size of the error bars and the data points did not fit a smooth curve. The sort serves to remove the noise shots from the spectrum and only select data corresponding to electron beams which produce radiation. However, it had failed to create a uniformity across the spectrum.

	Minimum	Maximum
X	15.84 mm	19.2 mm
Y	7.08 mm	8.64 mm
σ_x	0.72 mm	1.63 mm
σ_y	0.72 mm	1.63 mm
$\frac{\sigma_x}{\sigma_y}$	0.7	1.25
$\sigma_x \times \sigma_y$	0.23 mm^2	All
Charge	All	All

Table 6.1: Sort 1A: removed all shots which do not produce TR at 8.2μm and then was applied across the entire spectrum.

Sort 1B

This sort was created by fitting a Gaussian to each of the distributions shown in Figure 6.29. Only the shots with parameters inside the r.m.s. spreads were used. However, the distribution for both σ_x/σ_y and the charge are not a Gaussian. Therefore, a ratio of $1 \pm 50\%$ was used for σ_x/σ_y. All charge was accepted at this point. The standard deviation sort parameters are shown in Table 6.2.

Despite each data point in the spectrum having a small error in the mean, as shown in Figure 6.33(b), there was still a large shot to shot variation. The small error in the mean comes from the relatively large number of shots which make each of the data points. This sort leaves an average of 29 shots per data point. This is considerably more than sort 1A which left, on average, only 6 shots per data point. The large variations away from a smooth curve seen in this spectrum is understood when the average charge is looked at for each of the wavelengths, as in Figure 6.34. The sort fails to create a stability in the shot-to-shot variation in charge.

Sort 1C

This is shown in table 6.3. The sort includes quite a large range for most of the parameters and is similar to the r.m.s. sort parameters (sort 1B). However, sort 1C focuses

	Minimum	Maximum
X	16.2 mm	18.85 mm
Y	6.7 mm	9.67 mm
σ_x	1.15 mm	2.0 mm
σ_y	1.0 mm	2.0 mm
$\frac{\sigma_x}{\sigma_y}$	0.675	1.8
$\sigma_x \times \sigma_y$	1.5 mm^2	3.4 mm^2
Charge	All	All

Table 6.2: Sort 1B: sort parameters set by the standard deviation in each of the electron's transverse properties.

on using quite a narrow selection of charge. This will help to minimise the effect of variations in charge inducing large changes in the TR signal. Also, it will prevents any additional effects that charge variations could have on the electron bunch length.

Sort 1C is used in Figure 6.32, to create the example checks for uniformity. The wavelength to wavelength charge variations, were greatly reduced with this charge selection. Sort 1A gave and average charge of 2.96 pC with a standard deviation of 0.27 pC, the average scatter in charge at each wavelength is 1.15 pC. Sort 1B has a similar wavelength to wavelength charge variation of 0.23 pC on an average charge of 3.44 pC, the average spread at each wavelength is slightly reduced at 0.74 pC. Sort 1C has the most stable charge at just 0.06 pC across the wavelengths with a average charge of 3.1 pC. The sort was also more stable at each wavelength with an average scatter of 0.11 pC. This increased stability in the charge is demonstrated in Figure 6.34, where sort 1B and 1C are represented by black and red respectively. The points shows the average and standard deviation at each wavelength, and the average charge across the wavelengths is shown by the solid line and plus and minus one standard deviation is shown by the dashed lines. The red points show the 4 to 7 time stability increase and show why sort 1C gives the most stable spectrum.

	Minimum	Maximum
X	16.2 mm	18.6 mm
Y	6.72 mm	9.12 mm
σ_x	0.84 mm	2.16 mm
σ_y	0.84 mm	2.16 mm
$\frac{\sigma_x}{\sigma_y}$	0.5	2
$\sigma_x \times \sigma_y$	0 mm^2	4.32 mm^2
Charge	2.96 pC	3.34 pC

Table 6.3: Sort 1C: focuses on creating a narrow selection region for the charge.

Figure 6.35 shows the TR spectrum for sort 1C. The two data points at 5.7 μm

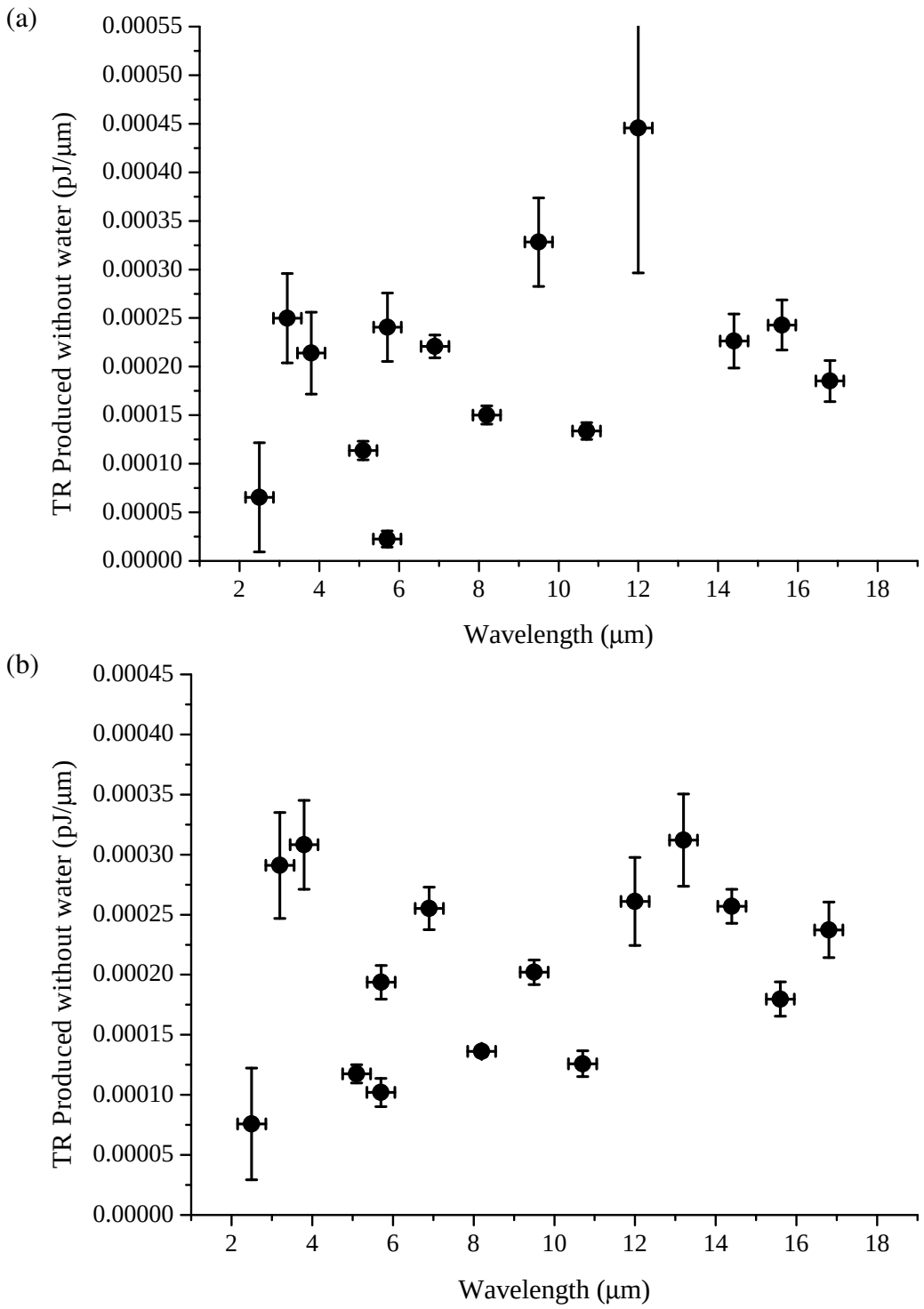

Figure 6.33: TR spectrum using (a) sort 1A and (b) sort 1B.

have been combined together. With sort 1C, the data point at 13.2 μm reduced to just 2 shots and therefore had an increased error so was removed. This spectrum shows quite a smooth curve with a clear dip in the spectrum at around $7-8$ μm, this is be discussed in more detail later in this section. This sort works well for most of the data

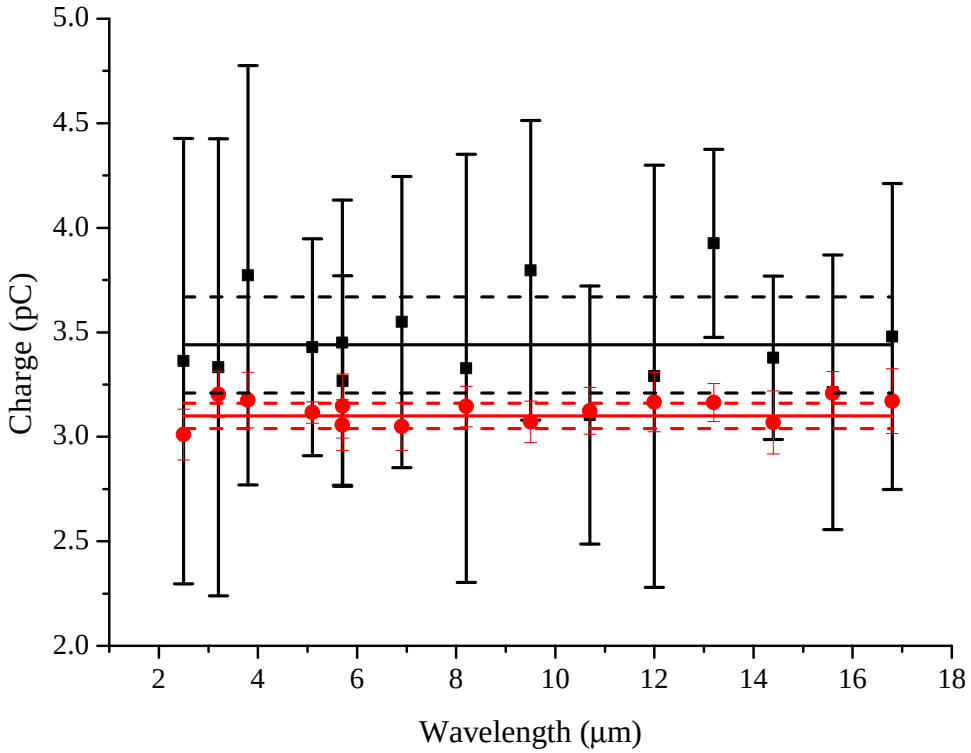

Figure 6.34: Distribution of charge across the spectrum for sort parameter 1B (black) and 1C (red). The average charge across the spectrum is shown by the solid line, with $\pm$ one standard deviation shown by the dashed line. Sort 1C has much lower scatter in the charge than 1B.

points, however, there are still some points where it is not successful. Most notably are the points at wavelength 13.2 μm and one of the points at 5.7 μm. As discussed earlier, 13.2 μm has not sorted well (as can be seen in Figure 6.32) and gives erroneous result due to the low number of shots remaining to make the data point. At 5.7 μm the two sets of data typically had similar values, however this sort region has not selected shots with transition radiation. It can be seen in Figure 6.33 that the other sorts demonstrate a similar signal level. The reduction in charge variation in Sort 1C reduced the average number of shots per data point to just 7.

As can be seen in Figure 6.35 there is a distinct shape to the spectrum (a peak around 4 μm, a dip around $7-8$ μm and a continuous rise to longer wavelengths). As discussed in Section 6.2.4, the shape of the spectrum is given by the Fourier transform of the longitudinal bunch shape. The Fourier transform of a single Gaussian bunch gives a single smooth curve, therefore to create structure there would have to be multi-

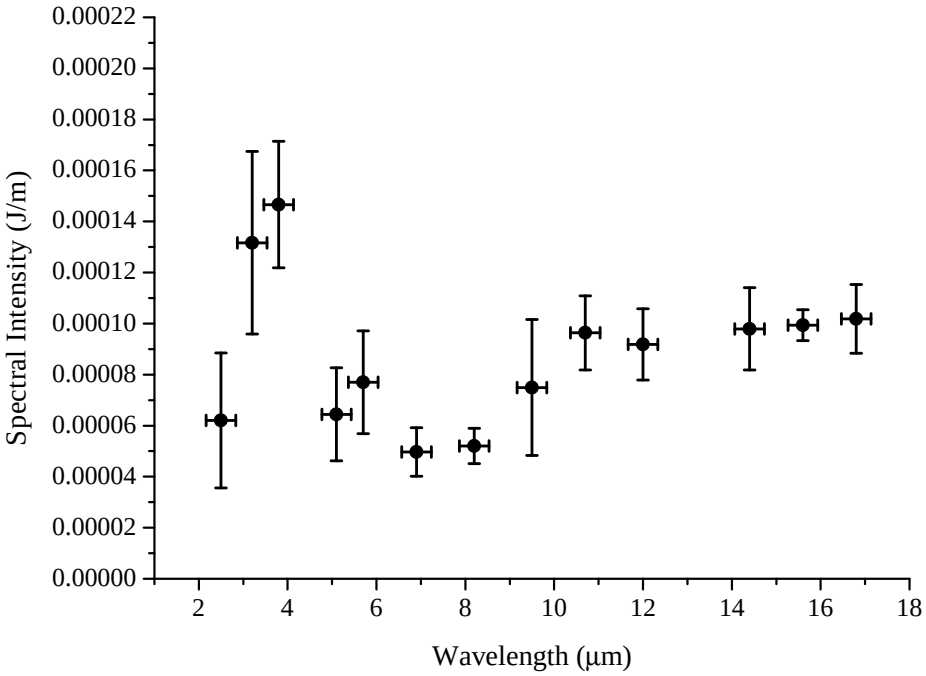

Figure 6.35: Spectrum from sort 1C, showing the smoothest spectrum due to the narrow range of electron charge.

ple peaks. For this spectrum the best fit comes from a short bunch which provides the peak at 3 μm. A longer bunch with much more charge will create the signal at longer wavelengths.

A structure in the electron bunch is required to create a fit for the structure seen in spectrum 1. A short duration bunch creates the coherent radiation at short wavelength whereas a longer duration structure creates longer radiation. To create the dip in the spectrum the long and short bunches must be separated so that they partially interfere at 7 μm.

Figure 6.36 shows the fit of a short (1.5 fs) bunch (green), a longer (5 fs) bunch (red) and combines the two bunches (5.9 fs - black). In this fit the bunch has a short (1.5 fs) "extreme" distribution followed 10 fs later by a longer (5 fs) Gaussian distribution. Other structures also fit this spectrum and this will be discussed further later. The short structure (green) clearly produces radiation at the short wavelength (2.5 to 4 μm) and continues to produce radiation through the dip (5 - 8 μm) but does not produce a high enough intensity at the long wavelength. However, the long structure does produce the correct long wavelength radiation and reduces in intensity at the dip. Simply combining the two structures, both centred at the same time, also combines

(a)

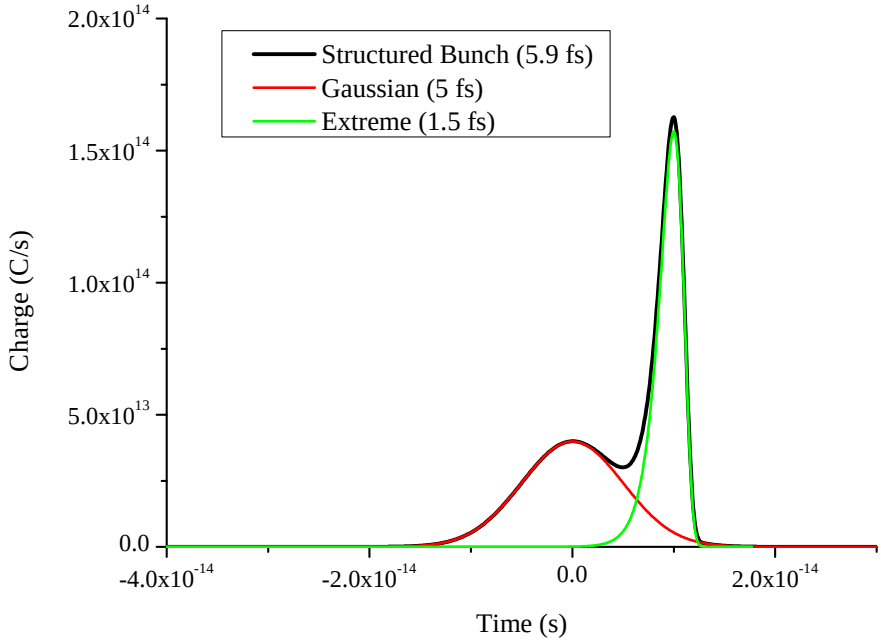

(b)

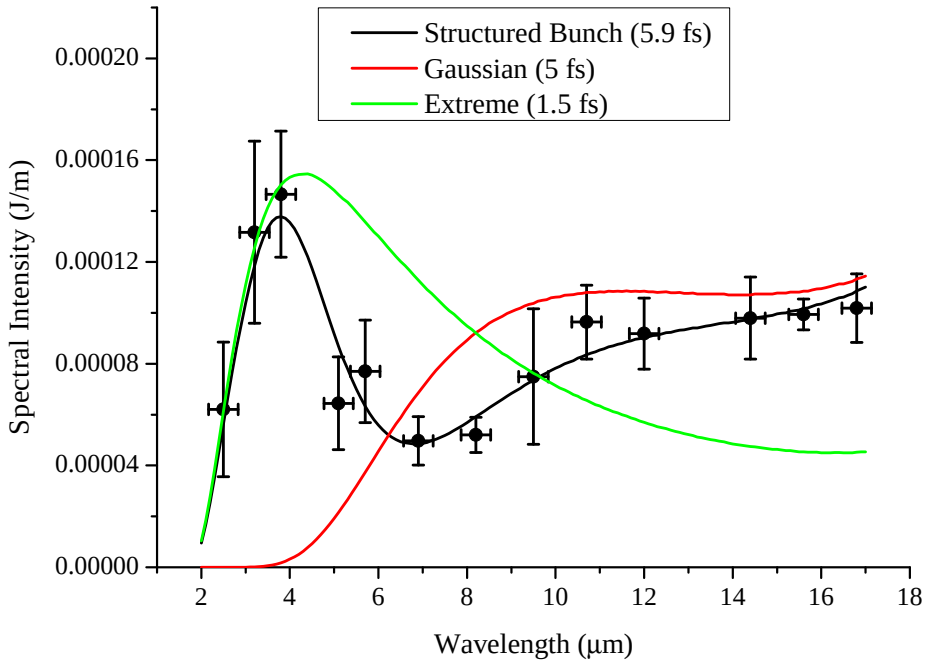

Figure 6.36: Electron bunch shape (a) and TR spectrum (b) for a short bunch (green) a long bunch (red) and the combined long bunch with a short structure (black).

their respective TR spectrum, creating a spectrum that fits well at the short and long wavelengths but does not drop in the dip. To create a spectrum that also fits the dip, the

long bunch must be delayed with respect to the short bunch by approximately 10 fs. This brings the front of the two bunches in line with creating the bunch shape which rises sharply in the front and dropping in the tail. (It should be noted that the bunch shape could be flipped in time, starting with the long bunch and finishing with the short bunch, as the spectrum is the Fourier transform of the peak but only one orientation is shown here.)

Effects of Varying the Bunch Shape

As discussed previously, to calculate the TR spectrum measured requires a structured electron bunch containing a short bunch and longer bunch separated by approximately 10 fs. Previously a short extreme bunch, followed by a longer Gaussian bunch where used, however it is possible to create a good fit with other shapes. Most short structures can be used as they only contribute to the first couple of data points on the spectrum. The Fourier transform of the long bunch, on the other hand, is required to drop to a low signal at approximately 6 μm so that the dip can be created. As is shown in Figure 6.8 symmetric structures (such as the square, Gaussian or extreme peak) drop to a low signal, whereas asymmetric structures (like the triangle, quadratic tail or exponential tail) more gradually drop to zero intensity. The gradual drop of the asymmetric bunch acts to fill the dip in the TR spectrum and thus does not create a good fit. Therefore, the long bunch is required to be, at least, quasi-symmetric. The fit of several structures is shown in Figure 6.37 with the details of each of the plots given in table 6.4.

Colour	Long Bunch (r.m.s. length)	Short Bunch (r.m.s. length)	Total r.m.s. length
Black	Gauss (5 fs)	Gauss (1.5 fs)	6.2 fs
Red	Gauss (5 fs)	Extreme (1.5 fs)	5.9 fs
Green	Gauss (5 fs)	Exponential (1.7 fs)	5.8 fs
Blue	Triangle (4.3 fs)	Exponential (1.7 fs)	5.5 fs

Table 6.4: Bunch shapes used in Figure 6.37, the two bunches are seperated by 10 fs.

All of the wide range of shapes fit the spectrum well. It is important to note that the variation in shape has little effect on the bunch length. All of the short bunches are 1.6 ± 0.2 fs and the long bunches are 5.0 ± 0.7 fs with a combined r.m.s. length of 5.8 ± 0.4 fs. The charge for each of the bunches also remain constant at 1.3 ± 0.2pC with $55 \pm 5\%$ of the charge in the long bunch.

(a)

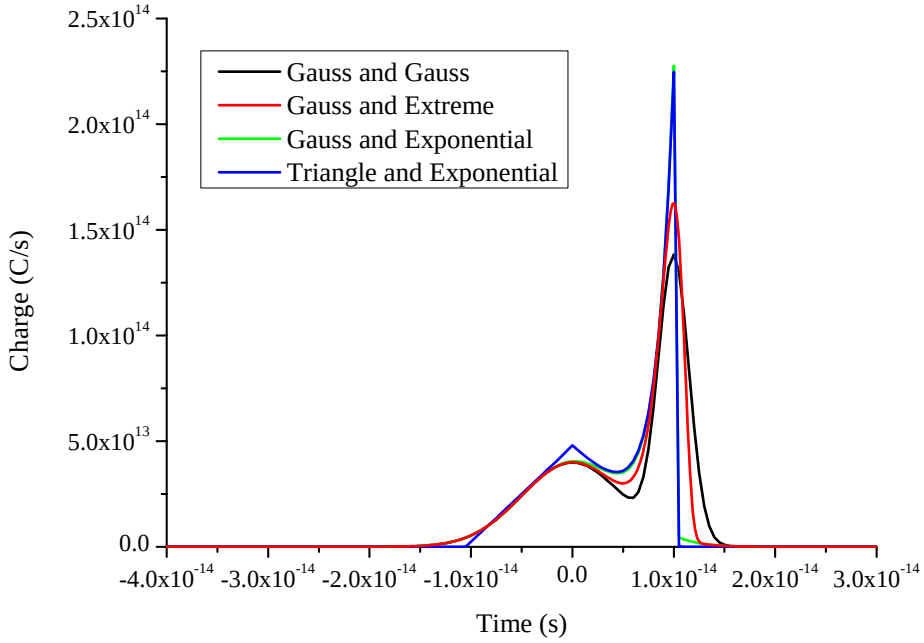

(b)

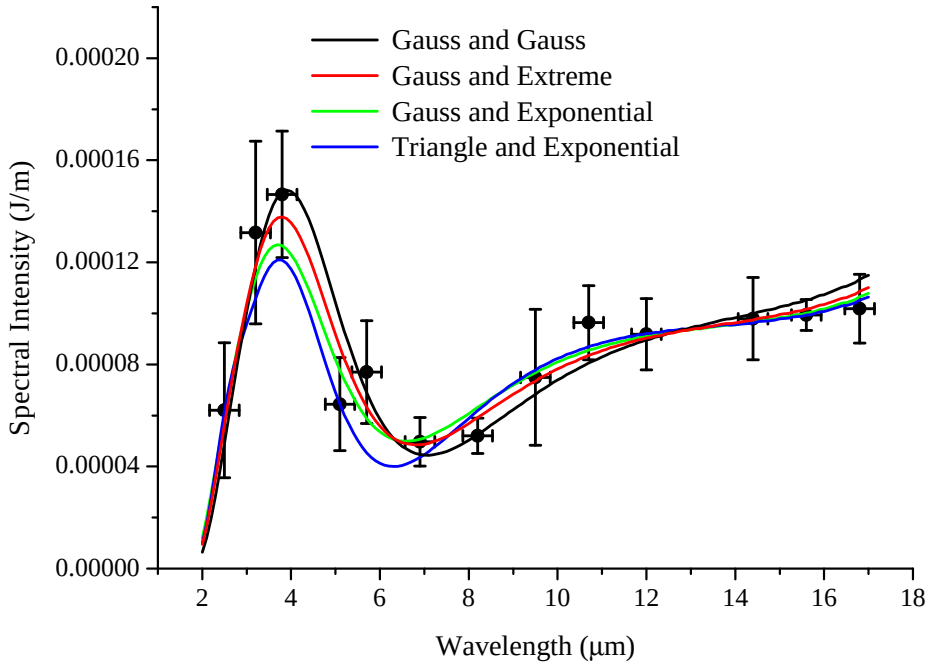

Figure 6.37: Varrious bunch shapes (a) and their TR spectrum (b).

Effects of Varying the Length

To investigate the sensitivity of bunch length on the TR spectrum fit, the spectrum of various lengths was fitted to the results shown in Figure 6.38. Shown are the range of

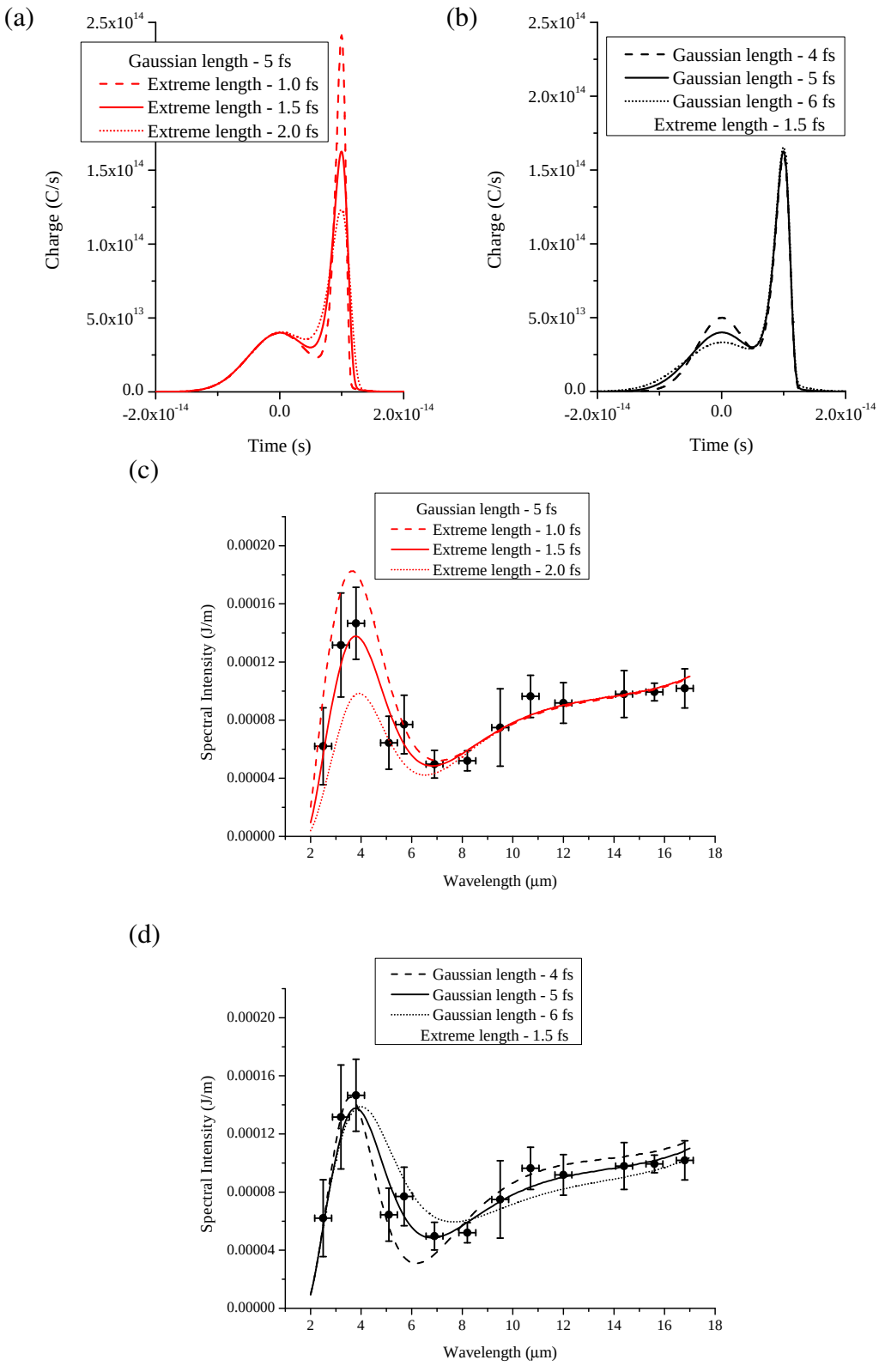

Figure 6.38: Effects of varying the bunch length on the TR spectrum.

lengths which fit $\pm$ 1 standard deviation of the results. As the two parts of the bunch can be calculated separately, variations on both bunches are calculated separately. The solid line represents the best fit, with a short bunch of 1.5 fs and a long bunch of 5 fs and an overall bunch length of 5.9 fs. When varying the short bunch the long bunch was fixed at 5 fs. Here it is shown that the short bunch can become as short as 1 fs (red dash) and should not be any longer than 2 fs (red dot). When combining this with the effects of varying bunch shape the short bunch length becomes 1.6 $\pm$ 0.8 fs. As the bunch becomes very short however the overall bunch length is dominated by the long bunch and does not become much shorter than 5.5 fs. Variations of the short bunch length have little effect at long wavelengths. Variations of the long bunch length do however have a large effect at the longer wavelengths. Here, the variation in the longer bunch suggest that bunch lengths range from 4 fs (black dot) to 6 fs (black dash). When combining this with the effects of varying bunch shape the long bunch length becomes 5 $\pm$ 1 fs. Similarly, the separation between the two bunches can vary to become 10 $\pm$ 1 fs. The overall r.m.s. bunch length which fits well within one standard deviation of the measurement is 5.9 ± 1 fs.

Effects of Varying the Electron Beam Energy

The average electron bunch energy for this measurement is 90 $\pm$ 15 MeV (standard deviation). As shown in Figure 6.13 the interference of the radiation between the two foils is strongly energy dependent. To create the fits found previously and in the rest of this chapter, the mean energy plus one standard deviation was used (105 MeV), as lower energys have been found to reduce the intensity of the shorter wavelength radiation. It is possible that an energy selection occurred when the specific beam divergence and charge were filtered to make the TR spectrum and plus one standard deviation is reasonable given the high spread of energies measured. Figure 6.39 shows the effect of varying the electron bunch energy on the fit of the TR spectrum.

It can be seen that as the electron bunch energy increases past 105 MeV (up to 120 MeV shown) that the spectrum does not change significantly. This is due to the interference moving to a wavelength much shorter than of those measured in the spectrum. However, as the energy moves to lower energy the interference attenuates the short wavelength, as explained in Section 6.3.1. At 90 MeV (red) there is still radiation produced at the short wavelengths but the attenuation makes a good fit impossible. Decreasing the energy to one standard deviation below the measured mean (75 MeV, green) completely attenuates the short wavelength radiation.

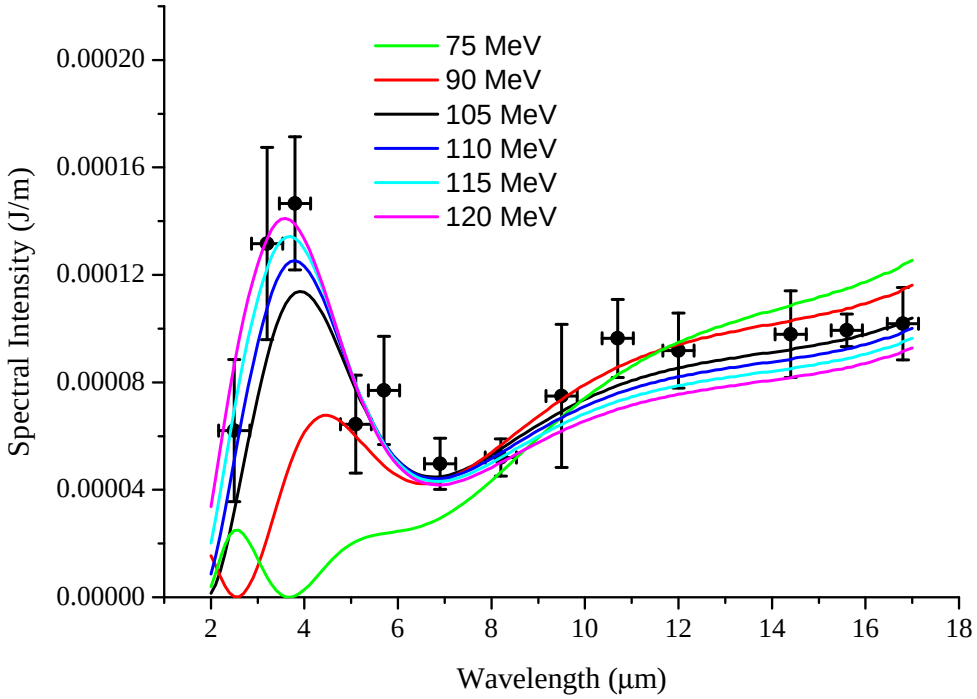

Figure 6.39: Effects of varying the electron beam energy on the TR spectrum.

Effects of Varying the Width of the Electron Beam

The electron beam width affects the off-axis coherent TR, as discussed in Section 6.2.6. This effect can be stronger for shorter wavelength radiation. It is therefore possible that a variation in bunch width could affect the TR spectrum creating a false measurement of bunch length. The electron bunch width was measured in two ways. The first was the direct measurement of the electron bunch width from the LANEX screen on the rear of the second TR foil. However, as this measures both the electron bunch and the part of the low energy tail which is transmitted through the permanent magnetic field quadrupoles (this is discussed in more detail in Section 6.4.3), it is possible that there is a slight error in the measurement. The beam width was therefore also measured by utilizing the natural shot-to-shot pointing variations of the beam. The TR emitted from the screen was scanned over the detector as the electron beam's position varied. The position of the electron beam and the signal intensity measured provides a second measurement of the electron beam width.

When measuring the beam width directly from the screen only the shots used to create the spectrum were used. This gave an r.m.s. beam width of 1.5 ± 0.2 mm. The beam width was slightly different on the x and y-axis by 0.1 mm (smaller on the x-axis)

but this is within the spread of the average beam width. Similarly when investigating the correlation between the beam position and TR signal, the data was filtered to use beam width and charge used to create the spectrum. However, if all beam positions where used as filtering this would underestimate the beam width. This method gave the same beam width as that directly measured on the screen of 1.5 ± 0.2 mm.

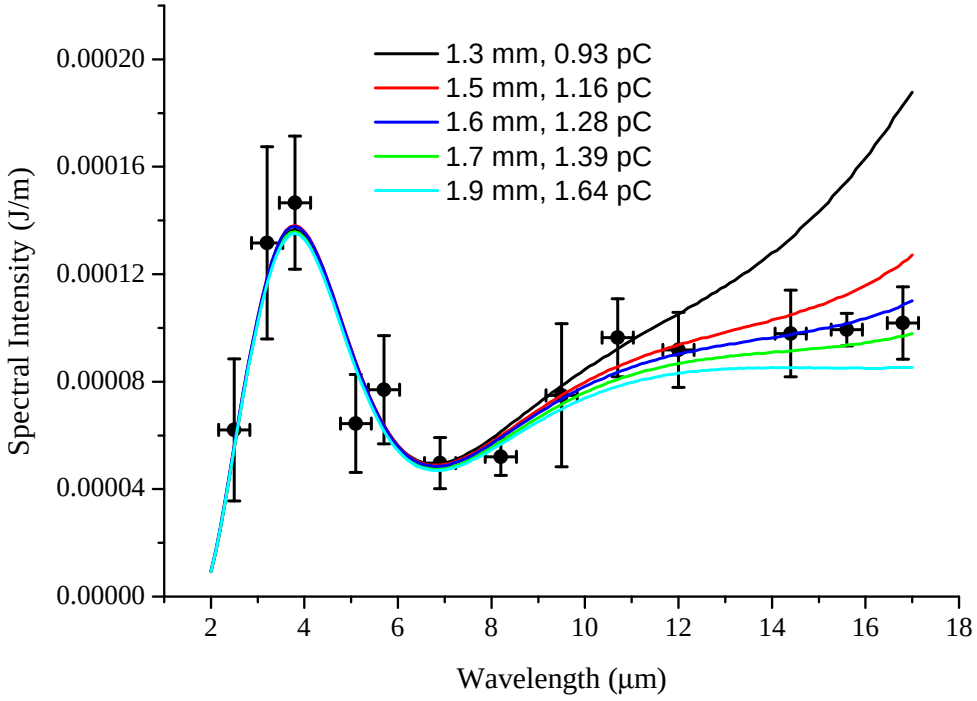

Figure 6.40: Effects of varying the electron beam width on the TR spectrum.

The effects of varying the beam width are shown in Figure 6.40. Here it can be seen that the fits of the spectrum for beam widths from 1.5 mm up to 1.9 mm (well above the measured value) do not have a great effect on the spectrum shape. 1.6 mm gives the best fit and is within the measured range and has therefore been used in the rest of the calculation, however only the last data point on the spectrum varies with electron beam width. For a beam width at the lower limit of the error of the width measurement, the calculated signal does start to increase for the longer wavelengths but still fits well with the rest of the spectrum. It should be noted that the beam width does alter the TR signal intensity produced over the entire spectrum. The wider electron beams attenuate more of the signal and therefore, to give the same measurement, the charge within the beam needs to be increased. Varying the beam width does not affect the bunch length measurement but does have an effect on the calculated charge within the bunch. The

measured charge range from the bunch width range is 1.3 $\pm$ 0.4 pC.

Effects of Varying the Angular Spread of the Electron Bunch

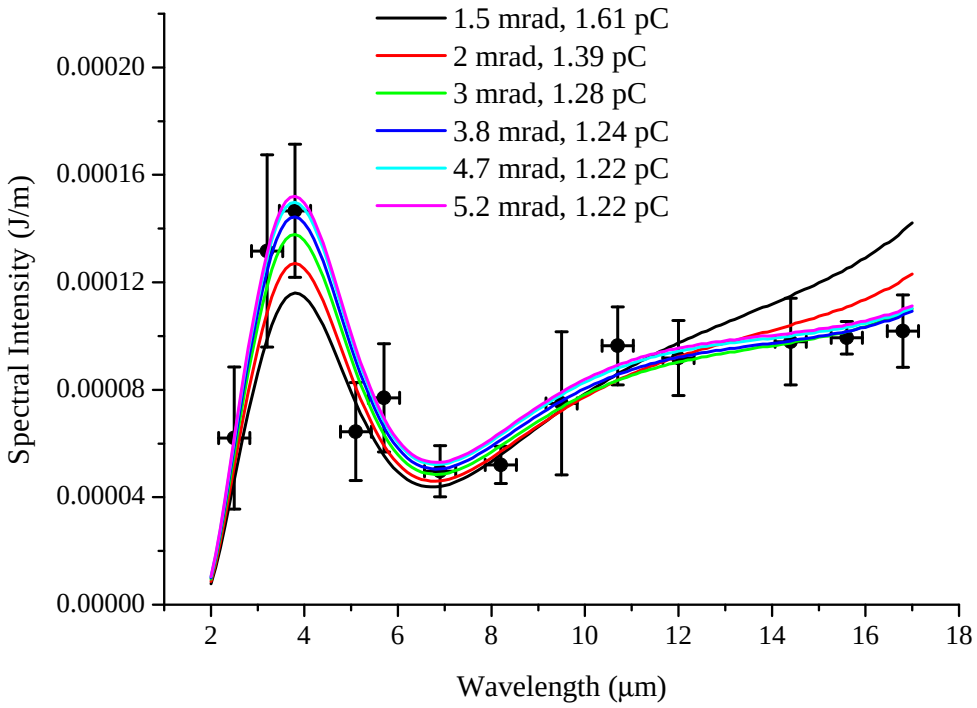

Figure 6.41: Effects of varying the electron beam angular spread on the TR spectrum.

As the angular spread of the electron bunch smooths out the $1/\gamma$ coning of the radiation and produces on axis radiation (as discussed in Section 6.2.1) the degree of spread may affect the TR signal generated. From the previous section it is known that the bunch width is 1.5 mm. As the foils are placed 1 m from the source this gives a minimum angular spread of 1.5 mrad. However, scattering in the first foil, the use of quadrupoles and resolution limits result in this value being an upper limit to the divergence of the beam from the source. The true divergence of the beam from the source is therefore 1.25 $\pm$ 0.25 mrad. The electron beam also propagates through the alimunium foil which scatters the beam increasing its angular spread as discussed in the emittance chapter. Thus the angular spread is larger than the minimum of 1.25 mrad. Figure 6.41 shows the effect of varying degrees of angular spread on the electron TR spectrum. For all angular spreads, the TR spectrum remains approximately constant. The spectrum of the beam with no scattering has a reduced signal at the short wavelength, however for

the thickness of the aluminium used (45 μm) an increase in angular spread of 2.5 mrad results in an overall angular spread of 3 mrad. Additional scattering will also come from the thin mylar film used to strengthen the aluminium foil. Figure 6.41 shows that the spectrum remains constant provided a threshold angular spread of 3 mrad is achieved. Even if the angular spread is only 2 mrad, the spectrum would be the same along with the measured bunch length and only an increases in the calculated charge to 1.35 pC would occur. The charge is within the range created from the error in the bunch width measurement.

Spectrum 2

A second spectrum was obtained during a separate experimental run. The data used to create the second spectrum was handled in the same way as in spectrum 1. The transverse parameters measured on the LANEX screen were used to sort the data to create a spectrum for similar electron beams. As in spectrum 1, different sort methods were applied, however only the final sort is discussed here. This sort method is similar to Sort 1C where there are fairly large ranges for most of the parameters while focusing on creating a stable charge. The sort parameters are shown in Table 6.5 and were used to create the spectrum shown in Figure 6.42 (b).

	Minimum	Maximum
X	16.8 mm	20.3 mm
Y	9.1 mm	11.3 mm
σ_x	1.3 mm	2.1 mm
σ_y	1.3 mm	2.1 mm
$\frac{\sigma_x}{\sigma_y}$	0.8	1.25
$\sigma_x \times \sigma_y$	2 mm^2	2.9 mm^2
Charge	4.9 pC	8.9 pC

Table 6.5: Sort 2: focuses on creating a narrow selection region for the charge.

Spectrum 2 looks different to Spectrum 1. The most noticeable difference is that there is no longer the distinctive structure in the spectrum. The spectrum now has a much more steady increase at longer wavelengths. At short wavelengths the Spectrum 2 no longer has the large structure that can be seen in Spectrum 1. This minimised structure in the spectrum indicates that there is no longer the same extremely short sub-structures in this bunch that would add the strong coherent components at the shorter wavelengths. Therefore, to create a spectrum with a small peak at short wavelengths the bunch cannot have the same short structure. To create the fit shown in Figure 6.42 (b) the two bunch structure shown in Figure 6.42 (a) is used. The two bunches are separated by 9 fs, the long, second bunch is 5.25 fs whereas the short first bunch is just

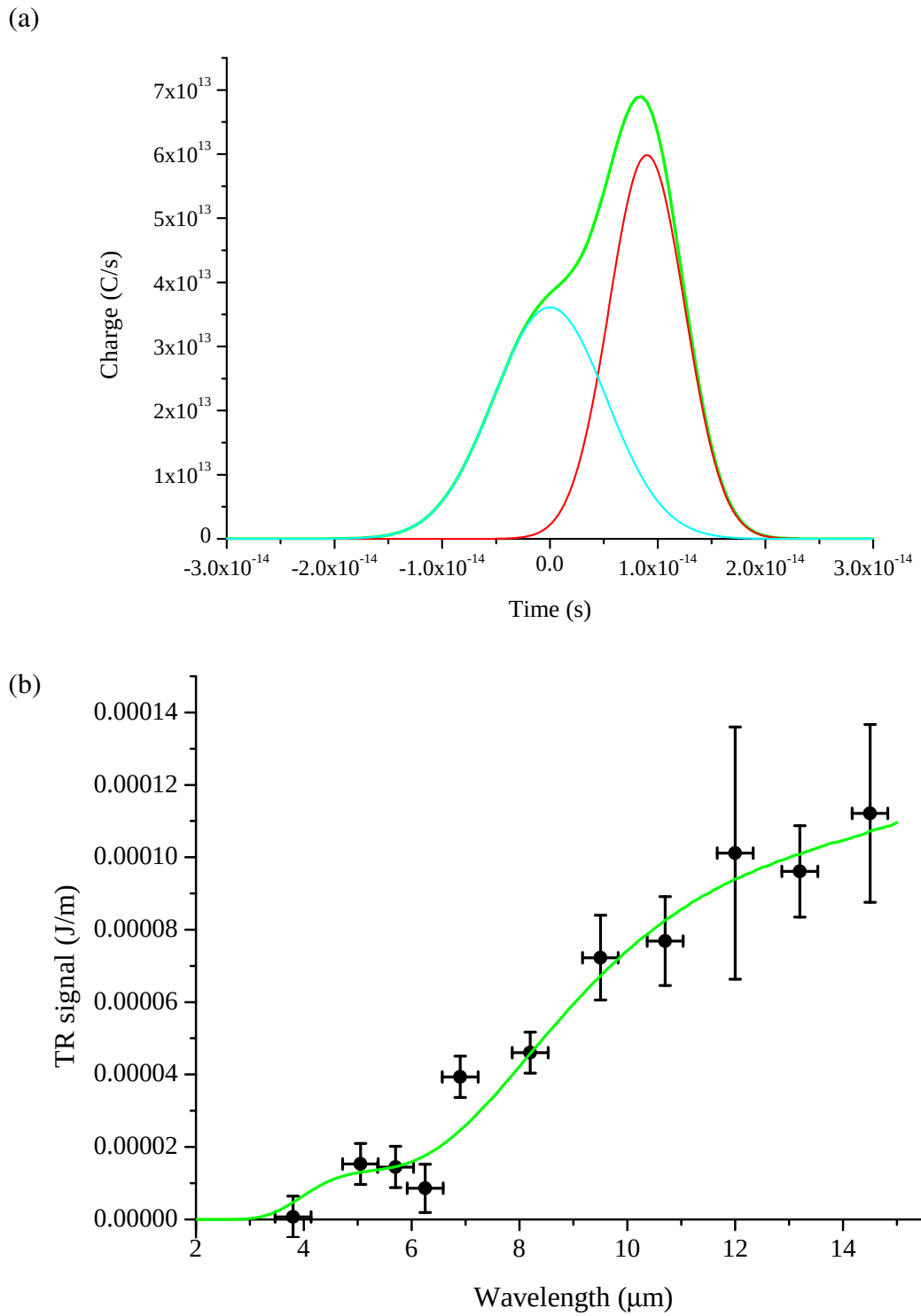

Figure 6.42: (a) Electron bunch shape (green) which consists of a substructure of two bunches (red and blue) and (b) TR spectrum.

3.5 fs and a total r.m.s. bunch length of 6.3 fs. The charge in the two bunches is 1.3 pC with 47.5% of the charge in the long bunch. This structure is very similar to the bunch measured in spectrum 1, however in this measurement the short bunch is not as short.

Effects of Varying the Length

Similarly to spectrum 1, a range in measured values of the electron bunch (such as divergence, beam width, etc.) could provide good fits with the spectrum. These parameters have been investigated, similar to spectrum 1, to investigate their effects on the required bunch parameters. For example, variations can be made to the bunch lengths and separations that still result in a reasonable fit. Figure 6.43 shows the effect of varying both the short bunch and the long bunch. Parts (a) and (c) show that the bunch range which gives a reasonable fit is 3.5 ± 1 fs. Similarly the second bunch can vary 5.25 ± 1 fs as shown in parts (b) and (d). Therefore the range of bunches which fit are short bunch, 3.5 ± 1 fs, long bunch is 5.25 ± 1 fs with a separation of 9 ± 1 fs. The complete r.m.s. bunch length is 6.3 ± 0.5. The bunch charge is 1.3 ± 0.4 pC.

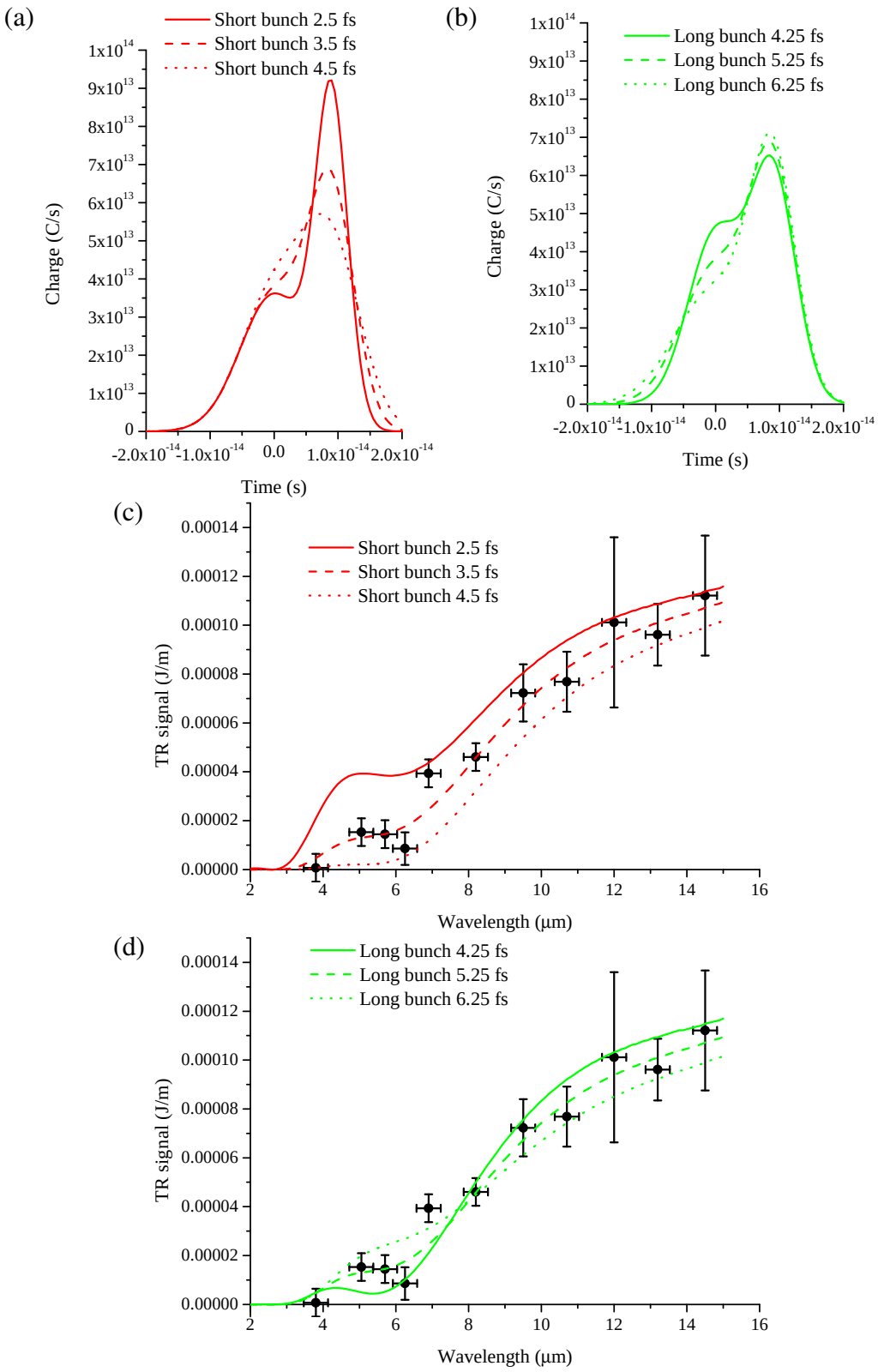

Figure 6.43: Effects of varying the bunch length on the TR spectrum.

Effects of Varying Bunch Shape

As in spectrum 1, there are several bunch shapes that will produce a good fit for the spectrum. Although the bunch shown in Figure 6.42 (a) is two bunches, they are sufficiently close that the structure is not very distinct. They can therefore in this instant be approximated by a single structure (slightly sacrificing the quality of the fit). Figure 6.44 shows the fit of several bunch shapes which give a good fit to the spectrum. The fit is of a square (black), quadratic (red), triangular (green), Gaussian (blue) and extreme (light blue) all with r.m.s. bunch lengths of 6.1 fs. The quadratic shape creates a slight structure at the short wavelength region of the spectrum because of its quasi-asymmetric structure, however this not a natural structure. All structures provide a reasonable fit, thus resulting in a bunch length of 6.1 fs regardless of the bunch shape.

Effects of Varying the Energy

The measured electron bunch energy for this experimental run is 89 ± 7 MeV (standard deviation). The spectrum shown in Figure 6.42, is plotted in Figure 6.45 for the mean energy at 89 MeV (red), minus one standard deviation at 82 MeV (black) and plus one standard deviation at 96 MeV (green). It can now be seen that the spectrum is not as sensitive to the bunch energy as the first spectrum. This is because the interference minimum caused by the interaction between the two foils, as shown in Figure 6.12, is well away from the measured short wavelengths measured

(a)

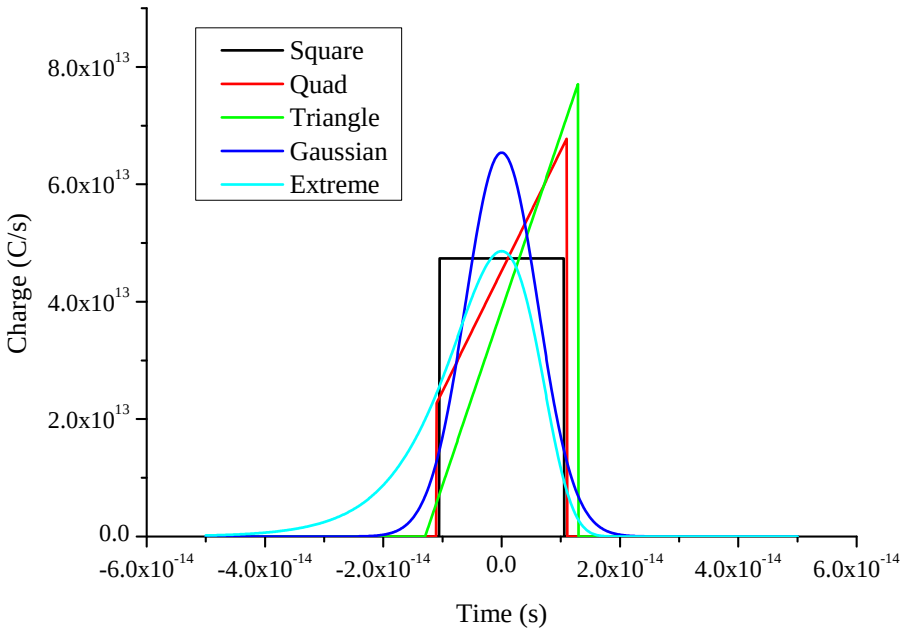

(b)

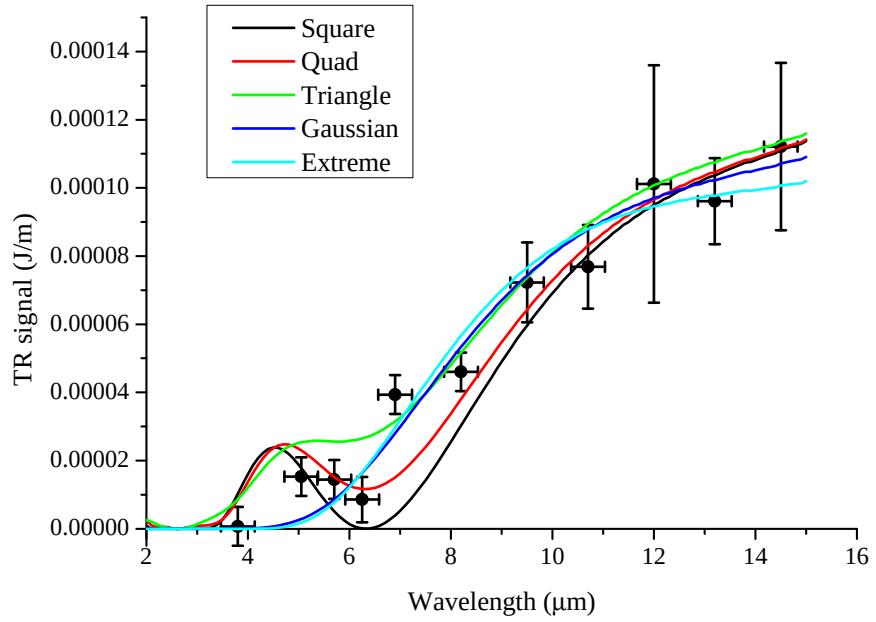

Figure 6.44: Various electron bunch shapes (a) and their TR spectrum(b).

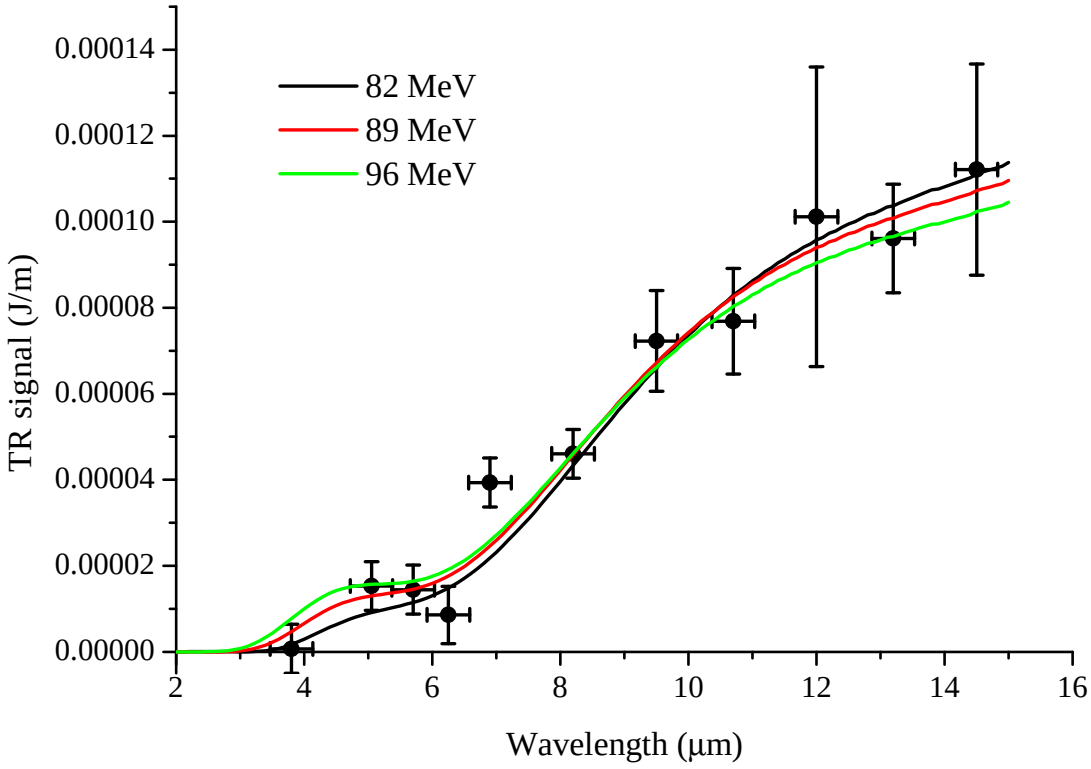

Figure 6.45: Effects of varying electron bunch energy. The structured electron bunch shape used to fit TR spectrum 2 (shown in Figure 6.45) is plotted for 96, 89 and 82 MeV shown by the solid green, red and black lines respectively.

6.4.3 Charge within the Electron Bunch

The charge was measured on the LANEX screen for every shot to correlate the charge within the electron bunch to the transition radiation signal . (LANEX screen charge calibration is discussed in Section 3.4.) However, not all the relativistic electrons produced from the wakefield accelerator are in the mono-energetic bunch and most of the charge is in a low energy exponential tail. The permanent magnetic quadrupoles were used to divert most of the low energy electrons by over-focusing them and preventing them from being delivered to the TR screen. Typically the permanent magnetic quadrupoles remove $\sim 80\%$ of the charge but, due to their configuration, still allow more than just the mono-energetic peak to pass through.

Effects of the Permanent Magnetic Quadrupoles on Charge

GPT was used to simulate the effects of the quadrupoles on the delivery of the charge. For this simulation, a Gaussian shaped peak of mono-energetic electrons (peak energy of 90 MeV) with an exponential tail (cutting off at E_k = 5 MeV, due to electron beam

divergence) as shown by the black line in Figure 6.46. A normalised emittance of 1 π mm mrad was chosen and the beam allowed to propagate the 1 m to the screen. The source size of the electron bunch was fixed at 1 μm and therefore lower energy electrons have a higher divergence to conserve emittance. Only electrons which hit the 1 cm radius TR screen were considered and, due to the high divergence of the low energy beam, only the electrons denoted by the red line in Figure 6.46 reach the screen.

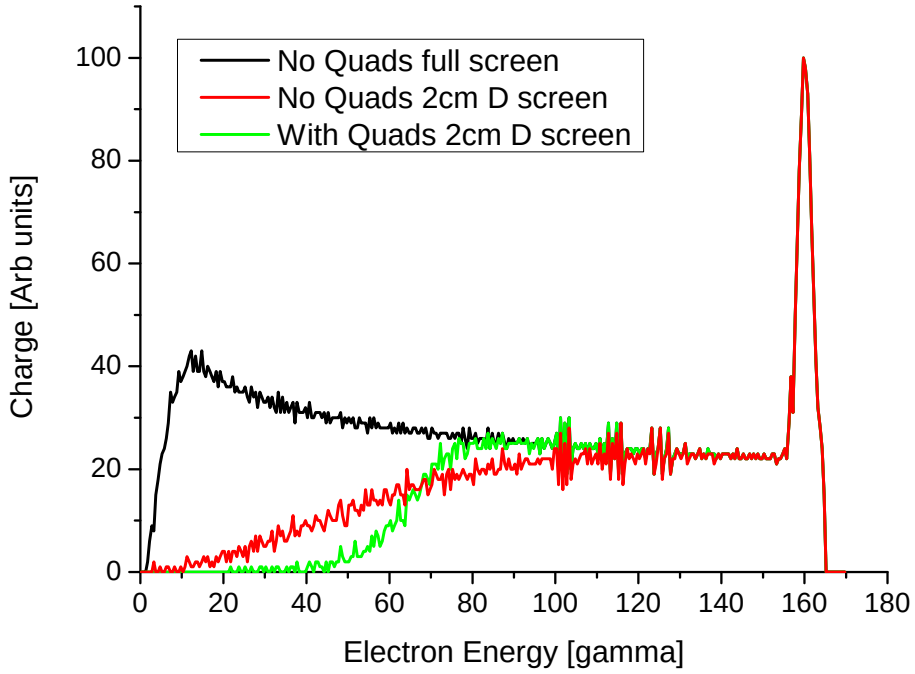

Figure 6.46: Electron propagation to the TR screen of a mono-energetic peak with a long tail at the screen position, measured for large diameter aperture ($>$ 5 cm) (black), measure in an aperture the same size as the TR screen (2 cm diameter) without the quadrupoles (red) and with the quadrupoles (green).

When the quads were put in place they over-focus the lower energy electrons, as expected, and act to cut of any electrons below 30 - 35 MeV as shown by the green line in Figure 6.46. (The red line shows the electrons delivered to the screen without the use of the quadrupoles. It can quite clearly be seen that the quadrupoles aid delivery of the electrons between 35 and 60 MeV.)

Analysis of Electron Energy Spectra

The energy spectra were analysed to more accurately establish the fraction of the beam within the mono-energetic part. The setting of the spectrometer clipped the low energy

electrons from the measurement at around 50 MeV, making it difficult to establish the charge directly. To correct for this problem the spectrum was fitted so that the curve would drop away at 35-40 MeV, where the electrons are cut-off by the quadrupoles. Figure 6.47 shows a typical example of a fitted spectrum.

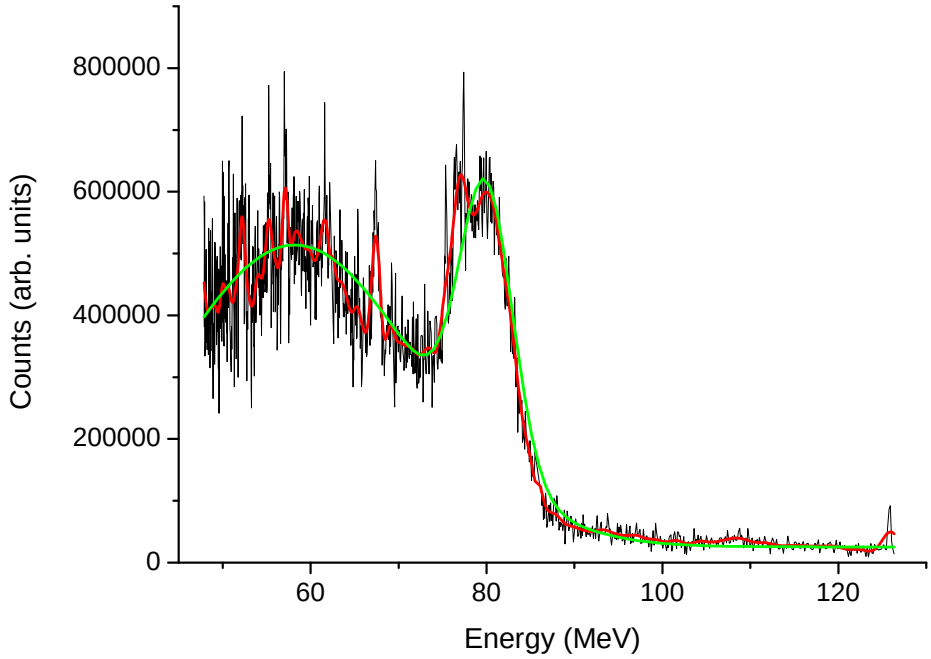

Figure 6.47: Example mono-energetic electron peak with low energy tail with the raw data (black), smoothed data (red) with a double Gaussian fit (green) used to obtain the fraction of the charge in the peak.

The black line is the raw data and the red line is a smoothing of the data to make the shape easier to see. The green line is the fit of the data, the mono-energetic peak at 80 MeV can be clearly be seen with a tail which rises until 60 MeV then starts to drop away to lower energies. The fit continues to drop away to the expected cut-off at around 35 MeV. (A small peak can be seen next to the main peak; this is due to damage to the Ce:YAG crystal and can be ignored. Similarly the peak at 67 MeV is the join between two crystals.) This peak contains 16% of the charge and is an example from the second TR spectrum.

Measured Fraction of the Electron Bunch Charge

The above process was carried out for all the electron energy spectra measured for the two TR spectra.

The fraction of charge measured from the electron spectra on the day of TR Spectrum 1 was $23 \pm 3\%$. The average charge measured on the LANEX screen was 7 pC and the charge used to create the fit was 1.3 $\pm$ 0.4 pC resulting in 19 ± 6 % of the charge being in the 5.4 fs bunch, this is similar to the charge in the mono-energetic part of the beam.

The fraction of charge measured from the electron spectra on the day of TR spectrum 2 was $8 \pm 1\%$. The average charge measured on the LANEX screen was 16.4 pC and the charge used to create the fit was 1.3 $\pm$ 0.4 pC resulting in $8 \pm 2\%$ of the charge being in the 6.1 fs bunch which is in good agreement with the charge in the mono-energetic part of the beam.

6.5 Conclusion and Future Work

In conclusion, this chapter represents the first bunch length measurements of a single laser driven wakefield accelerated electron bunches. The measurement was repeated and gave similar r.m.s. bunches lengths of 5.9 $\pm$ 1 fs and 6.3 $\pm$ 1 fs containing 1.3 $\pm$ 0.4 pC of charge respectively. Both of the measured bunches demonstrate the properties of a sub-structure inside the bunch. Both consist of a short and a long bunch separated in time. The long structures in both of the measured bunches is similar at 5 $\pm$ 1 fs and 5.25 $\pm$ 1 fs, the separation between the long and short bunch is similar at 10 $\pm$ 1 fs and 9 $\pm$ 1 fs and the charge is split quite evenly between the two substructures with 55 $\pm$ 5% and 47.5 $\pm$ 5% of the charge in the long structure for the first and second spectrum respectively. The two bunches differ with the short substructure. The first spectrum's short structure is 1.6 $\pm$ 0.8 fs whereas in the second spectrum it is longer at 3.5 $\pm$ 1 fs. This could be because the density of the plasma will be slightly greater in the first spectrum as the laser was interacting with the gas jet 1 mm closer to the nozzle at 7 mm distance rather than at 8 mm for the second spectrum. The increased plasma density will decrease the dephasing length allowing the first structure to reach dephasing and minimise its energy spread. A minimal energy spread will minimise the bunch drifting apart as it propagate down the beamline.

Electron bunch parameters, such as bunch width, angular spread, scatter and beam pointing, were taken into consideration and ultimately utilised to make the measurement. The short sub-structure measured in the first bunch is too short to be created by the measured energy spread (limited by spectrometer resolution) and therefore limiting the energy spread to 0.5%. For the resolution of the parameters measured, such as energy spread, it is impossible to accurately deconvolute the bunch back to the source, however, even if bunch lengthening is minimal, the maximum bunch length at

the source is < 2 μm. This length is much shorter than the bubble structure, which means the bubble has not been filled in the wake of the laser pulse and that there must a switching on and off of the injection process. the deconvolution of the bunch back at the source is discussed in more detail in Chapter 7.

Earlier transition radiation measurements of laser wakefield accelerated electrons set an upper limit to the bunch length of 130 ± 30 fs (FWHM) for a 20 MeV electron bunch (Ohkubo et al., 2007). However, this bunch had large energy spread (20 %) that would result in bunch lengthening as it drifts from the gas jet. Also, the charge in this measurement is large at 30 pC, which may mean the measurement include any energy tail as well as the mono-energetic peak. This bunch length was reduced by Faure, Glinec, Gallot, and Malka (2006) to < 50 fs. However, this was just one data point on the TR spectrum, which means a lot of information is missing in recreating the bunch length. This set-up was refined in Lundh et al. (2011) at the same time as the measurements made in this thesis, where a counter propagating injection laser was used to control the injection of the electrons into the bubble. Here, a bunch length of 1.4 - 1.8 fs was measured with a charge of 15 pC. It should be noted that a reduction in the signal is observed at a wavelength of 5 - 6 μm compared to the expected signal. This is similar to the dip measured in spectrum 1 of this Chapter.

Future experiments in bunch length measurements will need higher resolution of beam parameters (such as energy spread) to be able to accurately predict the bunch length at the source. Additionally, measuring the bunch length closer to the source will minimise the need for bunch length deconvolution. An interesting consequence of measuring a structure in the electron bunch is that it could allow for a diagnostic of the accelerating field itself. The beam's longitudinal distribution and energy within that distribution could calculated as it leaves the accelerator, if the beams's structure at several points along the beam line is combined with an accurate measurements of the energy structure. This will allow the longitudinal phase-space to be recreated and give a better understanding of the accelerating potential.

Chapter 7

Discussion

7.1 Narrow Energy Spread

The minimum energy spread measured in Chapter 5 is 0.8% (deconvolved to 0.5%. The bunch length must be short to obtain this energy spread, as discussed in Section 2.2.6. A chirped injected bunch obtains its minimum energy spread at dephasing. The lowest energy spread is obtained when the bunch is short compared to the electrostatic potential curve (Figure 2.5 (d)).

From Equation 2.29, for a bubble radius, $R = 5.8$ μm ($a_0 = 3$), and energy spread of 0.8 % has an upper limit of the bunch length of 0.42 μm at the source (deconvolution bunch length for an energy spread of 0.5% is 0.3 μm). An energy spread of 0.5% will give an increase in bunch length of 0.15 μm over 1 m, as given by Equation 6.19. The use of the permanent magnetic quadrupoles is simulated using GPT in Section 7.4. To obtain the 1.6 ± 0.8 fs bunch measured during the TR measurement ($\sigma_x = 1.25$ mm after 1 m and $\sigma_\gamma/\gamma = 0.5$ %) the bunch length would need to be less than the upper limit of 0.3 μm (0.9 fs) set during dephasing.

Therefore, to obtain a 0.5 % energy spread the initial bunch length is required to be < 0.3 μm. Conversely, to measure a 1.6 fs bunch after 1 m, the energy spread must be < 0.5 % and have a short initial length (assuming the bunch is at dephasing and no energy chirp).

7.2 Transverse Emittance

As is discussed in the emittance chapter, the average transverse emittance along the horizontal axis is 2.2 ± 0.7 π mm mrad with the best shot of 1.1 π mm mrad which is close to the resolution of the system. The vertical emittance has an average value of 2.3 ± 0.6 π mm mrad with the lowest emittance recorded at 1.2 π mm mrad (nor-

malised to 125 MeV). The beam divergence during this run was 1.5 mrad giving a source size of $6 \pm 2\mu$m.

The emittance of the beam is determined during the injection process where a large beam diameter will experience a large transverse force creating an increased emittance. This radius can be determined using Equation 2.22. For a 2.2 π mm mrad beam the injected beam radius is $3.4 \pm 0.4\mu$m, which is similar to the calculated final radius at the end of the acceleration process.

7.3 Charge Dependence

Section 5.3.3 shows the dependence of the measured energy spread on charge. As discussed in Section 2.2.6 and 2.2.7, there are two ways that the charge variation can effect the energy spread. The first is through increased beam loading, where the electron beam charge damps the wake and causes a longitudinal variation in the accelerating potential. The second is an increase in the bunch length resulting in electrons at the front of the bunch being in a different position in the dephasing process and therefore having different energies from those at the rear.

For mono-energetic injected bunches it is possible to under and overload the wake. Therefore, for a fixed bunch length, as the charge increases the energy spread decreases to a minimum at the optimal loading before increasing again at higher charges, as shown in Figure 5.13. However, underloading before a minimum energy spread is not observed. An increase in the bunch length with increasing charge would show this dependence, with rate of increase in energy spread depending on the degree of loading.

However, it is unlikely that electrons are injected simultaneously across the bunch length but are injected over a period of time. Under these circumstances the electrons injected first will undergo some acceleration, resulting in chirped injection, as discussed in Section 2.2.7. Now beam loading can only overload the wake, underloading will not occur and optimal loading (seen in Figure 2.9 for a mono-energetic injected bunch) will not exist. The energy spread due to bunch lengthening with charge for chirped injection will behave similarly to the mono-energetic injected bunch. Thus, for a chirped injected bunch, both increased beam loading and increased bunch length could cause the observed dependence of energy spread on charge.

If an increase in the charge was due to increased injection duration, resulting in a bunch length increase, then there would be no variation in charge per unit length (i.e. the current would remain the same) and, therefore, no variation in transverse forces. If, however, the increase in charge was due to increased injection rate, resulting in increased beam loading, then there would be an increase in charge pre unit length

(i.e. an increase in current) and a variation in the transverse force. This is shown in Figure 4.23 where the beam divergence varies with charge. The beam's emittance is depends on the charge per unit length Q/σ_z. The emittance from the source is the product of the width and divergence, σ_r/θ. Therefore, the divergence can be expected to vary with the charge as $\theta \propto Q^{1/2}$ for a fixed length and $\theta \propto Q^{1/3}$ for a varying length (J. Rosenzweig & Colby, 1994). The fit shows the divergence to vary with the $Q^{1/2}$ although a $Q^{1/3}$ is also within experimental error. Therefore, the bunch length either varies slowly with time or not at all.

The increase in divergence with charge shows that there must be increase in charge per unit length and therefore in increase in beam loading. The increase in energy spread with charge is therefore due to an increase in beam loading and only partially due to lengthening, if at all.

7.4 Multiple Electron Bunches

The structured bunch used to create the 1st TR spectrum, Figure 6.36, is actually two bunches separated by 10 fs. A short bunch gives the short wavelength radiation and a long bunch giving the increased intensity at longer wavelength. A complex injection process could create this two-bunch structure. For example, the electric field of the first bunch cuts off injection by loading the wake or deflecting the incoming electrons. As the electrons accelerate through the bubble away from the rear, injection turns on again creating a second bunch. Alternatively, the electrons could be injected into the rear in one long bunch but breaks up into smaller bunches later in the acceleration, for example through interaction with the rear of the laser pulse (Cipiccia et al., 2011; Nemeth et al., 2008).

The electron beam parameters measured for TR spectrum 1 (Figure 6.36) are an energy spread of 4.5 $\pm$ 0.3 % and a divergence of 1.25 $\pm$ 0.25 mrad. The long part of the bunch is similar to that measured in spectrum 2 (Figure 6.42). For the short structure it is impossible to measure a short bunch with the measured energy spread. As discussed previously the energy spread measured is close to resolution limit and a narrower energy spread would be impossible to measure. To obtain a bunch length of 1.6 fs then the maximum energy spread possible would need to be $\sim$ 0.5 % similar to that discussed in Section 7.1. However, an up chirp (low energy at the front of the bunch) could compress a longer bunch down to 1.6 fs.

The separation between the two bunches could be created in three different scenarios:

1. The two bunches are created at the same time but have an energy difference

which results in a temporal separation once the electrons have drifted to the foils.

2. The two bunches have the same energy but are started with the same 10 fs separation that they have at the foil.

3. A combination between the two, the two structures have both a temporal and energy separation, such that the electrons at the back have lower energy (a down chirp) which will serve to increase the separation as they drift to the foils.

Scenario 1 (Identical Initial Longitudinal Position)

If the initial longitudinal position of the two bunches is the same, then they requires an energy variation between the first and second bunch to be 9 MeV. The measured average energy spread for this measurement is 4.5 MeV. Even if this is close to the resolution of the spectrometer, it is still lower then that needed to create the 10 fs bunch separation. It could be possible the lower energy bunches had a larger energy spread and, therefore, lower peak charge which might make the bunch difficult to resolve over the large low energy tail. However, there is no position on the longitudinal electrostatic potential curve (discussed in Section 2.2.5) where the electron bunches could be at the same position but had different energy. It is therefore unlikely that this is the scenario in which the two bunches are created.

Scenario 2 (Identical Initial Energy)

If the bunches are assumed to have the same initial peak energy then they require a 10 fs bunch separation at the source. Figure 7.1 demonstrates the phase-space in this scenario. The two bunches have the same peak energy and have a separation Δz. The leading, first bunch of electrons has a lower energy at the front causing and up chirp. Whereas, the rear, second bunch of electrons have a higher energy at the front causing a down chirp. The up chirped bunch will compress as it drifts from the accelerator because the higher energy electrons at the back of the bunch will pass the lower energy electrons at the front. The second bunch on the other hand will stretch due to the down chirp. Under this situation the two bunches could evolve to consist of one short bunch and one long bunch, separated by 10 fs, at the TR screen.

Scenario 3 (Varied Initial Position and Energy)

It is not necessary that the electron bunches have exactly the same initial energy. The two bunches could be at any two points on the electrostatic potential curve, provided

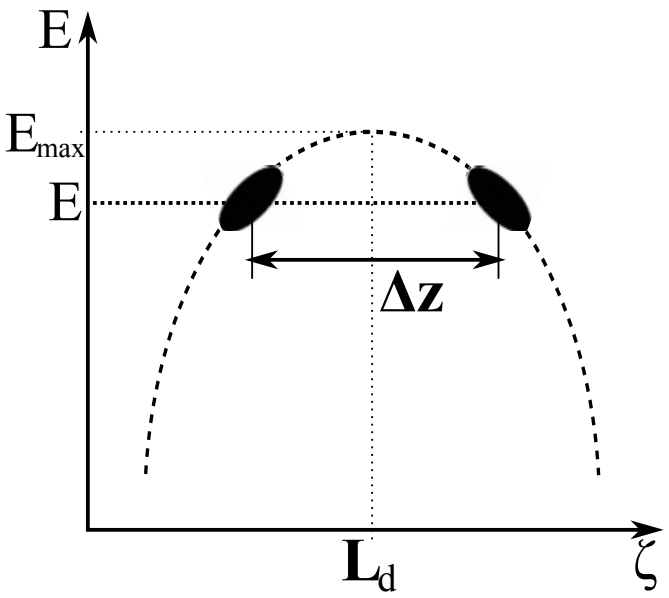

Figure 7.1: Phase-space plot with two electron bunches of the same energy. The first has passed de-phasing and has an up chirp whereas the second before de-phasing has a down chirp.

they are 10 fs apart when they reach the TR screen and one bunch is shorter than the other. Take for example, one bunch is at the de-phasing length with minimum energy spread and the other bunch is either before or after de-phasing as shown in Figure 7.2 (a) and (b) respectively. Here, the bunch at L_d has a minimum energy spread which results in minimum stretching.

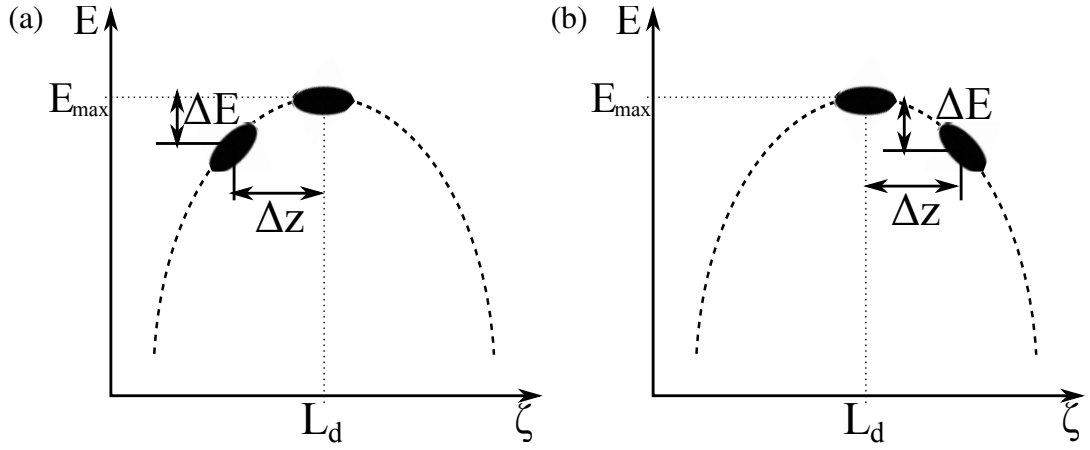

Figure 7.2: Phase-space of two bunches, one bunch at de-phasing with a minimum energy spread and the second bunch (a) before de-phasing and (b) after de-phasing.

In Figure 7.2 (a), the large energy electron bunch is before de-phasing. If the peak energy difference was 4 MeV, for example, between the two peaks, then the second

bunch would need to leave the bubble 5.7 fs after the first. In Figure 7.2 (b) the high energy spread bunch is after de-phasing and in front of the mono-energetic peak. This bunch would compress as it drifted. Depending on the gradient of the chirp, the bunch could compress to a short bunch at the TR screen, compress to a minimum before the screen and elongate again or the bunch might not compress by much and stay the same length. In addition, the separation between the two bunches would decrease as the higher energy mono-energetic bunch would catch or possibly even over take the other bunch.

A structure in the energy spectrum was observed during the high resolution energy measurements made in Chapter 5. The average structure measured consisted of a mono-energetic peak at 83 $\pm$ 1.3 MeV with an energy spread of 1.3 $\pm$ 0.3% (deconvoluted to 0.9 $\pm$ 0.3 %) and a second peak at 79 $\pm$ 1.7 MeV with a larger energy spread of 4.3 $\pm$ 0.9% (deconvoluted to 4.2 $\pm$ 0.9 %). The two peaks are separated by a 4.5 $\pm$ 1.8 % energy difference and 49 $\pm$ 4 % of the charge is in the mono-energetic peak. This energy structure is created when the mono-energetic peak is at dephasing and the second bunch is either in front or behind with a lower peak energy and a larger energy spread.

An energy difference of 4.5 $\pm$ 1.8 % and a radius of R = 5 - 6 μm (assuming and a_0 = 2- 3) gives an initial separation of 3.5 $\pm$ 1 fs (using Equation 2.29). Using an energy scaled to the 90 MeV peak energy of the TR measurement, as the bunch propagates 1 m the two bunches will separate by a further 5 $\pm$ 2 fs (using Equation 6.19) resulting and a 9 $\pm$ 2 fs separation at the screen. This agrees with the measured separation of 10 fs.

The energy spread distribution discussed above (scaled to 90 MeV) was simulated from the source over 1 m, using GPT. The initial bunch consisted of two electron bunches with peak energies of 90 MeV and 86 MeV (maintaining the 4.5% difference) separated by 3.8 fs. The leading 90 MeV bunch represents the electrons at dephasing and have an energy spread of 0.5% (minimum, deconvoluted measurement and at the bottom of the range of the average value). This energy spread has an upper limit to the length (set by Equation 2.29) of 0.3 μm, however, as this is an upper limit an initial length of 0.15 μm was also in the simulation to keep the final bunch short. The 86 MeV bunch uses a 4.2 % energy spread. The permanent magnetic quadrupoles were used in the simulation to create a final distribution a shown in Figure 7.3. The final r.m.s. bunch width, σ_x, after 1 m is 1.25 mm, which is within the error of the bunch width measured in the TR measurement. Figure 7.3 shows the bunch measured during the TR measurement, red, and the bunch calculated from energy spectrum for the narrow energy spread, initial bunch lengths of 0.3 μm, black, and 0.15 μm, green. It can be

seen that the general structure of the calculated bunch agrees well with the measured distribution, both have a narrow peak followed by a long bunch delayed by $\sim$ 10 fs. The calculated narrow peak is slightly longer than the measured length, this might be because the assumed initial conditions (such as energy spread and length) are an over estimation (demonstrated by the 0.3 μm and 0.15 μm sources) as they were obtained below the resolution of the spectrometer.

This is the only way that the measured bunch distribution and measured energy spread can have the same distribution after 1 m of propagation and agree with the theory of wakefield acceleration (assuming that the two beams are similar during the two seperate measurements). Therefore, the initial bunch at the accelerator must consist of two bunches, one at dephasing and the second before dephasing with a larger energy spread as shown in Figure 7.2 (a).

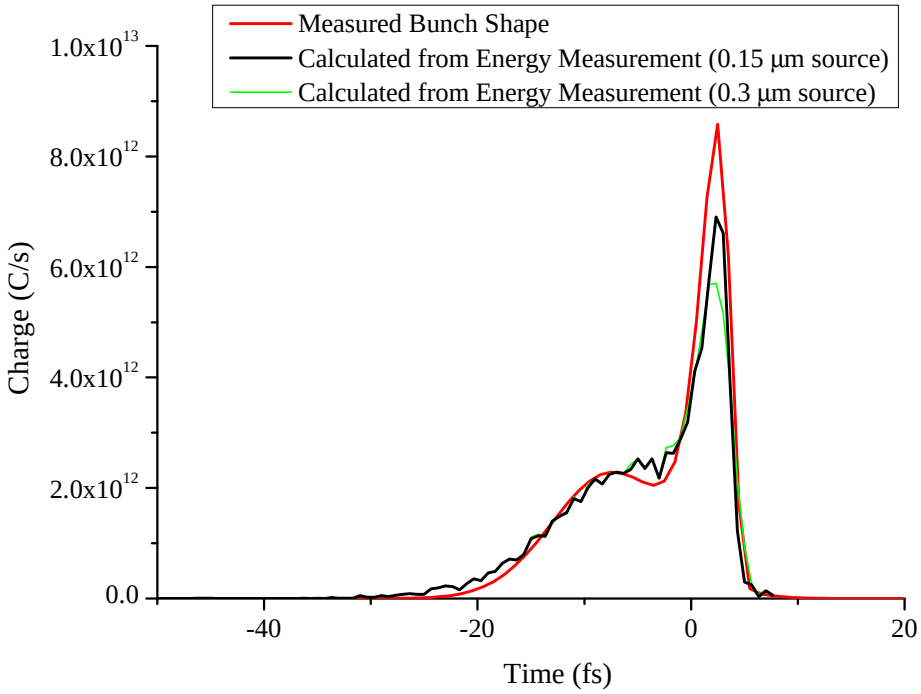

Figure 7.3: TR measured electron distribution (red) and a GPT calculated distribution from the high resolution measured energy spectrum with a 0.15 μm (black) and 0.3 μm (green) mono-energetic source bunch length.

TR Spectrum 2

TR spectrum 2 showed a similar structure in the bunch as spectrum 1. However, the short structure in this bunch is 2 fs longer than the bunch from spectrum 1. The pa-

rameters of the set-up are similar in both measurements, however in spectrum 2 the gas jet was 1 mm further away from the laser. This could have the effect of decreasing the plasma density and increasing the dephasing length. Therefore under the same acceleration length the electron might not make it to dephasing, thus leading to an increase in the energy spread. The additional bunch length of 2 fs could therefore easily be obtained from a 3% energy spread (increased from the 0.5% predicted in the first spectrum).

Chapter 8

Conclusion

This thesis demonstrates the measurement techniques for all of the main parameters of a relativistic electron bunch required to show the potential for application of these new accelerators. Through modelling and optimisation of a high resolution magnetic electron spectrometer, Chapter 5 showed the lowest energy spread measurement made of LWFA electron bunches with an energy spread as low as 0.85 % which can be deconvoluted down to $<$ 0.5 %. The curve of the electrostatic potential sets an upper limit to the bunch length. As the electrons slow during dephase the more energetic electrons at the front start to decelerate allowing the electrons at the rear to obtain the same energy minimising the energy spread. If the bunch length is short compared to the potential curve then the energy spread will be low. As the bunch length increases it will expand around the potential curve and increase the energy spread. It is therefore possible to calculate an upper limit to the bunch length for a measured energy spread. The deconvoluted energy spread of 0.5 % sets an upper limit to the bunch length of 0.3 μm.

In Chapter 4 modelling of the mask and simulations of the set-up allowed the development of a high resolution, thin masked pepper-pot technique which were capable of making the first single shot emittance measurement of the highly relativistic mono-energetic electron bunches. This measurement was able to set an upper limit to the emittance of $\varepsilon_{\mathrm{n,x}} = 2.2 \pm 0.7$ π mm mrad and $\varepsilon_{\mathrm{n,y}} = 2.3 \pm 0.6$ π mm mrad for the horizontal and vertical emittances respectively. The emittance has been normalised to a measured energy of 125 $\pm$ MeV averaged over 200 consecutive shots. To create a beam with this low emittance the electrons must be injected at the rear of the bubble inside a radius of 3.4 $\pm$ 0.4

In additions to the narrow energy spread and transverse emittance measurement, a charge dependence was also observed in both the energy spread and beam divergence. The observed increase in divergence with $Q^{\frac{1}{2}}$ or $Q^{\frac{1}{3}}$ shows that that there is an increase

in charge per unit length (or an increase in current) with little to no increasing in bunch length. This increase in current with bunch lengths means that the increasing energy spread with charge is mostly, if not entirely, due to beam loading and not due to the bunch lengthening around the electrostatic potential curve.

The final parameter measured in this thesis is bunch length with the use of coherent transition radiation developed in Chapter 6. The electron beam parameters such as bunch width, angular spread, scatter, etc were taken into consideration to measure structures in the bunch as short as 1.6 fs with a charge of 0.65 pC giving a current of 0.4 kA. This short bunch also sets an upper limit to the energy spread of the electron bunch of 0.5 % otherwise the bunch would lengthen by too much. Therefore both the energy spread and bunch length measurements agree well with each other.

A second structure of a 5 fs bunch, separated from the short bunch by 10 fs and containing $\sim$50 % of the total charge, was also observed in the longitudinal structure. A second peak with higher energy spread ($\sigma_\gamma/\gamma = 4.3$ %) but lower peak energy (-4.5 ± 1.8) and containing 50% of the total charge was also observed in the energy spectra. These two structures agree with each other where the narrow energy peak is at dephasing and the lower energy, broad peak is delayed by 3.5 ± 1 fs. When this initial bunch is allowed to propagate 1 m from the source, to the same place as the bunch length measurement was made, the bunch separation grows to 9 ± 2 fs, which agrees with the measured 10 fs separation. Similarly the narrow energetic peak remains short, whereas the larger energy spread peak increases in length such that the propagate bunch is very similar to the measured bunch.

It is essential that LWFA have as low an energy spread as possible if the bunches are to be used as a driving source for synchrotrons and FELs. A low energy spread will (1) reduce the bandwidth of radiation produced in a synchrotron, (2) prevent the bunch drifting apart longitudinally as it passes through the drift space ensuring the bunch stays short and keep the current at its maximum and (3) the gain length of a FEL will not be increased. These high quality beam parameter have further positive implication for the production of radiation on the ALPHA-X beam line at the University of Strathclyde. Here, the LPWA is coupled with an undulator in a plan to create synchrotron and FEL radiation. The undulator has a period of $\lambda_u = 1.5$ cm, an undulator parameter, $K = 0.4$ and overall length of 1.5 m. Focusing the beam through the undulator to keep the beam size as constant as possible will result in an angular spread of 0.1 mrad and a spot radius of 95 μm (equations 1.4 and 1.5) for a 90 MeV beam with the measured emittance of $\varepsilon_n = 2.2\ \pi$ mm mrad. This will produce 250 nm synchrotron radiation with a spread of $<$2% due to the energy spread of 0.85%.

The high peak current caused by the 1.6 fs bunch containing 0.65 pC will start

to cause FEL gain. Using the measured parameters (and assuming they will all be produced at the same time) the FEL parameter is $\rho = 0.0027$ and a gain length is 25 cm. This would mean that is would be possible to see some gain but, as saturation occurs at approximately 10 gain lengths (McNeil & Thompson, 2010), saturation could not occur. However, this beam line has access to a second identical undulator which can also be installed. Focusing the beam through this would cause a larger spot size (32 μm) increasing the gain length to 32 cm. With this gain length, FEL gain would become close to saturation making it possible to create a 250 nm FEL.

8.1 Future Work

There is possibility to improve all of the experiments, as was discussed at the end of each of the chapter. The energy spread measurement was near to the resolution limits of the spectrometer and it is therefore essential to improve this if the very low energy spread predicated by the TR result (< 0.5 %) are to be directly measured. In addition, it is important to charge calibrate the spectrometer to ascertain how much charge is in the mono-energetic bunch. Alternatively, it would be possible to use the undulator itself to diagnose the energy spread (Gallacher et al., 2009). The undulator radiations bandwidth is a function of the energy spread in the electron bunch and can therefore be used to find it provided the angular spread, etc. is known.

Similar to the energy spread measurement the emittance measurement was also close to the resolution limits. The resolution can be reduced through mask improvements, mask/detector positioning and refining the electron beamlet detection. The beam will need to be passed through focusing and steering optics if it is to be used in applications. Therefore, the beam should be measured at various places along the beam line to test the effects of the optics on increasing the emittance.

The TR measurement was limited and the short structure is an upper limit. The short structured measured could be shorter but was limited by the interference between the foils and wavelength that the IR detector could measure. Simply changing the detector and foil separation would allow limits to be changed and a shorter bunch length to be measured. To allow more information about accelerator, the longitudinal structure should be measured at several positions along the beam line to measure the beams evolution. The beams evolution can then be calculated back to the accelerator by combining the longitudinal structure with high resolution energy spectra.

For use in an FEL, all of the beam parameters would need to occur at the same time. For this to be checked would require a single shot simultaneous measurement of all of the parameters. The TR can be made single shot with the use of a multiple

channel MCT with each of the wavelengths measured by a different channel of the MCT. The emittance measurement is already single shot, however it is a destructive measurement and would therefore prevent the other parameters from being measured. It is possible to use TR to measure the emittance . This is done by looking at the far field, $1/\gamma$, TR structure which is smoothed out by angular spread (Sakamoto et al., 2005) or by monitoring the transverse properites of the beam as it passes through multiple TR screens (Thomas, Delerue, & Bartolini, 2011). The degree of smoothing of the structure will provide the angular spread of the bunch and combining it with the beam diameter gives its emittance. If the TR foil is thin enough or if it is placed at the beams focus, it should not destroy the beams emittance and therefore the electrons could continue onto the spectrometer for the energy spread measurement.

References

Agostinelli, S., Allison, J., Amako, K., Apostolakis, J., Araujo, H., Arce, P., et al. (2003). Geant4-a simulation toolkit. *Nuclear Instruments & Methods in Physics Research Section a-Accelerators Spectrometers Detectors and Associated Equipment*, *506*(3), 250-303.

Akhiezer, A. I., & Polovin, R. V. (1956). Theory of wave motion of an electron plasma. *Soviet Physics Jetp-Ussr*, *3*(5), 696-705.

Anderson, S. G., Rosenzweig, J. B., LeSage, G. P., & Crane, J. K. (2002). Space-charge effects in high brightness electron beam emittance measurements. *Physical Review Special Topics-Accelerators and Beams*, *5*(1).

Backus, S., Durfee, C. G., Murnane, M. M., & Kapteyn, H. C. (1998). High power ultrafast lasers. *Review of Scientific Instruments*, *69*(3), 1207-1223.

Bhat, C. M., Carneiro, J. P., Fliller, R. R., Kazakevich, G., Ruan, J., Santucci, J., et al. (2007). Envelope and multi-slit emittance measurements at fermilab a0-photoinjector and comparison with simulations. In *Ieee particle accelerator conference* (p. 2180-2182). Albuquerque, NM: Ieee.

Bonifacio, R., Pellegrini, C., & Narducci, L. M. (1984). Collective instabilities and high-gain regime in a free-electron laser. *Optics Communications*, *50*(6), 373-378.

Browne, C. P., & Buechner, W. W. (1956). Broad-range magnetic spectrograph. *The Review of Scientific Instruments*, *27*(11), 899-907.

Brunetti, E., Shanks, R. P., Manahan, G. G., Islam, M. R., Ersfeld, B., Anania, M. P., et al. (2010). Low emittance, high brilliance relativistic electron beams from a laser-plasma accelerator. *Physical Review Letters*, *105*(21), 4.

Casalbuoni, S., Schmidt, B., & Schmuser, P. (2005). Far-infrared transition and difraction radiation, part 1: Production, diffraction effects and optical propagation. *TESLA Report 2005-15*.

Chen, F. (2006). *Introduction to plasma physics and controlled fusion* (Vols. Vol.1, Plasma Physics). New York: Springer.

Cheriaux, G., Rousseau, P., Salin, F., Chambaret, J. P., Walker, B., & Dimauro, L. F.

(1996). Aberration-free stretcher design for ultrashort-pulse amplification. *Optics Letters*, *21*(6), 414-416.

Christov, I. P., Stoev, V. D., Murnane, M. M., & Kapteyn, H. C. (1996). Sub-10-fs operation of kerr-lens mode-locked lasers. *Optics Letters*, *21*(18), 1493-1495.

Cipiccia, S., Islam, M. R., Ersfeld, B., Shanks, R. P., Brunetti, E., Vieux, G., et al. (2011). Gamma-rays from harmonically resonant betatron oscillations in a plasma wake. *Nature Physics*, *7*(11), 867-871.

Dawson, J. M. (1959). Nonlinear electron oscillations in a cold plasma. *Physical Review*, *113*(2), 383-387.

Decker, C. D., Mori, W. B., Tzeng, K. C., & Katsouleas, T. (1996). Evolution of ultra-intense, short-pulse lasers in underdense plasmas. *Physics of Plasmas*, *3*(5), 2047-2056.

Delerue, N. (2011). Single shot transverse emittance measurement of multi-mev electron beams using a long pepper-pot. *Nuclear Instruments & Methods in Physics Research Section a-Accelerators Spectrometers Detectors and Associated Equipment*, *644*(1), 1-10.

Diels, J., & Rudoplh, W. (n.d.). *Ultrashort laser pulse phenomena*. Academic Press.

Edmund. (n.d.). *http://www.edmundoptics.com/optics/optical-lenses/ultraviolet-uv-infrared-ir-singlet-lenses/zinc-selenide-meniscus-lenses/3079.*

Esarey, E., Schroeder, C. B., & Leemans, W. P. (2009). Physics of laser-driven plasma-based electron accelerators. *Reviews of Modern Physics*, *81*(3), 1229-1285.

Esarey, E., Sprangle, P., Krall, J., & Ting, A. (1996). Overview of plasma-based accelerator concepts. *Ieee Transactions on Plasma Science*, *24*(2), 252-288.

Faure, J., Glinec, Y., Gallot, G., & Malka, V. (2006). Ultrashort laser pulses and ultrashort electron bunches generated in relativistic laser-plasma interaction. *Physics of Plasmas*, *13*(5), 12.

Faure, J., Glinec, Y., Pukhov, A., Kiselev, S., Gordienko, S., Lefebvre, E., et al. (2004). A laser-plasma accelerator producing monoenergetic electron beams. *Nature*, *431*(7008), 541-544.

Flottmann, K. (1996). Pepper pot design for spae charge dominated high brightness beams. *TESLA FEL-Report 1996-09*.

Fonseca, R. A., Silva, L. O., Tsung, F. S., Decyk, V. K., Lu, W., Ren, C., et al. (2002). Osiris: A three-dimensional, fully relativistic particle in cell code for modeling plasma based accelerators. *Computational Science-Iccs 2002, Pt Iii, Proceedings*, *2331*, 342-351.

Fritzler, S., Lefebvre, E., Malka, V., Burgy, F., Dangor, A. E., Krushelnick, K., et al. (2004). Emittance measurements of a laser-wakefield-accelerated electron

beam. *Physical Review Letters*, *92*(16), -.

Fuchs, M., Weingartner, R., Popp, A., Major, Z., Becker, S., Osterhoff, J., et al. (2009). Laser-driven soft-x-ray undulator source. *Nature Physics*, *5*(11), 826-829.

Fuji. (2008). *Internal report: Url: http://www.fujifilm.com/products/lifescience/ si-imgplate/imgplate.html.*

Gallacher, J. G., Anania, M. P., Brunetti, E., Budde, F., Debus, A., Ersfeld, B., et al. (2009). A method of determining narrow energy spread electron beams from a laser plasma wakefield accelerator using undulator radiation. *Physics of Plasmas*, *16*(9), 8.

Geddes, C. G. R., Toth, C., Tilborg, J. van, Esarey, E., Schroeder, C. B., Bruhwiler, D., et al. (2004). High-quality electron beams from a laser wakefield accelerator using plasma-channel guiding. *Nature*, *431*(7008), 538-541.

Ginsburg, V., & Frank, I. (1946). Radiation of a uniformly moving electron due to its transition from one medium into another. *Zhurnal Eksperimentalnoi I Teoreticheskoi Fiziki*, *16*(1), 15-28.

Ginzburg, V., & Trytovich, V. (1990). *Transition radiation and transition scattering*. Bristol and New York: Adam Hilger.

Ginzburg, V. L. (1982). Transition radiation and transition scattering. *Physica Scripta*, *T2*, 182-191.

Glinec, Y., Faure, J., Guemnie-Tafo, A., Malka, V., Monard, H., Larbre, J. P., et al. (2006). Absolute calibration for a broad range single shot electron spectrometer. *Review of Scientific Instruments*, *77*(10), 6.

Gruner, F., Becker, S., Schramm, U., Fuchs, M., Weingartner, R., Habs, D., et al. (2007). Design considerations for table-top, laser-based vuv and x-ray free electron lasers. *Applied Physics B-Lasers and Optics*, *86*(3), 431-435.

Humphries, S. (1990). *Charged particle beams*. John Wiley and Sons.

Ingleby, J. (2009). *Private communication with crystal supplier. url: http://www.ingcrys.com.*

Jackson, E. A. (1960). Nonlinear oscillations in a cold plasma. *Physics of Fluids*, *3*(5), 831-833.

Jackson, J. (1999). *Classical electrodynamics* (3rd edition ed.). John Wiley and sons, Inc.

Jaroszynski, D. A., Bingham, R., Brunetti, E., Ersfeld, B., Gallacher, J., Geer, B. van der, et al. (2006). Radiation sources based on laser-plasma interactions. *Philosophical Transactions of the Royal Society a-Mathematical Physical and Engineering Sciences*, *364*(1840), 689-710.

Jaroszynski, D. A., Ersfeld, B., Giraud, G., Jamison, S., Jones, D. R., Issac, R. C., et

al. (2000). The strathclyde terahertz to optical pulse source (tops). *Nuclear Instruments & Methods in Physics Research Section a-Accelerators Spectrometers Detectors and Associated Equipment*, *445*(1-3), 317-319.

Jing, T., Goodman, C., Cho, G., Drewery, J., Hong, W., Lee, H., et al. (1993). Evaluation of a structured cesium iodide film for radiation imaging purposes. *Nuclear Science Symposium and Medical Imaging Conference, 1993., 1993 IEEE Conference Record*, *3*, 1878-1882.

Kalmykov, S., Yi, S. A., Khudik, V., & Shvets, G. (2009). Electron self-injection and trapping into an evolving plasma bubble. *Physical Review Letters*, *103*(13).

Katsouleas, T. (2004). Accelerator physics - electrons hang ten on laser wake. *Nature*, *431*(7008), 515-516.

Katsouleas, T., Wilks, P., Chen, J., Dawson, J. M., & Su, J. (1987). Beam loading in plasma accelerators. *Part. Accel.*, *22*, 81-99.

Khan, S., Holldack, K., Kachel, T., Mitzner, R., & Quast, T. (2006). Femtosecond undulator radiation from sliced electron bunches. *Physical Review Letters*, *97*(7).

Kostyukov, I., Nerush, E., Pukhov, A., & Seredov, V. (2009). Electron self-injection in multidimensional relativistic-plasma wake fields. *Physical Review Letters*, *103*(17).

Kraus, H. G. (1990). Huygens-fresnel-kirchhoff wave-front diffraction formulation - paraxial and exact gaussian laser-beams. *Journal of the Optical Society of America a-Optics Image Science and Vision*, *7*(1), 47-65.

Kruer, W. (2003). *The physics of laser plasma interactions*. New York: Springer.

Leemans, W. P., Nagler, B., Gonsalves, A. J., Toth, C., Nakamura, K., Geddes, C. G. R., et al. (2006). Gev electron beams from a centimetre-scale accelerator. *Nature Physics*, *2*(10), 696-699.

Lu, W., Tzoufras, M., Joshi, C., Tsung, F. S., Mori, W. B., Vieira, J., et al. (2007). Generating multi-gev electron bunches using single stage laser wakefield acceleration in a 3d nonlinear regime. *Physical Review Special Topics-Accelerators and Beams*, *10*(6).

Luchini, P., & Motz, H. (1990). *Undulators and free-electron lasers*. Oxford Science Publications.

Ludziejewski, T., Moszynski, M., Kapusta, M., Wolski, D., Klamra, W., & Moszynska, K. (1997). Investigation of some scintillation properties of yag:ce crystals. *Nuclear Instruments & Methods in Physics Research Section a-Accelerators Spectrometers Detectors and Associated Equipment*, *398*(2-3), 287-294.

Lumpkin, A. H. (1997). On the path to the next generation of light sources. *Nuclear Instruments & Methods in Physics Research Section a-Accelerators Spectrometers*

Detectors and Associated Equipment, *393*(1-3), 170-177.

Lundh, O., Lim, J., Rechatin, C., Ammoura, L., Ben-Ismail, A., Davoine, X., et al. (2011). Few femtosecond, few kiloampere electron bunch produced by a laser-plasma accelerator. *Nature Physics*, *7*(3), 219-222.

Manahan, G. G., Brunetti, E., Shanks, R. P., Islam, M. R., Ersfeld, B., Anania, M. P., et al. (2011). High resolution, single shot emittance measurement of relativistic electrons from laser-driven accelerator. In *Conference on laser acceleration of electrons, protons, and ions and medical applications of laser-generated secondary sources of radiation and particles* (Vol. 8079). Prague, CZECH REPUBLIC: Spie-Int Soc Optical Engineering.

Mangles, S. P. D., Murphy, C. D., Najmudin, Z., Thomas, A. G. R., Collier, J. L., Dangor, A. E., et al. (2004). Monoenergetic beams of relativistic electrons from intense laser-plasma interactions. *Nature*, *431*(7008), 535-538.

Martinez, O. E. (1987). 3000 times grating compressor with positive group-velocity dispersion - application to fiber compensation in 1.3-1.6 mu-m region. *Ieee Journal of Quantum Electronics*, *23*(1), 59-64.

Martinez, O. E., Gordon, J. P., & Fork, R. L. (1984). Negative group-velocity dispersion using refraction. *Journal of the Optical Society of America a-Optics Image Science and Vision*, *1*(10), 1003-1006.

McNeil, B. W. J., & Thompson, N. R. (2010). X-ray free-electron lasers. *Nature Photonics*, *4*(12), 814-821.

Meadowcroft, A. L., Bentley, C. D., & Stott, E. N. (2008). Evaluation of the sensitivity and fading characteristics of an image plate system for x-ray diagnostics. *Review of Scientific Instruments*, *79*(11), 4.

Mori, W. B. (1997). The physics of the nonlinear optics of plasmas at relativistic intensities for short-pulse lasers. *Ieee Journal of Quantum Electronics*, *33*(11), 1942-1953.

Nakanii, N., Kondo, K., Suzuki, S., Kobayashi, T., Asaka, T., Yanagida, K., et al. (2007). Absolute calibration of imaging plate for electron spectrometer measuring gev-class electrons. In *5th international conference on inertial fusion sciences and applications(ifsa 2007)* (Vol. 112). Kobe, JAPAN: Iop Publishing Ltd.

Nemeth, K., Shen, B. G., Li, Y. L., Shang, H. T., Crowell, R., Harkay, K. C., et al. (2008). Laser-driven coherent betatron oscillation in a laser-wakefield cavity. *Physical Review Letters*, *100*(9), 4.

Ohkubo, T., Maekawa, A., Tsujii, R., Hosokai, T., Kinoshita, K., Kobayashi, K., et al. (2007). Temporal characteristics of monoenergetic electron beams generated by

the laser wakefield acceleration. *Physical Review Special Topics-Accelerators and Beams*, *10*(3), 6.

Pukhov, A., Gordienko, S., Kiselev, S., & Kostyukov, I. (2004). The bubble regime of laser-plasma acceleration: monoenergetic electrons and the scalability. *Plasma Physics and Controlled Fusion*, *46*, B179-B186.

Pukhov, A., & Vehn, J. Meyer-ter. (2002). Laser wake field acceleration: the highly non-linear broken-wave regime. *Applied Physics B-Lasers and Optics*, *74*(4-5), 355-361.

Reid, G., & Wynne, K. (2000). Ultrafast laser technology and spectroscopy. *Encyclopedia of Analytical Chemistry*, 13644-13670.

Reitsma, A. J. W., Cairns, R. A., Bingham, R., & Jaroszynski, D. A. (2005). Efficiency and energy spread in laser-wakefield acceleration. *Physical Review Letters*, *94*(8), -.

Rosenzweig, J., & Colby, E. (1994). Charge and wavelength scaling of rf photoinjector designs. In *6th advanced accelerator concepts workshop* (Vol. 335, p. 724-737). Fontana, Wi: Aip Press.

Rosenzweig, J. B., & Travish, G. (1994). Design considerations for the ucla pbpl slit-based phase space measurement systems. *PBPL Internal, http://pbpl.physics.ucla.edu/Literature/*.

Rule, D. W. (1987). Transition radiation diagnostics for intense charged-particle beams. *Nuclear Instruments & Methods in Physics Research Section B-Beam Interactions with Materials and Atoms*, *24-5*, 901-904.

Sakamoto, F., Iijima, H., Dobashi, K., Imai, T., Ueda, T., Watanabe, T., et al. (2005). Emittance and energy measurements of low-energy electron beam using optical transition radiation techniques. *Japanese Journal of Applied Physics Part 1-Regular Papers Brief Communications & Review Papers*, *44*(3), 1485-1491.

Schlenvoigt, H. P., Haupt, K., Debus, A., Budde, F., Jackel, O., Pfotenhauer, S., et al. (2008). A compact synchrotron radiation source driven by a laser-plasma wakefield accelerator. *Nature Physics*, *4*(2), 130-133.

Schroeder, C. B., Esarey, E., Tilborg, J. van, & Leemans, W. P. (2004). Theory of coherent transition radiation generated at a plasma-vacuum interface. *Physical Review E*, *69*(1), 12.

Sears, C. M. S., Buck, A., Schmid, K., Mikhailova, J., Krausz, F., & Veisz, L. (2010). Emittance and divergence of laser wakefield accelerated electrons. *Physical Review Special Topics-Accelerators and Beams*, *13*(9), 7.

Semushin, S., & Malka, V. (2001). High density gas jet nozzle design for laser target production. *Review of Scientific Instruments*, *72*(7), 2961-2965.

Settakorn, C. (2001). Generation and use of coherent transition radiation from short electron bunches. *Unpublished doctoral dissertation - Stanford University*, *SLAC-Report-576*.

Shanks, R. P., Anania, M. P., Brunetti, E., Cipiccia, S., Ersfeld, B., Gallacher, J. G., et al. (2009). Pepper-pot emittance measurement of laser-plasma wakefield accelerated electrons. In *Conference on harnessing relativistic plasma waves as novel radiation sources from terahertz to x-rays and beyond* (Vol. 7359). Prague, CZECH REPUBLIC: Spie-Int Soc Optical Engineering.

Shibata, Y., Ishi, K., Takahashi, T., Kanai, T., Arai, F., Kimura, S., et al. (1994). Coherent transition radiation in the far-infrared region. *Physical Review E*, *49*(1), 785-793.

Simon, J. D. (1989). Ultrashort light-pulses. *Review of Scientific Instruments*, *60*(12), 3597-3624.

Sprangle, P., Esarey, E., Ting, A., & Joyce, G. (1988). Laser wakefield acceleration and relativistic optical guiding. *Applied Physics Letters*, *53*(22), 2146-2148.

Stingl, A., Spielmann, C., Krausz, F., & Szipocs, R. (1994). Generation of 11-fs pulses from a ti-sapphire laser without the use of prisms. *Optics Letters*, *19*(3), 204-206.

Tajima, T., & Dawson, J. M. (1979). Laser electron-accelerator. *Physical Review Letters*, *43*(4), 267-270.

Tanaka, K. A., Yabuuchi, T., Sato, T., Kodama, R., Kitagawa, Y., Takahashi, T., et al. (2005). Calibration of imaging plate for high energy electron spectrometer. *Review of Scientific Instruments*, *76*(1), 5.

Thomas, C., Delerue, N., & Bartolini, R. (2011). Single shot transverse emittance measurement from otr screens in a drift transport section. *Journal of Instrumentation*, *6*, 14.

Treacy, E. (1969). Optical pulse compression with diffraction gratings. *Ieee Journal of Quantum Electronics*, *5*(9), 454-458.

Tzoufras, M., Lu, W., Tsung, F. S., Huang, C., Mori, W. B., Katsouleas, T., et al. (2008). Beam loading in the nonlinear regime of plasma-based acceleration. *Physical Review Letters*, *101*(14).

Van Der Geer, B., & Loos, M. (2001a). *The general particle tracer*. Unpublished doctoral dissertation.

Van Der Geer, B., & Loos, M. (2001b). *General particle tracer code: design, implementation and application*. Unpublished doctoral dissertation.

Wartski, L., Roland, S., Lasalle, J., Bolore, M., & Filippi, G. (1975). Interference phenomenon in optical transition radiation and its application to particle beam

diagnostics and multiple-scattering measurements. *Journal of Applied Physics*, *46*(8), 3644-3653.

Wiedemann, H. (2007). *Particle accelerator physics*. New York: Springer.

Wiggins, S. M., Anania, M. P., Brunetti, E., Cipiccia, S., Ersfeld, B., Islam, M. R., et al. (2009). Narrow spread electron beams from a laser-plasma wakefield accelerator. In *Conference on harnessing relativistic plasma waves as novel radiation sources from terahertz to x-rays and beyond* (Vol. 7359). Prague, CZECH REPUBLIC: Spie-Int Soc Optical Engineering.

Wiggins, S. M., Gallacher, J. G., Schlenvoigt, H. P., Schwoerer, H., Welsh, G. H., Issac, R. C., et al. (2011). Laser-driven radiation sources in the alpha-x project. In *Conference on harnessing relativistic plasma waves as novel radiation sources from terahertz to x-rays and beyond ii* (Vol. 8075). Prague, CZECH REPUBLIC: Spie-Int Soc Optical Engineering.

Wiggins, S. M., Issac, R. C., Welsh, G. H., Brunetti, E., Shanks, R. P., Anania, M. P., et al. (2010). High quality electron beams from a laser wakefield accelerator. *Plasma Physics and Controlled Fusion*, *52*(12), 8.

Wiggins, S. M., Shanks, R. P., Issac, R. C., Welsh, G. H., Anania, M. P., Brunetti, E., et al. (2010). High quality electron beams from a laser wakefield accelerator. *2010 Conference on Lasers and Electro-Optics (Cleo) and Quantum Electronics and Laser Science Conference (Qels)*, 2.

Yan, L. X., Du, Y. C., Xiang, D., Li, R. K., Qian, H. J., Huang, W. H., et al. (2008). Multislit-based emittance measurement of electron beam from a photocathode radio-frequency gun. *Chinese Physics Letters*, *25*(5), 1640-1643.

Zhang, M. (1998). Emittance formula for slits and pepper-pot measurement. *FERMILAB-TM-1998*.